Prifysgol Cymru
Y Drindod Dewi Sant
University of Wales
Trinity Saint David

Enhanced Magnetic Flux Leakage Analysis of the Distribution of Flux and The Effects of Velocity on Mild Steel Plates

Ashley Laurent Pullen

A thesis submitted to the University of Wales Trinity Saint David for the degree of

Doctor of Philosophy

Faculty of Architecture and Engineering

Supervisor: Professor Peter Charlton

Second Supervisor: Dr Nik Whitehead, Associate Professor

Industrial Supervisor: Professor Neil Pearson

2023

DECLARATION

This work has not previously been accepted in substance for any degree and is not being concurrently submitted in submitted in candidature for any degree.

Signed ..... (candidate)

Date .....

STATEMENT 1

This thesis is the result of my own investigations, except where otherwise stated. Where correction services have been used the extent and nature of the correction is clearly marked in a footnote(s). Other sources are acknowledged by footnotes giving explicit references. A bibliography is appended.

Signed ..... (candidate)

Date .....

STATEMENT 2

I hereby give consent for my thesis, if accepted, to be available for deposit in the University's digital repository.

Signed ..... (candidate)

Date .....

Acknowledgements

First of all, I would like to express my sincere gratitude to Professor Peter Charlton for his unending and unrivalled support, guidance, and sacrifices through difficult times that have made this thesis possible, and for that i am forever grateful. His passion for research and approach to supervision is truly inspiring. His dedication to his students and work in the field of NDT has provided an environment in which researchers can thrive.

Thanks must also go to Dr. Nik Whitehead Associate Professor who has provided superb advice and guidance throughout, who's knowledge and expertise provided great help both in the research and writing of this thesis.

Thank must also go to Professor Neil Pearson for the advice and guidance along the way. Thank you for making the practical testing undertaken within this thesis possible. I would also like to thank Ross Hannah for the crash course in MATLAB.

Thank you to my family, my parents, my partner and my siblings for the words of encouragement, support and belief.

Lastly, I would like to acknowledge the funding from the Knowledge Economy Skills Scholarships (KESS 2) and Eddyfi Ltd. Knowledge Economy Skills Scholarships (KESS 2) is a pan-Wales higher-level skills initiative led by Bangor University on behalf of the HE sector in Wales. It is part funded by the Welsh Government's European Social Fund (ESF) convergence programme for West Wales and the Valleys.

Abstract

This thesis focuses on an investigation into the velocity effects of a permanent magnet based magnetic flux leakage system. Both experimental and finite element analysis methods have been utilised to undertake a parametric study of the velocity effects on the induced flux and its distribution in plate thicknesses of $6mm$ through to $20mm$ thick 1020 grade steel. When there is a velocity difference between the plate and the excitation system, eddy currents are induced opposing the applied magnetic field distorting its profile. This has an adverse effect on MFL inspection by altering signal responses thus limiting achievable inspection velocities. An investigation of velocities ranging from 0.5 to $3m/s$ is undertaken on both defect free plates and plates containing spherical defects cut with a $22mm$ ball end cutter and varying percentage wall loss defects simulated for both near/top and far/bottom surfaces. From the results, it is indicated that the flux density distribution through the plate decreases as a function of depth. Once a plate depth of $16mm$ is reached it is shown that flux density is significantly reduced towards the underside of the plate. These combined effects influence defect detectability on larger plate thicknesses for the specific yoke design used in this paper.

The offset of signal changes laterally across the width of the magnetic yoke at the sensor position in practice. When the inspection material is considered to be saturated the signal offset is minor, and almost completely over-lapped where there is no defect present. This change in offset is significantly larger when the inspection material is under-saturated resulting in the channels becoming separated. Taking this into consideration, it is possible to identify if the inspection material is near saturation. Velocity also plays a key role in the signal offsets seen during a typical MFL inspection.

Taking this into consideration a solution to compensating for velocity and signal offset is provided identifying that signal offset is a function of instantaneous velocity and not a function of acceleration.

This thesis also demonstrates a novel method of compensating for changes in velocity during an inspection. This method requires system calibration to be undertaken at the lowest and highest speeds of the system and then interpolating between the two extremes to generate a Floating Calibration Curve (FCC). This provides a means of compensating for changes in scan velocity during an inspection increasing sizing accuracy and defect characterisation as a result.

Contents

List of Figures

List of Tables

Chapter 1

Introduction, Contributions and Organisation of Thesis

1.1 Introduction

The Magnetic Flux Leakage (MFL) method is a Non-Destructive Testing (NDT) technique that can be employed to identify and map material loss of ferromagnetic materials. The advantage of using this method over others is its ability to inspect large areas rapidly. Expanses coverable by an MFL system are in excess of hundreds of square meters in one day due to its $300mm$ wide sensor array travelling at speeds of up to $1.5m/s$, whilst detecting material loss with diameters in millimetres (mm)[1]. Although this technique is known for its rapid inspection speed, eddy currents produced in the plate by relative motion between the magnet assembly and the plate have an adverse effect on the signal response by distorting and opposing the induced magnetic fields [2]–[6]. In order to facilitate repair and keep storage tanks in-service for as long as possible defects need to be located and characterized accurately. The sizing of defects is a somewhat arduous process based upon the nature of how MFL testing is governed by measuring the leakage field of a defect that is affected by a multitude of parameters including defect volume, defect width, defect depth, saturation of the inspection specimen and the sensor lift-off. MFL is unable to provide basic defect geometries such as width and depth accurately. Pioneering work from Atherton [7]

and Charlton [8] both confirm that MFL is only capable of consistently estimating the volume of a defect. Since the work of Atherton [7] and Charlton [8] it has been attempted to characterise defects based on other characteristics such as defect width and, most commonly, depth. Defect depth is considered to be the most important parameter to characterise as it allows for storage tank integrity to be assessed with its remaining wall thickness. The relationship between defect depth and the signal response of the defect is non-linear. In order to fully assess a storage tank's integrity it first has to be prepared for inspection by emptying the contents and cleaning the inspection surface. Therefore, an internal investigation is time consuming and costly. Given the unknown characterisation of a defect with the potential of asset failure the need for understanding the principles of MFL inspection is paramount.

MFL is governed by several components, including levels of magnetisation, defect orientation, sensor configuration and component magnetic properties as well as other parameters including scanning velocity and the defect itself. For a permanent magnet based system the level of magnetic saturation achieved within each plate changes as a function of thickness. This is a direct result of supplied flux from a permanent magnet assembly. Saturation is considered to be the major factor of an MFL inspection and when saturation is achieved it is possible to detect smaller flaws than in a material that is under-saturated. Saturation levels differ with material properties, thus making MFL inspection difficult to characterise when alterations in material properties are seen through possible repairs or inconsistencies in material production. When an external magnetic field is applied to the ferromagnetic material via a relatively narrow yoke a non-homogeneous distribution of flux is induced into the plate. This effect is amplified when velocity is introduced along with under-saturated plates. Taking this into consideration it is possible for an MFL inspection to completely miss flaws based on their locations and characteristics. This emphasises the importance of magnetically saturating the test material, as will be shown in this thesis.

A material's capability to store magnetic flux is displayed in the form of a **BH**

Curve as seen in Figure 1.1. The **BH** curve refers to a material's capability to store magnetic flux density (**B**) as a function of the magnetic field strength (**H**) applied to a material that has no residual magnetisation. This is an illustration of the initial magnetisation of a typical ferromagnetic material showing the four stages of the magnetic domains as **H** is increased [9]. These four stages can be broken down as follows;

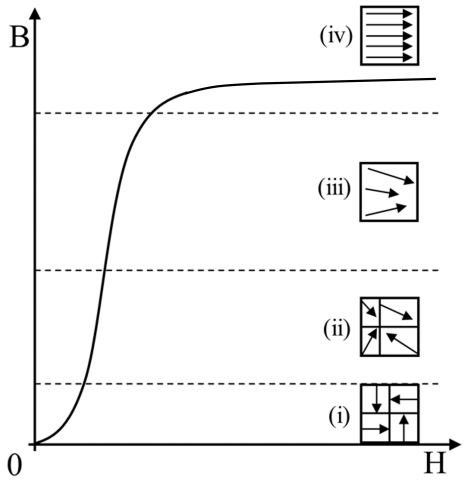

Figure 1.1: Illustration of a typical **BH** curve trend with the corresponding magnetic domains of a ferromagnetic material at each stage of the curve.

Stage (i) is the initial condition when the material is not influenced by an applied magnetic field, meaning that the domains are aligned randomly resulting in a net magnetisation of zero. This is caused by the domains being randomly aligned in a way where that each domain cancels the magnetising force of the other. Stage (ii) sees an increase in the applied **H** so that the plate becomes initially magnetised. This begins to align the magnetic domains within the plate. If the applied **H** field is increased further, stage (iii) is entered when the plate's magnetic domains are becoming almost fully aligned in the direction of the applied magnetic field. Finally, stage (iv) is when the material is in the state of saturation. This occurs when all magnetic domains become fully aligned in the direction to the applied **H** field. At this point an increase in **H** will not result in a significant change in **B**. During this state is where the most significant amount of leakage occurs due to the reduction in material volume without any flaws. This is a direct link to the increase of reluctance as the material's domains become aligned.

1.2 Background Information

The distribution of induced flux into the plate and how this is affected by scanning velocity is the main focus of this thesis. How the distribution is affected becomes most evident in un-saturated plates. Figure 1.2 illustrates the consequence of introducing velocities in such extreme scenarios using a 100 mm thick plate to clearly depict the problem at hand.

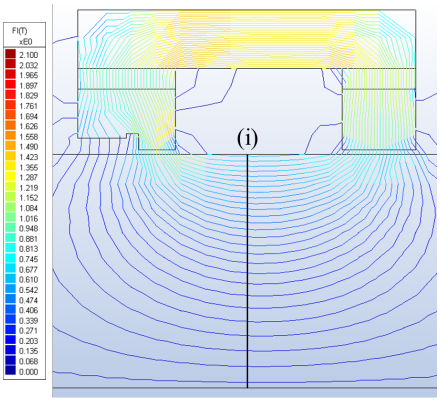

(a) 100 mm plate flux distribution with full penetration from the near labelled (i) through to the far surface for a stationary magnetiser.

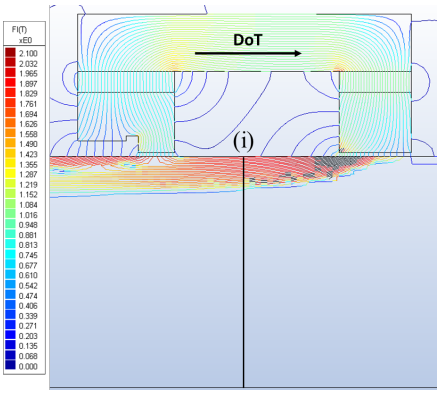

(b) Distribution of flux in a 100mm thick plate with a relative velocity of 3 m/s. A concentration of flux to the top surface of the plate is evident.

Figure 1.2: 100 mm extreme case incidents showing the severe alteration of the induced flux and its penetration. The direction of travel is labelled DOT in Figure 1.2b.

1.3 Aims and Objectives

- Investigate the effects of increasing scanning velocity of a commercial MFL floor scanner on a range of mild steel plate thicknesses that are most typically found in storage tanks using multiple 2D simulations to investigate the various effects caused by motion induced eddy currents. 3D simulation of these effects will also be acknowledged along with real world practical evaluation and testing of the simulated results.

- Investigate how the distribution of flux within the inspection material alters

with scanning velocity and plate thickness.

- Investigate the effects of the distribution of the flux within the material has on the signal amplitude of multiple defect sizes from 20 - 80% through wall thickness on the full range of plates at the four pre-defined scanning velocities and orientations.

1.4 Contribution to Knowledge

The distortion of the magnetic flux induced into the specimen due to the motional eddy current effect has yet to be documented and how this affect alters the ability to detect and characterise flaws based on its orientation during an inspection. It is found that the effects alters the signal amplitude from a defect based on its orientation (top/bottom surface flaw). Bottom surface flaws show a decrease in signal amplitude whereas top surface flaws increase in amplitude in unsaturated specimens as velocity increases. This is visible in both simulated and experimental data. As a direct result of this, if near surface flaws are to be singled out for detection then inspection speeds can be increased with no negative impact on detectability. Whereas the opposite is true for bottom surface defects.

A novel approach to compensate for changes in inspection velocity is investigated and how this can be applied in practice to improve defect sizing without moving the sensor location as suggested in previous studies [10], [11]. Moving the sensors to an optimal position will only be successful for a single velocity. Any deviation from an optimised velocity will result in changes to the defects responses. The method proposed in this thesis has been applied to simulated and practical results indicating that an alternative viable method can be used to compensate for variations in velocity during the acceleration and deceleration phases of scanning without the requirement of moving sensor positions.

1.5 Publications

Part of the work included in this thesis has been documented in the form of two journal papers. The following is a list of publications arising from the work in this thesis:

Journal Article – A. Pullen, P. Charlton, N. Pearson, N. Whitehead - Magnetic Flux Leakage Scanning Velocities for Tank Floor Inspection - Published in: IEEE Transactions on Magnetics (Volume 54, Issue: 9 Sep. 2018) – ISSN 1941-0069 – DOI: 10.1109/TMAG.2018.2853117 – https://ieeexplore.ieee.org/document/8418818

Journal Article - A. Pullen, P. Charlton, N. Pearson, N. Whitehead – Practical Evaluation of Velocity Effects on the Magnetic Flux Leakage Technique for Storage Tank Inspection – Published in: The British Institute of Non-Destructive Testing (Insight) – Non-Destructive Testing and Condition Monitoring, Volume 62, Number 2, February 2020, pp. 73-80(8) – https://doi.org/10.1784/insi.2020.62.2.73

As there is work that is included in both the publication articles and this thesis a statement will be made in each chapter of which publication the corresponding work relates. The publications are included in full in the appendices section of this thesis.

1.6 Organisation of Thesis

This thesis is organised into ***7*** chapters. Chapter 1 contains the Introduction, Background Information and outlines the motivation and main objectives of the research. An overview of the thesis and publications made from the work generated as part of this thesis. Furthermore, the main contributions to knowledge are also presented in this section of the thesis, along with resulting peer reviewed journal publications.

Chapter 2, where background information is given on the thesis as a whole. This includes storage tanks and the importance of maintenance, MFL principles accompanied by the relevant magnetic theory and the other techniques used in the inspection

process. Finally, a literature review and the motivation for conducting such research is given due to a gap in literature relating to the relative velocity of a magnetiser and specimen is also included.

The third chapter describes the methods used to acquire the data presented in this thesis. The model configuration and governing equations section will show the models used for the 2D Simulation work along with the parametric study that will be included for each model. Also covered in this chapter is the experimental set-up and equipment used to acquire data.

Chapter 4 is where the results and analysis of the outlined parametric study begins with investigating the effects of scanning velocity on a saturated and an un-saturated plate in extreme conditions. This highlights the key issue when undertaking MFL inspection in motion. This chapter will then continue to address a multitude of problems commonly encountered during an MFL inspection. Firstly, a parametric study where the plate thickness is varied over a range of 6 mm to 20 mm whilst cycling through scanning velocities of 0.5, 1, 1.5 and 3 m/s. Continuing from this a flaw is introduced of 20 - 80% through wall thickness again following the previous trend of velocities and also with the addition of altering plate thickness to identify a reason for why in most literature a trend of signal reduction is seen from a flaw when velocities are induced. There is one scenario where signal amplitude is said to increase when higher velocities are introduced when most suggest a reduction is seen. Finally, a parametric study where defect size is altered and the effects of this are investigated. The conclusion to this chapter will be the outline of why literature is contradicting and the reasons why both results can be achieved.

In chapter 5 the experimental results are given. This data is used to validate the outcomes from the Finite Element Analysis software package used in chapter 4. It is shown that the trends identified with the simulated data hold true for experimentation where similar results show an alteration in the leakage field due to the

velocity-induced eddy currents. There is also a finding that the lateral distribution of flux is not consistent when greater plate thicknesses are introduced.

Furthermore chapter 6, as described in a journal publication, explores the relationship between MFL signal offsets and velocity. It is identified that this is in fact a relationship involving instantaneous velocity and not a factor of acceleration. Following this a means of correcting signal amplitudes for instantaneous velocity is shown and discussed.

Finally, chapter 7 consists of the conclusions to the findings throughout this work along with suggestions for further work to support the argument to the contributions of knowledge made in this thesis.

Chapter 2

Background and Related Work

2.1 Introduction

The purpose of this chapter is to provide background to the work presented in this thesis. Firstly, an overview of storage tanks and the typical systems used to inspect them is given. Following this is a review of previous literature on the topics of MFL simulation and the induced eddy current effect. NDT is used to identify flaws in structural materials and components, usually for assessing whether the asset is considered safe or should be decommissioned from use. NDT is most commonly used to locate fatigue cracking and corrosion of specimens. It is essential to be able to collect and interpolate data sets within this industry to aid in the understanding of how a system operates and its efficiency. Without adequate techniques, any attempt at data collection and analysis can be dangerous and poorly conceived. If this is the case, valuable time and many resources are wasted with erroneous conclusions made. Therefore, it is essential for engineers and technicians alike to have a knowledgeable understanding of proper techniques for gathering and interpreting data [12].

In the oil and gas industry there are two key cases where assets are inspected, Above-ground Storage Tanks (ASTs) and pipelines; both are commonly made from carbon steel. It is well known that carbon steel is susceptible to corrosion and requires regular inspection to determine its life span and structural integrity. Failures of such

assets can cause serious harm and pollution to the surrounding atmosphere. It is also of importance to minimize the time an asset is out of service. Therefore, rapid inspection speeds are required. The use of MFL to inspect the asset integrity helps reduce this time. A typical MFL system scans at $0.5m/s$ with a scan width of $0.3m$, where single crystal Ultrasonic probes range from 10-50mm in diameter. Phased Array probes vary in size depending on application. Typical Phased Array probes used for corrosion mapping range from approx 23 - 130mm [13]. Taking the dimensions of Ultrasonic probes into consideration and the fact they need coupling and pushed by hand this is considerably more time consuming than a typical MFL scan for the same coverage area.

2.2 Bulk Liquid Storage Tank's, Failures and Inspection

During the 1880's wooden barrels became replaced by riveted steel tanks that were used to store petroleum and other liquid chemical products. Atmospheric storage tanks contain liquids at ambient pressure and at or near ambient temperatures. These tanks are most commonly fabricated from mild steel on a concrete base and are designed to withstand an internal pressure/vacuum of 0.07bar.

2.2.1 Storage Tank Failures

In May of 2006 a study was published documenting 242 incidents containing storage tanks that occurred in industrial facilities over the previous 40 years. Storage tanks in refineries and chemical plants contain large volumes of volatile chemicals that are usually both flammable and hazardous. The significance of failures can vary from product loss through leakage or as catastrophic events such as explosions and fires often resulting in a spread of fire igniting nearby storage tanks[14].

There have been many guidelines and standards for the construction, material selection, design and management of storage tanks and their accessories put in place by trade organisations and engineering societies such as the American Petroleum In-

stitute (API), the American Institute of Chemical Engineers (AIChE), the American Society of Mechanical Engineers (ASME), and the National Fire Protection Association (NFPA) [14]. From the 242 incidents acknowledged in this study 114 (47.11%) of them occurred in North America, 72 in Asia & Australia, 38 in Europe, 9 South America and 9 in Africa as seen in Table 2.1.

Table 2.1: Storage tank failures around the world [14].

Year	North America	Asia & Australia	Europe	South America	Africa	Total
1960-1969	3	7	6	1	0	17
1970-1979	18	9	6	1	2	36
1980-1989	26	9	9	5	4	53
1990-1999	36	33	12	2	2	85
2000-2003	31	14	5	0	1	51
Subtotal	114	72	38	9	9	242

2.2.2 Storage Tank Inspection

As with most other NDT methods it is of utmost importance to prepare the inspection surface before testing may commence. An MFL inspection can tolerate general dust and debris more than ultrasonic testing; therefore, it is not essential to grit blast the surface before inspection, this results in a reduced time that the AST may be decommissioned [15]. MFL inspection may also take place on a wet or dry surface unlike that of ultrasound. Ferromagnetic debris is a more significant factor for an MFL system due to the likeliness of such debris causing spurious signals that will be picked up by the scanning system. If this occurs and is noticed by the operator it is essential a re-scan is undertaken. It is recommended by API or EEMUA that out-of-service inspection is undertaken as often as every 3 years, but most commonly every 10 years dependent on tank age and condition during its last inspection [16].

2.3 NDT Inspection Techniques

There are multiple methods used to test the integrity of a storage tank. Typically there are strict procedures in place to facilitate inspection using multiple methods of

investigation.

2.3.1 Ultrasound

Ultrasonic Testing (UT) utilises a high frequency source of sound energy to observe a material's state by conducting time based measurements. Ultrasonic inspection can be used for flaw detection/evaluation, material characterisation or even as a means of dimensional measurement. A typical single crystal UT transducer in its most simple form with no angled wedges is used for 90° inspection. A typical set-up consists of a pulse/receiver, transducer, and display devices. A high frequency pulse is generated by the pulse/receiver to vibrate the piezoelectric transducer that in turn transmits a sound wave into the material [17]. When the propagating wave front encounters a boundary between mediums or a flaw is encountered a large portion of the propagating wave front is reflected back to the transducer and received through the pulse/receiver, processed and displayed on a display most commonly incorporated into the pulse/receiver[18].

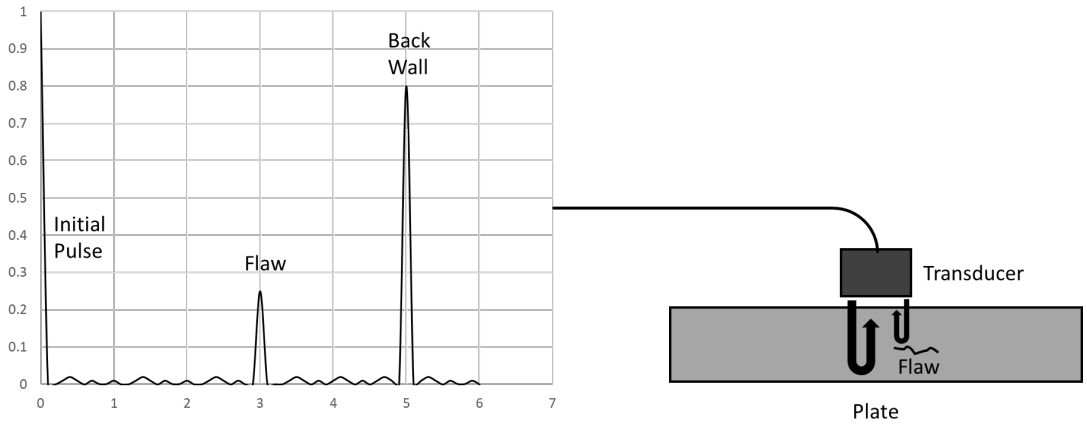

Figure 2.1: Illustration depicting a basic single crystal ultrasonic set-up used for volumetric flaw detection in a mild steel plate typical to what is found in storage tanks.

2.3.2 Magnetic Particle Inspection

Magnetic Particle Inspection (MPI) is a widely used technique on ferromagnetic materials for the detection of surface breaking, and occasionally sub-surface defects [19]. The technique involves applying a magnetic field to an inspection specimen either

from a magnet or an electrical current most commonly passed through the specimen in question. A solution containing a suspension of fine ferromagnetic particles is then applied to regions of interest. Where there are localised magnetic fields which develop around defects attract the particles causing high concentrations of fluid to produce an indication. A specific amount of flux is required to attract the particles suspended in the solution in order to produce an indication. Values that fall below this threshold will not be detected with MPI [19].

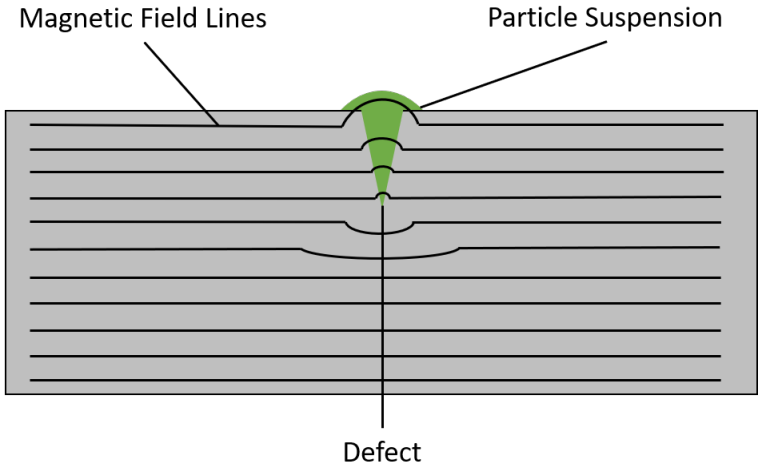

Figure 2.2: Showing an illustration of a typical MPI inspection where the lines of flux in and around the crack attracts the magnetic particles suspended in the fluid to highlight the defect.

2.3.3 Magnetic Flux Leakage

Magnetic Flux Leakage (MFL) is a widely-used and efficient non-destructive testing technique that has been extensively applied for defect inspection and characterisation of ferromagnetic structures, most commonly pipelines and AST. The principle behind MFL is the use of powerful rare earth or electromagnets to supply lines of flux into a ferrous material to the point of saturation. Where a geometric discontinuity or local anomalies are manifested in an abrupt change of magnetic permeability [3] and force magnetic flux to leak out of the specimen and be identified by an hall effect sensor or a pickup coil. The floors of ASTs are comprised of mild steel plates of varying thicknesses welded together. It is common practice to use thicker material around

what is known as the annular section of the tank. This is found around the circumference to support the tank walls. Typical thicknesses for annular plates are in the region of $16mm$. This proves difficult for inspection using a conventional permanent magnet yoke design as used in this thesis due to the constant supply of flux provided by the magnets not being able to saturate mild steel of such thicknesses. For the advantages of simplicity, low cost, air coupling and non-contact application MFL is extremely suitable for real time inspection. Although this method has a high probability of defect detection on saturated specimens, it is still fraught with problems associated with the sensitivity and interpretation of MFL signals. Many factors such as **BH** curves of the specimen and lift-off all play a crucial part in defect detection and sizing. This method is used to detect corrosion when large areas are required to be inspected in a short time scale and particularly when inspecting AST floors within the petrochemical industry where they are inspected periodically on a regular basis. To optimise the performance of MFL inspection, the environmental conditions should be considered as should the physical restrictions imposed by welds, risers and pipelines. The temperature inside and out of the tank can also affect inspection accuracy as ferromagnetic materials susceptibility to an induced field alters with temperature. The general condition of a storage tank is important and should be cleaned prior to inspection to remove ferromagnetic debris that can collect at the magnet poles resulting in the inability to scan. If this debris comes into contact with the sensor head unit between the poles alteration of the position can affect calibration and accuracy of test results.

MFL relies on the magnetic saturation of the inspected component where magnetic lines of flux flow through a permanent magnet assembly into the component. When a discontinuity is encountered, the magnetic flux is forced out from inside the material due to its reduced cross-sectional area resulting in flux leakage. An example is shown in Figure 2.3.

Due to the requirements of this particular inspection method for the use of AST

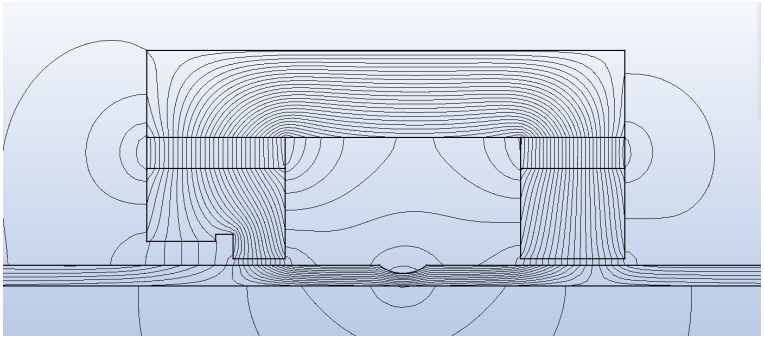

Figure 2.3: Model configuration showing the lines of flux penetrating into the inspection plate and a defect with the corresponding leakage field.

floors both top and bottom side defects are to be detected and therefore a strong magnetic field is required to be induced into the tank floor in order to achieve magnetic saturation. The closer the component becomes to magnetic saturation the more reliable and repeatable results will be. The typical level of saturation for steel AST floors is between 1.6 and 2.1 Tesla [20]. In this range residual magnetism from previous scans or other effects will be eliminated, providing relatively constant signal patterns. An inspection carried out below this threshold will result in a successful first scan but then reduces the reliability of the results due to residual magnetisation that can cause progressive deterioration of signal amplitude.

2.3.4 Commercial Floormap 3Di MFL System Overview

2.3.4.1 System Description

The Floormap FM3Di is the MFL scanner as seen in Figure 2.4 produced by Eddyfi UK Limited, previously called Silverwing (UK) Ltd that this work is based upon. This system is considered to be among the most advanced inspection systems to date. It allows for an array of alterations and adjustments to improve inspection. The FM3Di is the latest MFL tank floor scanner with complex mapping capabilities. The FM3Di has been developed using 20 years of AST floor inspection experience. This system incorporates state of the art technology alongside the latest research developments to provide a simple to use system that produces a comprehensive inspection solution.

Figure 2.4: An illustration of a typical Floormap FM3Di system that is modified to undertake the practical work in this thesis.

2.3.4.2 Data Acquisition Features

The FM3Di features both top and bottom surface discrimination via Eddyfi's innovative Surface Topology Reluctance Sensor (STARS) technology [21] [22]. The STARS technology is patent pending development and unique to Eddyfi. STARS utilise magnetism in a different way to MFL to provide a means of discriminating top from bottom side defects. Using the built in MFLi view the FM3Di offers a raw rectified view of the signals received from the inspection surface. This view is often used to distinguish between false and real defect identification by an experienced user. This technology may also be used to classify defect geometry i.e. lake or pipe-like defects providing an excellent verification tool to the operator. All data is captured in high resolution of 4.6 x $2mm$ with a scan speed of $500mm/s$, equating to a scan coverage of $9m^2$ every minute with a maximum scan length of 32metres. A DC motor with anti-static wheels ensures that the propulsion of the system causes no signal interference, providing the capability of such high speeds. The scan width is adjustable up to a maximum of

300mm. In order to capture the large amounts of data required to produce such complex inspection viewing methods the FM3Di utilises an array of 256 Hall Effect sensors with 64 channels. The FM3Di with its own on-board computer undertakes processing for the large amount of data, which may be instantaneously displayed for analysis. To aid in the analysis the system incorporates a dynamic cursor to assist with defect sizing. The system is powered by a 12V, 25amp-hour sealed lead acid battery that will provide up to two hours of operation and can operate in temperature between -30°C to 55°C. The FM3Di software provides the inspection system with means of instantaneously making an assessment of the previous scan. This is shown below in Figure 2.5.

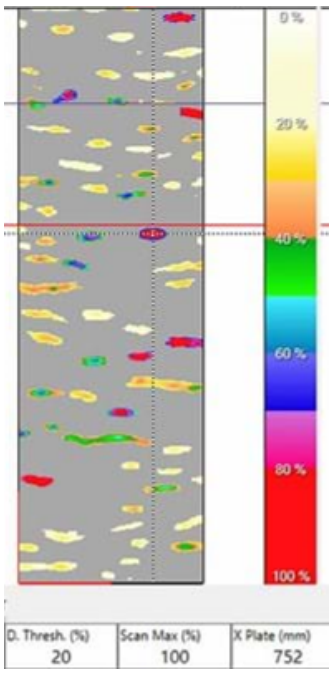

Figure 2.5: An example data set of a typical MFL scan of an Above Ground Storage Tank with defects measured in percentage wall loss ranging from 0% (white) to 100% (Red). In this case a threshold is set to not display any data below a 20% threshold. All data below the threshold is shown in Grey.

This allows for the inspector to easily identify the severity of the defect based on the colour pallet, red being 100% estimated percentage loss (EPL) and grey showing no present defects. It is also possible to use the cursor to define a location of the scanned area for an exact estimation of defect sizing along with 'x' and 'y' axis co-ordinates of the defect. This means that the defect may be pinpointed for further inspection using

other NDT methods. The magnet assembly used in the FM3Di is of the horseshoe type which dimensions allow for a scan width of $300mm$. The position of the sensor head assembly located between the magnet poles is to be set pre-inspection, this is known as adjusting the lift-off. Lift-off (the distance from the inspection surface to the sensor head position) directly affects the systems detection sensitivity. Low levels of lift-off are not always achievable during inspection due to the uneven surface of a corroded steel plate. When contact occurs between the inspection surface and the sensor head it is paramount to re-adjust the sensor head height to ensure consistent results.

2.3.5 Sensor Head

The sensor head is centred between the two poles of the magnet bridge and stretching the full scanning width of $300mm$. It consists of an array of Hall effect sensors that are spaced for optimum resolution and coverage. The spatial distance is sufficient enough to provide an overlap of the sensing range of each sensor to allow for full coverage. The Hall Effect sensors give a voltage signal proportional to the flux density of the field passing through the sensing element. The parallel positioning of the sensor head to the inspection surface allows for the normal (vertical) vectors of the magnetic flux leaked to be measured. It is also possible to arrange the sensor head tangential to the inspection surface allowing for the horizontal vector of the magnetic flux to be measured [23]. The sensor head assembly is positioned $2mm$ above the inspection surface to avoid unnecessary wear and contact with the surface to mitigate the likelihood of damage to the sensor array. Keeping the lift-off distance as low as possible also allows for an increase in sensitivity. This height is only altered during inspection where surface coatings are encountered and of satisfactory flatness to improve reliability of the results by increasing the system sensitivity. Due to the proximity of the sensor head to the inspection surface noise interference occurs during the scanning process. The main contributing factors to this are the material's variation of permeability and its surface roughness which will alter the amount of magnetic flux that can reside within the AST floor. There is also a large eddy current interference that is generated from the

movement of the magnet over the conducting inspection surface [18].

2.3.6 Signal Processing

To eliminate the noise generated from change in material permeability Eddyfi arrange their sensors in differential pairs. To further eliminate the noise caused from changes in surface variation it is possible to pass all signals through a low pass filter with a suitable cut-off frequency. It is also recommended that a threshold is set to reduce the number of spurious indications caused by signal noise. If it is required to clean the signal from the eddy current effects this can be done by breaking this effect into three stages. The first stage is the acceleration stage when the motorised carriage is brought up to speed causing a rising signal. The second is the constant inspection speed (steady state), and then finally a decreasing value when braking to a halt. Since the braking stage is sharper than that of the acceleration during start up, and the signals generated are of opposite polarity this can be eliminated by only measuring positive going signal arrangements. Passing all signals through a high pass filter with a suitable cut-off frequency will eliminate the start-up and constant speed state signals [18].

2.3.7 Signal Amplitudes and Affecting Factors

It is clear to indicate that there is a direct relationship between signal amplitude from a corrosion pit and the pit depth. However, as with many other NDT methods, the relationship is far more complex. Some of the known relationships that affect signal amplitude are the following:

- Flaw depth – this is the percentage loss of the specimen thickness.
- Flaw volume – the is the volume loss from the material
- Flaw shape – this is the profile of the corrosion pit
- Flaw aspect ratio – this is the ratio between the length and the width of the defected area

- Material permeability – a material's ability to retain a magnetic field
- Material thickness – this will affect the flux density levels achieved within the inspection surface.
- Magnetic force applied – this is a combination of the magnetic strength, lift-off, reluctance, and the magnetic material used
- Sensors – this is dependent on the sensor orientation, lift-off and the type used
- Hysteresis – hysteresis effects become problematic during repeat inspection when a plate is not fully saturated resulting in low repeatability and inconsistent results.
- Scanning Velocity – due to the movement of the permanent magnet eddy currents are induced into the plate. These eddy current generate magnetic flux in opposition to the magnetising field provided by the permanent magnet. This leads to distortions and non-linear distributions of induced plate flux density which can lead to distorted MFL signals being generated.

2.3.8 System Calibration

It is essential to calibrate the system on a plate thickness including surface finishes identical to that which is being inspected. It is also important that the calibration plate is made from material of similar magnetic properties. Adhering to this ensures that the system parameters are optimised for the inspection. Calibration plates consist of four pre-drilled defects of ranging from 20% estimated percentage of wall thickness loss (EPL) to 80% in increments of 20% as seen in the below in Figure 2.6. Calibration plates are manufacturer specific and therefore are designed and provided by Eddyfi in this instance.

It is required to complete scans with flaws on the top and bottom surface to ensure a complete calibration of both top and bottom surface defects. This also allows for the system to discriminate between top and bottom side flaws during inspection. It should also be noted due to the maximum diameter of the ball-end cutter used in

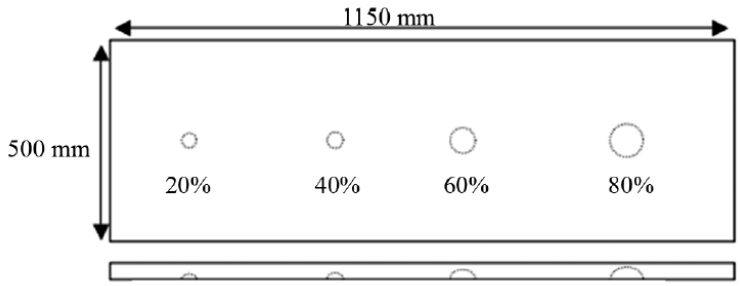

Figure 2.6: Showing typical calibration plate with multiple holes to be machined with a ball-end cutter.

this instance is $22mm$, defects can only be a maximum of $22mm$ wide. Once thicker plates are taken into consideration the ball-end defect will reach its maximum diameter creating a straight walled defect with a rounded bottom as demonstrated in Figure 2.7 where "w" is the defect width "d" is the defect depth, and "sp" is the straight portion of the defect wall where it has reached its maximum width. The defect depths are shown on a $20mm$ plate and the dimension are given in Table 2.2.

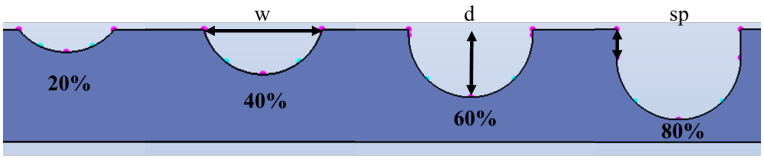

Figure 2.7: Illustration highlighting the dimension of defects cut into a $20mm$ thick plate with a $22mm$ ball end cutter.

Table 2.2: Table providing a list of defect parameters to indicate that defect width does not exceed $22mm$ in diameter for a $20mm$ thick plate.

Defect Size (%)	w (mm)	sp (mm)
20	16.97	n/a
40	21.7	n/a
60	22	1
80	22	5

2.4 Magnetic Principles

2.4.1 Material Magnetic Susceptibility

When a material is placed in a magnetic field, its reaction to this applied field at a molecular level is known as the Faraday Law of Magnetic Induction. However,

different materials react differently to an applied magnetic field [24]. This reaction is based on the material's atomic and molecular structure along with the strength of the applied magnetic field. The severity of this reaction is caused by three main factors in the material: electron motion, the change in motion caused by the external magnetic field, and the spin of the electrons.

In most cases electrons of an atom are found in pairs. When electrons are in pairs their spin direction is most commonly in opposed directions resulting in a net magnetisation of zero. Therefore, when atoms without full pairs are encountered they will have a magnetic field and will react more severely to an external field. Most materials can be classified as diamagnetic, paramagnetic or ferromagnetic[25].

2.4.1.1 Diamagnetic

Diamagnetic materials have a weak susceptibility to applied magnetic fields. Materials that fall into the diamagnetic category repel magnet fields and do not retain the magnetic properties when the applied field is removed [26]. In diamagnetic materials all the electrons are paired so there is no permanent net magnetic moment per atom. Diamagnetic properties arise from the realignment of the electron paths under the influence of an external magnetic field. Most elements in the periodic table, including copper, silver, and gold, are diamagnetic.

2.4.1.2 Paramagnetic

Paramagnetism is when a material is only slightly affected by an externally applied magnetic field positively. This means that the material is slightly attracted by a magnetic field but does not retain its magnetic properties when the field is removed. This state is seen when not all electrons have formed pairs, and where the alteration of alignment of the unpaired electrons is due to the external field [27].

2.4.1.3 Ferromagnetic

Ferromagnetic materials are strongly attracted to a magnetic force. This is exhibited by Iron (Fe), Nickel (Ni), Cobalt (Co) and Galodinium (Gd). These materials are

easily susceptible to a magnetic field and if the applied field is strong enough the material will reach a point known as saturation. Once the magnetic field is removed the material will remain magnetised. This is known as hysteresis [28]. This residual magnetisation can be removed in several ways. The most common method is to heat the material to its Curie temperature at which point the material behaves differently, losing its magnetic properties and becoming paramagnetic, although returns to a ferromagnetic state when cooled below this point. The magnetism in ferromagnetic materials is caused by the alignment of their constituent atoms, which causes them to act as elementary electromagnets. Ferromagnetism can be explained using the concept that groups of atoms in the material crystal lattice possess a common magnetic moment in such a way that an atom itself is an elementary electromagnet that is produced by the flow of electrons about its nucleus and by the spin of its electrons on their own axis. Most ferromagnetic materials halve half filled electron shells which, due to quantum interactions, gives rise to alignment of magnetic moments in neighbouring atoms. These atoms group together in what are referred to as magnetic domains [29]. Magnetic domains, and how a ferromagnetic material behaves when subject to an external magnetic field is discussed in the following sections 2.4.2, and 2.5.

2.4.2 Magnetic Domains

Magnetic domains are regions within a material that carry a magnetic moment in a uniform direction within the region. When a material is said to be demagnetised theses domains are randomly aligned in such a way that they cancel the magnetisation affect from each other [30]. When a ferromagnetic material is magnetised from an external magnetising field the magnetic domains become aligned, resulting in a net magnetisation in the same direction of the applied field.

2.5 Magnetism and Lines of Force

2.5.1 BH Curve

The **BH** curve refers to a materials capability to store magnetic flux density (B) as a function of the magnetic field force (**H**) applied to a material that has no residual magnetisation. The below figure shows the relationship between the **B** & **H** factors for steel. The initial relationship for steel is slow to begin with and then becoming almost linear up until a point of near saturation and begins to level-off to the point at which it becomes almost horizontal meaning a change in **H** does not result in a significant change in **B**. It is most common that flux density (**B**) is measured in Tesla (T) and **H** in Ampere-turns per metre (At/m) [25].

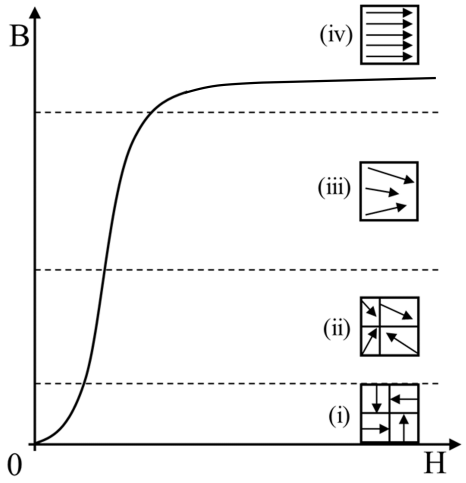

Figure 2.8: Illustration of a typical **BH** curve trend with the corresponding magnetic domains of a ferromagnetic material at each stage of the curve.

Work done by Charlton, Drury and Donne, [8] demonstrated by using computer modelling of various permanent magnets assemblies used during this period by Silverwing Ltd. The simulations taken place indicate that it is possible to achieve saturation of EN2 Carbon Steel plate with thicknesses up to and including 10mm. This was achievable by the magnet assembly used at this time .

2.5.2 Magnetic Hysteresis

Hysteresis is at the heart of the behaviour of magnetic materials. This phenomenon refers to the irreversibility of the magnetisation and demagnetisation process of a specific material. Permanent magnets rely on particular aspects of hysteresis. When an external magnetic field is applied to a ferromagnetic substance such as iron, the atomic dipoles align themselves with the external magnetic field direction. Once the magnetic field has been removed, a partial amount of alignment retains and the material has become magnetised. To remove this residual magnetisation the material is required to be heated above its Curie temperature so the magnetic domains re-align and cancel out. Also, a magnetic field may be applied in the opposite direction [31]. A material's magnetic properties can be shown in the form of a hysteresis loop. A hysteresis loop shows the nonlinear relationship between an induced magnetic flux density (**B**) and the magnetising force (**H**). The loop is generated by measuring the magnetic flux of a ferromagnetic material while the magnetising force is changed. A material that has not been previously magnetised or has been demagnetised completely will follow the curve shown by the dashed line in the below Figure 2.9.

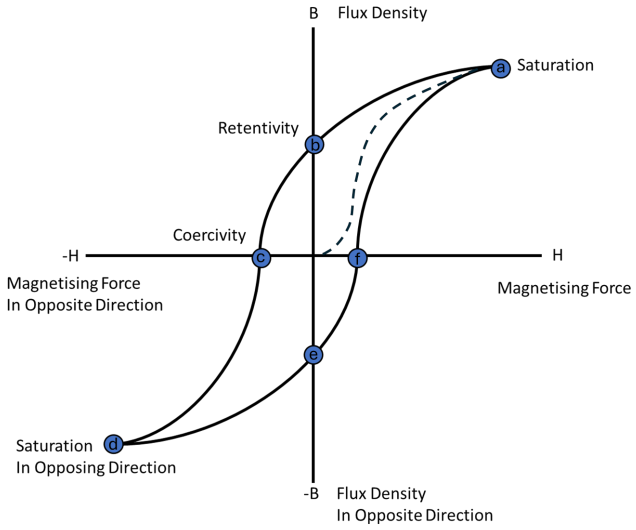

Figure 2.9: Illustration showing a typical Hysteresis loop.

There a number of points labelled in the above Figure of a typical hysteresis loop. At point 'a' almost all the magnetic domains are completely aligned within the material

meaning an increase in the applied magnetic field will result in an insignificant change in flux density therefore, reaching magnetic saturation. When the magnetising force is removed the curve will move from 'a' to point 'b'. At this point although the magnetising force has been removed there is still residual flux density in the material and may be referred to as the point of retentivity ('b'). The increase of the magnetising force in the opposite direction the point at which the material operates moves to point 'c' where the magnetising force has rotated enough magnetic domains to reduce the net flux to zero. This is the point of coercivity 'c', therefore the magnetising force required to remove the residual magnetism (retentivity 'b') is called the coercive force.

If the magnetising force is further increased in the opposite direction, the material will then become magnetically saturated in this opposite direction 'd'. If the magnetising force is removed the the curve will move to point 'e'. Point 'e' is the retentivity point 'b'. If **H** is increased further in the positive direction the curve will continue to points 'f' coercivity and 'a' magnetic saturation completing the loop.

2.5.3 Induced Magnetism

Given that the system modelled in this thesis uses a permanent magnet it becomes difficult to control the amount of magnetism that is imparted into the inspection material. Changes in magnetic flux density are dependent on surface thickness, meaning a corroded surface that alters in thickness varying from the nominal. There are three states of magnetic saturation; it can be ideally-, over-, or under-saturated. The following section consists of a number of Figures 2.10 2.11 2.12 identifying and explaining each of these states. It is also important not to allow prolonged contact between the MFL magnet's magnetic field and the inspection plate, to minimise the generation of an induced magnetic field. De-magnetisation of calibration plates should be undertaken on a regular basis to ensure that no residual magnetisation is stored within the reference plate causing an invalid calibration.

2.5.3.1 Ideal saturation

Achieving an ideal level of saturation means that all magnetic flux is contained within the inspection surface. This means that any leakage of flux is caused from present defects as shown in Figure 2.10.

Figure 2.10: Showing ideal saturation.

Achieving ideal saturation levels is also beneficial when undergoing an MFL inspection as previous scans will not have an impact resulting in consistent leaking fields from defects. This ensures that errors in defect sizing from the MFL system is likely to be from irregular defect geometry.

2.5.3.2 Under-saturation

Varying levels of under-saturation can occur dependant on material properties and thickness. If this is not accounted for it can have an adverse effect on defect detection and sizing capabilities.

Figure 2.11: showing a ferromagnetic material when under-saturated.

The magnetic field leaked from a given defect can vary depending on the level of under-saturation. The field may also be affected by prior scans that have already taken place meaning that repeatability is limited or inconsistent results are achieved. This problem is caused by the level of magnetic saturation achieved on a **BH** curve.

2.5.3.3 Over-saturation

Over-saturation is where the magnetic flux in the plate has reached its maximum and excess flux resides outside of the inspection surface regardless of defect presence. Over-saturation has no effect on repeatability, this means that leakage fields will be consistent for a certain defect and should be highly repeatable.

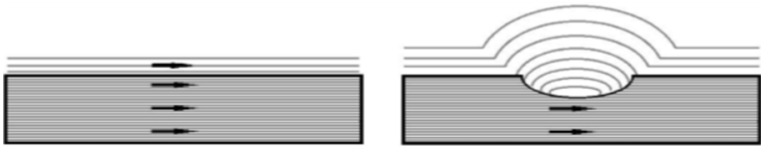

Figure 2.12: showing a ferromagnetic material that is over-saturated.

Low levels of over saturation are desirable due to minor changes in the leakage field being easier to detect with sensor head lift-off that is required for most inspection surfaces.

2.6 Literature Review

In 1985 Blakely et al [19] investigated the importance of the flux leakage field from an applied current and fields. In this report a range of cracks were used in a carbon-manganese steel specimen with width of 10 to 15µm with depths of 0.5 to 4.5mm. The magnetic disturbance caused by the defects was measured using a magneto-resistive film. Defects of similar dimensions were subsequently modelled using existing finite element software. The predictions of the models were in close agreement with flux measurements and were then used to determine the surface forces produced by magnetisation which act upon the particles used in magnetic particle inspection.

Förster [32] published on the non-destructive inspection of defects using the magnetic flux leakage method and presents a number of theoretical and experimental difficulties in 1985. It is documented that the leakage field strength from the defect is linearly linked with the field strength inside it. Förster states that discrepancies between measurement and calculations using the method of finite elements emphasise the need to fully understand the magnetic field strength inside the defect.

Following this Atherton and Quek [7] in 1988 demonstrated the capability to correlate two data streams in order to determine the orientation of a defect in underground oil and gas pipelines. This system distinguishes between near and far-side corrosion signals obtained by magnetic flux leakage detectors used in pipeline inspection. The method used involves a five stage approach to signal processing to aid in improving signal to noise ratio, identify potential defects, amplify and smooth defect signals selected by the previous stage. The fourth stage produces a simple output that indicates and distinguishes any potential top or bottom-side defects and finally the fifth stage enhances the output of the fourth stage by removing undesirable transient indications mainly caused by the offset in detector positions for the top and bottom sides.

Rodger et al [33] investigated the problems associated with 3D eddy currents generated by velocity effects. A 3D finite element formulation for a moving conductor problem is outlined. In 1992 Ito et al [34] provides an up-wind finite element solution of a travelling magnetic field along with the eddy currents produced in 3D at 30m/s.

Shin and Lord 1993 [35] numerically modelled the moving probe effects for elec-

tromagnetic non-destructive evaluation. It is stated that due to the nature of non-destructive testing methods and the associated geometries it is paramount that time transient analysis is necessary. The well known up-winding technique shows too much dissipation when time stepping is used.

In 1994 M. Marinescu and N. Marinescu [36] published on the importance of the computation of the leakage field for the magnetostatic detection method of defects in ferromagnetic materials. Many of previous computational methods are based on the dipole model. The dipole method is said to produce good results that are only applicable to defects that are thin rectangular slots. The method proposed is based on the experimentally confirmed assumption that the leakage field is negligible compared to the flux in the plate. It is said that the distribution in the plate can be reduced to a 2D problem.

In the same year (1994) Sun [5] observed that when velocities are introduced into a non-destructive electromagnetic tool distortion of the corresponding signal responses from leakage are identified. Sun states that this problem is under-investigated with complex magnet assemblies with only the simplest of geometries being considered leading to a lack of application in real world NDT problems. The results published by Sun [5] indicate a consistent reduction in signal amplitudes to far surface defects when velocities are increased from 0 m/s up to 10 m/s. It is noted that these results are affected by multiple parameters such as sensor location, air gap size and permeability. It finishes with the requirement for further investigation into optimisation of such parameters for increased inspection sensitivity for the detection and characterisation of electromagnetic NDT tools.

A numerical model of crack detection by magnetic flux leakage that takes into account the saturation of the induction flux density with the applied field was developed by Altschuler and Pignotti in 1995 [37]. The model contains no free parameters and is validated with measurements of materials properties and magnetic fields reported by Förster. It is then used to discuss the dependence of signals on the tube wall thickness, crack depth and width, and the strength of the applied field. An estimation is used to to analyse the signal to noise ratio to compute the optimal applied field

for crack detection. Difficulties arising in internal crack detection of shallow cracks in thick-walled pipes are also discussed in the paper.

Zhang et al. [38] published in 1995 on the magnetic flux leakage due to sub-surface defects in ferromagnetic specimens where two internal defects are taken into consideration, both of which are two dimensional. Firstly, a rectangular defect with the second elliptical in nature. Analytical expressions for calculating the leakage field due to the defects located under the surface were derived based on a simple domain boundary method, specifically the mirror method. The leakage field results were then compared with experimentally obtained values and were found to be within close agreement thus giving more useful information for evaluating sub-surface defects in ferromagnetic materials in the field of NDT.

Also in 1995 Charlton [8] completed a PhD thesis titled "A Theoretical and Experimental Study of the Magnetic Flux Leakage Method for the Analysis of Corrosion Defects in Carbon Steel Plate" where a computational analysis of the magnetic flux leakage method is undertaken and experimentally validated. Quarter symmetry 3D FEA was undertaken.

In 1996 Krause et al. [39] published on the variation of the stress-dependent magnetic flux signal with defect depth and flux density. In this paper multiple measures are taken to manipulate the flux within the magnetic circuit created between two permanent magnets a yoke and the pipeline material. Two methods were used to alter the flux density within the circuit. Firstly the size of the permanent magnets were reduced resulting in a reduction of flux density within the pipe wall. Secondly, steel bars were placed at the ends of the magnets to short the magnetic circuit, diverting a portion of the flux directly from the north to south pole of the same magnet. This diversion of the flux also reduced the flux density achieved within the pipe wall.

An investigation of examining the flux distributions in ferrite magnetic structures with the availability and power of the scientific visualisation tools was carried out by Skutt and Lee [40] at the time allowed for complex physical phenomena to be analysed. These tools were used to visualise the influence that geometrical shape and material characteristics can have on the distribution of magnetic flux in selected examples of

ferrite cores. It is suggested that the flux is non-uniformly distributed within ferrite cores. It is also suggested that it should be possible to improve designs for commercial and custom cores.

It has been found by Leonard and Atherton [41] that when conducting an MFL pipeline inspection variations in line pressure, bending, or residual stresses cause changes in the resultant signals from the leakage field. These changes in amplitude are thought to be due to the stress-induced changes in the bulk magnetic anisotropy on the preferred easy axis of the steel pipe wall. These suggestions are supported by the results presented in the form of finite element calculations. It is shown that an increase in signal amplitude and an increase of permeability in the axial direction is attributed to the higher flux density in the pipe wall resulting in more flux being diverted into the high reluctance air gap path. The decrease of MFL signal amplitude with an increase in permeability in the circumferential direction of the pipe is attributed to the flux path around the high reluctance defect instead of into the air gap.

In 1996 Mandayam et al. [42] published a paper titled "Invariance Transformation for Magnetic Flux Leakage Signals". In this paper the authors state that the MFL signal amplitude is dependent on the permeability of the material. This value is not consistent throughout and varies based on location within a material. The **BH** curve is dependent on the type of material and its grade and any residual stresses. The grade of material used can drastically alter the material's capability to store flux [42]. It is also noted when scanning speeds of greater than 0.9m/s are achieved over a defect the resultant signal becomes distorted, and overall reduced in magnitude. From this the authors provide a means of correcting the distorted signal near to that of its original state.

Katragadda et al. [43] note that axisymmetric numerical codes are often used when modelling NDT phenomena to approximate geometries which are not truly axisymmetric in nature. This is often the case when the computational requirements are too high for hardware capabilities to model exact geometries. Therefore a comparative study of 3D and axisymmetric magnetic assemblies for the use of MFL inspection in

pipelines is undertaken. In this paper it is observed that the signals obtained from the axisymmetric magnet assembly is much larger than that of the 3D scenario. This is somewhat attributed to the observation that the region under the defect is under much higher levels of saturation in the axisymmetric case. Also concluded in this study is that if quantitatively reasonable results are to be obtained the geometry should be modelled in its entirety. Authors hold the assumption that velocity effects on the signal amplitude is minimal below $4\mathrm{m\,s^{-1}}$. However, they suggest that further investigation into the effects of velocity at the higher speeds of up to $10\mathrm{m\,s^{-1}}$ and the axisymmetric and 3D cases be compared.

In 1997 Shin [44] published a paper of a numerical prediction of operating condition's for magnetic flux leakage inspection of moving steel sheets. Optimal operating condition for MFL inspection of moving steel sheets are predicted by using a 2D finite element model and a time step algorithm. Through numerical modelling of motional induction phenomena, signal variations due to velocity are investigated. It is found that the peak to peak signal changes along with the signal level but are said not to be proportional with velocity. The ideal sensor position of where the maximum peak to peak value is achieved also changes with velocity. Moving the sensor in the direction of travel increases the peak to peak value when compared to a sensor located in the centre of the magnet assembly improving the signal to noise ratio.

In 2004 Park [2] investigates the distortion of MFL signals produced due to the velocity induced eddy currents. The distortion of defect signals with inspection velocities of 0, 1, 2, 4 and 5 m/s are investigated. It is also worth noting that the results from this study are of a magnetically saturated specimen again with a far surface defect. Park's findings state that due to the magnetic field applied being able to saturate the specimen and running at high speeds there are strong velocity-induced eddy currents which cause a distortion of corresponding MFL signals. Supporting Sun [5]in 1994 it is concluded that increasing velocity reduces the peak amplitude of the signals.

Zuoying et al. [45] in 2006 states MFL to be the most cost effective form of NDT for corrosion mapping and is most commonly used in pipeline inspection. The investigation of this paper is undertaken to accurately assess a 3D model of a magnetic yoke

under typical pipeline inspection conditions. A defect is included and the resultant leakage signals given between the poles of the magnet yoke. A study is undertaken to change the lift-off value and measure the effect this has on the resultant leakage field for three defects of increasing volume. It is found that lift-off has the greatest effect on the peak-peak signal response between 1 and 2mm. After this point the peak-peak difference has a reduced rate of decay when lift-off is increased. Also an investigation of defect geometry and its effect on the resultant leakage signal is investigated by changing individual geometrical measurements at a time under the same inspection conditions. Firstly, the depth of the defect is altered from 10 to 100% through wall thickness in 10% intervals with lift-off changes from 1 to 5mm in increments of 1mm. From the results it is evident that defect depth has a significant role in the leakage field from a defect where the peak-peak values increase almost linearly with an increasing depth if all other parameters remain the same [45]. Following this the effect of defect width on the peak-peak leakage field is measured. Similarly to the depth of a defect the peak-peak leakage field increases along with the width of the MFL signal when the width of a defect is increased. When the length of the defect is taken into consideration the effect on the resultant peak-peak MFL signal amplitude is not as significant over defects with lengths from 10 - 80mm in length. The overall peak-peak signal decreases slightly when the defect length is increased. Increasing lift-off consistently has a negative impact on the MFL signal by reducing them regardless of the defect dimensions investigated in this paper.

Al-Naemi et al. [46] cover the Finite Element Method (FEM) methods of modelling the magnetic flux leakage NDT technique for ferromagnetic plate inspection. The two main methods of interest in this paper are both FEM techniques, 2D and 3D packages are used to solve the same problem. The excitation source used in this paper is of similar dimension to that used in this thesis. For both investigations in this paper a 6mm mild steel plate of the same material properties is considered as the inspection material. A lower flux density is seen in the plate in 3D when compared to that of 2D simulations. This in turn has an affect on the leakage field from the 80% through wall thickness spherical defect shape used for both simulations. It is stated that

the induced eddy currents that would normally distort the MFL signals as a result of relative motion between the excitation assembly and the inspection plate are not taken into consideration. Therefore, results are solved statically and then the defect is moved a distance under the excitation assembly and then re-solved. This is done multiple times to achieve a full signal response from the defect. As a result of this the signal responses are slightly larger than what is expected to be true. The comparison of the 2D and 3D results show that the signal amplitudes are found to be higher in the 2D case. The lower amplitude signals from the 3D simulations are marginally inflated when compared to experimentally taken measurements. Taking this into consideration the 2D models are acceptable for demonstrating the technique and relationships but will result in inflated results, whereas, the 3D model is closer to that of experimentally gathered data and is therefore the preferred option.

In 2006 Li [47] comments that the need for MFL type inspection is in great demand for in-line metal inspection and defect characterisation with emphasis to rail track and pipeline applications. Li states that the induction of the eddy currents due to the relative velocities distort the magnetic field making it difficult for defect characterisation. The effects of the relative velocity and the induced eddy currents along with several defect depths are examined. Li further concludes that signal magnitudes are reduced resulting in lower signal to noise ratio for greater scanning velocities.

Again the finite element method is used to assess a permanent magnet assembly used for the NDT method of MFL. In this paper by Xiuli et al. in 2007 [48] utilises a commercial finite element analysis package to interrogate a circumferential magnetiser with two permanent magnets utilising the 2.5D axisymmetric nature of the component. This will give an understanding of how the magnetiser behaves during an inspection. It is noted that not all the flux supplied by the magnets enter into the inspection material resulting in leakage fields around each magnet. A statement is made that this can be used to further optimise a system's performance to where the desired amount of flux is achieved in the inspection material is a common statement made throughout literature. Within this paper Xiuli takes measurements both within the inspection material and 2mm above the inspection surface between the two magnets.

This is said to be a common position for MFL sensor equipment.

Using the 3-D finite element method (FEM) Zhiye [49] investigated the velocity effect of MFL signals in 2008. Again, it was noted that the induced eddy currents alter the profile of the magnetic field due to the relative motion between the magnetiser and a specimen. It is stated that not only do the eddy currents have an effect on the signal magnitude but also its shape. It is concluded that the effects are amplified when larger defects are modelled.

Wang [3] in 2014 further investigates the eddy current effects of moving electromagnetic inspection for defect characterisation. In this study for near surface flaws Wang indicates that signal responses of defects under high speed MFL testing results in an increase in signal amplitude and sensitivity. This contradicts previous work. There are three main differences seen in this investigation to that of previous studies, initially the defect size, orientation and high velocities of up to 200 km/h are investigated.

A similar study has been conducted with rectangular defects and only addressing the leakage signals monitored from sensors. In 2015 Zhang [50] found that the induced eddy current effect has a correlation with the optimal sensor position at multiple velocities ranging from 0.1 to 20 m/s. It is stated that the peak to peak value of the leakage field moves from the centre of the magnetic bridge opposite to the direction of yoke travel.

Recently in 2017 Lu [51] has investigated the reconstruction of arbitrary defect profiles considering the velocity effects in MFL testing. Lu's simulation study indicates a reduction in signal amplitudes when velocities are increased following the trend of [2], [5], [47], [49], [50].

Most recently in 2023 L. Zhang et al. [52] explores how acceleration affects MFL signals produced in non-destructive testing. Both experimental and simulation work was carried out to investigate this issue. The results indicate that the pk-to-pk value of the leakage signal decreases by 15.1% to 26.6% when acceleration is present. The simulation results suggest that this decrease is caused by differences in magnetic field distortion, which is influenced by the distribution of eddy currents in the material

being tested. These findings can assist in optimising magnetic flux leakage systems to more accurately measure main defect features during system acceleration. Furthermore, the study emphasises the importance of conducting measurements at a constant velocity whenever possible.

2.7 Conclusions

This chapter has provided an overview of storage tank failures, inspection, magnetic methods and theory has been given. A focused literature review has been presented highlighting key findings This thesis will investigate why Wang [3] has achieved an increase in signal amplitude when all other work indicates a reduction of signal responses when undertaking MFL inspections with increasing velocities. It is initially noted that Wang uses a near surface defect and observes an increase and others who use far surface defects have a reduced signal amplitude. This thesis bridges the gap between these scenarios and investigates why this occurs.

Chapter 3

Methodology

3.1 Introduction

This chapter provides the theoretical and experimental methods of MFL principles used in the gathering of data within this thesis. It provides both the computational and experimental methods. The use of FEM modelling is firstly undertaken as it provides the necessary benchmarking and visual predictions of the magnetic fields within the specimen for the experimental phase as this cannot be directly measured or visualised experimentally.

There are multiple methods used for solving MFL problems computationally. The methods considered are a numerical magnetic circuit model to introduce the theory behind the phenomena of MFL testing and to identify the capabilities of the FM3Di that is being investigated. Secondly a FEM method is used to benchmark the system and investigate its characteristics and how it performs under inspection conditions and its interaction with and without defects statically and with the introduction of inspection velocity. The predicted values achieved can than be utilised for the prediction and expectation of how the system will perform experimentally.

3.2 Magnetic Circuit Theory and Governing Equations

3.2.1 Generating a Magnetic Field

A magnetic field is created when there is an electrical charge in motion. This can be due to an electrical current flowing through a conductor as was first discovered by Oersted in 1819. A magnetic field may also be generated by a permanent magnet. In this case, there is no conventional electric current, but the orbital motion and spins of electrons (also known as the Amperian Currents) within the magnetic material causing magnetisation of the material and a field is formed outside. This field exerts a force on current-carrying conductors and permanent magnets alike.

Firstly the force between two current carrying wires per unit length is given in equation 3.1

$$\mathbf{F} = \frac{\mu}{2\pi}.\frac{I_1 I_2}{r} \tag{3.1}$$

where F is the force between the wires, I_1, I_2 is the current flowing through each wire. The distance from the wire is shown by r and the permeability μ is the relationship between the relative permeability and that of free space by equation 3.2

$$\mu = \mu_0 \mu_r \tag{3.2}$$

where μ_0 is the permeability of free space ($4\pi \times 10^{-7} H/m$) and μ_r is the permeability relative to free space. As the permeability of a material is not constant and can change based on the magnetisation level or position within a material μ may be calculated if the flux density $\mathbf{B}$ and the applied magnetic force $\mathbf{H}$ are known factors from equation 3.3

$$\mu = \frac{\mathbf{B}}{\mathbf{H}} \tag{3.3}$$

The flux density ($\mathbf{B}$) can be calculated at a specified distance (r) from a current (I) carrying wire in equation 3.4

$$\mathbf{B} = \frac{\mu I}{2\pi r} \tag{3.4}$$

The intensity of the magnetic field may also be calculated by the equation 3.5

$$\mathbf{H} = \frac{\mathbf{B}}{\mu} \tag{3.5}$$

3.2.1.1 Biot-Savart Law

Calculating the magnetic field **H** generated by an electrical current can be done by using the Biot-Savart law, one of the fundamental laws of electromagnetism. In its traditional form the law gives the field contribution generated by a current flowing in an elementary length of conductor [25].

$$\delta\mathbf{H} = \frac{1}{4\pi r^2} i\delta l \times u \tag{3.6}$$

where i is the current flowing in an elemental length δl of a conductor, r is the radial distance, u is a unit vector along the radial direction, $\delta\mathbf{H}$ is the contribution to the magnetic field at r due to the current element $i\delta l$

3.2.1.2 Ampere's Law

Ampère found that a magnetic field is generated by an electrical charge in motion. Ampère demonstrated the magnetic field generated by an electrical circuit depended on the shape of the circuit and the current carried. Assuming each circuit is made of an infinite number of currents elements, each contributing to the field, and by summing or integrating these current contributions at a point to determine the field, Ampère derived the following [25]:

$$Ni = \int \mathbf{H}.\partial l \tag{3.7}$$

where N is the number of current carrying conductors, each carrying a current i amperes. This is then the source of the magnetic field **H**, and l is a line vector. This equation only holds true for constant currents [53].

3.2.2 Magnetic Circuit Theory and Calculator

A simplistic analytical approach can be undertaken to firstly understand and predict the behaviour of the magnetic assembly, and then to estimate the required amount of flux to saturate steel plates of varying thickness. Firstly, the dimensions of the magnetic assembly must be entered, including the magnet yoke dimensions, inspection material thickness, and the lift-off. The total required magneto motive force (mmf) needed to saturate the inspection material can be calculated from the following equation;

$$NI = \oint \mathbf{H}.\partial l = \sum mmf = \sum \mathbf{H}.l \tag{3.8}$$

where; N is the number of turns in a coil, I is the current in amps, $\mathbf{H}$ is the magnetic field intensity in A/m, l is the path length of the magnetic circuit in m, and mmf is the magnetomotive force

As the assembly in question is a permanent magnet based system the following equation is used;

$$\sum mmf = \sum \mathbf{H}.l \tag{3.9}$$

An example circuit is given in Figure 3.1 where the blue solid line is the magnetic yoke and the solid orange outline is the inspection material. the path length is broken down into multiple regions: the path through the yoke, path through the inspection material and finally the air gap/lift off distance. The cross-sectional area of each path is also calculated from a specified depth of the model.

For simplification purposes it is assumed that the material of the magnetic yoke and the inspection material are the same, 1020 grade mild steel. To find the magnetic field intensity $\mathbf{H}$ required in each component of the circuit the material $\mathbf{BH}$ curve must be known and in this instance is a reference curve taken from Oersted V930. Once the $\mathbf{BH}$ curve has been evaluated a saturation point of $2.1T$ is selected just prior to the linear portion of the curve. The value of $\mathbf{H}$ is extrapolated from the $\mathbf{BH}$ curve

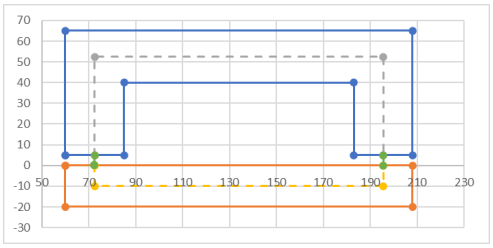

Figure 3.1: An example of a simple yoke geometry outlined in blue, plate geometry outlined in orange, and the dashed grey, green, and yellow lines are the yoke, air gap, and plate path lengths respectively.

at the point where **B** is at the saturation value of $2.1T$ as seen in Figure 3.2.

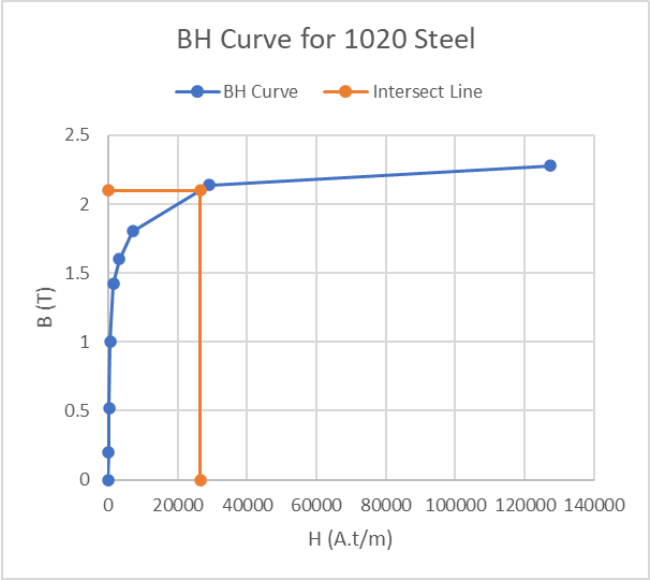

Figure 3.2: Showing the **BH** curve values and the saturation point.

Making the assumption the flux is constant throughout the circuit and that the cross-sectional area of the inspection material that is required to be at $2.1T$ it is possible to calculate the amount of flux in each component of the circuit using equation 3.10;

$$\mathbf{B} = \frac{\Phi}{A} \therefore \Phi = \mathbf{B}A \tag{3.10}$$

where; **B** is the flux density in T, A is the cross-sectional area in m^2 and Φ is flux in Webers (Wb). Given the assumption that the flux within the magnetic circuit is constant, it is then possible to calculate the flux density for all other sections of the circuit using equation 3.11;

$$\mathbf{B} = \frac{\Phi}{A} \tag{3.11}$$

Once the flux density of each component of the circuit is known, the **H** value can then be extrapolated from its corresponding **BH** curve and recorded accordingly. The magnetic field intensity in the air gap can be calculated using eqation 3.12

$$\mathbf{B} = \mu\mathbf{H} \therefore \mathbf{H} = \frac{\mathbf{B}}{\mu_0} \tag{3.12}$$

where **B** is the flux density, **H** is the field intensity and μ is the permeability of the material. In this case the air gap has a permeability of that of free space $4\Pi \times 10^{-7}$ Henries/m. Now that the **H** value of each component of the circuit along with its corresponding path lengths have been computed it is possible to calculate the required mmf from equation 3.9 repeated below.

$$\sum mmf = \sum \mathbf{H}.l$$

Applying the above method and altering the plate thickness and lift-off a graph can be generated showing the required mmf needed to saturate a 1020 grade steel plate to the required flux density of 2.1T at multiple plate thicknesses and lift-off values from 0-5mm as seen in Figure 3.3. This is assuming a straight leakage path in the air gap. However, a more accurate model may be generated if a leakage factor is taken into consideration within the air-gap. This model demonstrates the need of a more powerful magnet (**H**) to saturate the specimen when specimen thickness and lift-off distance from the surface of the specimen to the yoke is increased.

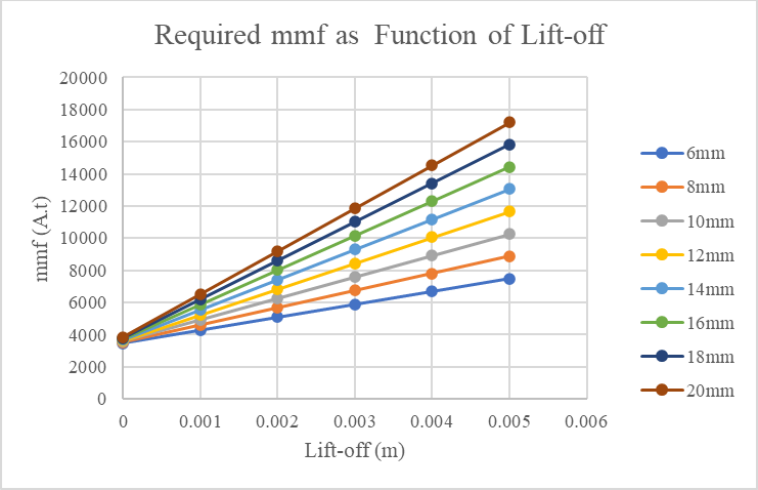

Figure 3.3: Magnetic circuit calculator generated results to illustrate when plate thickness and lift-off is increased the required mmf to saturate the specimen is also greater.

3.3 FEA Modelling

3.3.1 Finite Element Modelling

The FEM package used to perform the analytical modelling for the work presented in this thesis is Integrated Engineering's Oersted V930. The ideal scenario for simulations is to provide a solid foundation and understanding of the underpinning physics that can otherwise not be visualised or measured in certain aspects during the experimental phase. Having a validated simulation package also removes the need for significant amounts of experimental work. The work carried out is separated into two categories: 2D simulation where Oersted was used and experimental validation.

The two-dimensional modelling is carried out in Oersted. Oersted is an Eddy current solver from Integrated Engineering with the capability of transient electromagnet field solving using the Boundary Element Method (BEM) with the FEM solver providing powerful tools for magnetic field analysis.

The static modelling technique involves magnetising the specimen with the magnetic assembly equivalent to that of the FM3Di and then measuring the flux distribution from the top surface through to the bottom. This allows for the evaluation of the

magnetised state of the specimen and its operating point of the **BH** curve whether it lies in saturation or not. Over-saturation would lead to increased offset values and in some cases saturate the sensor array. Under-saturation cannot be determined. However, the permanent magnet assembly is designed and optimised for a range of plate thicknesses. Secondly, the distribution of the flux throughout the material when relative velocity between the plate and the magnetic yoke is introduced. In a static case scenario, the magnetic flux is somewhat evenly distributed throughout the material. The magnetisation level is dependent on the material thickness. This level of magnetisation has a direct correspondence with the leakage field that will be achieved when a defect is introduced. Similarly, a material that is over-saturated can cause a reduction in the signal to noise ratio due to an increased offset caused by the residual flux interfering with the sensor and in some cases saturation of the sensors can occur. Under-saturation cannot be determined. However, the permanent magnet assembly is designed and optimised over a set range of plate thicknesses.

The modelling process can be broken down into multiple stages consisting of the modelling/setup phase, solving and analysis phases. These phases are discussed in more detail in the following:

- **Modelling Phase** – The initial process in the modelling phase is the creation of the required component's geometry of the magnet yoke and the specimen.

- **Assigning Material Properties** – The material's characteristics are to be introduced including the **BH** curve, electrical conductivity, permeability, permittivity etc.

- **Solver Type** – The next step is to select the solver type along with mesh creation chosen for either each component or the whole model. The chosen solver type is often dependent on a particular mesh for optimal performance with the choice to alter between desired mesh types from a list containing triangular, rectangular etc. Triangular mesh is faster than quadrilateral (rectangle) mesh, however, can be less accurate [54]. Due to the translational transient nature of the simulations in this thesis triangular mesh is chosen due to time to solve each

solution and the total number of simulations undertaken. Practical validation is undertaken to ensure the validity of the simulated results.

- **Solving** – The algorithm used during this stage will depend on the type of solver that was chosen in the previous step between the static or transient solvers provided within the software package. Where there is no relative motion needed between the magnet assembly and the plate a static solver is chosen. Where there is a velocity term introduced and a relative motion between the plate and the magnetic assembly is required a transient solver is used.

- **Analysis** – After running the simulation the solved numerical values are stored within the mesh. This data can be displayed with a colour map and field lines for a visual representation. The values can also be extracted as a graph through a line in an area of interest. A value at a specific point may also be extracted by using a field probe.

3.4 Model Configuration & Optimisation

In order to emulate MFL inspection on storage tank floors with localised corrosion machined flaws are used in the form of spherical defects with a variety of depths ranging from 20 - 80% through wall thickness in increments of 20%. In such a case the relative motion between the plate and yoke causes a change in the motional induced currents, resulting in a truly transient problem. Simulations are performed using a 2D magnetics translational transient capable software Oersted V930.

As discussed earlier in the thesis, there are a number of paramaters that will influence the MFL signal amplitude. The main contributing factors to consider are:

- **Velocity**

  The velocity difference between a plate and a permanent magnet yoke causes eddy currents to be introduced leading to a reduction in the applied magnetic field. Li [47] supports these statements making similar claims.

- **Plate Thickness**

Altering the thickness of plate has a direct result on its mean operating point on a **BH** curve. With a permanent magnetic yoke, only a finite amount of flux can be supplied to the plate. Taking this into consideration, increasing the cross-sectional area (thickness) causes a reduction in **B** when the same levels of **H** are applied.

- **Material**

  In this study a 1020 grade mild steel plate has been chosen for both the magnet assemble and the plate alike. Identical materials are introduced to maintain consistency to rule out dissimilar materials as a causing factor. 1020 grade steel is a typical parent material for storage tank floors.

- **Defect Volume**

  For MFL inspection the volumetric loss of material causes the leakage field to occur when the flux can no longer be contained within the inspection material due to the reduction in the cross-sectional area of the plate. In an attempt to mimic corrosion defects, a spherical form of defect wwas chosen to represent surface volumetric defects as opposed to rectangular defects used to represent cracks and other types of planar defect. Conducting 2D simulation assumes that the defect geometry would become elongated through the full depth of the model in this case $300mm$ as seen in Figure 3.4. Therefore larger signal amplitudes are expected from 2D simulations than is expected from experimental validation.

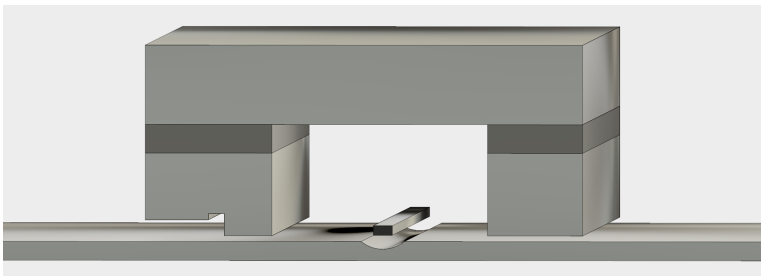

Figure 3.4: This illustration is representative of the models geometry and is used for the sole purpose of showing the reader the assumption of the extended 2D model into 3D.

- **Sensor Position**

Sensor positioning is a crucial component in defect detection and characterisation; when velocities are introduced this is of more significance. It is frequently reported in MFL applications where relative motion is a factor that the position of the sensors should be moved in the opposite direction to that of travel as the output from a defect is distorted in this direction [55]. It should also be noted there would therefore be an optimal sensor position for each given velocity. There are also negative affects of moving the sensor closer to the magnetic poles where fringing is seen that would likely result in the saturation of sensors. Taking this into consideration and to reduce influences from the magnetic poles the sensor is positioned in the centre of the magnet assembly although as described by Zhang [55] there could be a more optimal sensor position if a constant velocity was considered. However, as this study utilises multiple velocities the sensors are located in the central position between the magnet poles as this also represents the location of the sensors of the FloorMap3Di.

- **Defect Orientation (near/far surface defect)**

  The orientation of a defect can have a direct effect on detection sensitivity. Therefore, defects are simulated for both near and far surfaces. This will investigate why far surface defects are reported to have lower signal responses, e.g. where Wang [3] documents an increase in top surface feedback at velocities up to $200Km/h$.

3.4.1 Configuration

The magnetic assembly considered in this thesis is from a commercial floor scanning system. The asymmetric shape of the magnetic assembly allows for sensors to be placed between the pole and plate to distinguish top and bottom surface defects. However, for the purpose of this study when defects are being considered, only MFL signals indicated by the $\mathbf{B}_Y$ components in Figure 3.5 are extracted. The yoke is travelling with a defined velocity in the direction illustrated by the arrow labelled DoT (Direction of Travel) in Figure 3.5. Multiple velocities are considered in the simulated experiments with a consistent defect shape used throughout with varying plate

thicknesses. The exact dimensions of the model are not displayed due to commercial sensitivity and disclosure reasons.

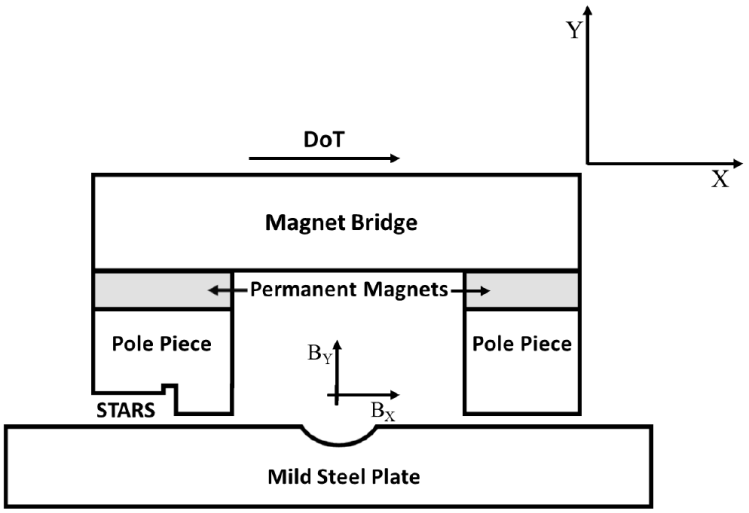

Figure 3.5: Illustration of the magnet assembly and defect shape used in the parametric study accompanied by the corresponding $\mathbf{B}_X$ and $\mathbf{B}_Y$ directions relative to the model assembly.

3.4.2 Governing Equation

The governing equation for this 2D transient problem is

$$v\nabla^2\mathbf{A} - \sigma\frac{\partial\mathbf{A}}{\partial t} - \sigma V\frac{\partial\mathbf{A}}{\partial x} = -J \tag{3.13}$$

where v, $\mathbf{A}$, σ, V and J are the reluctivity, magnetic vector potential, conductivity, velocity of the plate and the current density respectively [6].

3.4.3 Model Parameters & Optimisation

Mesh density optimisation is undertaken prior to conducting the translational transient simulations for the results displayed in this thesis. Although Oersted V930 has a built in adaptive meshing solution based on the translational and transient nature of the simulations it is still possible to define areas of interest where mesh weighting and a desired element count can be applied. The magnetic vector potential $\mathbf{A}$ boundary conditions are set to 0 at the distant model boundaries. All simulations are conducted with the translational transient operation where motion is present solving for fields

as per the model and motional requirements of this work. Secondly the depth of the model is set at $300mm$ as per the width of the magnet assembly this work is based on and all simulations are carried out at 20°C. An example of the global parameters used can be seen in Figure 3.6.

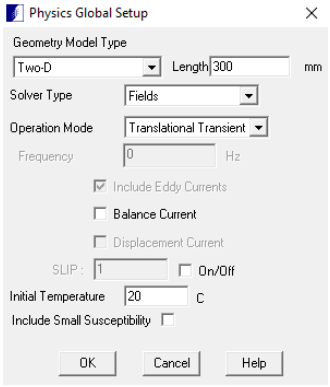

Figure 3.6: Image showing parameters used for all translational transient problems within this thesis. It should be noted that Oersted uses length to describe the Z axis into the model/page.

3.4.3.1 Material selection

The material selection is based on what is currently used in the commercial system (1020 grade steel). The material of the specimen/plate is kept consistent for the work carried out in this thesis. This is to mitigate any issues caused by a difference in material type/properties eliminating an additional variable. There are multiple material properties that govern the outcome of a translational transient magnetics problem such as; magnetisation/**BH** curve, permeability and the electrical conductivity of a ferromagnetic material. Images of the data used for the 1020 steel used in the simulations are displayed in Figures 3.7a & 3.7b.

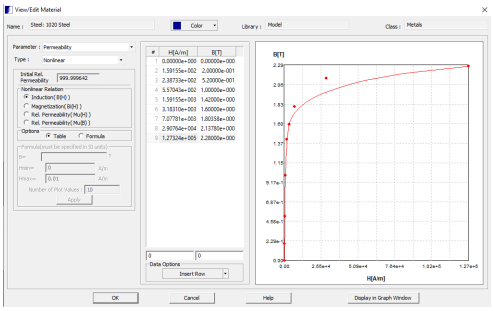

(a) Image showing the **BH** curve used for 1020 grade steel used to undertake the work carried out.

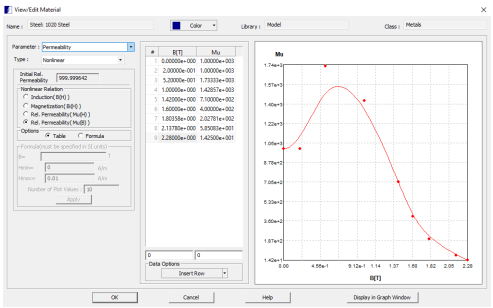

(b) Image showing relative permeability graph used for 1020 grade steel to conduct the simulations undertaken throughout.

Figure 3.7: Figure showing material properties for 1020 grade steel used in Oersted V930 to conduct simulations within this thesis.

3.4.3.2 Magnet Selection

The magnet used for the simulations and results shown in this thesis is typical to that used on the commercial based system that this work is a representation of. The magnet of choice is N45 with a remanent flux density $\mathbf{B}r$ value of $1.35T$ which can be seen below in Figure 3.8.

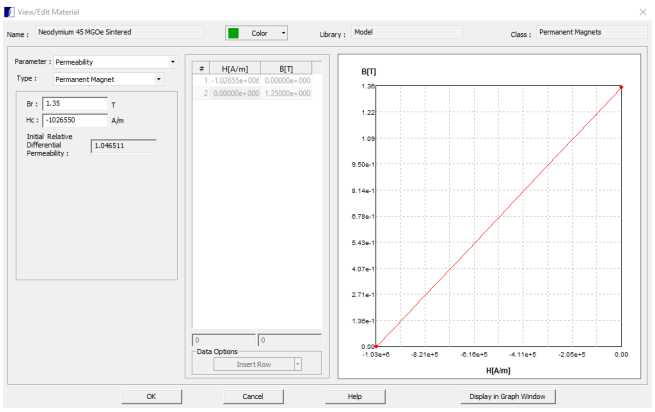

Figure 3.8: $\mathbf{B}r$ for a typical N45 magnet used for the simulations going forward.

3.4.3.3 Defining areas of interest

In order to improve element count and the reliability of the results, an area surrounding the field probe where measurements are taken is defined. The element count and element weighting is increased within this area that stretches down to the top surface of the plate. This will in turn increase the accuracy of the leakage field generated by the defect as it passes through the sensor location. Similarly to increase the accuracy

of the results surrounding the defect two more areas of interest are defined where element count is increased. Multiple areas like this are required as the plate and magnet assembly and probe area move independently of one another. These areas can be seen in Figure 3.9 where an example of a solving solution can be seen.

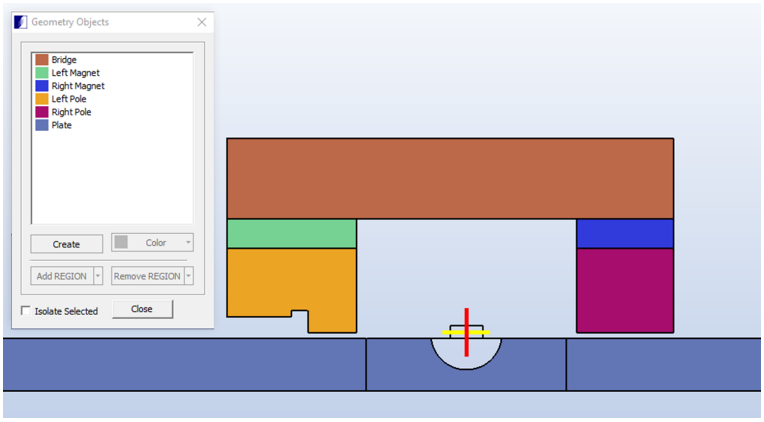

Figure 3.9: Screen capture showing the defined areas of interest added to increase element weighting in significant areas. A legend is included to indicate each object within the simulation and its relative colour. The sensor location is also included shown with a red and yellow cross located centrally between to the left and right pole pieces.

3.4.3.4 Mesh weighting and results

Results are taken from a field probe in a position where the sensor array is located on the commercial floor scanning system in the centre of the poles at a height of $2mm$ above the inspection surface. It is noted that the sensor height is adjustable on the commercial system dependent on surface roughness of the plate being inspected. However a sensor height of $2mm$ is taken at the optimal and lowest setting of the system to demonstrate a best case scenario. Oersted V930 utilises automated meshing for the translational transient solver used for this parametric study. However, the self-adaptive accuracy factor can be altered to increase the mesh density and therefore improve the validity of the results. This option was used to carry out an optimisation study where the magnet assembly is centred over the top of 40% defect on a larger $16mm$ thick plate as seen in Figure 3.9 and the mesh density in Figure 3.10 where there is 2193 triangles in the area of interest surrounding the sensor, 6014 within the central area below the plate and 3122 within the defect area and approximately 70,000

triangles as a whole. The problem is then solved with a velocity term of $0.5m/s$ and the value of $\mathbf{B}_x$ is recorded and plotted as a function of self-adaptive accuracy as seen in Figure 3.11.

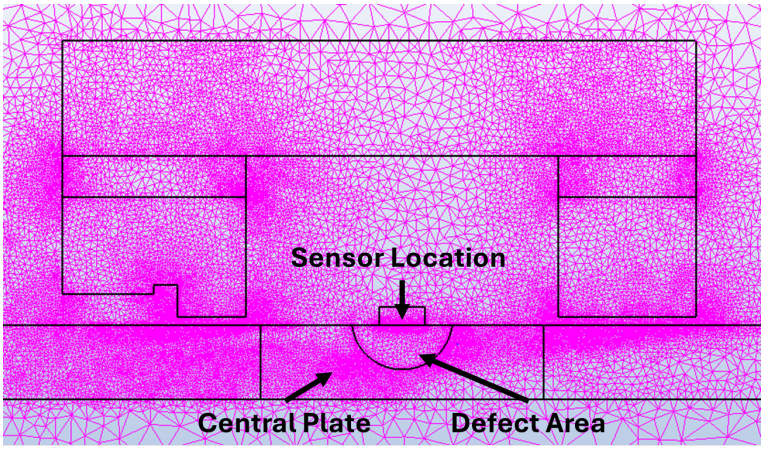

Figure 3.10: Image showing the mesh density for the chosen accuracy with the areas of interest labelled. It should be noted that due to the adaptive meshing nature of the software used this varies with each iteration.

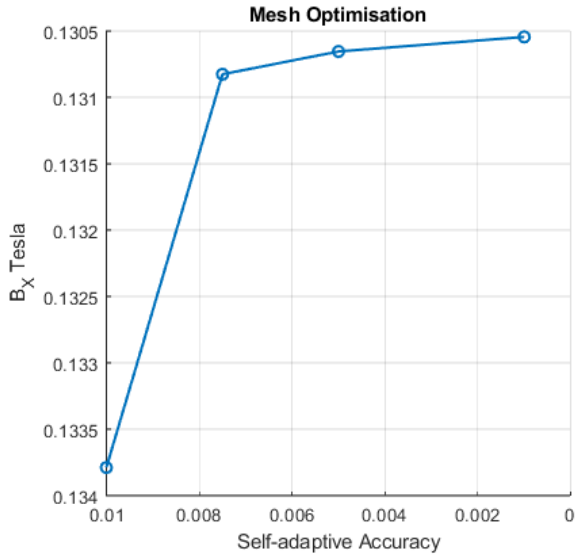

Figure 3.11: Graph displaying the results of the mesh optimisation study where $\mathbf{B}_x$ is plotted as a function of self-adaptive accuracy.

Taking into consideration the results of the mesh optimisation study and the computational time needed to solve each problem solved every $0.25mm$ over $160mm$ resulting in 640 iterations per simulation, a self-adaptive accuracy factor of 0.0075 was chosen to undertake the parametric study displayed within this thesis with only a 0.215% difference from 0.0075 to 0.001. Table 3.1 displays the parameters used for each velocity. The scan duration is the time taken to travel $160mm$ at the stated velocity and the time/step is the time step between solutions to meet the desired

$0.25mm$ resolution.

Table 3.1: Table displaying the translational transient parameters used to undertake the parametric study carried out in this thesis.

Speed (m/s)	**Distance (m)**	**Scan Duration (s)**	**No Steps**	Time/Step (s)	**Resolution (mm)**
0.5	0.16	0.32	640	5×10^{-4}	0.25
1	0.16	0.16	640	2.5×10^{-4}	0.25
1.5	0.16	0.11	640	1.67×10^{-4}	0.25
3	0.16	0.05	640	8.33×10^{-5}	0.25

3.5 Experimental set-up

The experimental method used to investigate the phenomena between a permanent magnet MFL yoke taken from the Silverwing branded Eddyfi FM3Di tank inspection scanner and the relative motion between it and the inspected material. The experimental investigation is based on the process completed within the modelling stages keeping specimen thicknesses and velocities as close as possible for validation of the modelling method implemented in this thesis.

The experimental procedure is set out to determine the defect characterisation of defects in mild steel plates of ranging thickness from 6 to 16mm. The characterisation of defect changes with specimen thickness, defect size, orientation and velocity. Multiple test specimens will therefore be used. A single specimen of a stated thickness has defects machined with equal spacing and contain a range from 20 to 80% through wall thickness in 20% increments. Each specimen will be scanned 30 times in total. five inspections at three velocities on the top surface, and then again with the defects on the bottom surface. This allows for averaging of the results and to show repeatability of the test procedure. The leakage field from the defects is measured using an array of Hall effect sensors spanning 40mm in lateral width to allow for drift during the inspection and held in place using a 3D printed holder. The data is captured and then post-processed in MATLAB. The equipment setup, inspection conditions and processing are outlined in the following sections.

The inspection is carried out by preparing the system and aligning it centrally to the machined defects within the specimen. Specimens are made to allow for the acceleration time needed to achieve a constant velocity before the first defect is encountered. Once a scan of a specimen is complete the data is stored, and the procedure is repeated.

3.5.1 Equipment

The experimental equipment shown in Figure 3.12. A modified Floormap 3Di (FM3Di) system with variable speed is used during this test procedure. The system has been stripped back to a functional shell where all data capture is undertaken externally using Eddyfi's surface array and tube inspection test instrument, Ectane 2 coupled with the Magnifi capture software. The sensor array consists of eight 5mV/G Hall effect sensors spanning 40mm and positioned at a height of 0.5mm above the inspection surface. A bespoke sensor array and mountings were developed for this testing and therefore a reduced lift-off is achieved. The system uses an incremental encoder that produces a spatial resolution of 1mm in the scan direction.

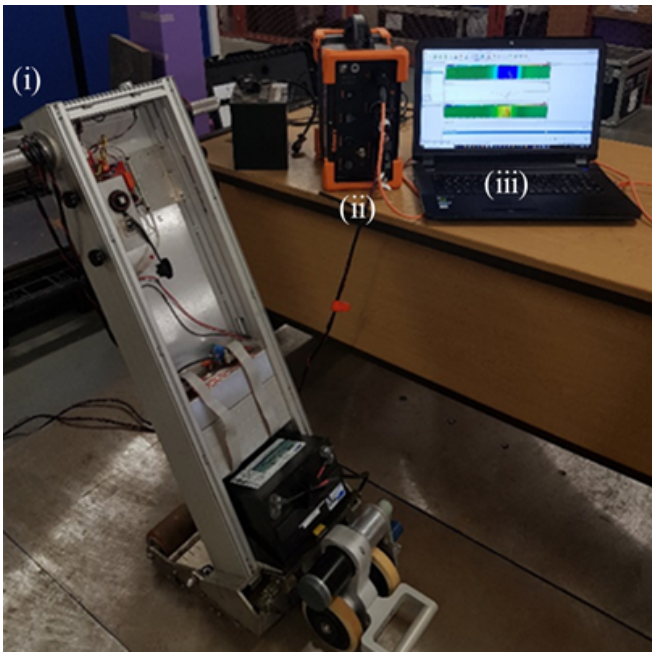

Figure 3.12: Experimental equipment; (i) Modified Floormap 3Di, (ii) Eddyfi Ectane 2, (iii) Magnifi data acquisition and analysis software and Mild Steel calibration plates with relative defect depths.

3.5.1.1 Specimen

Specimen thickness has a direct effect on the magnetisation level within the inspection material. As the permanent magnet assembly of the commercial system used supplies enough flux to saturate up to 8mm thick plates, an increase in plate thickness beyond this will result in a lower level of induced flux density. The result of this is a reduction in **B** as only a fixed amount of H can be applied by the permanent magnet assembly. In practical terms this is constantly changing due to the manufacturing tolerances of mild steel plates altering in thickness engineered with a tolerance of +/- 0.3mm together with the non-homogeneous composition of the material. The experimental work utilised plate thicknesses of 6, 8, 10, 12 and 16mm. The plate thickness of 6 and 12mm used in these experiments covers the range typically seen within the main section of a storage tank floor, while the 16mm plate represents the annular sections of the storage tanks, which are generally thicker to support the shell.

3.5.1.2 Defects

The defects considered in this experiment are known spherical shapes bored with a 22mm ball end cutter. These mimic corrosion at the specified depths of 20, 40, 60 and 80% through wall thickness as recommended in the UK Health and Safety Executive (HSE) recommended practice for magnetic flux leakage inspection of atmospheric storage tank floors [6]. The orientation of the defect (top side/bottom side) also plays a significant role in defect detection and the shape of the corresponding signal responses is also considered.

3.5.1.3 Velocity

In a paper published on the work of this thesis [1] it was shown that the relative velocity difference between the plate and a permanent magnetic yoke causes eddy currents to be introduced into the specimen leading to a reduction in the applied magnetic field. This also influences the distribution of flux within the inspected material resulting in changes to signal amplitudes. The net result is that the flux concentrates towards the near surface resulting in an increased signal response from near surface defects

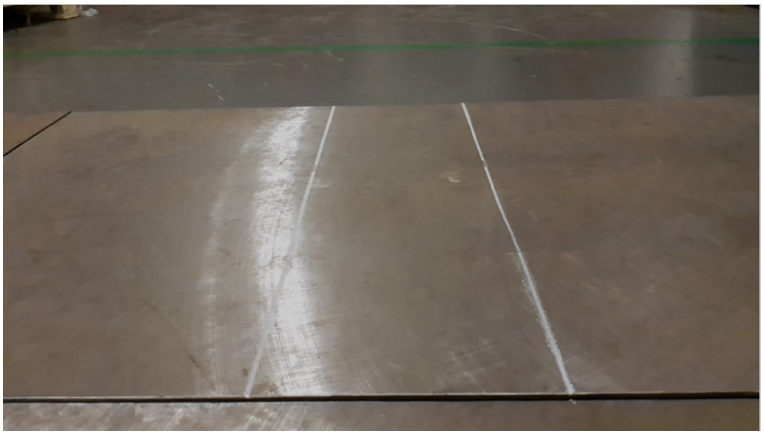

Figure 3.13: Showing lines marked 200mm apart on a 16mm plate.

as velocity increases. The opposite happens for far surface flaws where a reduction in signal amplitude is seen due to the distribution concentrating nearer to the top surface again when saturation is no longer achieved. Plate thicknesses of 6 to 16mm are tested at three velocities: slow (0.51 - 0.57m/s), medium (0.74 - 1m/s) and fast (0.95 - 1.25m/s). The inspection velocity varies slightly as a function of plate thickness and is therefore specific to each specimen.

Measuring Velocity

The MFL scanner FM3Di has no direct means of outputting inspection velocity therefore an alternative method of measuring velocity is required. The velocity of the system is measured by marking two lines on the surface of the specified plate thickness at $200mm$ apart in the centre of the plate as seen in Figure 3.13. The measurements are taken at the centre of the plate to ensure the system has time to accelerate and reach constant velocity.

The system is then recorded with a high frame rate camera with 170fps. The video is then analysed and broken down frame by frame and timestamps are taken when the system wheel hits the first and second chalked lines in Figures 3.14a and 3.14b respectively. The time is then taken for the system to traverse the $200mm$ distance and then the system velocity can be calculated using equation 3.14.

$$s = \frac{d}{t} \therefore s = \frac{0.2}{0.39}$$
$$s = 0.51m/s \tag{3.14}$$

where s is speed in m/s, d is distance travelled in m, and t is the time taken to travel the $200mm$ distance as marked on the plate.

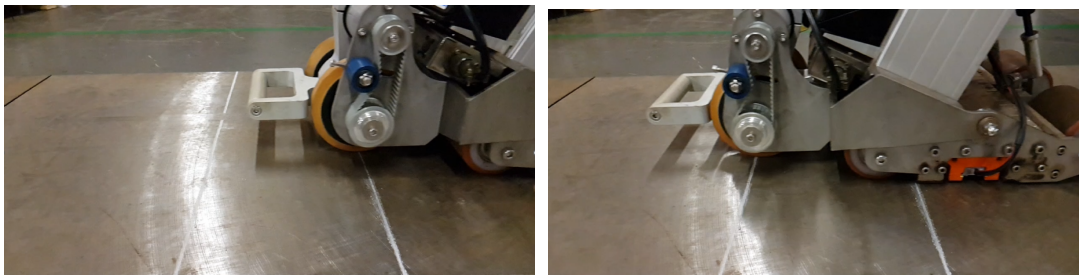

(a) **(b)**

Figure 3.14: Images of the MFL system passing each line marked on $16mm$ thick plate where measurements are taken to calculate inspection velocity.

3.5.1.4 Sensor Position

The positioning of sensors is frequently noted as affecting defect characterisation of MFL applications. The sensor position for this experiment remains in the centre of the magnet bridge at a fixed height of 0.5mm above the inspection surface. This is then secured within a 3D printed probe holder, as shown in Figure 3, where, (i) is the probe holder and (ii) is the array of Hall effect sensors mounted between the magnetic poles. It has been suggested in other studies [7] that sensors should be offset opposite to the direction of travel. The sensor array being positioned centrally helps to minimise stray leakage fields from the magnet assembly interfering with the Hall effect sensors. It is also fixed in this position as the literature suggests that there is an optimal position for a given velocity. As the velocity varies between plate thicknesses a different optimal position would be needed for each case. Taking this into consideration it was decided to remove this as a variable and to fix the position of the sensor to ensure the same point of interest was used for all measurements taken.

Figure 3.15: Showing the sensor array in a 3D printed housing to give a lift-off of 0.5mm where; (i) is the 3D printed housing and (ii) is the array of eight 5mV/G Hall effect sensors.

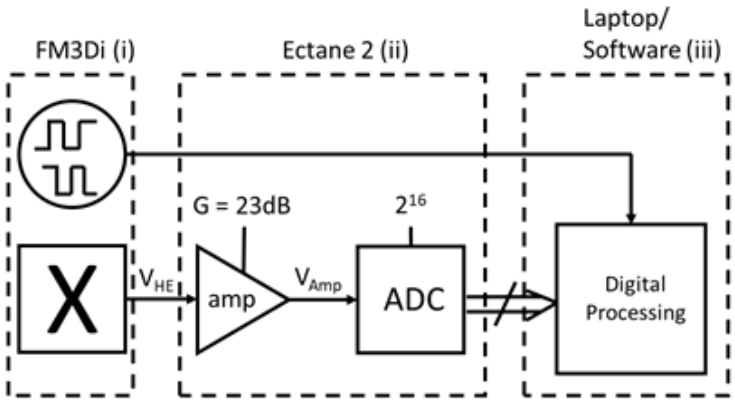

Figure 3.16: Illustration of the signal processing chain of the experimental set-up.

3.5.1.5 Data Acquisition Scaling

The signal processing chain of the system is shown in Figure 3.16. As the data acquired is in the form of ADC values, reverse signal scaling is required to obtain flux density. An example data set can be seen in Figure 3.17 with an 8 channel overlay where each sensor is considered as a separate data channel. The 'Y' axis shows the raw ADC values and right 'Y' axis shows the values in T after the conversion to **B** has taken place. The process of converting the signal back to its raw format is given in equations 3.15 and 3.16.

$$G_{db} = 20log_{10}\frac{V_{AMP}}{V_{HE}} \tag{3.15}$$

where GdB, VAmp and VHE are the signal amplification applied in dB, the signal

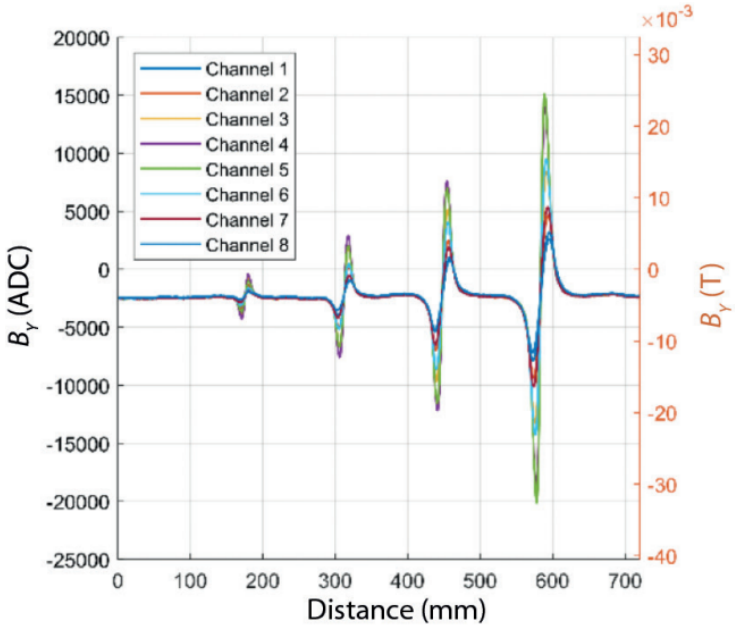

Figure 3.17: Experimental data set taken from a 6mm calibration plate.

voltage after gain is applied and the voltage from the Hall effect sensor before gain alteration respectively. As the gain is fixed by the pre-amplifier of the system to 23dB and the amplified signal voltage are known factors it is possible to convert the amplified data to its un-amplified state using the following equation;

$$V_{HE} = \frac{V_{AMP}}{10^{1.15}} \tag{3.16}$$

This value may then be converted into gauss as the Hall effect transfer function of 5mV/gauss is known. The value for gauss is then divided by 10,000 to complete the conversion to T. Once scaling of the data is complete the channel with the highest pk-pk value is then recorded. Five independent scans are performed over each defect at each velocity and each plate thickness, allowing for an average pk-pk value to be calculated from 5 samples per defect. This is executed for both defect orientations.

3.6 Conclusion

This chapter concludes the experimental and practical approach taken to generate the results and findings of the work carried out in the following results chapters of

this thesis. The chapter began with magnetic theory setting the scene and providing the necessary equations to analytically outline the required mmf required for a simple magnet design and how this applies to more complex models like the one investigated in the work carried out in this thesis. The approach taken in the Finite Element Modelling processes and the parametric studies were outlined discussing the set-up and parameters used. Finally, the experimental set-up, equipment used, specimens, defect type and size were described. A breakdown of how video capture was used to measure the velocity of the system on a range of samples was provided, and the data acquisition and scaling system used were also described.

Chapter 4

Simulated Results

4.1 Introduction

This chapter investigates through simulation the velocity effects of a commercial MFL system for tank floor inspection, the FM3Di. This system contains two permanent magnets and an array of Hall effect sensors with the capability of adjusting inspection velocity as outlined in Chapter 3. Four velocities are taken into consideration based on the capability of the system: 0.5, 1 and $1.5m/s$ which are typical inspection speeds achievable by the system and then an extreme velocity of $3m/s$.

An extreme case scenario of an MFL inspection undertaken on a $100mm$ thick plate is given to exaggerate the effects identified that will affect the capability of sizing and characterising defects. This is undertaken to provide context on the effects that are noted within the simulated results of this Chapter.

4.2 Results

4.2.1 Flux Distribution

To demonstrate the effects of velocity on a permanent magnet MFL system two simulations are conducted. Firstly, an extreme case scenario of a static model with no relative motion on a 100mm thick plate is performed to provide an exaggerated effect seen on an un-saturated plate. The same assembly is then simulated when relative motion is introduced between the magnet assembly and the plate with a velocity of $3m/s$. This is then repeated for plate thicknesses ranging from $6mm$ to $20mm$.

4.2.1.1 Extreme Static Case

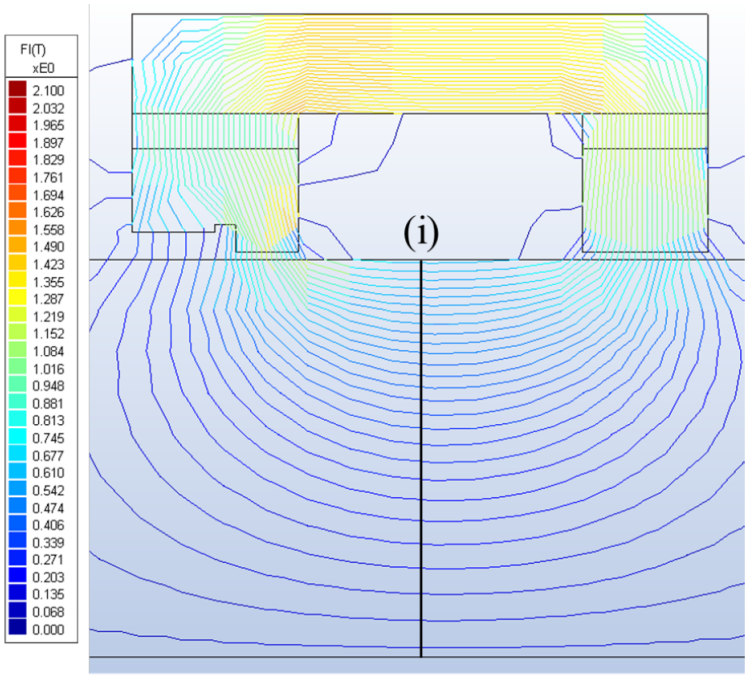

Figure 4.1: Extreme static case of the magnetic flux distribution throughout a $100mm$ steel plate with a fairly even distribution of flux penetrating the full depth of the plate. Measurements are taken from the vertical line marked (i) through to the far side of the plate.

From Figure 4.1 of a static simulation undertaken on a $100mm$ thick plate it can be seen that the flux is distributed throughout the full depth of the plate with a relatively even distribution.

4.2.1.2 Extreme Velocity Case

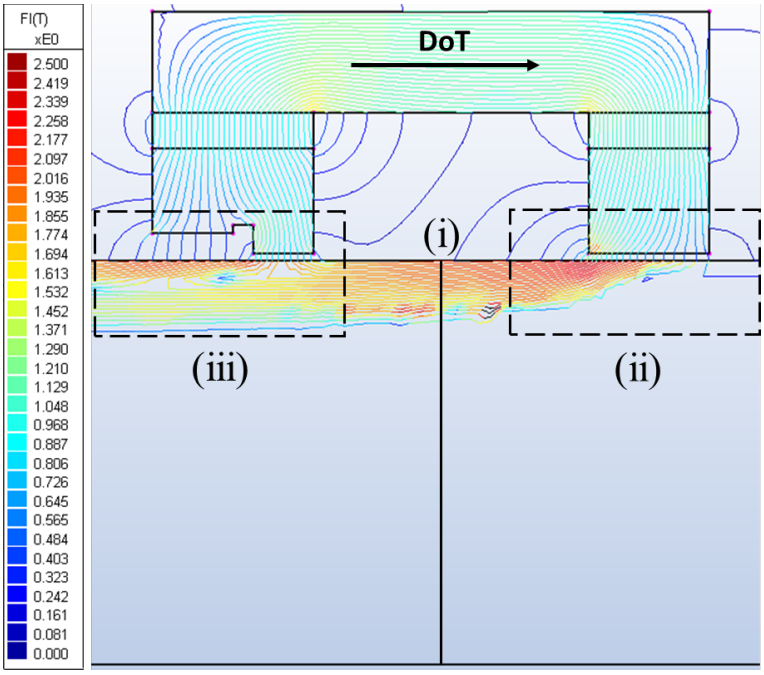

Figure 4.2: Extreme moving case of the magnetic flux distribution throughout a $100mm$ steel plate showing a distorted induced field with limited penetration of approximately 37 mm at $3m/s$. The direction of travel for the yoke is shown with the arrow labelled DoT (Direction of Travel). Measurements of flux distribution are taken from the vertical line labelled (i) at the near surface through to the far surface. The wake effect is also evident where the flux enters and leaves the plate indicated within dashed boxes labelled (ii) and (iii) respectively.

From Figure 4.2 the distribution of flux throughout the plate is significantly reduced resulting in a penetration of only $37mm$ through the plate whereas in the static case flux is distributed through the entirety of the 100mm thick plate. The velocity case has a reduced penetration due to the induced eddy currents as a direct result of the eddy current braking effect as supported by Coramik et al. [56]. A wake effect is also evident where the flux enters and leaves the plate indicated within the dashed boxes in 4.2 labelled (ii) and (iii) respectively [57]

4.2.1.3 Average flux density throughout plates of varying thicknesses for the static case

From Figures 4.1 and 4.2 the measurement of flux distributed through the $100mm$ thick plate is taken along the vertical line central to the leading and trailing poles from the near surface of the plate through to the bottom. The position the data is acquired

within the simulations are at the central location between the magnetic poles where the flux would be most evenly distributed in a static case. These measurements are used to provide two types of analysis. The first is to identify the mean level of induced flux density in the plate, for the static case results can be seen in Figure 4.1 . Secondly, the distribution of the flux through the material plays a significant role in defect detection. This measurement is then taken when relative motion is introduced, resulting in a non-linear distributed flux pattern through the plate material as illustrated previously in Figure 4.2.

A number of simulations are undertaken statically for a range of plate thicknesses from 6 - 100mm. The average $|\mathbf{B}|$ value is calculated through the plate thickness at the centre of of the bridge as previously described for 4.1. The results of these simulation are shown in Figure 4.3. Taking into consideration the saturation level of 1020 grade mild steel used being 2.1T only the 6mm plate is fully saturated. Plates thicker than 6mm are no longer in saturation. It is clear that plate thickness has a direct effect on the induced flux density. A typical inspection range for the design in question would be between 6 and 14mm of plate thickness.

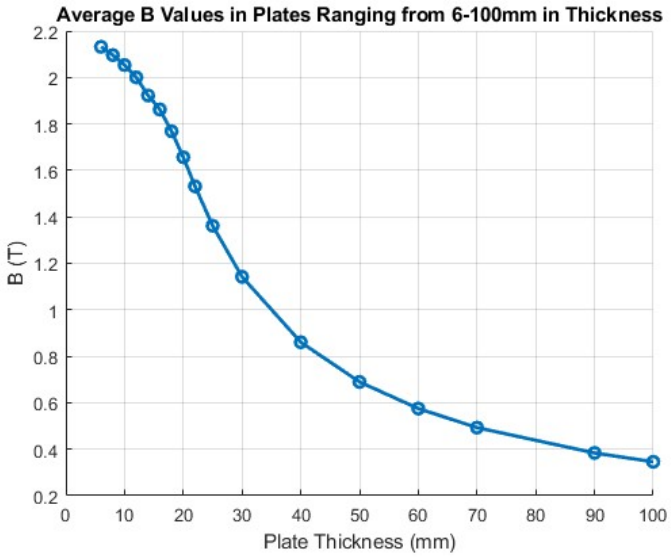

Figure 4.3: Mean flux density results of plates varying from 6 to 100mm. When an increase in plate thickness is seen, there is a resultant drop in the $|\mathbf{B}|$ values throughout the plate.

4.2.2 Flux Density Distribution for Varying Velocities

Initial simulations were undertaken to benchmark the system to identify relationships between plate thickness and inspection velocity where no defects are present. In this study realistic velocities of 0.5, 1, 1.5m/s were used along with an exaggerated velocity of 3m/s simulated against plate thicknesses of 6, 8, 10, 12, 14, 16, and 20mm. This covers the full range of plate thicknesses typically encountered in the field.

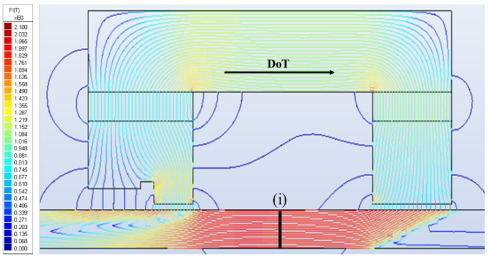

(a) 10mm steel plate at 0.5m/s with a consistent flux distribution with measurements taken from the black line labelled (i) as indicated on the illustration from the near surface through to the far surface.

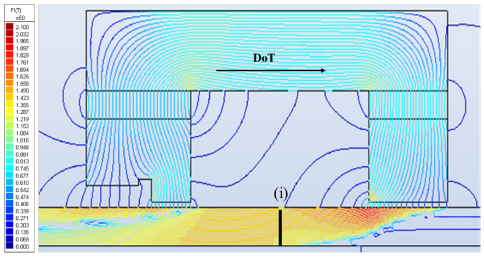

(b) Displaying measurement locations and distribution of flux at 3m/s. The flux distribution in the plate is taken along the vertical black line labelled (i). Measurements are taken from the near surface through to the bottom.

Figure 4.4: Example simulation of 10mm plate thickness at 0.5 and 3m/s highlighting increased waked effect and difference in the induced flux density.

Figures 4.4a & 4.4b show results for simulations undertaken with a plate thickness of 10mm at two velocities. Figure 4.4a shows the results obtained at 0.5m/s (the lesser of the two velocities), there is a higher level of induced flux density than that obtained at the higher velocity of 3m/s illustrated in Figure 4.4b. The reduction in the overall flux density in the 3m/s case is caused by the relative motion between the magnetiser and the specimen inducing a larger Eddy Current field that creates a magnetic field opposing the field induced by the magnet thus causing a reduction, this is known as the Eddy Current braking effect. Also, these is an increased wake effect distorting the induced magnetic field causing the flux within the plate to trail behind the leading and back edge of the magnetic poles at a scanning speed of 3m/s. For this part of the study measurements of the flux distribution through each plate thickness are analysed in the regions depicted in Figures 4.4a & 4.4b with a thick black line labelled (i) taken from the near/top surface to the far/bottom surface.

Understanding how the flux is distributed in the cross-sectional area of the plate, (i) in Figures 4.4a & 4.4b will assist in understanding of how flaws may go undetected for increased plate thickness and higher scanning velocities.

4.2.2.1 6mm Plate Thickness

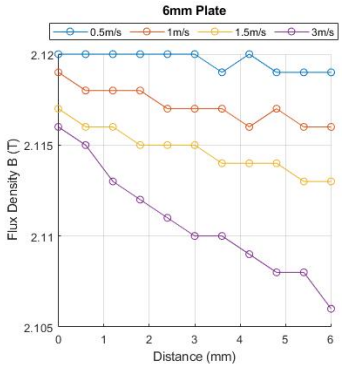

(a) Distribution of flux taken from (i) in Figure 4.4a on a $6mm$ plate showing a minor change the distributed flux when velocity is introduced. This is exaggerated with a concentrated 'Y' axis.

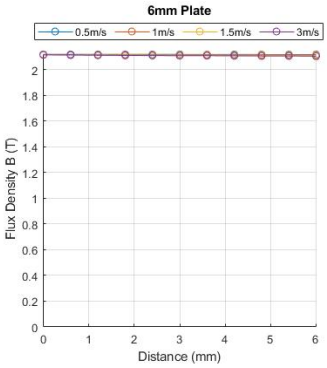

(b) Results of the distribution of flux taken from (i) in Figure 4.4a throughout the $6mm$ steel plate indicating an almost consistent level of induced flux at all velocities.

Figure 4.5: Simulation results of $6mm$ plate thickness at 0.5, 1, 1.5 & $3m/s$ depicting the distributed flux at differing velocities.

At $6mm$ plate thickness velocity has a somewhat reduced effect on the distribution of flux throughout the plate. This is a direct result of the plate being in a saturated state of $2.1T$ and above. Figure 4.5a shows a minor change from $2.12T$ at $0.5m/s$ at the near surface and a decrease to $2.119T$ at $0.5m/s$ remaining somewhat consistent. At $3m/s$ a reduction from $2.116T$ $3m/s$ to $2.106T$ is seen. Figure 4.5b is given to show that the change in flux distribution is minor and is still considered to be in saturation but follow the trend identified by Li [47] by seeing a reduced level of induced flux when velocity is increased. This is indicated by the separation of each flux density trace incrementally decreasing with each velocity step.

4.2.2.2 8mm Plate Thickness

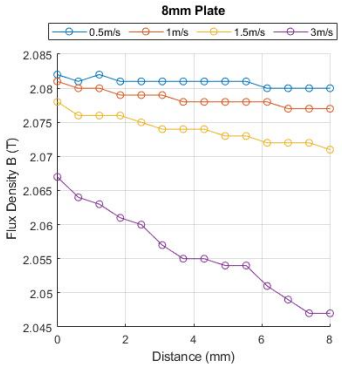

(a) Distribution of flux taken from (i) in Figure 4.4a in an $8mm$ plate again showing a minor change in the flux distribution when velocity is introduced.

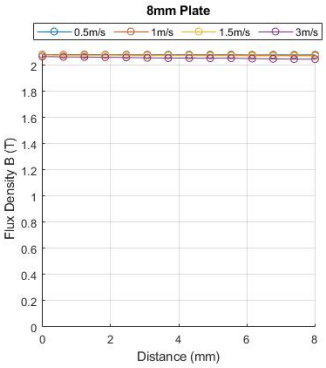

(b) Results of the distribution of flux taken from (i) in Figure 4.4a throughout the $8mm$ steel plate indicating an almost consistent level of induced flux at all velocities.

Figure 4.6: Simulation results of $8mm$ plate thickness at 0.5, 1, 1.5 & $3m/s$ depicting the distributed flux at differing velocities.

The flux distribution in an $8mm$ plate follows the trend of a $6mm$ plate. An overall reduction in flux density is also seen comparatively to the $6mm$ plate as inspection velocity is increased. Although the relationship between the two plate thickness holds true, the $8mm$ plate results indicate a more significant reduction in the induced **B** from $2.067T$ from the top-surface down to $2.047T$ at the bottom-surface, a change of $0.02T$ at $3m/s$ as seen in 4.6a compared to the $0.014T$ difference seen at $6mm$ plate thickness in Figure 4.5.

4.2.2.3 10mm Plate Thickness

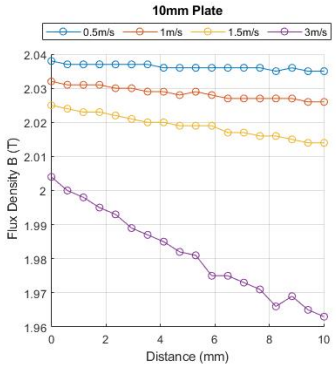

(a) Distribution of flux taken from (i) in Figure 4.4a in a 10mm plate showing a minor change in the flux distribution when velocity is introduced.

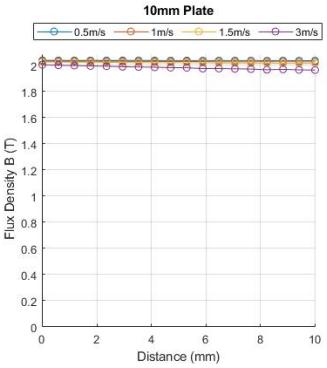

(b) Results of the distribution of flux taken from (i) in Figure 4.4a in throughout the 10mm steel plate indicating an almost consistent level of induced flux at all velocities.

Figure 4.7: Graphical representation of the flux distribution throughout a 10mm plate at varying velocities.

At 10mm the trend shown in the 6 & 8mm plate thicknesses is also present. However, there is a more significant difference in the relationship. This can be seen by the increased separation of traces between velocities, with the most significant being the jump from 1.5 to 3m/s. It should also be noted that when velocity is increased the overall flux density at the surface continues to reduce. The data is shown in two graphs as part of Figure 4.7 to indicate that although there is a more pronounced difference it is not as significant as it first appears once the full data range from 0 - 2.5T is considered.

4.2.2.4 12mm Plate Thickness

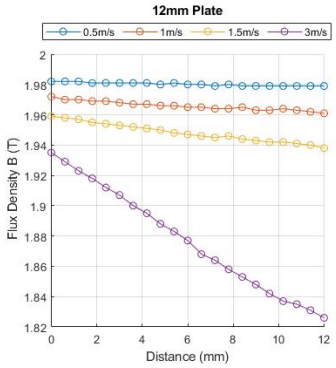

(a) Distribution of flux taken from (i) in Figure 4.4a in 12mm plate again showing a minor change in the flux distribution when velocity is introduced.

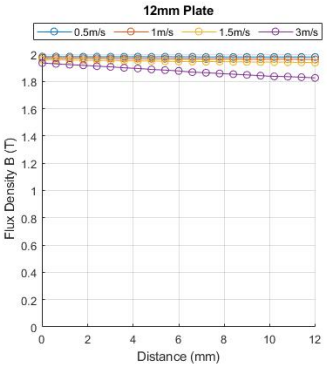

(b) Results of the distribution of flux taken from (i) in Figure 4.4a in throughout the 12mm steel plate indicating an almost consistent level of induced flux at all velocities.

Figure 4.8: Graphical representation of the flux distribution throughout a 12mm plate at varying velocities.

Following the trend for of all plate thicknesses prior to the 12mm plate, a reduction in $\mathbf{B}(T)$ is seen when velocity is increased on a 12mm plate as seen above in Figures 4.8a & 4.8b. There is a greater decrease in the distribution of the flux as is it penetrates through the plates thickness and is a somewhat linear decay from $1.935T$ to $1.826T$ at the far side of the plate resulting in a reduction of $0.109T$ throughout the 12mm thickness of the plate.

4.2.2.5 14mm Plate Thickness

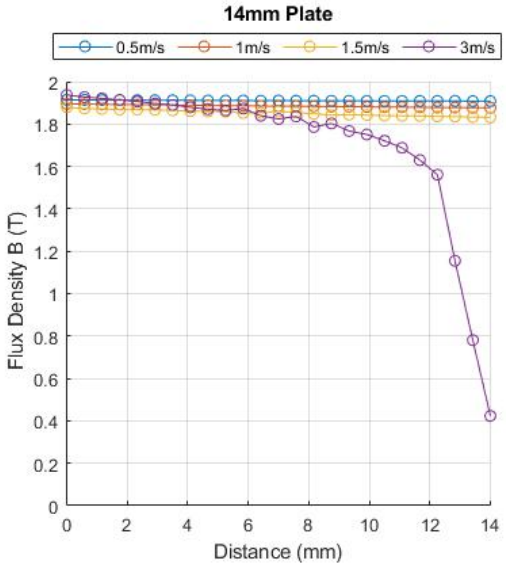

Figure 4.9: Results showing the flux distribution taken from (i) in Figure 4.4a through a 14mm plate where a decrease in flux distribution is seen beyond 12.5mm.

For the 14mm thick plate there is a significant drop off in the distribution of flux passed 12.5mm depth at 3m/s as shown in Figure 4.9. The decrease in flux density passed 12.5mm in depth continues to decrease somewhat linearly down to 0.4235T at the far side of the plate at 14mm. This decrease is a result of the flux shifting towards the top surface due to the eddy current braking effect and the 14mm plate being under-saturated. Plate thicknesses of 12mm and below are saturated and therefore this effect is not present. However this is not true for the 0.5 - 1.5m/s velocities indicating that the flux is far more evenly distributed at 14mm plate thickness which in turn indicates a this as an acceptable inspection velocity for this given magnet assembly for a 14mm thick plate. It is also shown that this is where a shift happens and the flux distribution becomes more concentrated at the top surface of the plate at 3m/s compared to that of the 12mm plate shown in Figure 4.8 where at 3m/s the distribution is reduced at the near surface of the plate.

4.2.2.6 16mm Plate Thickness

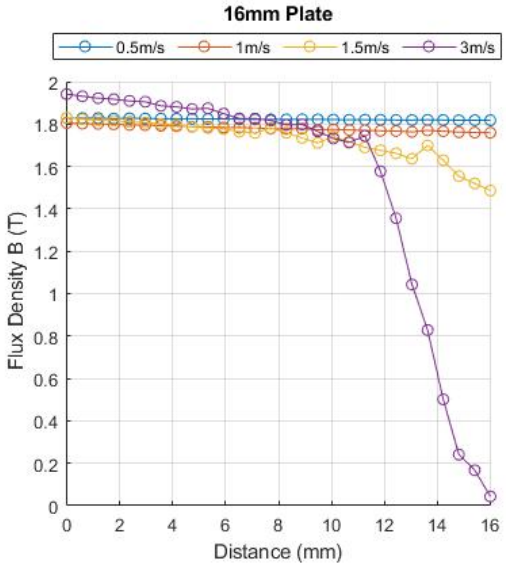

Figure 4.10: Results showing the flux distribution taken from (i) in Figure 4.4a through a 16mm plate where a decrease in flux distribution is seen beyond 11.25mm.

Following on from the trend represented by the 14mm plate in Figure 4.8, the shift in flux becomes more heavily concentrated to the top surface of the plate as a result of the relative motion between the yoke and the plate, falling off rapidly at 11.5mm deep with an almost linear decay down to 0.04347T at the bottom of a 16mm thick plate at 3m/s as depicted in Figure 4.10. This phenomenon is also present but less significant at 1.5m/s indicating that the recommended velocity for inspection of a 16mm thick plate with this magnet assembly should be limited to 1m/s and below.

4.2.2.7 20mm Plate Thickness

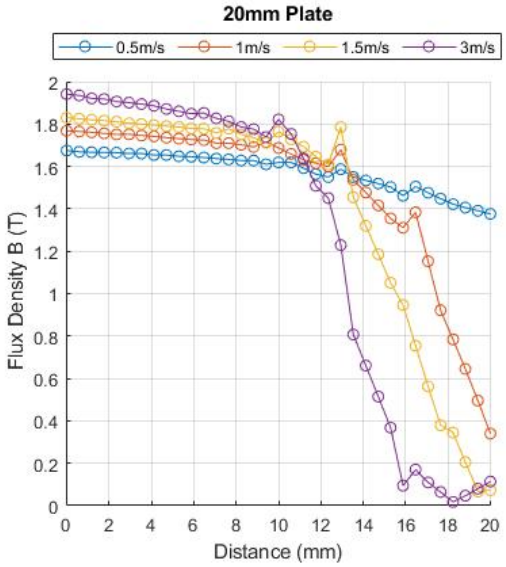

Figure 4.11: Results showing the flux distribution taken from (i) in Figure 4.4a through a 16mm plate where a decrease in flux distribution is seen beyond $10mm$ where it reaches almost $0T$ beyond $16mm$ in depth.

Similarly to that of the 14 & $16mm$ plate thicknesses the $20mm$ thick plate follows the same trend as seen in Figure 4.11. However, this is more significant again where at $3m/s$ the distribution follows the same trend as the $16mm$ thick specimen dropping off to almost $0T$ after $16mm$ of depth. The other velocities of 0.55-$1.5m/s$ have been somewhat consistent up until this point, there is a significant fall off for 1 & $1.5m/s$ after $12.5mm$ through the specimen. Taking this into consideration the $20mm$ thick sample should be scanned at the lowest velocity possible to limit these effects playing a significant part in defect detectability. Although mesh optimisation was undertaken as per the mesh optimisation section, however there are some artefacts within the data caused Oersted's self adapting mesh feature with limited user control. A summary of all the results considering flux distribution can be found in the following section 4.2.2.8.

4.2.2.8 Flux Distribution Summary

Below are the **B** values taken at the near-surface and far-surface of each plate thickness and velocity, including the difference between them displayed in tabular from in Table 4.1 that have been shown in graphical form throughout this section of the thesis. This allows the reader to easily see the impact that increased velocity has on the distributed flux when the inspection medium is under-saturated. A more complete conclusion will be undertaken at the end of this chapter in the thesis.

Table 4.1: Table summarising the relationship between flux distribution, plate thickness, velocity.

	0.5m/s			1m/s			1.5m/s			3m/s		
Plate Thickness (mm)/Surface	Top	Bottom	Difference	Top	Bottom	Difference	Top	Bottom	Difference	Top	Bottom	Difference
6	2.1200	2.1190	0.0010	2.1190	2.1160	0.0030	2.1170	2.1130	0.0040	2.1160	2.1060	0.0100
8	2.0820	2.0800	0.0020	2.0810	2.0770	0.0040	2.0780	2.0710	0.0070	2.0670	2.0470	0.0200
10	2.0380	2.0350	0.0030	2.0320	2.0260	0.0060	2.0250	2.0140	0.0110	2.0040	1.9630	0.0410
12	1.9820	1.9790	0.0030	1.9720	1.9610	0.0110	1.9590	1.9380	0.0210	1.9350	1.8260	0.1090
14	1.9140	1.9080	0.0060	1.8950	1.8770	0.0180	1.8790	1.8310	0.0480	1.9370	0.4235	1.5135
16	1.8290	1.8180	0.0110	1.8050	1.7590	0.0460	1.8300	1.4860	0.3440	1.9410	0.0435	1.8975
20	1.6750	1.3760	0.2990	1.7680	0.3402	1.4278	1.8300	0.0666	1.7634	1.9410	0.0174	1.9236

Where Table 4.1 shows the difference in **B** values at the top and bottom surfaces of the plate, Tables 4.2, 4.3 and 4.4 show the gradient changes throughout the thicker plates when the flux is not evenly distributed throughout the plate. This is split into two section for each of the plates, a linear section and a "drop-off" section. The linear section is where the flux in the section of the plate is somewhat consistent and the "drop-off section is where the flux within the plate decays rapidly for the remaining thickness. A diagram of how the sections are divided is given in Figure 4.12 where the linear portion and the drop off section is shown. This is repeated for 14, 16, and 20mm plate thicknesses.

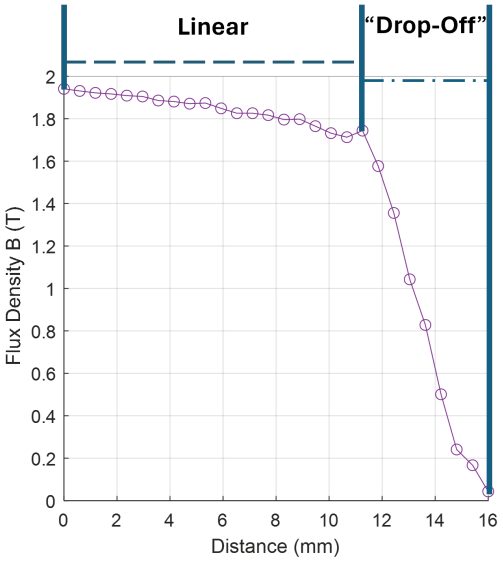

Figure 4.12: Image showing the linear and "drop-off" sections of how the data provided in the following tables is taken.

Table 4.2: Table showing the gradient of the flux distributed within the plate both when linear and the "drop-off" phase for a 14mm thick plate.

Plate Thickness (mm)	Speed (m/s)	Linear Gradient (T/mm)	Drop-off Gradient (T/mm)
14	0.5	0.0004	N/A
	1	0.0013	N/A
	1.5	0.0034	N/A
	3	0.0274	0.6771

Table 4.3: Table showing the gradient of the flux distributed within the plate both when linear and the "drop-off" phase for a 16mm thick plate.

Plate Thickness (mm)	Speed (m/s)	Linear Gradient (T/mm)	Drop-off Gradient (T/mm)
16	0.5	0.0007	N/A
	1	0.0029	N/A
	1.5	0.0215	N/A
	3	0.0222	0.3719

Table 4.4: Table showing the gradient of the flux distributed within the plate both when linear and the "drop-off" phase for a 20mm thick plate.

Plate Thickness (mm)	Speed (m/s)	Linear Gradient (T/mm)	Drop-off Gradient (T/mm)
20	0.5	0.0149	N/A
	1	0.0176	0.1989
	1.5	0.0035	0.2198
	3	0.0378	0.3900

4.2.3 Defect Response & Orientation Sensitivity

The flux distribution within a plate as discussed in section 4.2.2 can affect the systems defect detectability by both masking and amplifying defects. When higher velocities are simulated a shift in flux concentration is seen within the plate as demonstrated in the previous section 4.2.2. This shift takes place towards the near surface resulting in the flux manifesting in this region. This is more evident on thicker plates where even for the static case magnetic saturation is not achieved.

As a direct result of the distortion of the applied magnetic field and its concentration towards the near surface it is possible that a reduction in far surface defect sensitivity at higher velocities will be perceived. The orientation (either near or far surface) of the flaw will play a significant role in its detectability, and in particular in this case when a plate thickness of 16 mm and thicker is encountered. In this section of the thesis due to the number of graphs produced these will be displayed with multiple images on a singular page with text referring to image numbers. In the event of a specific set of results being pivotal to the claims to knowledge within this thesis the image may be re-used and expanded upon in more detail.

4.2.3.1 20% Defect Response

6mm plate thickness

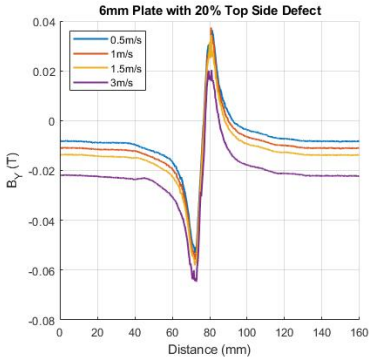

(a) $\mathbf{B}_Y$ response for a 20% top side defect on a $6mm$ plate.

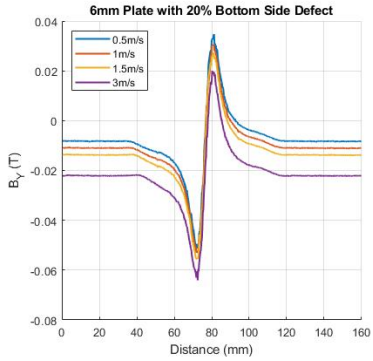

(b) $\mathbf{B}_Y$ response for a 20% bottom side defect on a $6mm$ plate.

Figure 4.13: Figure displaying the $\mathbf{B}_Y$ response from a 20% top and bottom side defects on $6mm$ plate.

Figure 4.13a displays the $\mathbf{B}_Y$ signal response from the 20% top side defect and Figure 4.13b for the bottom side defect on a $6mm$ thick plate. As $\mathbf{B}_Y$ signal is now taken into consideration where there is not defect present the response is close to zero. However this offset close to zero alters with inspection velocity as can be seen in Figure 4.13. The peak-to-peak values taken from Figure 4.13 are displayed in Table 4.5 below. These indicate that there is not a significant difference in defect responses from a $6mm$ thick plate when velocity is increased for a 20% through wall ball end type defect with a -5.0223% reduction in top surface defects from and 0.5 to $3m/s$ and -2.3229% for the bottom side defect for the same velocity change. However, it can be seen that there is a change of offset in the overall signal response when velocity is increased. This will be investigated further in a later section of this thesis in both simulation and practice.

Table 4.5: Displaying the peak-to-peak values $\mathbf{B}_Y(T)$ for a $6mm$ plate with a 20% defect at 0.5, 1, 1.5 & $3m/s$ alongside the percentage change between 0.5 and $3m/s$.

	$0.5m/s$	$1m/s$	$1.5m/s$	$3m/s$	% Change from 0.5 to $3m/s$
Top	0.0896	0.0932	0.0925	0.0851	-5.0223
Bottom	0.0861	0.0835	0.0829	0.0841	-2.3229

8mm plate thickness

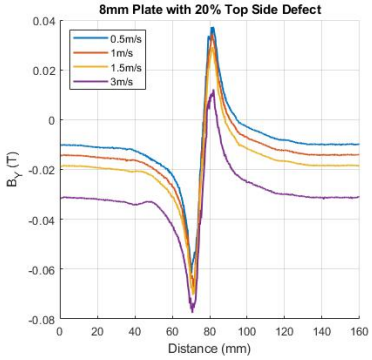

(a) $\mathbf{B}_Y$ response for a 20% top side defect on a $8mm$ plate.

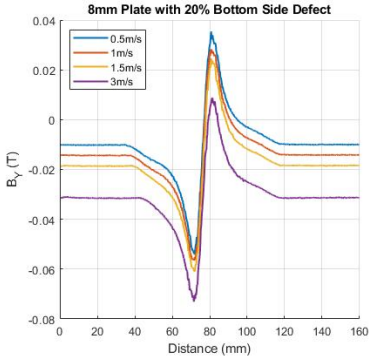

(b) $\mathbf{B}_Y$ response for a 20% bottom side defect on a $8mm$ plate.

Figure 4.14: Figure displaying the $\mathbf{B}_Y(T)$ response for a 20% through wall thickness defect on an $8mm$ plate.

The $8mm$ plate with a 20% through wall thickness defect as shown in Figure 4.14 above. The results indicate that for a top surface defect this isn't a significant change in the peak-to-peak signal response from 0.5 - $1.5m/s$ inspection speed as can be seen in Table 4.6 below. However for the top surface defect at $3m/s$ there is a drop of $0.0098T$ or -9.2929% from $0.5m/s$ indicating that velocity is beginning to have an effect on the MFL signals by reducing its amplitude as stated by Li [47] . For the bottom side defect a drop of $0.0077T$ or -8.6034% is seen from 0.5 to $3m/s$ showing only a small change in the peak-to-peak amplitudes of a 20% bottom side defect on an $8mm$ plate for the range of velocities considered in this study, following the trend of the $6mm$ plate with a 20% defect. The full range of peak-to-peak values are given below in Table 4.6.

Table 4.6: Displaying the peak-to-peak values $\mathbf{B}_Y(T)$ for a $8mm$ plate with a 20% defect at 0.5, 1, 1.5 & $3m/s$ alongside the percentage change between 0.5 and $3m/s$.

	$0.5m/s$	$1m/s$	$1.5m/s$	$3m/s$	% Change from 0.5 to $3m/s$
Top	0.0990	0.1017	0.0996	0.0898	-9.2929
Bottom	0.0895	0.0847	0.0856	0.0818	-8.6034

10mm Plate thickness

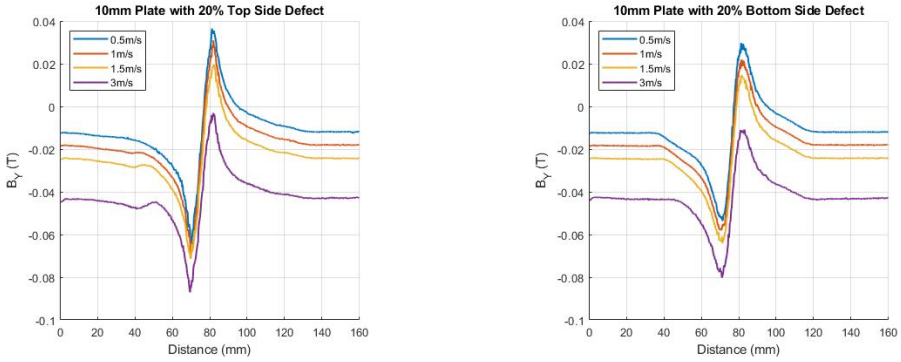

(a) $\mathbf{B}_Y$ response for a 20% top side defect on a $10mm$ plate.

(b) $\mathbf{B}_Y$ response for a 20% bottom side defect on a $10mm$ plate.

Figure 4.15: Figure displaying the $\mathbf{B}_Y$ response from a 20% top and bottom side defects on $10mm$ plate.

Figure 4.15 shows the results for a $10mm$ plate with a 20% defect on the top and bottom surfaces. The results shown in Figure 4.15a there is a continual reduction in the peak-to-peak signal amplitude for a top surface defect again agreeing with the claims of Li [47]. Again when considering a bottom side 20% defect there is a continual reduction in signal amplitude once the difference in offset has been taken into consideration as indicated Li [47]. The results for all MFL signals produced are displayed in Table 4.7 where it can be seen that there is a reduction of approx -16% for both top and bottom side defects from 0.5 to $3m/s$ scanning velocity. It is noted that for the top surface defect the signal response is becoming somewhat elongated in comparison to that of a bottom side defect. This is a trend that will become more apparent when defect size and plate thickness is increased further.

Table 4.7: Displaying the peak-to-peak values $\mathbf{B}_Y(T)$ for a $10mm$ plate with a 20% defect at 0.5, 1, 1.5 & $3m/s$ alongside the percentage change between 0.5 and $3m/s$.

	$0.5m/s$	$1m/s$	$1.5m/s$	$3m/s$	% Change from 0.5 to $3m/s$
Top	0.1006	0.1000	0.091	0.0840	-16.5010
Bottom	0.0833	0.0800	0.0786	0.0694	-16.6867

12mm Plate thickness

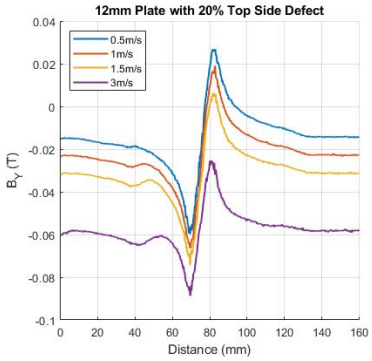

(a) $\mathbf{B}_Y$ response for a 20% top side defect on a $12mm$ plate.

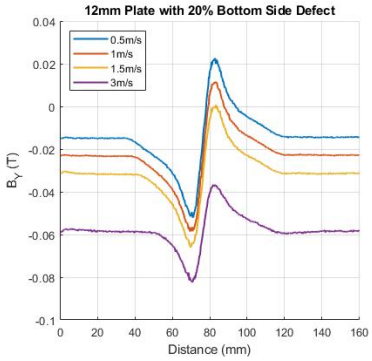

(b) $\mathbf{B}_Y$ response for a 20% bottom side defect on a $12mm$ plate.

Figure 4.16: Figure displaying the $\mathbf{B}_Y$ response from a 20% top and bottom side defects on $12mm$ plate.

Figures 4.16a & 4.16b present the signal responses from top and bottom side 20% defects respectively, on a $12mm$ thick plate. Similar to that of the $10mm$ plate there is a continual reduction in signal amplitude at each increased velocity increment as stated by [47]. For the bottom side defect this is when there is a significant reduction seen in the detectability of a 20% defect at $3m/s$. There is a reduction of $0.0289T$ or -38.7399% seen from 0.5 to $3m/s$. However, there is a reduction of -26.9896% seen for the top surface defect indicating a shift if the flux within the specimen. All peak-to-peak values are given in Table 4.8 below. This is complemented by the results of the flux distribution within a $12mm$ plate as previously seen in Section 4.2.2.4 begins to drop off at the $12mm$ plate thickness at $3m/s$. Also, considering the results from the flux distribution of the 14, 16 and $20mm$ plates this phenomena is expected to be more significantly exaggerated in the following results.

Table 4.8: Displaying the peak-to-peak values $\mathbf{B}_Y(T)$ for a $12mm$ plate with a 20% defect at 0.5, 1, 1.5 & $3m/s$ alongside the percentage change between 0.5 and $3m/s$.

	$0.5m/s$	$1m/s$	$1.5m/s$	$3m/s$	% Change from 0.5 to $3m/s$
Top	0.0867	0.0855	0.0807	0.0633	-26.9896
Bottom	0.0746	0.0703	0.0668	0.0457	-38.7399

14mm Plate thickness

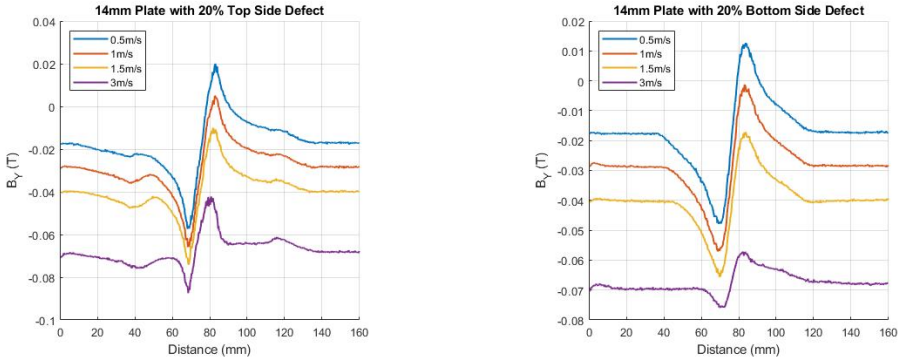

(a) $\mathbf{B}_Y$ response for a 20% top side defect on a $14mm$ plate.

(b) $\mathbf{B}_Y$ response for a 20% bottom side defect on a $14mm$ plate.

Figure 4.17: Figure displaying the $\mathbf{B}_Y$ response from a 20% top and bottom side defects on $14mm$ plate.

The MFL signal response of a 20% defect on a $14mm$ plate is shown in Figure 4.17. Following the previous trend where top surface defects become further elongated and distorted at all velocities as seen in Figure 4.17a. Again, a consistent reduction of signal amplitude is seen as velocity is increased as published by Li [47] with a reduction of -41.3972% for the top surface defect. This also holds true for the bottom side defect where a more significant drop in peak-to-peak signal amplitude of-68.9796% from 0.5 to $3m/s$ is shown in Figure 4.17b. This is where the results show the bottom side defect at $3m/s$ has become almost undetectable. This shift will begin to impact the detectability of defects when the signal to noise ratio is introduced in a practical scenario. This will be discussed in the practical results section of this thesis. For this magnet assembly it is recommended that if the defect threshold is at 20% a velocity of no greater than $1.5m/s$ should be used on a $14mm$ thick plate. However, a defect threshold as low as 20% is not commonly encountered during AST inspections.

Table 4.9: Displaying the peak-to-peak values $\mathbf{B}_Y(T)$ for a $12mm$ plate with a 20% defect at 0.5, 1, 1.5 & $3m/s$ alongside the percentage change between 0.5 and $3m/s$.

	$0.5m/s$	$1m/s$	$1.5m/s$	$3m/s$	% Change from 0.5 to $3m/s$
Top	0.0773	0.0710	0.0640	0.0453	-41.3972
Bottom	0.0606	0.0558	0.0485	0.0188	-68.9769

16mm Plate thickness

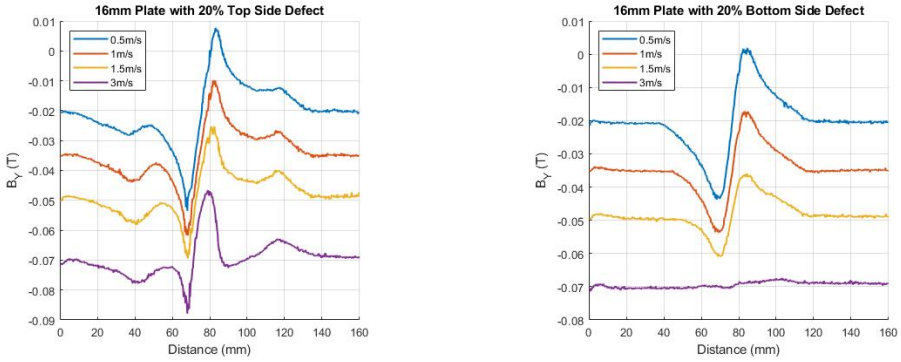

(a) $\mathbf{B}_Y$ response for a 20% top side defect on a 16mm plate.

(b) $\mathbf{B}_Y$ response for a 20% bottom side defect on a 16mm plate.

Figure 4.18: Figure displaying the $\mathbf{B}_Y$ response from a 20% top and bottom side defects on 16mm plate.

The 16mm plate with a 20% defect results are shown in 4.18 above. Figure 4.18b at 3m/s on the 16mm plate a 20% defect becomes undetectable continuing the trend as for the 14mm plate. The top and bottom side defects show a consistent reduction in peak-to-peak signal amplitude as seen in Table 4.10. This confirms the claims made in the contributions to knowledge of this thesis where increased velocity can mask defects by manifesting the induced flux to the near surface of the specimen. This is evident from the reduction of the signal amplitudes when the velocity is increased but also the difference in percentage change between the top and bottom side defects from 0.5 to 3m/s is significant. The top surface defect demonstrates a reduction of -32.5163% and the bottom surface defect has a reduction of -91.2473% change in the peak-to-peak signal response. Again, signal offsets are affected by the change in velocity.

Table 4.10: Displaying the peak-to-peak values $\mathbf{B}_Y(T)$ for a 12mm plate with a 20% defect at 0.5, 1, 1.5 & 3m/s alongside the percentage change between 0.5 and 3m/s.

	0.5m/s	1m/s	1.5m/s	3m/s	% Change from 0.5 to 3m/s
Top	0.0612	0.0519	0.0442	0.0413	-32.5163
Bottom	0.0457	0.0365	0.0249	0.0040	-91.2473

20mm Plate thickness

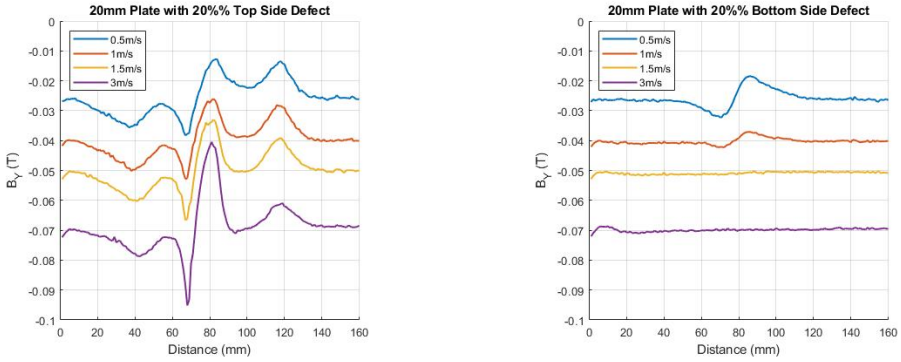

(a) $\mathbf{B}_Y$ response for a 20% top side defect on a 20mm plate.

(b) $\mathbf{B}_Y$ response for a 20% bottom side defect on a 20mm plate.

Figure 4.19: Figure displaying the $\mathbf{B}_Y$ response from a 20% top and bottom side defects on 20mm plate.

The $\mathbf{B}_Y$ signal response for a 20% defect on a 20mm thick plate is shown in Figure 4.19. It can be seen in Figure 4.19a for the top surface defect an increase in velocity returns an increased signal amplitude with a percentage change of 113.6719% over doubling the peak-to-peak signal response when velocity is increased form 0.5 to mm/s. As a result of the large top surface defect the defect edges are beginning to create separate dipoles. If the defect size was to continue to grow in width each edge of the defect would generate a signal, resulting in two signals produced for the same defect. The bottom side response found in Figure 4.19b reduces in signal amplitude by -89.9281% when inspection velocity is increased supporting the claims to knowledge made within this thesis. The values for the peak-to-peak signal responses of each defect trace can be seen below in Table 4.11.

Table 4.11: Displaying the peak-to-peak values $\mathbf{B}_Y(T)$ for a 20mm plate with a 20% defect at 0.5, 1, 1.5 & 3m/s alongside the percentage change between 0.5 and 3m/s.

	0.5m/s	1m/s	1.5m/s	3m/s	% Change from 0.5 to 3m/s
Top	0.0256	0.0269	0.0337	0.0547	113.6719
Bottom	0.0139	0.0053	0.0014	0.0014	-89.9281

4.2.3.2 20% Defect Summary

This section provides a summary of the data given in the tables above for a 20% defect response on all plate thicknesses and velocities considered within the work of this thesis. This will allow the reader to view the data in graphical form for a visual comparison. This data will be displayed in two formats. Firstly, the peak-to-peak $\mathbf{B}_Y$ responses are shown for all plate thicknesses for a given velocity in Figure 4.20 where it can be seen at the slower speeds of 0.5 and $1m/s$ there is consistent trend between Top and Bottom side defects at all plate thicknesses. For speeds of 1.5 and $3m/s$ the top surface defects show an amplification when the larger plate thicknesses are taken into consideration. The amplification is velocity dependent showing an increase at 1.5 m/s on a $20mm$ plate, whereas at $3m/s$ the amplification of top surface defects and the reduction in bottom surface defects begins at smaller plate thicknesses of $14mm$ due to the flux concentration towards the top surface. Following this the peak-to-peak values are shown for individual plate thicknesses at the full range of velocities used for the work carried out in this thesis. The data for each plate thickness can be found in Figure 4.21.

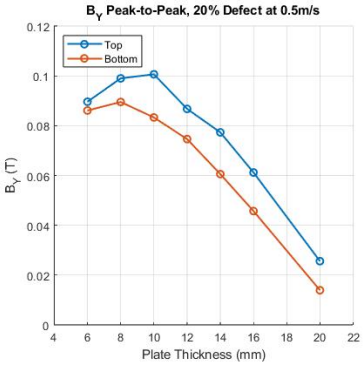

(a) $\mathbf{B}_Y$ peak-to-peak response for a 20% top and bottom side defects on all plate thicknesses at $0.5m/s$.

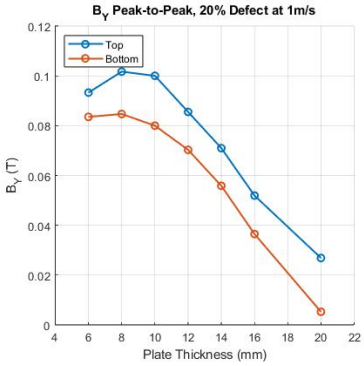

(b) $\mathbf{B}_Y$ peak-to-peak response for a 20% top and bottom side defects on all plate thicknesses at $1m/s$.

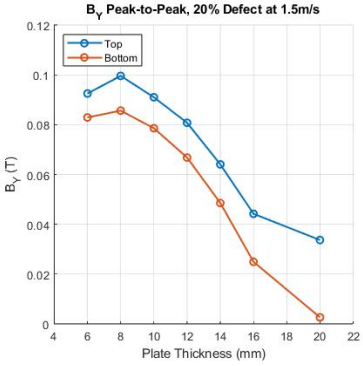

(c) $\mathbf{B}_Y$ peak-to-peak response for a 20% top and bottom side defects on all plate thicknesses at $1.5m/s$.

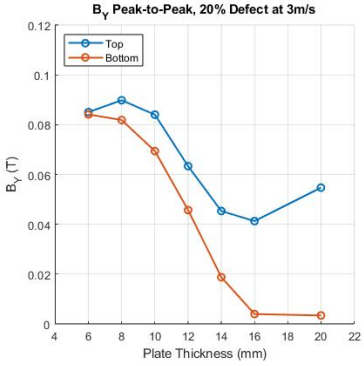

(d) $\mathbf{B}_Y$ peak-to-peak response for a 20% top and bottom side defects on all plate thicknesses at $3m/s$.

Figure 4.20: Figure displaying the $\mathbf{B}_Y$ response from a 20% top and bottom side defects at all plate thicknesses at 0.5, 1, 1.5 and $3m/s$.

When considering the data in Figure 4.20 it is shown that for a 20% defect a consistent response of the top side showing a larger peak-to-peak signal than that of the bottom side defect. In Figure 4.20b between 16 and $20mm$ plate thickness there is a separation in peak-to-peak amplitudes beginning to emerge. This becomes increasingly noticeable on the $1.5m/s$ results shown in Figure 4.20c. At $3m/s$ this affect takes place at $14mm$ plate thickness. For the top side defect there is an increase in signal amplitude from 16 to $20mm$ indicating an increased flux density near to the top side of the plate, as is one of the claims made as a contribution to knowledge in this thesis. It is also shown that at $1m/s$ a 20% bottom defect response of a $20mm$ plate is insignificant and would likely be lost within signal noise on a practical system. At

$3m/s$ this type of defect is considered undetectable at $16mm$ plate thickness.

Figure 4.21 shows the summary of all plate thicknesses at the four velocities. It can be seen that the top and bottom side defects for plate thicknesses of 6 - $10mm$ in Figures 4.21a to 4.21c show a relatively consistent response at all velocities as a result of the plate being saturated. As the plate thickness increases beyond $12mm$ and the flux density within the plate decreases defect detection is affected at higher velocities. The affects of velocity can be seen most clearly on plate thicknesses of 16 and $20mm$ in Figures 4.21f and 4.21g respectively. The $16mm$ results show large separation at $3m/s$ where the top side defect is marginally reduced in amplitude whereas the bottom surface defect is deemed undetectable. For a $20mm$ thick plate a continual increase in peak-to-peak signal amplitude is identified at throughout all velocities and the bottom side defect becomes undetectable at a velocity of $1m/s$.

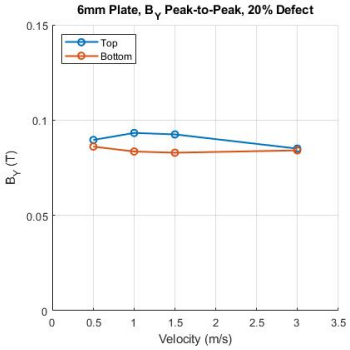

(a) 6mm plate summary with 20% defect.

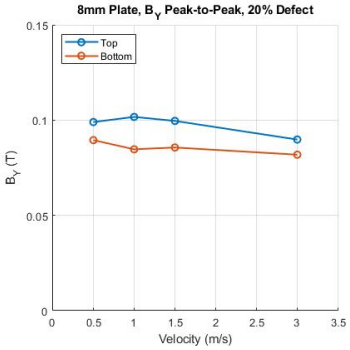

(b) 8mm plate summary with 20% defect.

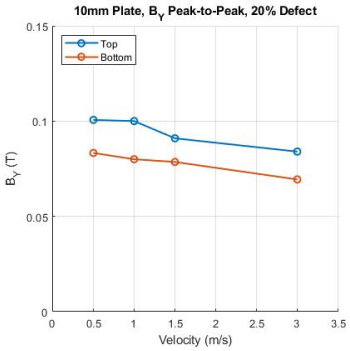

(c) 10mm plate summary with 20% defect.

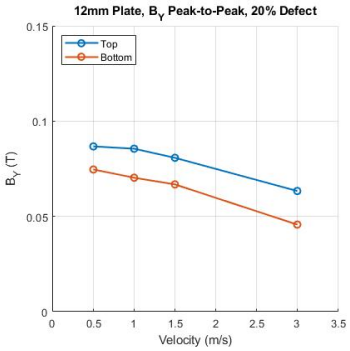

(d) 12mm plate summary with 20% defect.

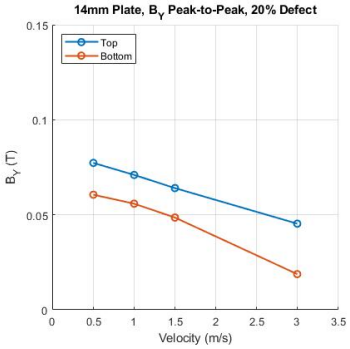

(e) 14mm plate summary with 20% defect.

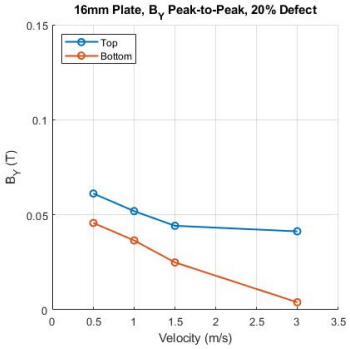

(f) 16mm plate summary with 20% defect.

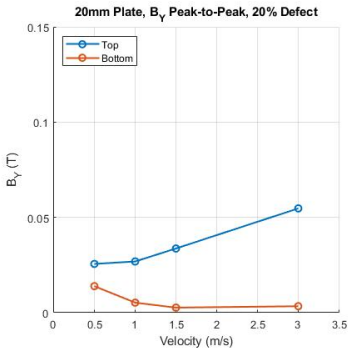

(g) 20mm plate summary with 20% defect.

Figure 4.21: 20% peak-to-peak defect summary for each plate thickness.

4.2.3.3 40% Defect Response

6mm plate thickness

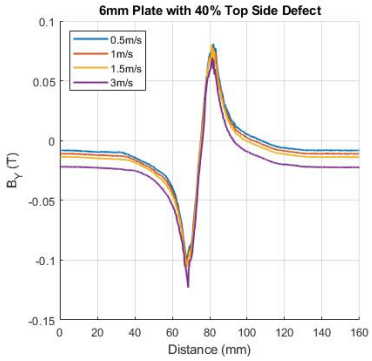

(a) $\mathbf{B}_Y$ response for a 40% top side defect on a $6mm$ plate.

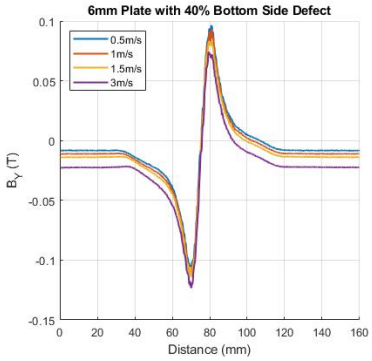

(b) $\mathbf{B}_Y$ response for a 40% bottom side defect on a $6mm$ plate.

Figure 4.22: Figure displaying the $\mathbf{B}_Y$ response from a 40% top and bottom side defects on $6mm$ plate.

Figure 4.22 displays the results for a 40% defect on a $6mm$ thick plate. The results indicate a reduction in the peak-to-peak values for bottom side defects of -4.7734%, following the trend as described by [47] and also that shown in the previous data shown for a $6mm$ plate with a defect of 20% through wall thickness. However, for the top side data shown in Figure 4.22a and Table 4.12 an increase of the peak-to-peak signal amplitude is indicated $0.0114T$ or 6.2983% from a velocity of $0.5m/s$ to $3m/s$. Again, a change in offset is seen with changing velocities. One of the major considerations of this data set is that the bottom side defect produces a higher peak-to-peak signal amplitude than that of a top side defect. This is a possible result of the flux traversing the path of least reluctance through the material when a defect of such significance is seen on bottom side of a saturated plate.

Table 4.12: Displaying the peak-to-peak values $\mathbf{B}_Y(T)$ for a $6mm$ plate with a 40% defect at 0.5, 1, 1.5 & $3m/s$ alongside the percentage change between 0.5 and $3m/s$.

	$0.5m/s$	$1m/s$	$1.5m/s$	$3m/s$	% Change from 0.5 to $3m/s$
Top	0.1810	0.1806	0.1864	0.1924	6.2983
Bottom	0.2074	0.2063	0.1978	0.1975	-4.7734

8mm plate thickness

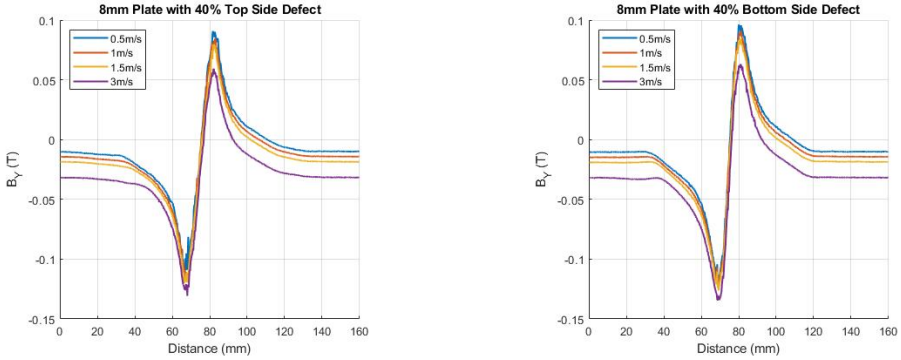

(a) $\mathbf{B}_Y$ response for a 40% top side defect on a $8mm$ plate.

(b) $\mathbf{B}_Y$ response for a 40% bottom side defect on a $8mm$ plate.

Figure 4.23: Figure displaying the $\mathbf{B}_Y$ response from a 40% top and bottom side defects on $8mm$ plate.

Following the trend identified on the $6mm$ plate, bottom side defects produce a greater peak-to-peak signal amplitude when compared to that of the top side defect for the same inspection velocity as shown in Table 4.13. However, overall both top and bottom side defects see a peak-to-peak signal reduction when velocity is incrementally increased as seen in Figures 4.23a & 4.23b above. The change from 0.5-3m/s is a reduction of $0.0133T$ or -6.5912% whereas the bottom side has a decrease in peak-to-peak signal amplitude of $0.01763963T$ or -2.1356%.

Table 4.13: Displaying the peak-to-peak values $\mathbf{B}_Y(T)$ for a $8mm$ plate with a 40% defect at 0.5, 1, 1.5 & $3m/s$ alongside the percentage change between 0.5 and $3m/s$.

	$0.5m/s$	$1m/s$	$1.5m/s$	$3m/s$	% Change from 0.5 to $3m/s$
Top	0.2033	0.2007	0.2000	0.1899	-6.5912
Bottom	0.2154	0.2133	0.2108	0.1978	-2.1356

10mm plate thickness

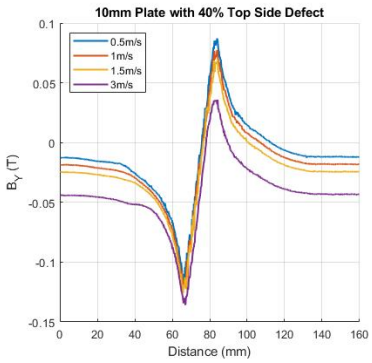

(a) $\mathbf{B}_Y$ response for a 40% top side defect on a $10mm$ plate.

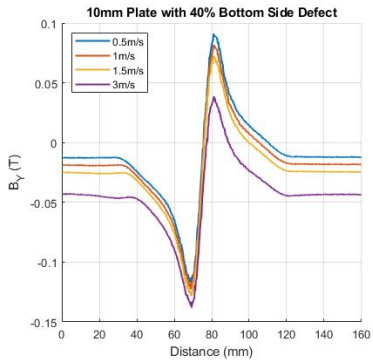

(b) $\mathbf{B}_Y$ response for a 40% bottom side defect on a $10mm$ plate.

Figure 4.24: Figure displaying the $\mathbf{B}_Y$ response from a 40% top and bottom side defects on $10mm$ plate.

The peak-to-peak values taken from Figure 4.24 for 40% top and bottom side defects on a $10mm$ thick plate are displayed in Table 4.14 below. The peak-to-peak values indicate that there is a reduction in signal amplitude when velocity is increased for both top and bottom side defects as agreed with [47]. The overall reduction in the peak-to-peak values for both top and bottom is in the region of 15%. Similarly to the 6 & $8mm$ plate thicknesses the bottom side defects produce a greater peak-to-peak signal response than that of a top side defect. The top and bottom signal responses are becoming more laterally spread as seen in Figures 4.24a & 4.24b.

Table 4.14: Displaying the peak-to-peak values $\mathbf{B}_Y(T)$ for a $10mm$ plate with a 40% defect at 0.5, 1, 1.5 & $3m/s$ alongside the percentage change between 0.5 and $3m/s$.

	$0.5m/s$	$1m/s$	$1.5m/s$	$3m/s$	% Change from 0.5 to $3m/s$
Top	0.2045	0.2021	0.1955	0.1718	-15.9902
Bottom	0.2084	0.2046	0.2010	0.1767	-15.2111

12mm plate thickness

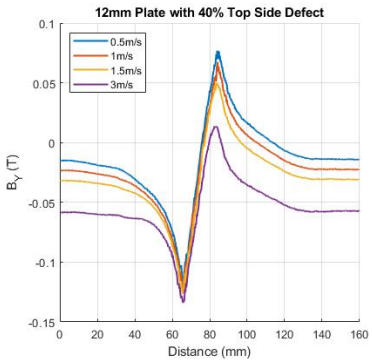

(a) $\mathbf{B}_Y$ response for a 40% top side defect on a $12mm$ plate.

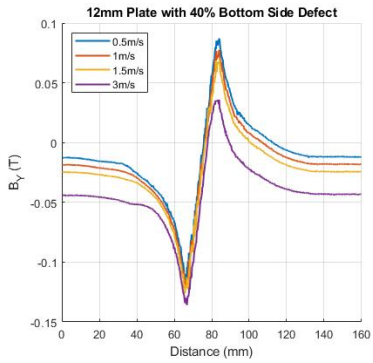

(b) $\mathbf{B}_Y$ response for a 40% bottom side defect on a $12mm$ plate.

Figure 4.25: Figure displaying the $\mathbf{B}_Y$ response from a 40% top and bottom side defects on $12mm$ plate.

The $\mathbf{B}_Y$ signal response for a 40% through wall defect on a $12mm$ plate is shown in Figure 4.25 above. From this and combined with the peak-to-peak values shown in Table 4.15 below it can be seen that the signal amplitude of the bottom side defect at all velocities considered is higher than a top surface defect for the same velocities shown in Figures 4.25a & 4.25b. This follows the trend as previously seen on the 6 to $10mm$ plate thicknesses. However taking into consideration previous results shown in both the distribution and defect response results thus far this trend is expected to change in the larger plate thicknesses from this point forward for the 40% defect considered within this subsection of the thesis.

Table 4.15: Displaying the peak-to-peak values $\mathbf{B}_Y(T)$ for a $12mm$ plate with a 40% defect at 0.5, 1, 1.5 & $3m/s$ alongside the percentage change between 0.5 and $3m/s$.

	$0.5m/s$	$1m/s$	$1.5m/s$	$3m/s$	% Change from 0.5 to $3m/s$
Top	0.1938	0.1897	0.1766	0.1477	-23.7874
Bottom	0.2045	0.2021	0.1955	0.1718	-15.9902

14mm plate thickness

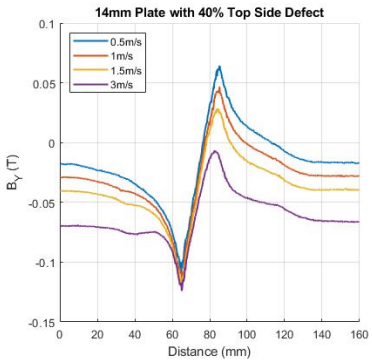

(a) $\mathbf{B}_Y$ response for a 40% top side defect on a $14mm$ plate.

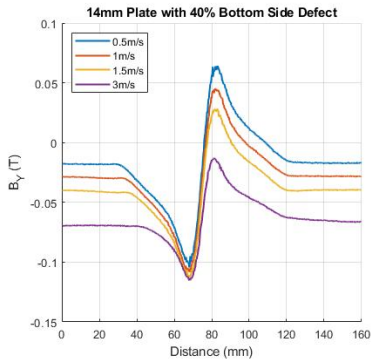

(b) $\mathbf{B}_Y$ response for a 40% bottom side defect on a $14mm$ plate.

Figure 4.26: Figure displaying the $\mathbf{B}_Y$ response from a 40% top and bottom side defects on $14mm$ plate.

The $14mm$ plate thickness is where the signal peak-to-peak values show that the bottom side defects no longer produce a greater response than a top surface defect as shown in Table 4.16 below. Figures 4.26a & 4.26b when compared, both show a wider signal response in comparison to that of the thinner plate thickness for the same 40% defect response. This wider signal narrows with increased velocity for bottom side defects which suggests there may be a more optimal sensor position for scanning with increased velocity. It is suggested that for a 40% detection threshold for this particular system a slower scanning speed is more beneficial at the given plate thickness to give more consistent results. Looking back at previous results and taking into consideration the increased defect size, the signal responses for the $3m/s$ scanning speed is estimated to decline rapidly on the 16 and $20mm$ plate thicknesses.

Table 4.16: Displaying the peak-to-peak values $\mathbf{B}_Y(T)$ for a $14mm$ plate with a 40% defect at 0.5, 1, 1.5 & $3m/s$ alongside the percentage change between 0.5 and $3m/s$.

	$0.5m/s$	$1m/s$	$1.5m/s$	$3m/s$	% Change from 0.5 to $3m/s$
Top	0.1726	0.1607	0.1468	0.1175	-31.9235
Bottom	0.1687	0.1533	0.1411	0.1023	-39.3598

16mm plate thickness

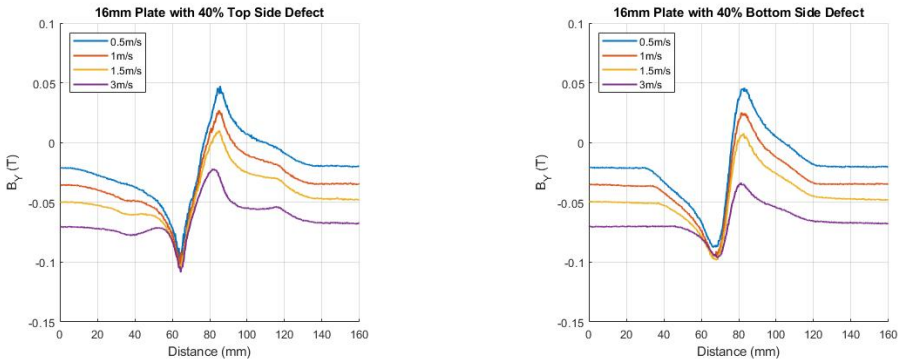

(a) $\mathbf{B}_Y$ response for a 40% top side defect on a $16mm$ plate.

(b) $\mathbf{B}_Y$ response for a 40% bottom side defect on a $16mm$ plate.

Figure 4.27: Figure displaying the B_Y response from a 40% top and bottom side defects on $16mm$ plate and the dimensions of the defect in relation to plate thickness.

Figure 4.27a indicates that the defect response for the top surface has become distorted due to the elongated defect at $16mm$ plate thickness. This is a result of the defect width becoming large enough to distort the signal at $19.8mm$ wide at the top surface. The Bottom side defect signal response at $3m/s$ is reduced by $\frac{1}{2}$ of the peak-to-peak value of that at $0.5m/s$ as can be seen in Figure 4.27b above and Table 4.17 below. again following the trend of previous results the signal offset is continuously decreasing with inspection velocity. Taking this into consideration it is recommended that this system scanning velocity should not exceed $1m/s$ but should be scanned as slowly as possible for the most reliable results.

Table 4.17: Displaying the peak-to-peak values $\mathbf{B}_Y(T)$ for a $16mm$ plate with a 40% defect at 0.5, 1, 1.5 & $3m/s$ alongside the percentage change between 0.5 and $3m/s$.

	$0.5m/s$	$1m/s$	$1.5m/s$	$3m/s$	% Change from 0.5 to $3m/s$
Top	0.1454	0.1300	0.1152	0.0866	-40.4402
Bottom	0.1337	0.1209	0.1059	0.0637	-52.356

20mm plate thickness

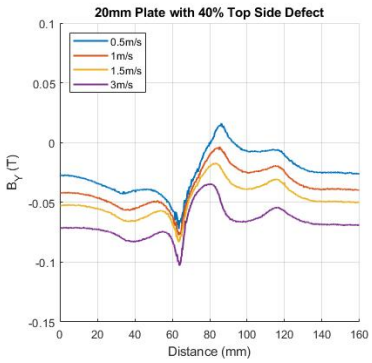

(a) $\mathbf{B}_Y$ response for a 40% top side defect on a $20mm$ plate.

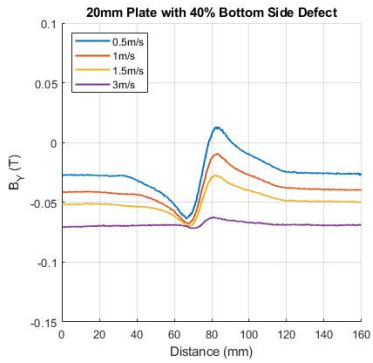

(b) $\mathbf{B}_Y$ response for a 40% bottom side defect on a $20mm$ plate.

Figure 4.28: Figure displaying the $\mathbf{B}_Y$ response from a 40% top and bottom side defects on $20mm$ plate.

Following the trend of the $16mm$ plate, the $20mm$ thick plate has a more a greater distorted top side signal as seen in Figure 4.28a. Again the defect is wider than the plate is thick. A significant drop in peak-to-peak signal amplitude is seen when velocity is increased for the bottom side defect with a reduction of -86.7876%. As can be seen in Figure 4.28b a 40% bottom side defect on a $20mm$ plate is almost undetectable. Taking into consideration, that these are simulated results it is predicted that this defect would not be detectable on a system in practice due to the increased signal to noise ratio that is encountered during a typical Magnetic Flux Leakage inspection. The peak-to-peak values are displayed below in Table 4.18.

Table 4.18: Displaying the peak-to-peak values $\mathbf{B}_Y(T)$ for a $20mm$ plate with a 40% defect at 0.5, 1, 1.5 & $3m/s$ alongside the percentage change between 0.5 and $3m/s$.

	$0.5m/s$	$1m/s$	$1.5m/s$	$3m/s$	% Change from 0.5 to $3m/s$
Top	0.0883	0.0737	0.0661	0.0687	-22.1971
Bottom	0.0772	0.0588	0.0427	0.0102	-86.7876

4.2.3.4 40% Defect Summary

In this section a breakdown of the data given in the tables above for the 40% defect response is given. This will allow the reader to view the data in graphical form for a visual comparison across all plate thicknesses and velocities. The data will be displayed in two formats, firstly, the peak-to-peak $\mathbf{B}_Y$ responses are shown for all plate thicknesses for a given velocity in Figure 4.29. From these images it is clear to see that velocity has an increased affect on the signal response on thicker plate thicknesses indicated by the increased separation of the peak-to-peak values on the 14, 16 and $20mm$ plate thicknesses. Secondly, graphical representation of the data displayed in each table above for the 40% defects are given where the separation is shown and also the flip in signal response from the bottom to top side becoming larger in Figure 4.30.

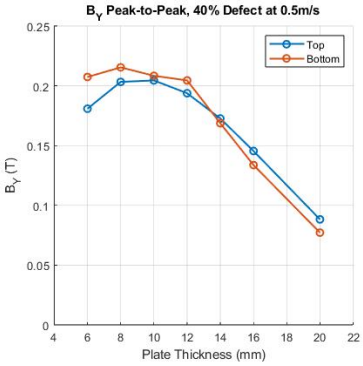

(a) $\mathbf{B}_Y$ peak-to-peak response for a 40% top and bottom side defects on all plate thicknesses at $0.5m/s$.

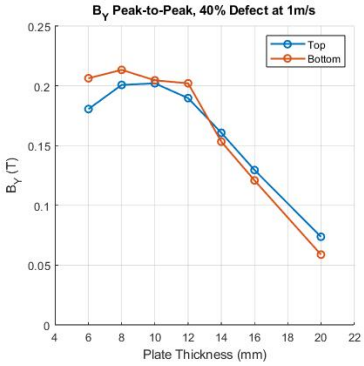

(b) $\mathbf{B}_Y$ peak-to-peak response for a 40% top and bottom side defects on all plate thicknesses at $1m/s$.

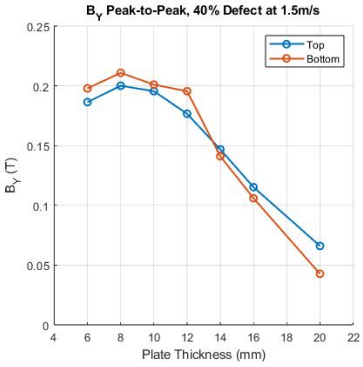

(c) $\mathbf{B}_Y$ peak-to-peak response for a 40% top and bottom side defects on all plate thicknesses at $1.5m/s$.

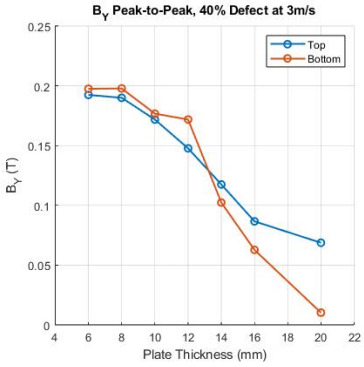

(d) $\mathbf{B}_Y$ peak-to-peak response for a 40% top and bottom side defects on all plate thicknesses at $3m/s$.

Figure 4.29: Figure displaying the $\mathbf{B}_Y$ response from a 40% top and bottom side defects at all plate thicknesses at 0.5, 1, 1.5 and $3m/s$.

Analysing the data presented in Figure 4.29 for a 40% defect there are four individual graphs each representing an inspection velocity. For each graph of a specific velocity the peak-to-peak values are displayed as a function of plate thickness. For all velocities considered it should be noted that bottom side responses indicate a larger peak-to-peak amplitude over the top surface up to $12mm$ plate thickness. Plate thicknesses greater than $12mm$ display a larger response from the top surface defect of 40% at all velocities. At a velocity of $1.5m/s$ a separation is seen to emerge between top and bottom side defect responses at $14mm$ plate thickness and increasing up to the maximum considered plate of $20mm$ as seen in Figure 4.29c. This separation identified at $1.5m/s$ is also present with an increased effect at $3m/s$. The 40% bottom defect becomes undetectable at $3m/s$ following the trend of the 20% defect.

The data displayed in Figure 4.30 are individual plate thicknesses at 0.5, 1, 1.5 and $3m/s$. The defect responses for a $6mm$ plate indicate the effects of velocity increasing signal response above $1m/s$ show an increase in the peak-to-peak value for a top side defect and a reduction in bottom side defects, as seen in Figure 4.30a. From 8 to $12mm$ plate thickness in Figures 4.30b to 4.30d the bottom surface shows a greater peak-to-peak signal response comparatively to that of the bottom side defect with a consistent reduction in signal amplitude with increasing velocity. Figures 4.30e to 4.30g show a flip where the top surface response becomes larger than the bottom. a small separation emerges at $3m/s$ in Figure 4.30e and is exaggerated in Figure 4.30f fora $16mm$ thick plate. Similar to the 20% defect on a $20mm$ plate Figure 4.30g shows the same trend from 1.5 to $3m/s$ there is a peak-to-peak signal amplitude increase for a top surface defects. With the same change in velocity for the bottom side defect, the change in signal response renders this defect undetectable for this particular magnet assembly.

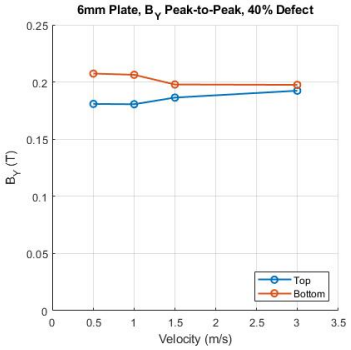

(a) 6mm plate summary with 40% defect.

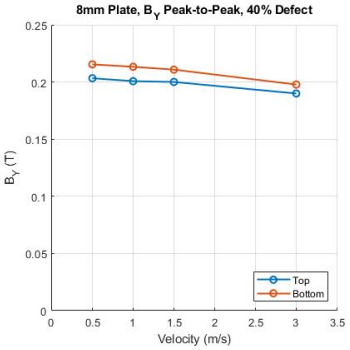

(b) 8mm plate summary with 40% defect.

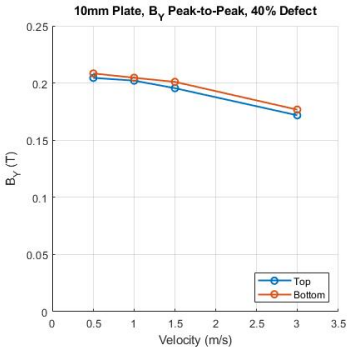

(c) 10mm plate summary with 40% defect.

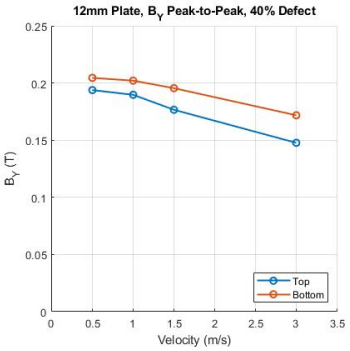

(d) 12mm plate summary with 40% defect.

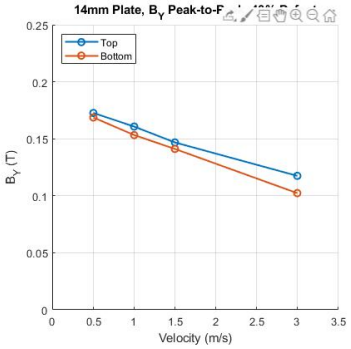

(e) 14mm plate summary with 40% defect.

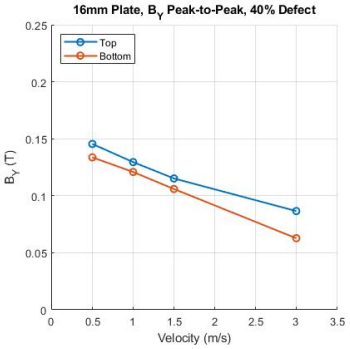

(f) 16mm plate summary with 40% defect.

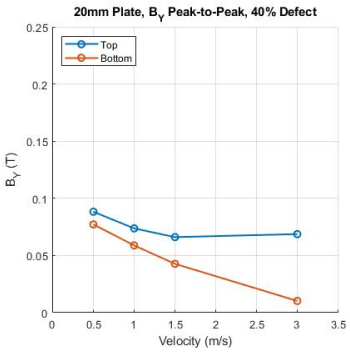

(g) 20mm plate summary with 40% defect.

Figure 4.30: 40% peak-to-peak defect summary for each plate thickness.

4.2.3.5 60% Defect Response

6mm plate thickness

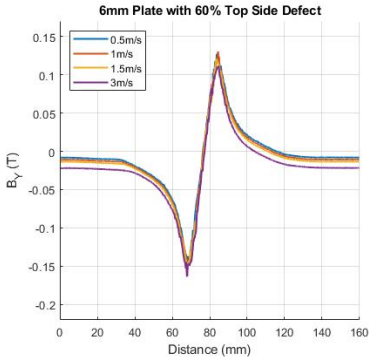

(a) $\mathbf{B}_Y$ response for a 60% top side defect on a $6mm$ plate.

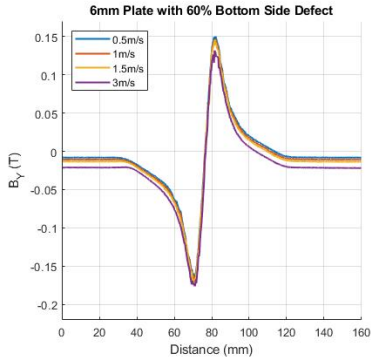

(b) $\mathbf{B}_Y$ response for a 60% bottom side defect on a $6mm$ plate.

Figure 4.31: Figure displaying the $\mathbf{B}_Y$ response from a 60% top and bottom side defects on $6mm$ plate.

Similarly to that of the 40% defect depth on a $6mm$ plate the bottom side defects peak-to-peak signal values of a 60% defect are greater than that of a top surface defect. The results of which can be seen in Figure 4.31 & Table 4.19. The results indicate that there is not a significant difference in defect amplitudes when the values are taken into consideration indicating velocity has little to no affect on the results obtained from this type of defect scanned at the velocities considered within this work. The top and bottom surface detects change by 0.4020% and -2.5649% respectively from 0.5 to $3m/s$. Following the trend of previous simulations there is a consistent change in offset with velocity.

Table 4.19: Displaying the peak-to-peak values $\mathbf{B}_Y(T)$ for a $6mm$ plate with a 60% defect at 0.5, 1, 1.5 & $3m/s$ alongside the percentage change between 0.5 and $3m/s$.

	$0.5m/s$	$1m/s$	$1.5m/s$	$3m/s$	% Change from 0.5 to $3m/s$
Top	0.2736	0.2779	0.2747	0.2747	0.4020
Bottom	0.3158	0.3183	0.3207	0.3077	-2.5649

8mm plate thickness

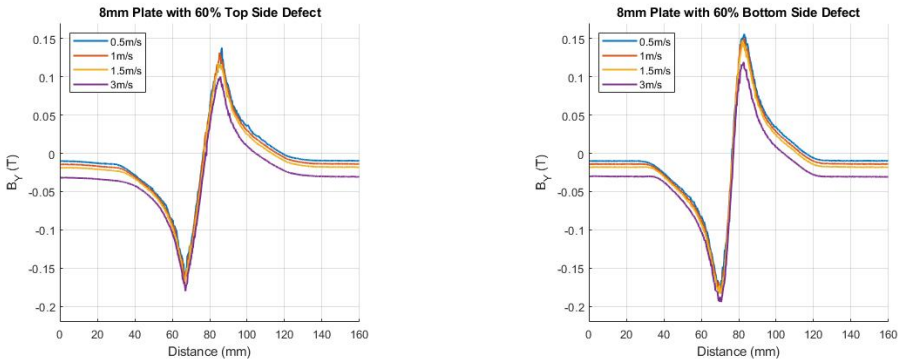

(a) $\mathbf{B}_Y$ response for a 60% top side defect on a $8mm$ plate.

(b) $\mathbf{B}_Y$ response for a 60% bottom side defect on a $8mm$ plate.

Figure 4.32: Figure displaying the $\mathbf{B}_Y$ response from a 60% top and bottom side defects on $6mm$ plate.

Figures 4.32a & 4.32b show the signal responses from a 60% defect on the top and bottom surfaces respectively on an $8mm$ thick plate. Although it is not easily identifiable from the graphical representation of the data in Figure 4.32, there is a reduction in peak-to-peak signal amplitudes with increased velocity with only a 1.2689% difference between top and bottom surface defects as seen in Table 4.20. The data presented in the table also indicates that the bottom side defect is still showing a greater response over the top surface defect. As expected from trends that have been forming throughout the work thus far it is shown that the top surface defect has a wider signal response that the bottom side defect. Interestingly, the $8mm$ thick plate had an increased signal response over that of the $6mm$ plate results as shown previously in 4.19.

Table 4.20: Displaying the peak-to-peak values $\mathbf{B}_Y(T)$ for a $8mm$ plate with a 60% defect at 0.5, 1, 1.5 & $3m/s$ alongside the percentage change between 0.5 and $3m/s$.

	$0.5m/s$	$1m/s$	$1.5m/s$	$3m/s$	% Change from 0.5 to $3m/s$
Top	0.3018	0.2978	0.2876	0.2801	-7.1901
Bottom	0.3327	0.3312	0.3316	0.3130	-5.9212

10mm plate thickness

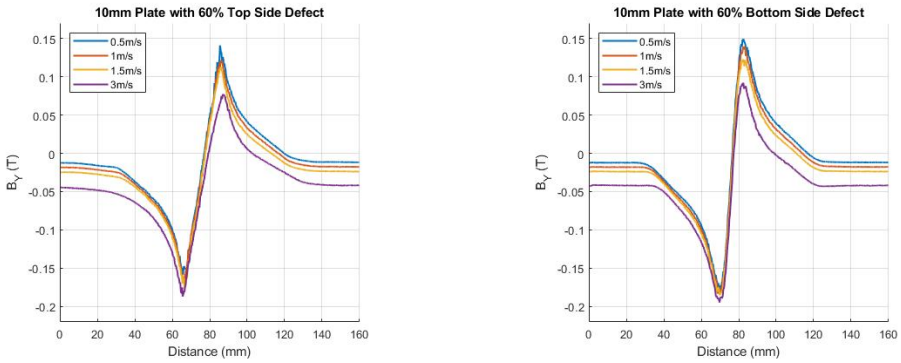

(a) $\mathbf{B}_Y$ response for a 60% top side defect on a $10mm$ plate.

(b) $\mathbf{B}_Y$ response for a 60% bottom side defect on a $10mm$ plate.

Figure 4.33: Figure displaying the $\mathbf{B}_Y$ response from a 60% top and bottom side defects on $10mm$ plate.

As can be seen in Figure 4.33 above for the results displayed for a 60% defects top and bottom on a $10mm$ plate, the defect response from the top side defect is more spatially spread over the scan distance when compared to the bottom side defect of the same size. Again the data in Table 4.21 indicates the bottom side defect is showing a larger response over the top surface for an identical defect type and size. There is a continual reduction in peak-to-peak signal amplitude when velocity is increased on both top and bottom side defects in agreement with [47].

Table 4.21: Displaying the peak-to-peak values $\mathbf{B}_Y(T)$ for a $10mm$ plate with a 60% defect at 0.5, 1, 1.5 & $3m/s$ alongside the percentage change between 0.5 and $3m/s$.

	$0.5m/s$	$1m/s$	$1.5m/s$	$3m/s$	% Change from 0.5 to $3m/s$
Top	0.3046	0.2877	0.2902	0.2639	-13.3618
Bottom	0.3282	0.3231	0.3074	0.2867	-12.6447

12mm plate thickness

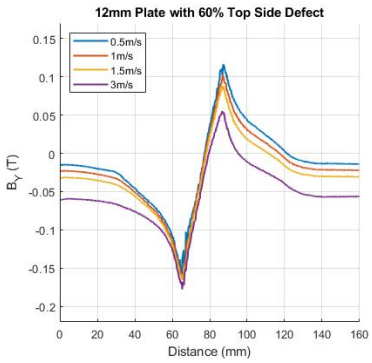

(a) $\mathbf{B}_Y$ response for a 60% top side defect on a $12mm$ plate.

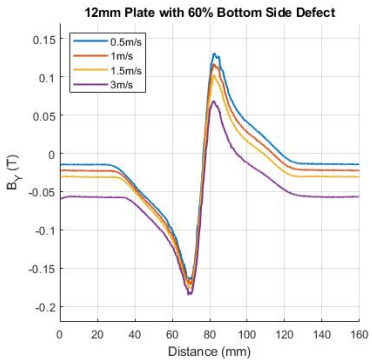

(b) $\mathbf{B}_Y$ response for a 60% bottom side defect on a $12mm$ plate.

Figure 4.34: Figure displaying the $\mathbf{B}_Y$ response from a 60% top and bottom side defects on $12mm$ plate.

Figures 4.34a & 4.34b present the signal responses from top and bottom side 60% defects respectively, on a $12mm$ thick plate. The peak-to-peak amplitudes continue to show an overall reduction as inspection speeds are increased as concluded by [47]. However, there is still a larger signal response from a bottom surface defect when compared to that of a top surface for this magnet assembly, sensor position and plate thickness. The peak-to-peak values are displayed below in Table 4.22 to support these claims as the signals appear to be similar in amplitude when compared graphically.

Table 4.22: Displaying the peak-to-peak values $\mathbf{B}_Y(T)$ for a $12mm$ plate with a 60% defect at 0.5, 1, 1.5 & $3m/s$ alongside the percentage change between 0.5 and $3m/s$.

	$0.5m/s$	$1m/s$	$1.5m/s$	$3m/s$	% Change from 0.5 to $3m/s$
Top	0.2753	0.2659	0.2536	0.2326	-15.5104
Bottom	0.2953	0.2883	0.2789	0.2540	-13.9858

14mm plate thickness

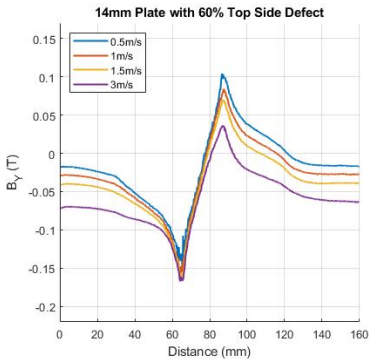

(a) $\mathbf{B}_Y$ response for a 60% top side defect on a $14mm$ plate.

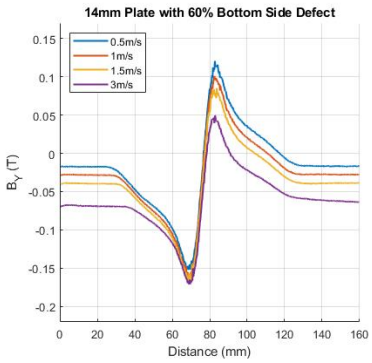

(b) $\mathbf{B}_Y$ response for a 60% bottom side defect on a $14mm$ plate.

Figure 4.35: Figure displaying the $\mathbf{B}_Y$ response from a 60% top and bottom side defects on $14mm$ plate.

When compared to the previous set of results for the $14mm$ 40% defect this is the point where the top surface defect becomes larger than the bottom. However this is not the case for a 60% defect. The 60% defect indicates a larger signal response from the bottom side defect as seen in 4.23 below for the same plate thickness. The spatial difference of responses from the top surface defect are becoming increasingly distorted and noticeable as seen in Figure 4.35a above and is more significant when compared to that of the top surface signal response found in Figure 4.35b. Following the trend of the previous data set there is a continual reduction in peak-to-peak signal amplitude when velocity is increased as demonstrated by [47].

Table 4.23: Displaying the peak-to-peak values $\mathbf{B}_Y(T)$ for a $14mm$ plate with a 60% defect at 0.5, 1, 1.5 & $3m/s$ alongside the percentage change between 0.5 and $3m/s$.

	$0.5m/s$	$1m/s$	$1.5m/s$	$3m/s$	% Change from 0.5 to $3m/s$
Top	0.2543	0.2444	0.2303	0.203	-20.1730
Bottom	0.2723	0.2665	0.2555	0.2202	-19.1333

16mm plate thickness

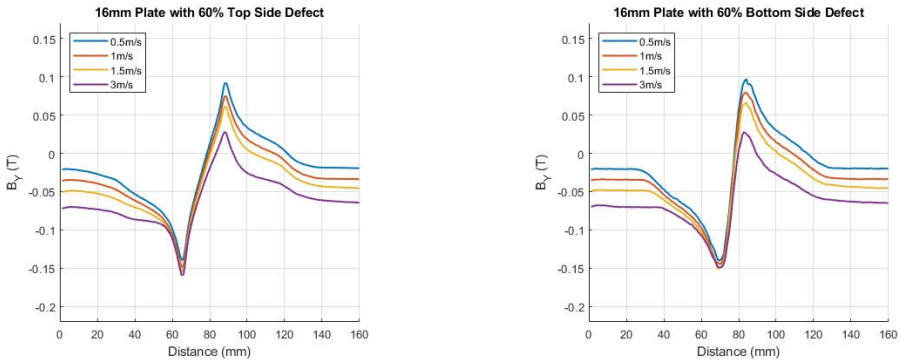

(a) $\mathbf{B}_Y$ response for a 60% top side defect on a 16mm plate.

(b) $\mathbf{B}_Y$ response for a 60% bottom side defect on a 16mm plate.

Figure 4.36: Figure displaying the $\mathbf{B}_Y$ response from a 60% top and bottom side defects on 16mm plate.

From the data displayed in Table 4.24 peak-to-peak amplitudes have become almost identical taking this into consideration, it is suspected that the 20mm thick plate will generate a result where the top side becomes larger than the bottom surface defect. The results from Table 4.24 follows the trend of a reduction in signal amplitude with increased inspection velocities. Again, greater distortion of both signal traces are seen from Figures 4.36a and 4.36b when compared to that of the previous 14mm plate thickness. There is a larger separation between top and bottom surfaces on this 16mm plate when compared to the other smaller plate thicknesses. The top defect shows a reduction of -19.1810% and the bottom side defect has a larger reduction of -25.3586%.

Table 4.24: Displaying the peak-to-peak values $\mathbf{B}_Y(T)$ for a 16mm plate with a 60% defect at 0.5, 1, 1.5 & 3m/s alongside the percentage change between 0.5 and 3m/s.

	0.5m/s	1m/s	1.5m/s	3m/s	% Change from 0.5 to 3m/s
Top	0.232	0.2237	0.2158	0.1875	-19.1810
Bottom	0.2370	0.2245	0.2174	0.1769	-25.3586

20mm plate thickness

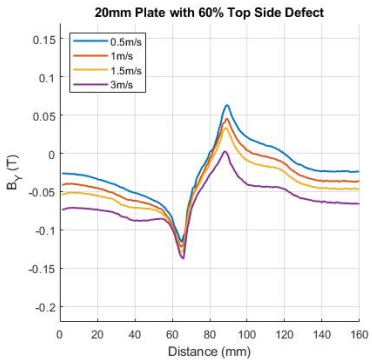

(a) $\mathbf{B}_Y$ response for a 60% top side defect on a $20mm$ plate.

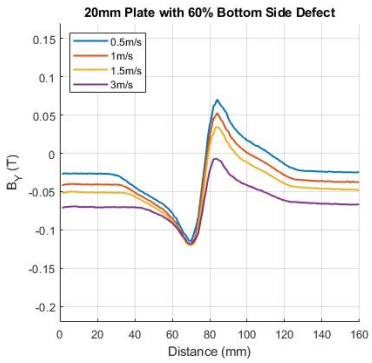

(b) $\mathbf{B}_Y$ response for a 60% bottom side defect on a $20mm$ plate.

Figure 4.37: Figure displaying the $\mathbf{B}_Y$ response from a 60% top and bottom side defects on $20mm$ plate.

The peak-to-peak values taken data displayed in Figure 4.37 are displayed in Table 4.25 below. Comparing the data in Graphical and Tabular form indicates similar peak-to-peak amplitudes are shown for both top and bottom side defects at 0.5 to $1.5m/s$ with a separation emerging at $3m/s$ showing the bottom side defect indicating a greater reduction complimenting the results shown in the flux distribution section of this thesis. It can be seen that the bottom side defect decreases by -40% where the top surface is only reduced by -21% indicating a shift in the flux within the specimen when inspection velocity is increased from 0.5 to $3m/s$, resulting in a larger difference to that of the $16mm$ plate thickness.

Table 4.25: Displaying the peak-to-peak values $\mathbf{B}_Y(T)$ for a $20mm$ plate with a 60% defect at 0.5, 1, 1.5 & $3m/s$ alongside the percentage change between 0.5 and $3m/s$.

	$0.5m/s$	$1m/s$	$1.5m/s$	$3m/s$	% Change from 0.5 to $3m/s$
Top	0.1794	0.1681	0.1622	0.1405	-21.6834
Bottom	0.1853	0.1731	0.1550	0.1108	-40.2051

4.2.3.6 60% Defect Summary

A summary of the data given in the tables above is presented in a graphical format for the 60% peak-to-peak signal responses for all plate thicknesses and velocities to provide the reader with an overview of the results in an easily digestible format. The results are presented in an identical format to the 20 and 40% defects that have been analysed previously. First the peak-to-peak values for all plate thicknesses are considered at each velocity as displayed in Figure 4.38. Following this the results are presented with individual plate thicknesses at all velocities as seen in Figure 4.39.

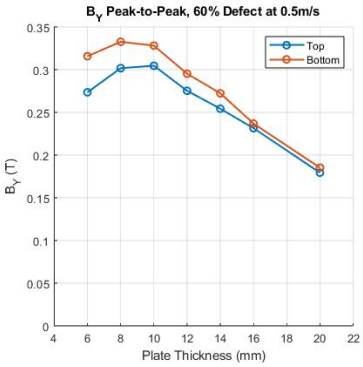

(a) $\mathbf{B}_Y$ peak-to-peak response for a 60% top and bottom side defects on all plate thicknesses at $0.5m/s$.

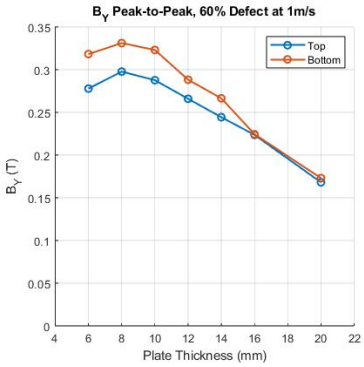

(b) $\mathbf{B}_Y$ peak-to-peak response for a 60% top and bottom side defects on all plate thicknesses at $1m/s$.

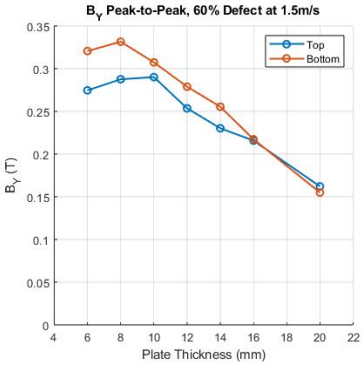

(c) $\mathbf{B}_Y$ peak-to-peak response for a 60% top and bottom side defects on all plate thicknesses at $1.5m/s$.

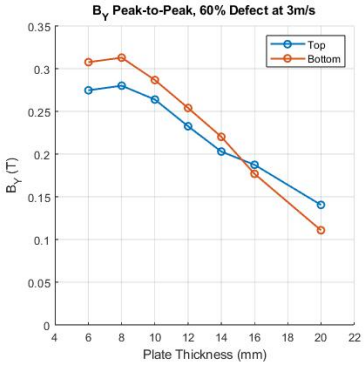

(d) $\mathbf{B}_Y$ peak-to-peak response for a 60% top and bottom side defects on all plate thicknesses at $3m/s$.

Figure 4.38: Figure displaying the $\mathbf{B}_Y$ response from a 60% top and bottom side defects at all plate thicknesses at 0.5, 1, 1.5 and $3m/s$.

The data presented in Figures 4.38 above for a 60% defect following the trend where the bottom side defect produces a larger peak-to-peak response than that of the top side defect up to 14mm plate thickness. At 16mm plate thickness this trend holds true for inspection velocities of 0.5, 1, and 1.5m/s as can be seen in Figures 4.38a to 4.38c. At 3m/s the 16mm plate indicates a larger response for the top surface defect as seen in Figure 4.38d. At 20mm plate thickness there is a clear separation between top and bottom side defects as seen in Figure 4.38d when compared to the other velocities.

Figure 4.39 show the summary of all palate thicknesses at 0.5, 1, 1.5, and 3m/s as considered throughout this thesis. It is clearly identifiable that peak-to-peak signal responses for plate thicknesses of 6 to 14mm produce a larger bottom side response in comparison to a top side defect for all velocities considered in Figures 4.39a to 4.39e. At 16mm plate thickness the peak-to-peak values at 0.5 to 1.5m/s are almost identical, with a separation beginning to emerge at 3m/s as seen in Figure 4.39f. This effect is further exaggerated at 20mm plate thickness where the top side defect response becomes larger at 1.5m/s and increasing at a velocity of 3m/s as seen in Figure 4.39g.

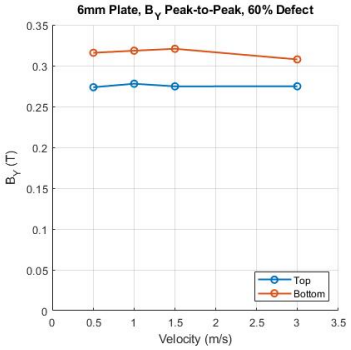

(a) 6mm plate summary with 60% defect.

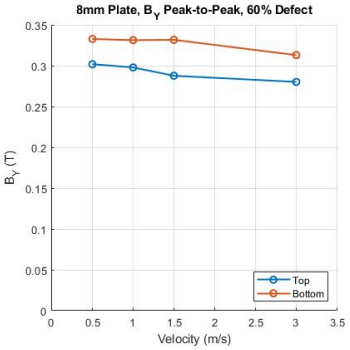

(b) 8mm plate summary with 60% defect.

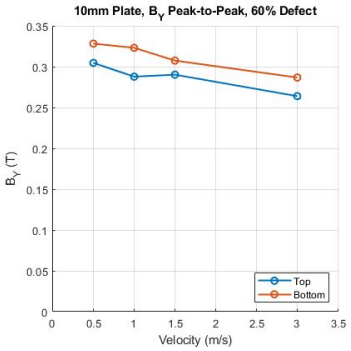

(c) 10mm plate summary with 60% defect.

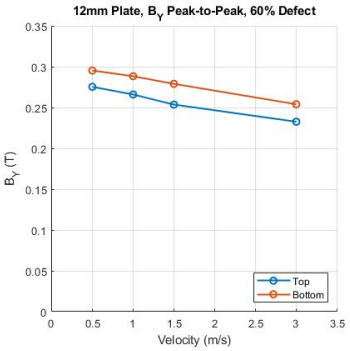

(d) 12mm plate summary with 60% defect.

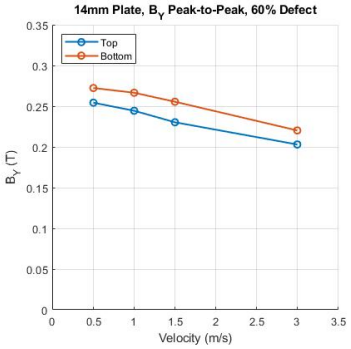

(e) 14mm plate summary with 60% defect.

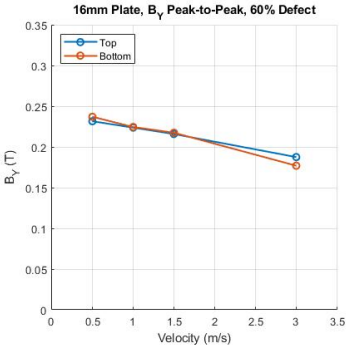

(f) 16mm plate summary with 60% defect.

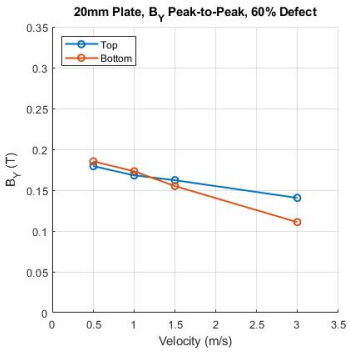

(g) 20mm plate summary with 20% defect.

Figure 4.39: 60% peak-to-peak defect summary for each plate thickness.

4.2.3.7 80% Defect Response

6mm plate thickness

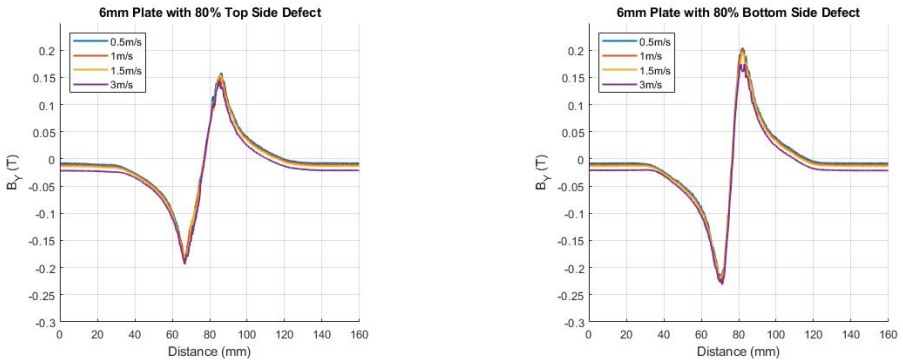

(a) $\mathbf{B}_Y$ response for a 80% top side defect on a $6mm$ plate.

(b) $\mathbf{B}_Y$ response for a 80% bottom side defect on a $6mm$ plate.

Figure 4.40: Figure displaying the $\mathbf{B}_Y$ response from a 80% top and bottom side defects on $6mm$ plate.

Figure 4.40a displays the $\mathbf{B}_Y$ signal response from the 80% top side defect and Figure 4.40b for the bottom side on a $6mm$ thick plate. The peak-to-peak values taken from Figure 4.40 are displayed in Table 4.26 below. These values indicate that similar to the 40% and 60% defects the bottom side peak-to-peak amplitude is greater than the top surface defect. Due to the defect size it is clear that the signal response is elongated for the top surface defect as have been the trend shown throughout the results of the larger defects thus far.

Table 4.26: Displaying the peak-to-peak values $\mathbf{B}_Y(T)$ for a $6mm$ plate with a 80% defect at 0.5, 1, 1.5 & $3m/s$ alongside the percentage change between 0.5 and $3m/s$.

	$0.5m/s$	$1m/s$	$1.5m/s$	$3m/s$	% Change from 0.5 to $3m/s$
Top	0.344	0.3452	0.3415	0.3379	-1.7733
Bottom	0.4267	0.4269	0.4208	0.4059	-4.8746

8mm plate thickness

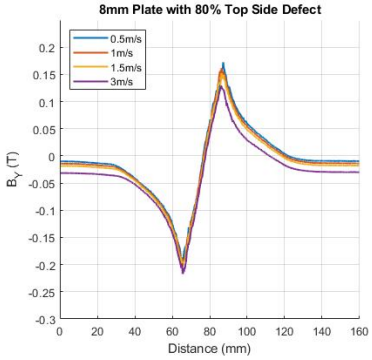

(a) $\mathbf{B}_Y$ response for a 80% top side defect on a $8mm$ plate.

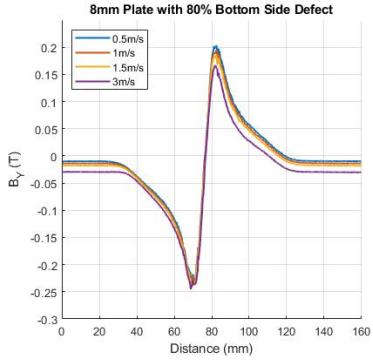

(b) $\mathbf{B}_Y$ response for a 80% bottom side defect on a $8mm$ plate.

Figure 4.41: Figure displaying the $\mathbf{B}_Y$ response from a 80% top and bottom side defects on $8mm$ plate.

The results for a $8mm$ plate thickness with a 80% though wall top and bottom side defect are displayed in Figures 4.41a & 4.41b respectively. Following the trend of the previous $6mm$ 80% defect an overall reduction in peak-to-peak signal amplitude is seen for when inspection velocity is increased for the $8mm$ plate as seen in Table 4.27. The results shown in this table also indicate that the bottom side defect again shows an increased amplitude when compared to the top surface defect for the same velocity. The overall signal reduction between velocities of 0.5 and $3m/s$ are both in the region of -5%. The trend almost identical reduction in signal amplitude continues up to plate thicknesses of $20mm$ as seen previously with a 60% through wall defect this only held true for plate thicknesses of $14mm$ and below.

Table 4.27: Displaying the peak-to-peak values $\mathbf{B}_Y(T)$ for a $8mm$ plate with a 80% defect at 0.5, 1, 1.5 & $3m/s$ alongside the percentage change between 0.5 and $3m/s$.

	$0.5m/s$	$1m/s$	$1.5m/s$	$3m/s$	% Change from 0.5 to $3m/s$
Top	0.3655	0.3560	0.3503	0.3463	-5.2531
Bottom	0.4356	0.4308	0.4246	0.4113	-5.5785

10mm plate thickness

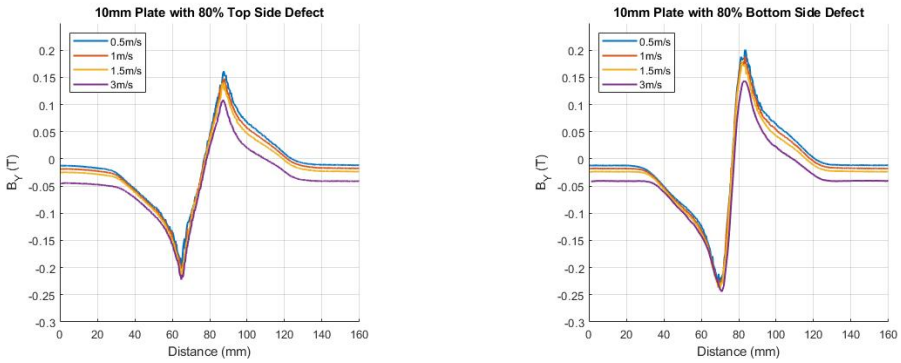

(a) $\mathbf{B}_Y$ response for a 80% top side defect on a $10mm$ plate.

(b) $\mathbf{B}_Y$ response for a 80% bottom side defect on a $10mm$ plate.

Figure 4.42: Figure displaying the $\mathbf{B}_Y$ response from a 80% top and bottom side defects on $10mm$ plate.

The results for a 80% defect are on a $10mm$ plate are displayed in Figure 4.42. As expected from previous results the spatial response of the top side defect is significantly more spread out in comparison to the bottom side defect response. The bottom side defect produces a larger peak-to-peak signal than that of the top side defect consistent with previous results of the larger defects. The peak-to-peak values are give in Table 4.28 for comparison0. The defect responses from 0.5 to $1.5m/s$ are similar in amplitude but reduce the most from a velocity 1.5 to $3m/s$, with a more significant drop seen for a bottom side defect.

Table 4.28: Displaying the peak-to-peak values $\mathbf{B}_Y(T)$ for a $10mm$ plate with a 80% defect at 0.5, 1, 1.5 & $3m/s$ alongside the percentage change between 0.5 and $3m/s$.

	$0.5m/s$	$1m/s$	$1.5m/s$	$3m/s$	% Change from 0.5 to $3m/s$
Top	0.3624	0.3500	0.3559	0.3311	-8.6369
Bottom	0.4284	0.4267	0.4200	0.3878	-9.4771

12mm plate thickness

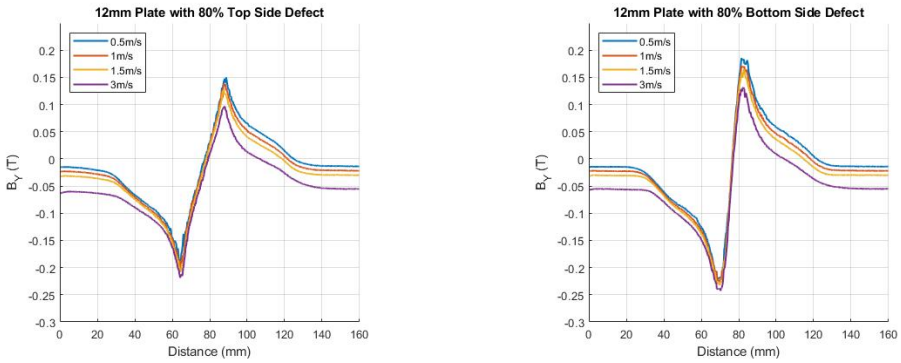

(a) $\mathbf{B}_Y$ response for a 80% top side defect on a $12mm$ plate.

(b) $\mathbf{B}_Y$ response for a 80% bottom side defect on a $12mm$ plate.

Figure 4.43: Figure displaying the $\mathbf{B}_Y$ response from a 80% top and bottom side defects on $12mm$ plate.

Figure 4.43a and Figure 4.43b show the peak-to-peak signal responses for a top and bottom side 80% through wall thickness defect respectively. Similarly to the previous results of the $10mm$ thick plate the $12mm$ also indicates a larger signal response from the bottom side defect with a large drop in amplitude from 1.5 to 3mm/s. The peak-to-peak values for all scans are given in Table 4.29 below.

Table 4.29: Displaying the peak-to-peak values $\mathbf{B}_Y(T)$ for a $12mm$ plate with a 80% defect at 0.5, 1, 1.5 & $3m/s$ alongside the percentage change between 0.5 and $3m/s$.

	$0.5m/s$	$1m/s$	$1.5m/s$	$3m/s$	% Change from 0.5 to $3m/s$
Top	0.3452	0.3415	0.3366	0.3158	-8.5168
Bottom	0.4073	0.3976	0.3975	0.3744	-8.0776

14mm plate thickness

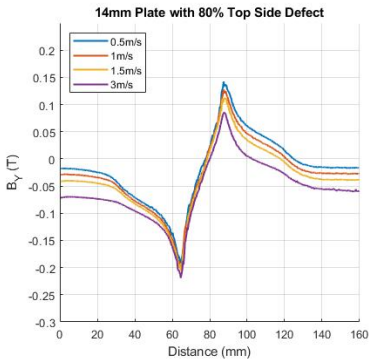

(a) $\mathbf{B}_Y$ response for a 80% top side defect on a $14mm$ plate.

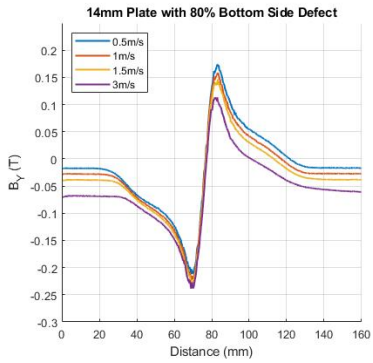

(b) $\mathbf{B}_Y$ response for a 80% bottom side defect on a $14mm$ plate.

Figure 4.44: Figure displaying the $\mathbf{B}_Y$ response from a 80% top and bottom side defects on $14mm$ plate.

Figure 4.44a shows the $\mathbf{B}_Y$ signal response for a 80% top side defect and the bottom side response is given in Figure 4.44b. The peak-to-peak values are displayed in Table 4.30, these values combined with Figure 4.44 show that the bottom side defect is producing a greater response than the bottom side defect. Due to the large defect not only is the top side signal distorted as previously indicated, but also the bottom side defect is also becoming elongated. Both top and bottom side defects show a reduction in signal amplitude whit increased inspection velocity.

Table 4.30: Displaying the peak-to-peak values $\mathbf{B}_Y(T)$ for a $14mm$ plate with a 80% defect at 0.5, 1, 1.5 & $3m/s$ alongside the percentage change between 0.5 and $3m/s$.

	$0.5m/s$	$1m/s$	$1.5m/s$	$3m/s$	% Change from 0.5 to $3m/s$
Top	0.3336	0.3294	0.3176	0.3054	-8.4532
Bottom	0.3864	0.3821	0.3771	0.3523	-8.8250

16mm plate thickness

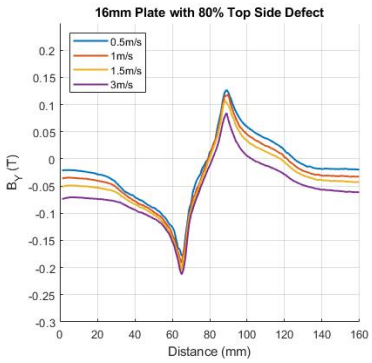

(a) $\mathbf{B}_Y$ response for a 80% top side defect on a $16mm$ plate.

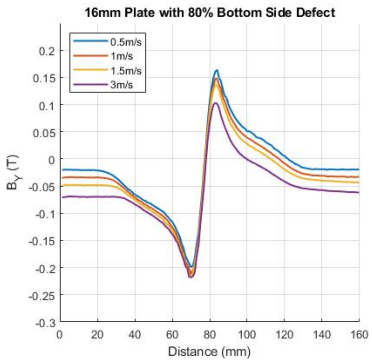

(b) $\mathbf{B}_Y$ response for a 80% bottom side defect on a $16mm$ plate.

Figure 4.45: Figure displaying the $\mathbf{B}_Y$ response from a 80% top and bottom side defects on $16mm$ plate.

Following the trend of the previous 80% defect results the bottom side defect produces a larger peak-to-peak amplitude as can be seen in Figure 4.45 above. The peak-to-peak value of of the top side defect increases between 0.5 and $1.5m/s$ whereas a consistent reduction in signal amplitude is seen for the bottom side defect as displayed in Table 4.31 below.

Table 4.31: Displaying the peak-to-peak values $\mathbf{B}_Y(T)$ for a $16mm$ plate with a 80% defect at 0.5, 1, 1.5 & $3m/s$ alongside the percentage change between 0.5 and $3m/s$.

	$0.5m/s$	$1m/s$	$1.5m/s$	$3m/s$	% Change from 0.5 to $3m/s$
Top	0.3060	0.3104	0.3130	0.2973	-2.8431
Bottom	0.3638	0.3611	0.3534	0.3215	-11.6273

20mm plate thickness

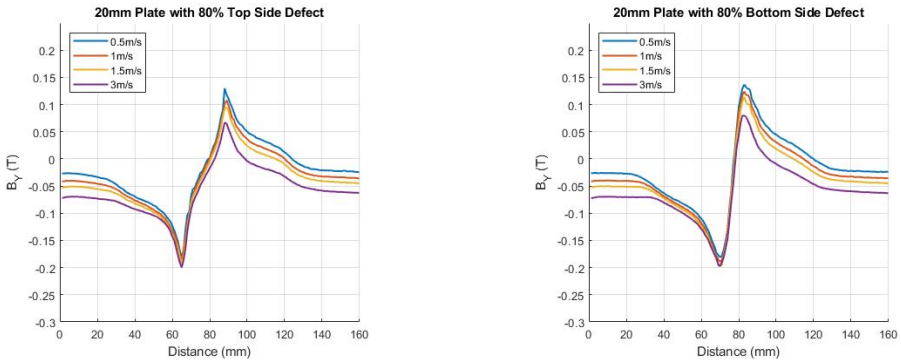

(a) $\mathbf{B}_Y$ response for a 80% top side defect on a $20mm$ plate.

(b) $\mathbf{B}_Y$ response for a 80% bottom side defect on a $20mm$ plate.

Figure 4.46: Figure displaying the $\mathbf{B}_Y$ response from a 80% top and bottom side defects on $20mm$ plate.

The results for a $20mm$ thick plate with an 80% defect are displayed in Figure 4.46 and Table 4.32. The results indicate the bottom side defect has a greater peak-to-peak amplitude over the a top surface defect as can be seen in Table 4.32. A continual reduction in signal amplitude is shown with increased velocity in agreement with [47].

Table 4.32: Displaying the peak-to-peak values $\mathbf{B}_Y(T)$ for a $20mm$ plate with a 80% defect at 0.5, 1, 1.5 & $3m/s$ alongside the percentage change between 0.5 and $3m/s$.

	$0.5m/s$	$1m/s$	$1.5m/s$	$3m/s$	% Change from 0.5 to $3m/s$
Top	0.3112	0.2933	0.2876	0.2668	-14.2674
Bottom	0.3181	0.3136	0.3101	0.2778	-12.6690

80% Defect Summary

This section provides a breakdown of the data given in the tables throughout 80% defect results. This will allow the reader to analyse the data provided in values to be viewed in graphical form to provide a clear visual comparison of each plate thickness and velocities. The data is displayed in a cluster of graphs split into two Figures. Figure 4.47 provides a summary of all plate thicknesses at individual velocities. Following this, Figure 4.48 provides an overview of each individual plate thickness at the four velocities considered during this work.

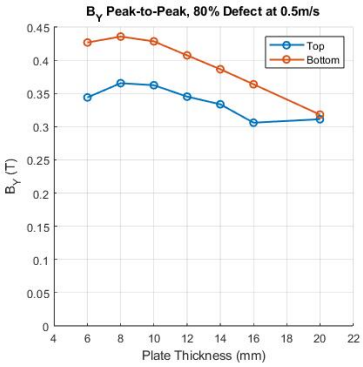

(a) $\mathbf{B}_Y$ peak-to-peak response for a 80% top and bottom side defects on all plate thicknesses at $0.5m/s$.

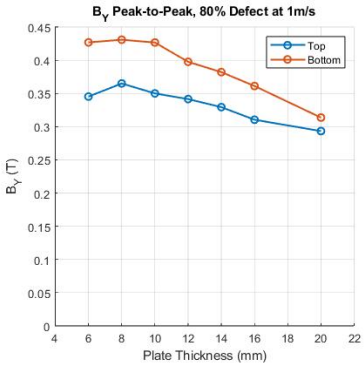

(b) $\mathbf{B}_Y$ peak-to-peak response for a 80% top and bottom side defects on all plate thicknesses at $1m/s$.

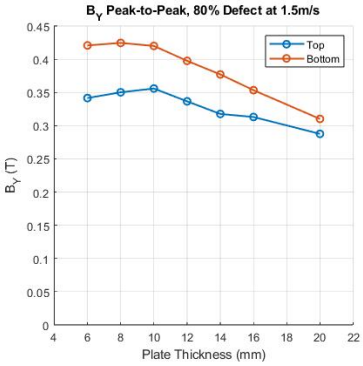

(c) $\mathbf{B}_Y$ peak-to-peak response for a 80% top and bottom side defects on all plate thicknesses at $1.5m/s$.

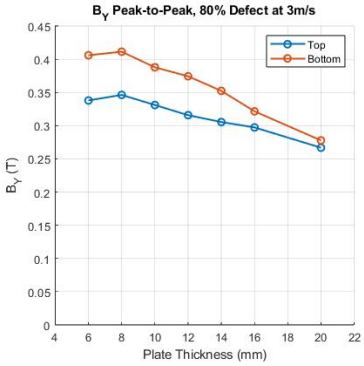

(d) $\mathbf{B}_Y$ peak-to-peak response for a 80% top and bottom side defects on all plate thicknesses at $3m/s$.

Figure 4.47: Figure displaying the $\mathbf{B}_Y$ response from a 80% top and bottom side defects at all plate thicknesses at 0.5, 1, 1.5 and $3m/s$.

Analysing the data presented in Figure 4.47 for an 80% through wall defect are four individual graphs each representing a single inspection velocity of 0.5, 1, 1.5, and $3m/s$ as a function of plate thickness. It is noted that at 80% wall loss the bottom side defect produces a greater peak-to-peak signal response at all plate velocities and plate thicknesses. Although the bottom side defect produces consistently higher peak-to-peak amplitudes the thicker the plate the closer the values become as can be seen in Figures 4.47a to 4.47d above.

Figure 4.48 summarises the results for all plate thicknesses from 6 to $20mm$ at all four inspection velocities. All responses produced by the larger 80% defect indicate a greater response from the bottom side defect. At $6mm$ plate thickness top and bottom results show that velocity does not have a significant affect on signal amplitude as seen in Figure 4.48a. As plate thickness is increased defect peak-to-peak amplitudes become closer.

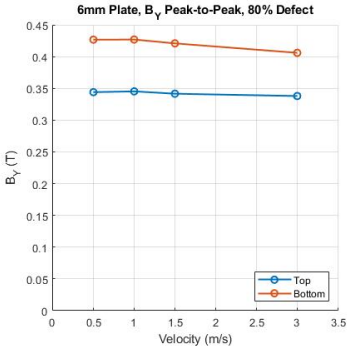

(a) 6mm plate summary with 80% defect.

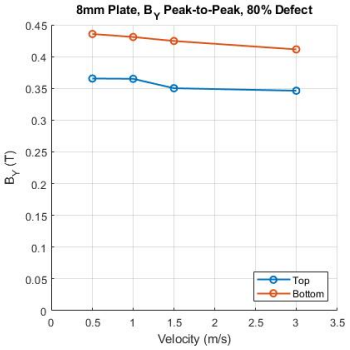

(b) 8mm plate summary with 80% defect.

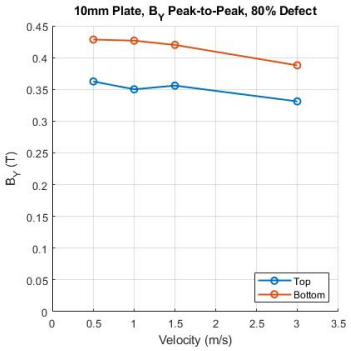

(c) 10mm plate summary with 80% defect.

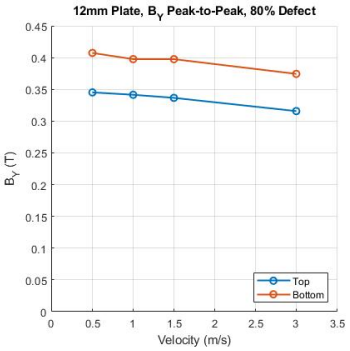

(d) 12mm plate summary with 80% defect.

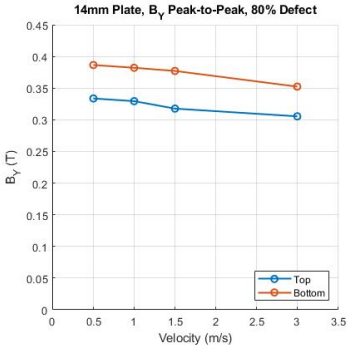

(e) 14mm plate summary with 80% defect.

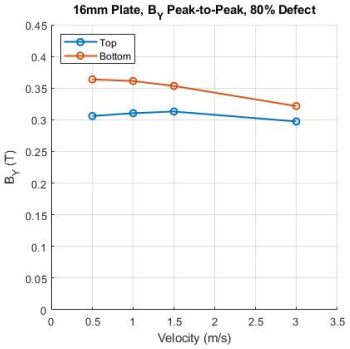

(f) 16mm plate summary with 80% defect.

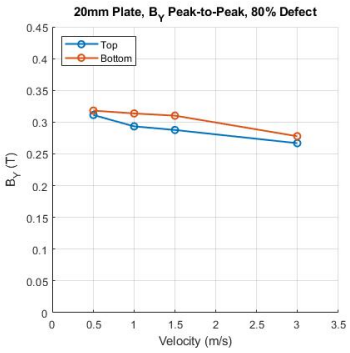

(g) 20mm plate summary with 80% defect.

Figure 4.48: 80% peak-to-peak defect summary for each plate thickness.

4.2.4 Velocity and the effects on DC Signal Offset

As the distribution of the induced flux density is altered with velocity this has a resultant effect on the DC signal offset of the system. An alteration in the offset is noted with the change in velocity. For the system analysed in this study the offset increases negatively when velocity is increased. The significance of the change in the offset value is dependent on velocity and plate thickness. When an increase in velocity is introduced the DC offset increases for a given plate thickness. This effect is evident but does not play a significant role in defect detection as part of the simulated results as the relative motion between the system and the plate is always at a constant without an acceleration phase. However, this will play a significant role in defect detectability in a practical sense when the system is accelerating to inspection speed. If a defect lies along the acceleration phase of a scan then a defect will be distorted due to the continually changing offset (until inspection speed is achieved). Work will be carried out later in the thesis and highlight this problem in practice and provide a possible solution for correcting signals within the acceleration phase based on an instantaneous velocity approach suggesting the offset is determined by velocity and not acceleration as per the results shown in Figure 4.49 on the following page. The average offset values for each plate thickness and velocity are given below in Table 4.33 below.

Table 4.33: Displaying the average offset of $\mathbf{B}_Y(T)$ for all plate thicknesses considered as part of the parametric study at speeds of 0.5, 1, 1.5 and $3m/s$.

	$0.5m/s$	$1m/s$	$1.5m/s$	$3m/s$
6mm	-0.0081	-0.0109	-0.0137	-0.0221
8mm	-0.0104	-0.0145	-0.0187	-0.0318
10mm	-0.0126	-0.0186	-0.0247	-0.0441
12mm	-0.0151	-0.0232	-0.0316	-0.0584
14mm	-0.0177	-0.0287	-0.0400	-0.0700
16mm	-0.0208	-0.0348	-0.0488	-0.0703
20mm	-0.0266	-0.0407	-0.0514	-0.0712

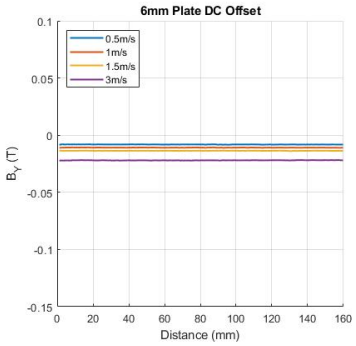

(a) DC Offset on a 6mm plate.

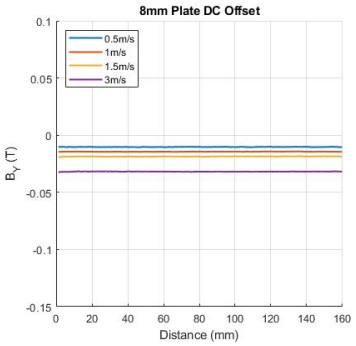

(b) DC Offset on a 8mm plate.

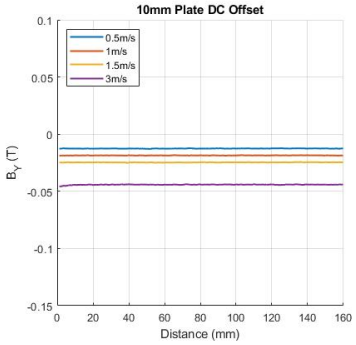

(c) DC Offset on a 10mm plate.

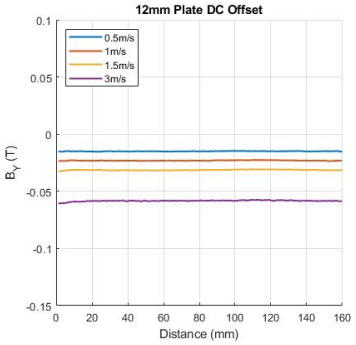

(d) DC Offset on a 12mm plate.

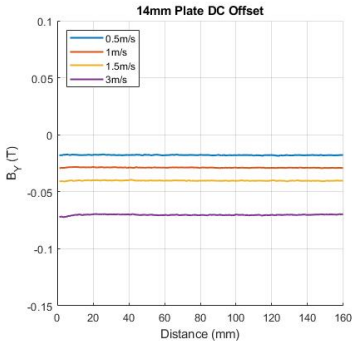

(e) DC Offset on a 14mm plate.

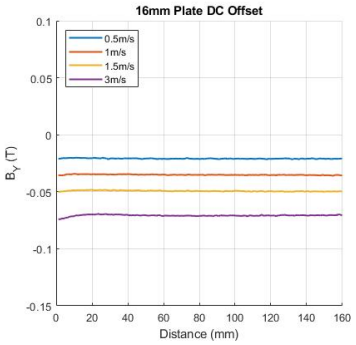

(f) DC Offset on a 16mm plate.

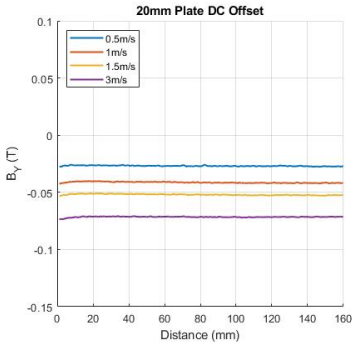

(g) DC Offset on a 20mm plate.

Figure 4.49: DC offset at multiple velocities as a function of plate thickness.

DC Offset Summary

This section provides summary graphs of the affects of velocity and plate thickness on the DC signal offset. The data presented above in Table 4.33 is displayed and analysed here in graphical form. This provides the reader with a visual representation of the affect that velocity has on the DC offset for each plate thickness from 6 to 20mm at 0.5, 1, 1.5 and 3m/s as seen in Figure 4.50. The R^2 values for each data set indicate good correlation of the trend-line and its fit to the data. From this it is possible to generate a correction function to correct for change in inspection velocity based on the simulated results if the plate thickness is known. This will be repeated for the experimental results in Chapter 5 to ensure this holds true in practice.

Table 4.34: Table of R^2 values for the associated trend-line for each plate thickness.

6mm	8mm	10mm	12mm	14mm	16mm	20mm
0.9632	0.9618	0.9603	0.9597	0.9706	0.9951	0.9957

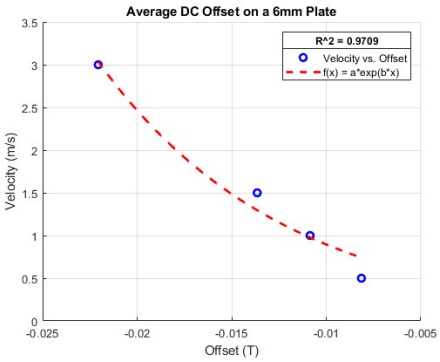

(a) DC Offset summary on a 6mm plate.

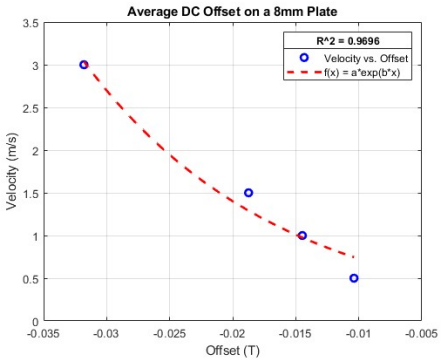

(b) DC Offset summary on a 8mm plate.

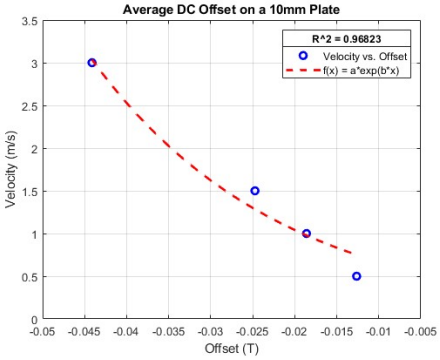

(c) DC Offset summary on a 10mm plate.

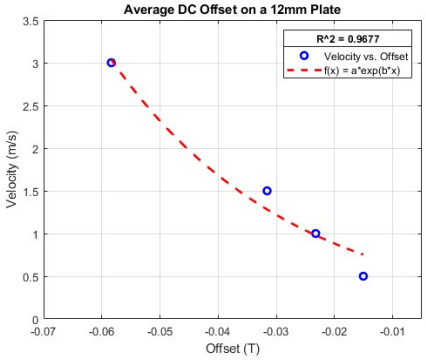

(d) DC Offset summary on a 12mm plate.

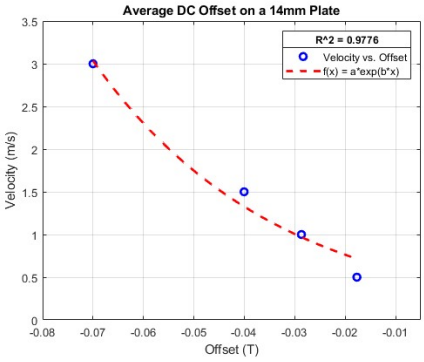

(e) DC Offset on a 14mm plate.

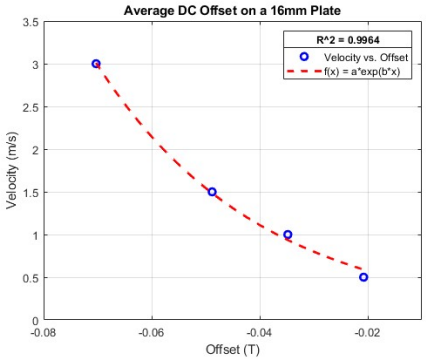

(f) DC Offset on a 16mm plate.

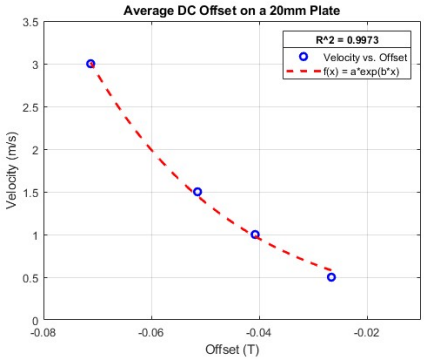

(g) DC Offset on a 20mm plate.

Figure 4.50: DC offset at multiple velocities as a function of plate thickness.

4.3 Conclusion

In conclusion to this chapter there have been a number of key findings:

- As plate thickness increases, flux density **B** is reduced throughout the plate. This is exaggerated when velocity is introduced. $6mm$ plate indicates a starting **B** of $2.122T$ and a reduction to $2.082T$ resulting in a -1.89% difference at $8mm$ plate thickness at $0.5m/s$.

- As velocity is increased, the distribution of induced flux becomes focused at the surface nearest to the magnetiser (near side) resulting in an increased defect response to near surface defects, and a reduction in far surface signal amplitude responses when plate thicknesses are increased to $14mm$ and thicker.

- A distortion in the distribution of flux throughout the plate is identified, altering defect detection capabilities. The induced flux distribution is not linearly distributed through the entire plate thickness when a velocity term is introduced. Increasing scanning speed from 0.5 to $3m/s$ on a $16mm$ plate with a far surface defect reduces its signal amplitude lowering chances of detection and will result in the under-sizing the defect.

- Magnetic saturation governs the speed at which MFL inspection can be undertaken without significantly affecting the results. It is shown within this chapter that when a plate is magnetically saturated inspection velocities can be increased to $3m/s$ while not having a significant affect on signal magnitudes seen from defects. However, the DC signal offset is noted to be marginally affected.

- At a velocity of 3 m/s, near surface defect responses are amplified on unsaturated plates. This is most evident in Figure 4.51a of a 20% defect on a $20mm$ plate.

- Similarly, this has the opposite effect on far surface flaws resulting in a reduction of signal responses on unsaturated plates. Again, this is most clear on the $20mm$ plate where a signal reduction of 87% is given from 0.5 to $3m/s$.

- 40% defects give a higher signal response from the bottom side of saturated plates. Once the plate is considered to be unsaturated $14mm$ and above bottom side defects produce a lower response than that of a top side defect.

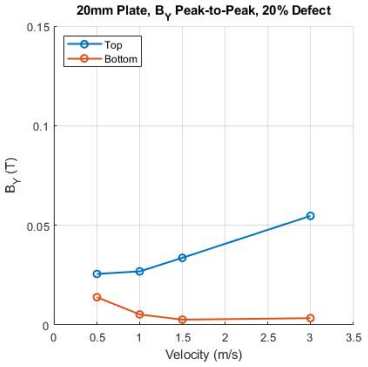

(a) $20mm$ plate summary with 20% defect.

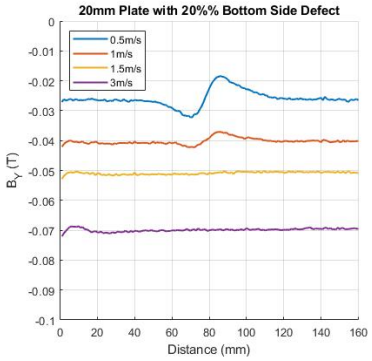

(b) $\mathbf{B}_Y$ response for a 20% bottom side defect on a $20mm$ plate.

Figure 4.51: Highlighting the significance of velocity on the peak-to-peak signal response when inspection velocity is increased on a $20mm$ plate

Furthermore, experimental validation of the phenomena highlighted within this chapter is undertaken in Chapter 5.

Chapter 5

Experimental Results

5.1 Introduction

This chapter provides a practical evaluation of the effect of scanning velocity on defect detection in mild steel plates with thicknesses ranging from $6mm$ to $16mm$ using the fixed magnetic yoke assembly as described previously in chapters 3 and 4. Each inspection plate contains four semi-spherical defects machined with a $22mm$ ball end cutter at depths of 20% to 80% through wall thickness. Scanning velocity and its effects on defect sizing is investigated. Scanning speeds vary depending on plate thickness due to the eddy current brake effect impacting the acceleration and top speed of the system. The maximum drive force is limited by the constant voltage supplied to the drive motor. Therefore these tests are completed at three stages of output: minimum, half and maximum speed; as a result, velocity cannot be directly controlled. The method of constant velocity estimation are undertaken as described in chapter 3. An example of the results collected are shown in Figure 5.1 below.

Figure 5.1 is an example of how the system displays post-processed scan data. In order to evaluate the true performance of the system the raw data is considered from this point forward. A total of 15 scans are undertaken for a given plate thickness, 5 each at the slow, medium and fast speeds. The maximum peak-to-peak signal across all 8 sensor channels is taken for all 5 scans, then the value of each defect peak-to-peak

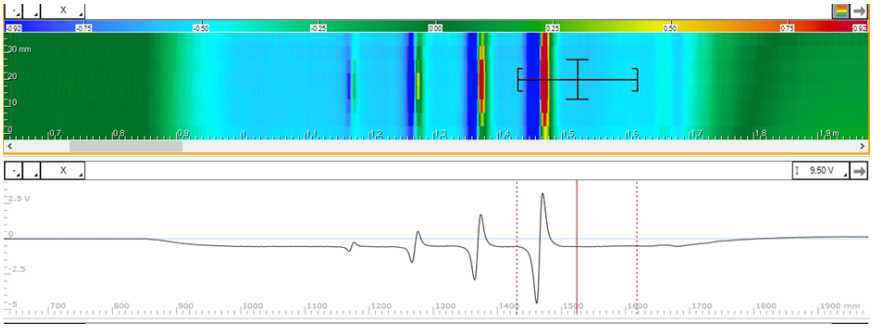

(a) $6mm$ plate thickness scanned with a velocity of $0.5m/s$ with bottom side defect.

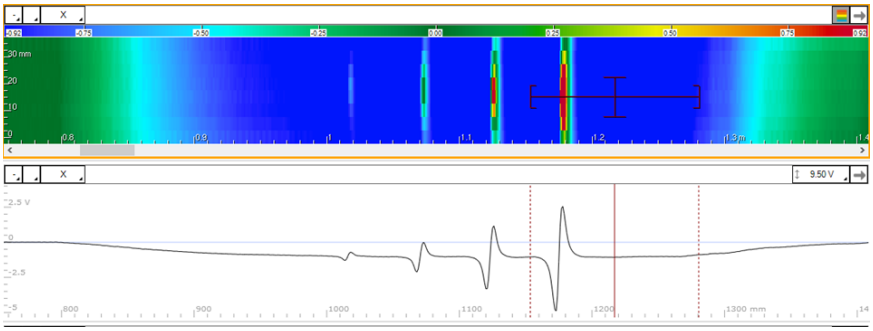

(b) $6mm$ plate thickness scanned with a velocity of $1.2m/s$ with bottom side defect.

Figure 5.1: Example data of the $\mathbf{B}_Y$ signal response and how the data is displayed within the Magnifi software suite with filtering.

is taken and averaged over the 5 scans for each inspection speed. This is undertaken to ensure validity and prove trends that occur from the simulated results still hold true when put into practice.

5.2 Results

5.2.1 Raw Data

Multiple examples of the raw data traces generated from the practical scans for three plate thicknesses of 6, 12 and 16mm are given in Figures 5.3, 5.4 and 5.5 respectively. A range of plate thicknesses are shown to highlight the change in acceleration, deceleration, peak-to-peak signal amplitudes and signal offset and how this changes with plate thickness. For each plate thickness full traces are displayed at three velocities (velocities vary as a function of plate thickness) with defects on the top and bottom sides of the plate resulting in a matrix of six figures for each plate thickness. A labelled trace can be seen in Figure 5.2 where the acceleration phase is highlighted with a red dashed box, the deceleration phase with a blue dashed box and the defect response from each defect labelled next to each signal response. The scan direction and order of defects are consistent throughout these results.

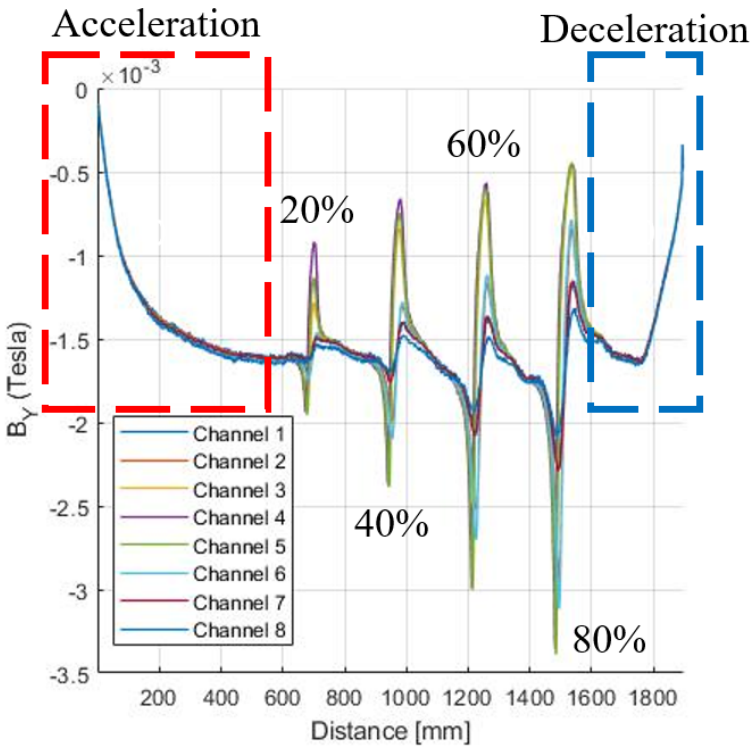

Figure 5.2: Data trace for a slow top side defect scan of a 12mm thick plate.

5.2.1.1 6mm Plate thickness - Raw traces

As can be seen for the $6mm$ plate thickness in Figure 5.3, the acceleration and deceleration phases at the start and end of each trace become longer with increased inspection speed as expected. This is identified by the longer duration of the change in offset before the trace becomes consistent when a constant velocity has been reached. The acceleration phase for a $6mm$ plate at the slowest scan speed of $0.57m/s$ takes approximately $200mm$ as seen in Figures 5.3a and 5.3b. It should also be noted that the bottom side defects for 60% through wall thickness and above generate a larger peak-to-peak signal response when compared to the top side defects. When the medium inspection speed of $1m/s$ is considered in Figures 5.3c and 5.3d the time taken to reach a constant velocity is further increased, as expected to approximately $350mm$ in length, and the offset has increased negatively as a result of the increased scanning speed. This is also consistent with the further increased inspection speed of $1.25m/s$ where both the distance to achieve a constant velocity is increased to $400mm$ with a further reduction in signal offset as seen in Figures 5.3e and 5.3f. The peak-to-peak analysis for the this plate will be investigated in more detail in a later section of the thesis but a note should be taken of the difference in peak-to-peak values between top and bottom surface defects and the separation in signal amplitude between the 8 channels/sensors.

6mm

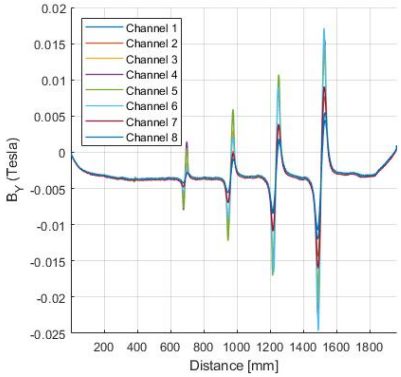

(a) Data trace for a slow top side defect scan of a 6mm thick plate.

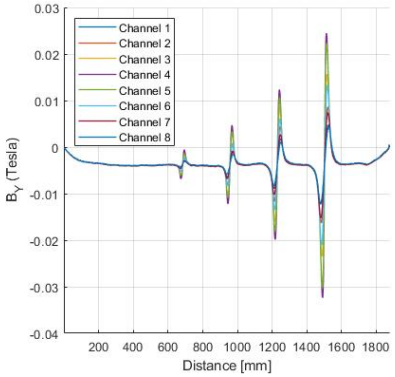

(b) Data trace for a slow bottom side defect scan of a 6mm thick plate.

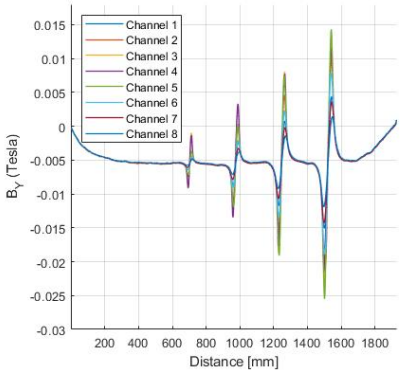

(c) Data trace for a medium top side defect scan of a 6mm thick plate.

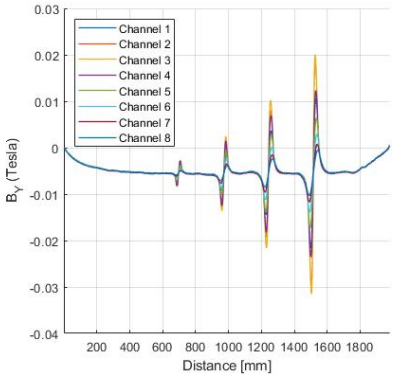

(d) Data trace for a medium bottom side defect scan of a 6mm thick plate.

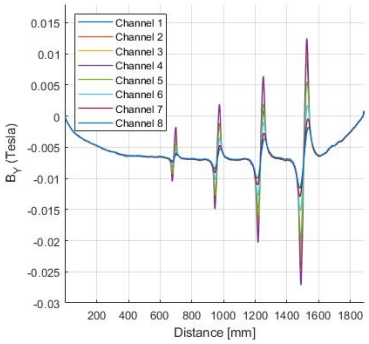

(e) Data trace for a fast top side defect scan of a 6mm thick plate.

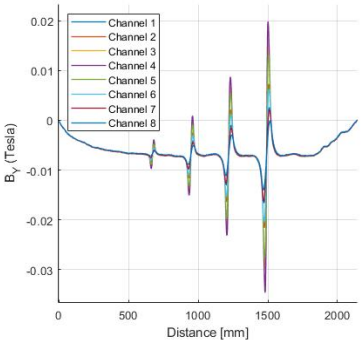

(f) Data trace for a fast bottom side defect scan of a 6mm thick plate.

Figure 5.3: Raw full trace scans 6mm.

5.2.1.2 12mm Plate thickness - Raw Traces

As previously described for the 6mm plate, the full trace of each scan for top and bottom side defects for the 12mm plate at three velocities are displayed in Figure 5.4. Similarly with increased inspection velocity larger offsets are observed. The change however is more significant for the thicker $12mm$ plate thickness. At $0.51m/s$ the acceleration phase is longer at $12mm$ plate thickness taking approximately $500mm$ as can be seen in Figures 5.4a and 5.4b, when compared to that of $200mm$ at $6mm$ plate for the lowest scanning velocity. This is due to the increased flux being supplied into the specimen. At the medium inspection velocity of $0.8m/s$ the acceleration phase lasts approximately $600mm$ as observed in Figure 5.4c. Figure 5.4d indicates a reduction in the peak-to-peak signal amplitude of the bottom side defects. These are reducing in amplitude with increased velocity as can be seen in Figure 5.4f with a scanning velocity of $0.95m/s$ with an even further reduction in the peak-to-peak defect signal amplitudes. The acceleration phase is further elongated at $0.95m/s$ taking approximately $800mm$ to reach a consistent velocity. It should be noted that the 20% through wall defect is on the tail end of the acceleration phase of the faster inspection velocity of $0.95m/s$. The signal to noise ratio is reducing and is beginning to impact the detectability of bottom side defects at increased inspection speeds. Under real inspection condition with alterations in surface roughness and general surface corrosion it would become difficult to accurately determine and call the 20% through wall defect.

12mm

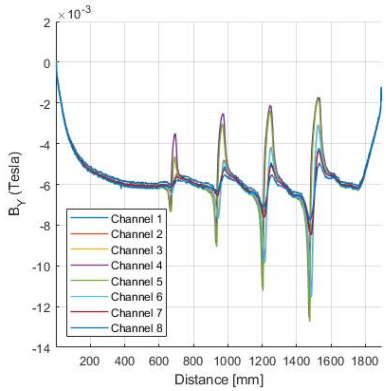

(a) Data trace for a slow top side defect scan of a 12mm thick plate.

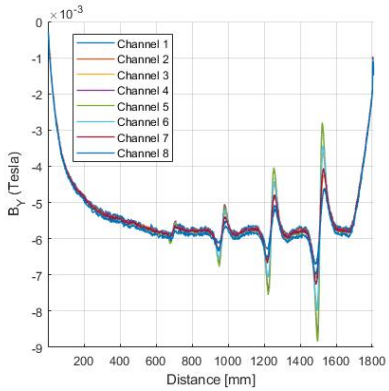

(b) Data trace for a slow bottom side defect scan of a 12mm thick plate.

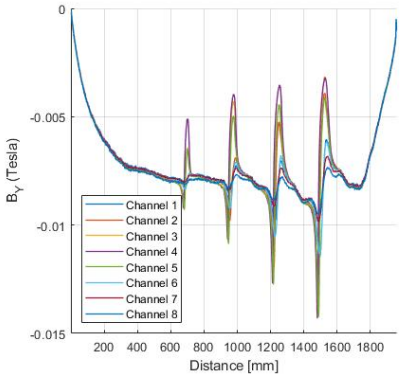

(c) Data trace for a medium top side defect scan of a 12mm thick plate.

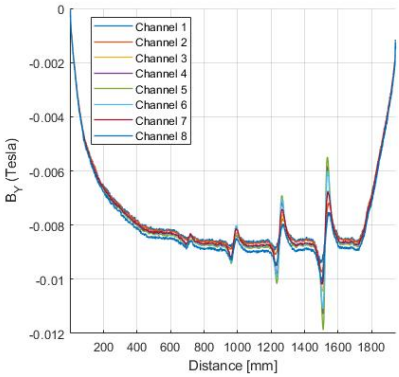

(d) Data trace for a medium bottom side defect scan of a 12mm thick plate.

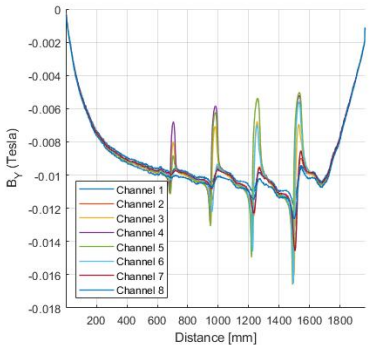

(e) Data trace for a fast top side defect scan of a 12mm thick plate.

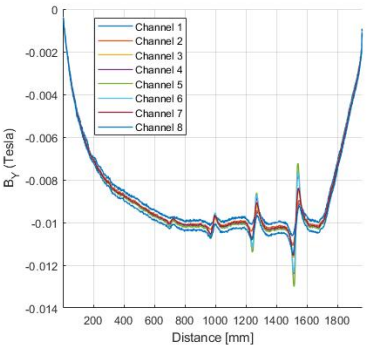

(f) Data trace for a fast bottom side defect scan of a 12mm thick plate.

Figure 5.4: Raw full trace scans 12mm.

5.2.1.3 16mm Plate thickness - Raw Traces

The last example of full traces are given for a $16mm$ plate thickness at three velocities, 0.52, 0.74, and $1.11m/s$ are considered for the slow, medium and fast inspection speeds respectively. Similar offsets to the $12mm$ thick plate with increased velocity can be seen throughout the graphs in Figure 5.5. However, the peak-to-peak signal responses from top and bottom surface defects are significantly different. All top side defects are detectable and also increase in amplitude when velocity is increased as can be noted when comparing Figures 5.5a, 5.5c and 5.5e. When the bottom side defects are considered it is observed in Figures 5.5b, 5.5d and 5.5f that signal to noise ratio is evidently masking 20% defects at all velocities. However the signal amplitudes of all defects reduce with velocity making defects more difficult to differentiate from noise. This supports the results from the simulated data indicative of a shift in flux within the plate to the top side resulting in an amplified topside defect response and a reduced bottom side peak-to-peak signal response.

16mm

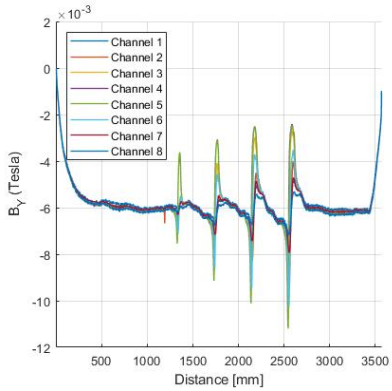

(a) Data trace for a slow top side defect scan of a 16mm thick plate.

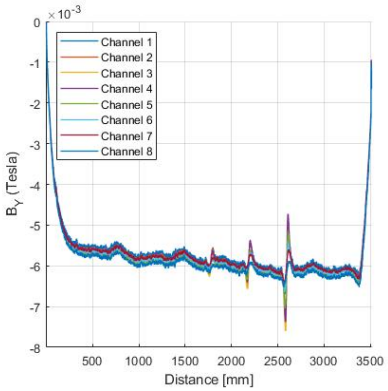

(b) Data trace for a slow bottom side defect scan of a 16mm thick plate..

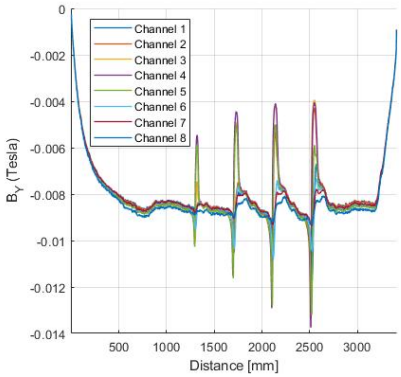

(c) Data trace for a medium top side defect scan of a 16mm thick plate.

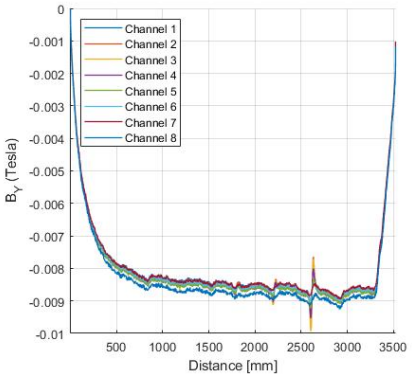

(d) Data trace for a medium bottom side defect scan of a 16mm thick plate.

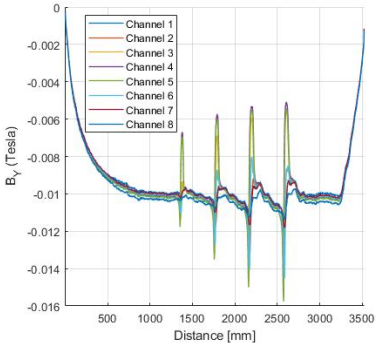

(e) Data trace for a fast top side defect scan of a 16mm thick plate.

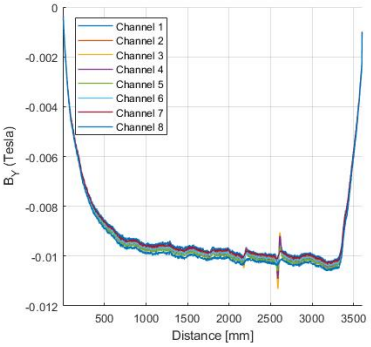

(f) Data trace for a fast bottom side defect scan of a 16mm thick plate.

Figure 5.5: Raw full trace scans 16mm.

5.2.2 Experimental Defect Response & Orientation Sensitivity

Due to the large amount of experimental data collected a summary of defect results for each plate thickness will be presented and analysed. The $\mathbf{B}_Y$ signal response for the smallest detectable defect will also be given at the minimum and maximum velocities for a bottom side defect to highlight the effects that velocity has on defect detectability.

6mm Plate Summary

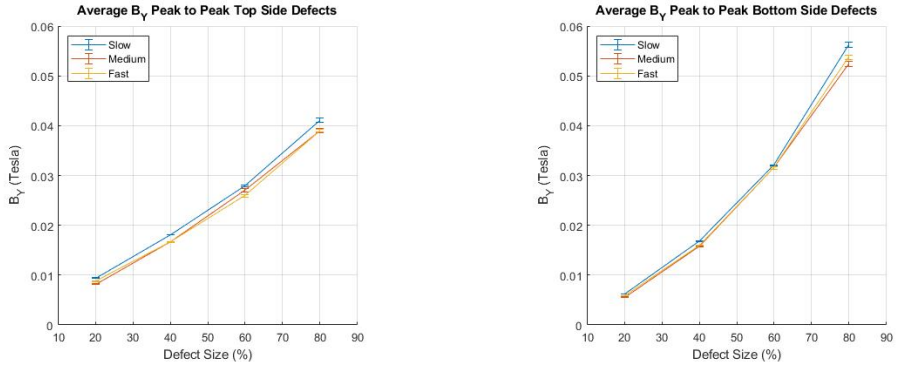

(a) $\mathbf{B}_Y$ response for top side defects on a $6mm$ plate.

(b) $\mathbf{B}_Y$ response for bottom side defects on a $6mm$ plate.

Figure 5.6: Figure displaying the $\mathbf{B}_Y$ response from all top and bottom side defects on $6mm$ plate.

The data in Figure 5.6 show the peak-to-peak amplitudes generated by top and bottom side defects for a plate thickness of $6mm$ at inspection speeds of $0.57m/s$, $1m/s$ and $1.25m/s$. In Figures 5.6a and 5.6b, the separation between peak-to-peak signal amplitudes is greatest for an 80% defect both top and bottom. All responses at a $6mm$ plate thickness show a reduction in signal amplitude as seen in the simulated results previously demonstrated. The bottom side 80% defect shows the largest reduction in signal amplitude of -6.82% for a velocity increase of $0.68m/s$. The lack of separation between defect responses and a reduction in peak-to-peak amplitudes when inspection speed is increased is indicative of a magnetically saturated material. This further validates the findings presented in the simulation results in chapter 4.

In all cases, larger defects result in larger peak-to-peak amplitudes. For the 20% it

is shown that the top side defect has a larger response than the bottom side. At a defect size of 40% for both top and bottom side defects the peak-to-peak signal responses are similar. When a 60% defect is considered, the bottom side defect signal becomes larger than that from the top surface. This observation has been made previously by Charlton [8]. This phenomena holds true for the 80% defect, resulting in a significantly higher amplitude of the bottom side defect when compared to the 80% top side defect.

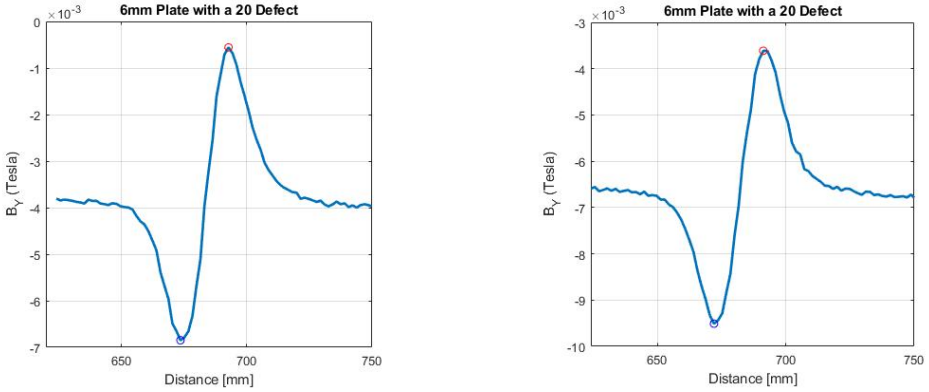

(a) $\mathbf{B}_Y$ response for a 20% bottom side defect on a $6mm$ plate at the slowest scanning speed.

(b) $\mathbf{B}_Y$ response for a 20% bottom side defect on a $6mm$ plate at the fastest scanning speed.

Figure 5.7: Figure displaying the $\mathbf{B}_Y$ response from a 20% through wall defect on a $6mm$ plate at the slowest and fastest scanning speeds.

Figure 5.7 presents the peak-to-peak signal response for both slow and fast scanning speeds respectively for a 20% bottom side defect. The difference in signal amplitude of a bottom side 20% defect at slow and fast speeds are minimal as displayed in Figure 5.7a for slow and 5.7b for the faster inspection speed. Note difference in scale and offset of the signal response due to the increased velocity. The peak-to-peak values rounded to four decimal places are displayed in Table 5.1 below for comparison.

Table 5.1: Average $\mathbf{B}_Y$ peak-to-peak signal responses from 20-80% through wall defects on a $6mm$ plate.

	Slow		Medium		Fast	
Defect Size (%}	Top	Bottom	Top	Bottom	Top	Bottom
20	0.0094	0.0063	0.0082	0.0056	0.0088	0.0059
40	0.0181	0.0168	0.0168	0.0158	0.0167	0.0160
60	0.0279	0.0320	0.0270	0.0315	0.0260	0.0315
80	0.0411	0.0562	0.0390	0.0524	0.0390	0.0537

8mm Plate Summary

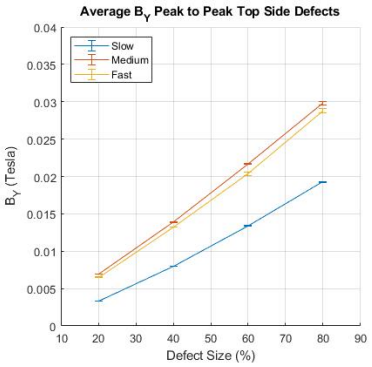

(a) Average peak-to-peak $\mathbf{B}_Y$ response for top side defects on a $8mm$ plate.

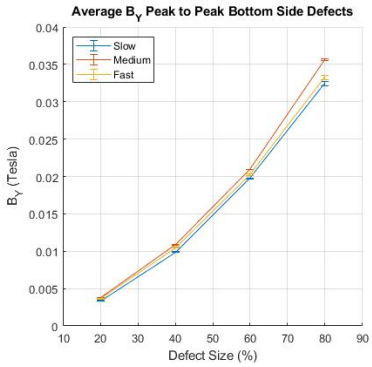

(b) Average peak-to-peak $\mathbf{B}_Y$ response for bottom side defects on a $8mm$ plate.

Figure 5.8: Figure displaying the average $\mathbf{B}_Y$ peak-to-peak responses from all top and bottom side defects on an $8mm$ thick plate.

The results for an $8mm$ thick plate with top and bottom side defects are shown in Figures 5.8a and 5.8b respectively. It is clear to see that velocity has an amplification effect on the average peak-to-peak signal response of top side defects as seen in Figure 5.8a which indicates a shift in the flux and induced eddy currents within the plate producing a somewhat linear increase with increased defect size. Similar to the results of the $6mm$ plate, the bottom side results show that velocity does not have a significant effect on defects from 20% to 60% with only a small increase in amplitude. A greater increase in the peak-to-peak response of an 80% defect a larger separation is identified.

When the slowest inspection speed is considered defects of 40% through wall thickness and above produce a greater average peak-to-peak signal response when compared to the same velocity of bottom side defects. For increased inspection velocities the

20% and 40% defects produce a greater response from top side defects, for a defect sizes of 60% top and bottom side produce similar amplitudes. However, for an 80% defect the bottom side defect produces a higher average peak-to-peak signal than a top side defect as seen in Figure 5.8.

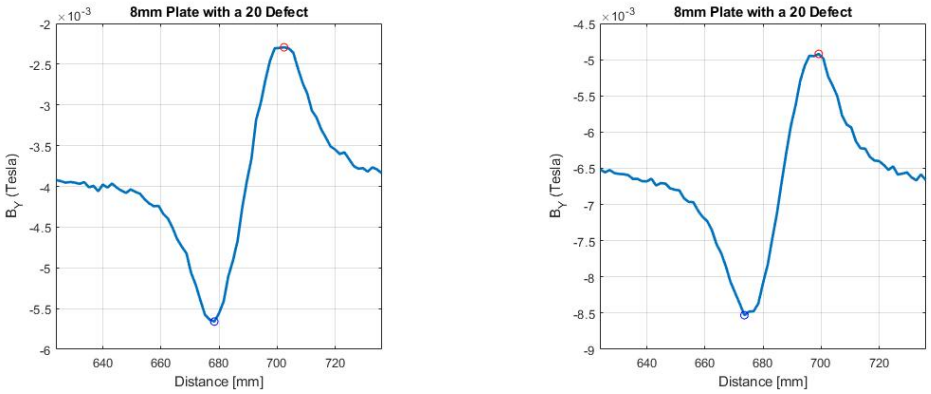

(a) $\mathbf{B}_Y$ response for a 20% bottom side defect on a $8mm$ plate at the slowest scanning speed.

(b) $\mathbf{B}_Y$ response for a 20% bottom side defect on a $8mm$ plate at the fastest scanning speed.

Figure 5.9: Figure displaying the $\mathbf{B}_Y$ response from a 20% through wall defect on a $8mm$ plate at the slowest and fastest scanning speeds.

The average peak-to-peak signal response for a 20% bottom side defect for slow and fast scanning speeds are given in Figure 5.9. The peak-to-peak amplitude difference for a 20% top and bottom side defect for an $8mm$ thick plate are not significant. The change in offset should be noted between the slow and fast scanning speeds. The values for each defect response at all velocities are given in Table 5.2.

Table 5.2: Average $\mathbf{B}_Y$ peak-to-peak signal responses from 20-80% through wall defects on a $8mm$ plate.

	Slow		Medium		Fast	
Defect Size (%}	Top	Bottom	Top	Bottom	Top	Bottom
20	0.0033	0.0034	0.0069	0.0038	0.0065	0.0036
40	0.0080	0.0099	0.0139	0.0109	0.0133	0.0105
60	0.0134	0.0197	0.0217	0.0209	0.0204	0.0203
80	0.0192	0.0325	0.0298	0.0356	0.0288	0.0333

10mm Plate Summary

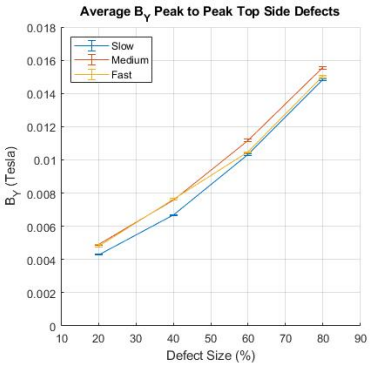

(a) Average peak-to-peak $\mathbf{B}_Y$ response for top side defects on a $10mm$ plate.

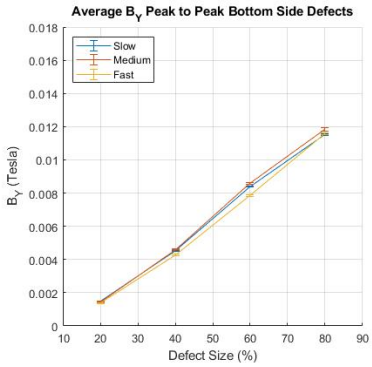

(b) Average peak-to-peak $\mathbf{B}_Y$ response for bottom side defects on a $10mm$ plate.

Figure 5.10: Figure displaying the average $\mathbf{B}_Y$ peak-to-peak responses from all top and bottom side defects on an $10mm$ thick plate.

The data displayed in Figure 5.10 are the average peak-to-peak values of all top and bottom side defects on a $10mm$ thick plate. At a plate thickness of $10mm$ bottom side defects no longer produce a larger signal response than top side defects at each defect size. This indicates the flux density in the plate is reducing in saturation and the flux is beginning to shift towards the top side of the plate. When a higher inspection velocity is used, an effect on the peak-to-peak signal amplitudes of top side defects is noted, as seen in Figure 5.10a, where signal amplitude is increased with velocity from the slow, medium and fast speeds. The increase of amplitude of the top side peak-to-peak responses would suggest that a reduction in amplitude would be seen from bottom side defects, however this is not the case. The average peak-to-peak values from bottom side defects are somewhat consistent when inspection speed is increased as seen in Figure 5.10b. This is similar to the results of an $8mm$ plate.

The amplification of top side defects support the findings of the simulated data where a concentration of flux is observed at the top side of the plate when velocity is increased. This means inspection velocity can aid in the detection of top side defects on a $10mm$ thick plate with this set-up. An example of the peak-to-peak signal response from top and bottom side defects of 20% through wall thickness are given in Figure 5.11.

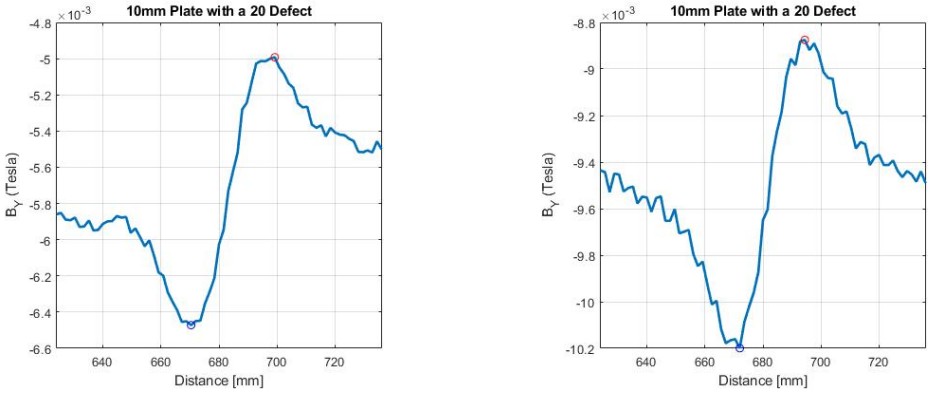

(a) $\mathbf{B}_Y$ response for a 20% bottom side defect on a $10mm$ plate at the slowest scanning speed.

(b) $\mathbf{B}_Y$ response for a 20% bottom side defect on a $10mm$ plate at the fastest scanning speed.

Figure 5.11: Figure displaying the $\mathbf{B}_Y$ response from a 20% through wall defect on a $10mm$ plate at the slowest and fastest scanning speeds.

Figure 5.11 shows the peak-to-peak signal response for a 20% defect at two velocities; fast and slow. Figures 5.11a and 5.11b indicate a worsening signal to noise ratio when compared to that of the $8mm$ thick plate for the same size defect. The values for all peak-to-peak responses are given in Table 5.3.

Table 5.3: Average $\mathbf{B}_Y$ peak-to-peak signal responses from 20-80% through wall defects on a $10mm$ plate.

	Slow		Medium		Fast	
Defect Size (%}	Top	Bottom	Top	Bottom	Top	Bottom
20	0.0043	0.0015	0.0049	0.0015	0.0048	0.0014
40	0.0067	0.0045	0.0076	0.0046	0.0077	0.0043
60	0.0103	0.0084	0.0112	0.0086	0.0104	0.0078
80	0.0148	0.0115	0.0155	0.0118	0.0150	0.0116

12mm Plate Summary

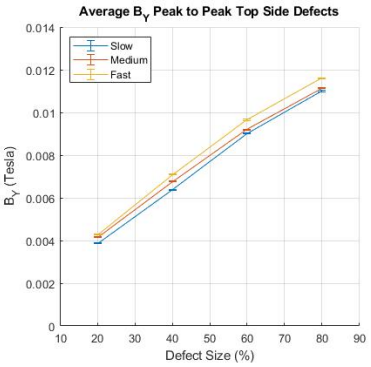

(a) Average peak-to-peak $\mathbf{B}_Y$ response for bottom side defects on a $12mm$ plate.

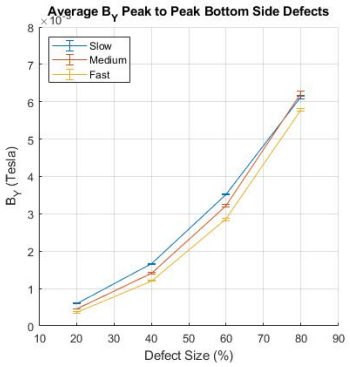

(b) Average peak-to-peak $\mathbf{B}_Y$ response for top side defects on a $12mm$ plate.

Figure 5.12: Figure displaying the average $\mathbf{B}_Y$ peak-to-peak responses from all top and bottom side defects on an $12mm$ thick plate.

In this section, the results for a plate thickness of $12mm$ are analysed. The distribution of flux is affected by inspection velocity and, in turn, affect defect sensitivity. When higher velocities are used, a shift in flux concentration is observed within the plate at high inspection velocities as seen in the simulated results presented previously in chapter 4. In practice, the shift of flux concentration takes place on smaller plate thicknesses and lower velocities.

The shift in flux towards the top surface results in a higher flux density in this region and is more evident on larger plate thicknesses, resulting in an amplification of top side defects and making them easier to detect by increasing signal peak-to-peak responses. As expected, the opposite effect occurs with bottom side defects. Here, a reduction in signal amplitude is encountered as the inspection velocity is increased due to the decrease in flux density in the lower regions of the plate where the defect is situated. An increase of 7.63% is indicated for the 60% top side defect with an increase in velocity of $0.44m/s$, as seen in Figure 5.12b. The bottom side defect demonstrates a reduction of -18.96% with the same change in velocity as seen in Figure 5.12a.

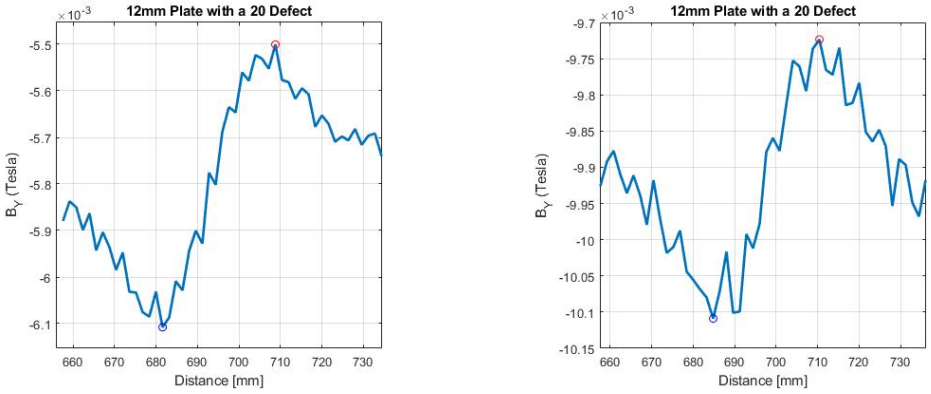

(a) $\mathbf{B}_Y$ response for a 20% bottom side defect on a $12mm$ plate at the slowest scanning speed.

(b) $\mathbf{B}_Y$ response for a 20% bottom side defect on a $12mm$ plate at the fastest scanning speed.

Figure 5.13: Figure displaying the $\mathbf{B}_Y$ response from a 20% through wall defect on a $12mm$ plate at the slowest and fastest scanning speeds.

Following on from the $10mm$ plate thickness the signal to noise ratio for the $12mm$ plate for a 20% through wall defect has become significant to the point where defect detectability is being affected as seen in Figure 5.13. The peak-to-peak amplitude and signal to noise ration between slow and fast scanning speed as seen in Figures 5.13a and 5.13a respectively, indicate velocity has an affect on signal clarity and defect detectability. The peak-to-peak values are displayed in Table 5.4.

Table 5.4: Average $\mathbf{B}_Y$ peak-to-peak signal responses from 20-80% through wall defects on a $12mm$ plate.

	Slow		Medium		Fast	
Defect Size (%}	Top	Bottom	Top	Bottom	Top	Bottom
20	0.0039	0.0006	0.0041	0.0005	0.0043	0.0004
40	0.0064	0.0017	0.0068	0.0014	0.0071	0.0012
60	0.0090	0.0035	0.0092	0.0032	0.0097	0.0028
80	0.0110	0.0061	0.0111	0.0062	0.0116	0.0058

16mm Plate Summary

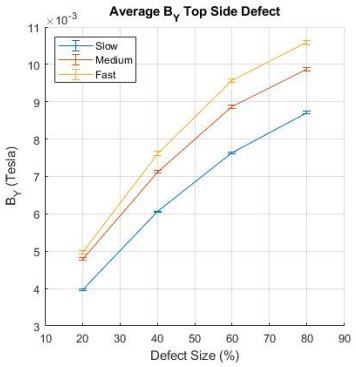

(a) Average peak-to-peak $\mathbf{B}_Y$ response for top side defects on a $16mm$ plate.

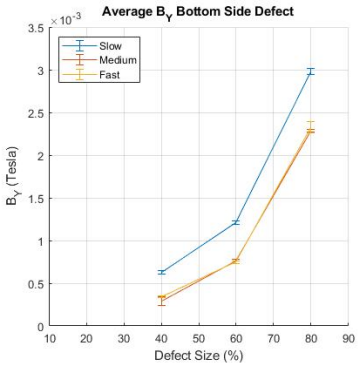

(b) Average peak-to-peak $\mathbf{B}_Y$ response for bottom side defects on a $16mm$ plate.

Figure 5.14: Figure displaying the average $\mathbf{B}_Y$ peak-to-peak responses from all top and bottom side defects on an $16mm$ thick plate.

The results for a $16mm$ plate thickness are shown in Figures 5.14a and 5.14b. It is clearly demonstrated by the average peak-to-peak signal responses that velocity alters the flux distribution within a $16mm$ thick plate. In Figure 5.14a indicate a 20.89% increase in the signal amplitude of an 80% defect when velocity is increased from 0.52 to $1.11m/s$. Also, a decrease of -21.94% is seen in the peak-to-peak amplitude for the 80% bottom side defect.

The bottom surface defects have noticeably lower peak-to-peak amplitudes when compared to top side defects. At this plate thickness the 20% top side defect has a greater peak-to-peak amplitude than that of the 80% bottom side defect. This is due to the lack of flux penetrating through to the bottom side resulting in an insufficient flux density within the lower regions of the inspection material. The 20% bottom side defect becomes undetectable as the signal is lost within the background noise.

An example of how increasing velocity affects the detectability of bottom-side defects is shown in Figure 5.15, where a signal trace is given for two velocities, $0.52m/s$ and $1.11m/s$ respectively. To highlight the decrease in the signal-to-noise ratio (SNR) where the SNR of $0.52m/s$ with a 40% bottom side defect is 7.57, and a velocity of $1.11m/s$ achieves an SNR of only 3.67 for the same defect. The reduction in the SNR

ratio where velocity is increased from the bottom side defect response is an indication of the distribution of flux within the material concentrating to the top surface. From Figures 5.15a and 5.15b, it can be seen that there is a reduction in peak-to-peak amplitude when the velocity increases from 0.52 m/s to 1.11 m/s. This is also accompanied by an increase in signal offset. The average peak-to-peak values for all defect sizes and speeds as shown in Figure 5.14 are given in Table 5.5 below.

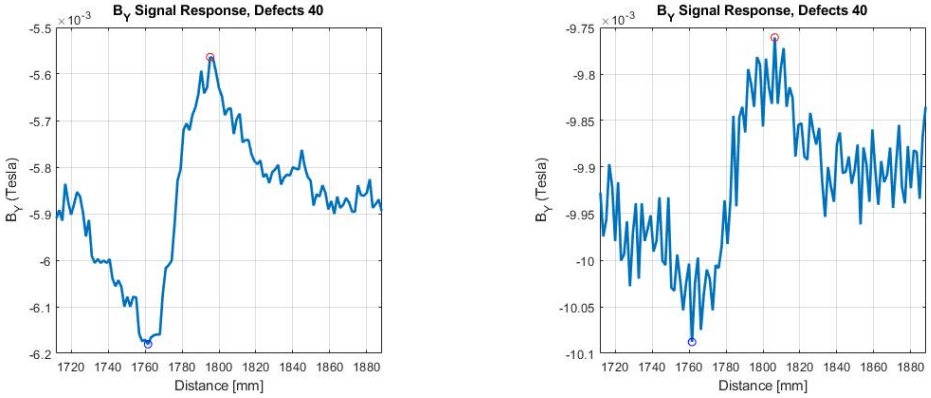

(a) $\mathbf{B}_Y$ response for a 40% bottom side defect on a 16mm plate at the slowest scanning speed.

(b) $\mathbf{B}_Y$ response for a 40% bottom side defect on a 16mm plate at the fastest scanning speed.

Figure 5.15: Figure displaying the $\mathbf{B}_Y$ response from a 40% through wall defect on a 16mm plate at the slowest and fastest scanning speeds.

Table 5.5: Average $\mathbf{B}_Y$ peak-to-peak signal responses from 20-80% through wall defects on a 16mm plate.

	Slow		Medium		Fast	
Defect Size (%}	Top	Bottom	Top	Bottom	Top	Bottom
20	0.0040	0.0000	0.0048	0.0000	0.0050	0.0000
40	0.0061	0.0006	0.0071	0.0003	0.0076	0.0003
60	0.0076	0.0012	0.0089	0.0008	0.0096	0.0007
80	0.0087	0.0030	0.0099	0.0023	0.0106	0.0023

5.2.2.1 Velocity and the effects on DC Signal Offset in practice

The resulting sensor DC offsets due to velocity are presented in Figure 5.16. This data is taken at points where the system has reached a constant velocity in defect free regions for the most accurate estimates. This is carried out for all plate thicknesses at three velocities, which as previously stated vary between plate thicknesses. Supporting the findings of the simulated data it is demonstrated in practice that the DC offset generated is a function of velocity and plate thickness. It is noted that in all instances velocity has an effect on the displayed signal offset. During inspection conditions if the plate thickness is known it may be possible to determine velocity based on the signal offset generated as a result of the relative motion between a magnet and a plate. The average offset values for all plate thicknesses and velocities are given in Table 5.6.

Table 5.6: Table showing the average DC offset of $\mathbf{B}_Y T$ for all plate thicknesses and velocities.

Plate Thickness (mm)	Slow	Medium	Fast
6	-0.0038	-0.0057	-0.0072
8	-0.0041	-0.0063	-0.0076
10	-0.0053	-0.0080	-0.0099
12	-0.0055	-0.0088	-0.0100
16	-0.0058	-0.0088	-0.0102

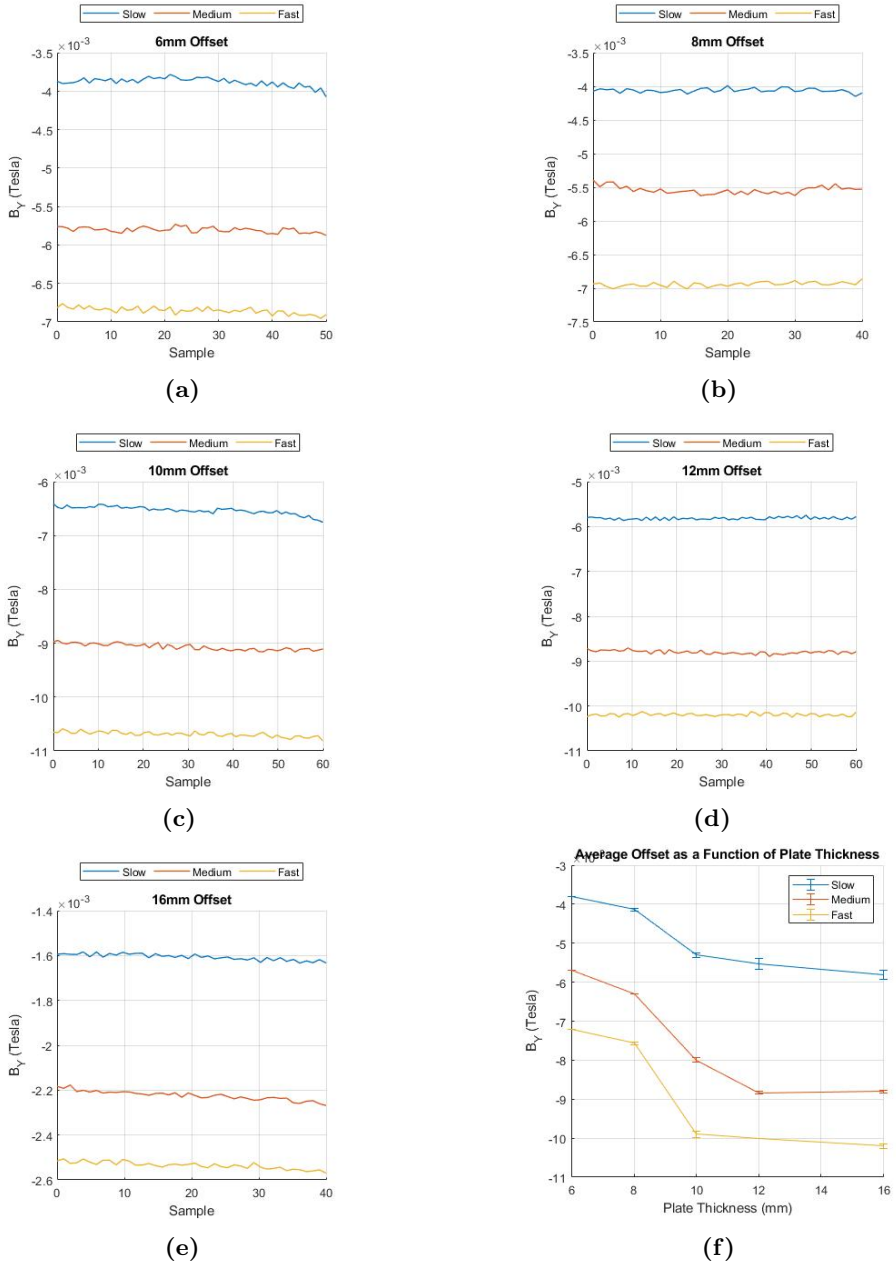

Figure 5.16: Showing the changes in DC offset in a defect free regions of each scan changing with plate thickness and scanning velocity.

5.3 Conclusion

It is noted that scanning velocity has a direct affect on defect sizing and characterisation capabilities due to the distorted magnetic field analysed in Chapter 4.

- Inspection speed can impact the minimum required reporting threshold. Both of these factors are determined by the capability of the magnet to magnetically saturate a plate. For the permanent magnet-based system used, a plate thickness of $12mm$ and thicker should be scanned at the lowest speed possible (plate dependent) to increase the likelihood of bottom-surface defect detection. If the top surface is of interest, then inspection speeds may be increased to allow for a higher sensitivity.

- When analysing the full scan traces it is found that a plate thickness of $6mm$ has consistent offsets across the sensor range at the same speed, whereas plate thicknesses of $12mm$ and thicker show a spread of offset values across the eight channels, becoming greater with increased plate thickness. This suggests that the smaller spread is due to the saturated material. When the spread of the channels increases, backing up the findings of an earlier thesis [8] this is an indication that the material is undersaturated.

- A system with controllable speed is desirable for a more accurate comparison between velocities and to keep the speeds at which tests are completed consistent. The resistance to motion varies with plate thickness and velocity due to the induced eddy currents. The maximum drive force is limited by the constant voltage supplied to the drive motor. Taking this into consideration, the tests are completed at three selected stages of the available voltage supply: minimum, half and maximum; therefore, the velocity is not directly controlled as a function of speed. A system where the velocity is consistent between plates regardless of thickness is desirable.

- During an MFL inspection, the acceleration and deceleration phase can affect the ability of the system to detect and characterise flaws. A more accurate

method of calculating the acceleration/deceleration value at a given point is desired when a defect is present in order to measure the impact that the acceleration/deceleration has on defect characterisation. This is explored in more detail in the following chapter.

- Inspection procedures should be altered based on inspection requirements so that these phenomena are taken into consideration.

- Results are consistent with simulated data showing a shift in flux concentrating at the top surface and reducing signal amplitude of bottom side of unsaturated plates with increased inspection velocities.

5.3.1 Simulated and Practical Comparison

Comparing the simulated and practical results is essential to ensure the trends observed within the simulated models can be shown to produce results that are comparable to that of experimental testing. This comparison is undertaken on a $6mm$ thick plate where the plate is magnetically saturated for both experimental and simulated models with defects of 20, 40, 60 and 80% through wall thickness. A direct comparison between the simulated and experimental results are given in Table 5.7 and Figure 5.17. Table 5.7 shows that the simulated results are somewhat an order of magnitude (10 times) greater than the measured practical results. This is caused by the elongated defect spanning the whole width of the magnet assembly when carrying out 2D simulations. To obtain more accurate simulated results 3D simulation is required. However, when Figure 5.17 is taken into consideration there is a clear trend between the simulated and practical results when displayed on separate axis thus indicating that the trends seen from the 2D simulated data hold true in practice.

Table 5.7: Table of results showing the simulated and practical $\mathbf{B}_Y$ results for a $6mm$ plate at $0.5m/s$. This indicates that the experimental results are approx an order of magnitude different from the simulated results, demonstrating the need to carry out 3D simulations.

Defect Size (%)	Simulation	Experimental
20	0.0896	0.0094
40	0.181	0.0181
60	0.2736	0.0279
80	0.4267	0.0411

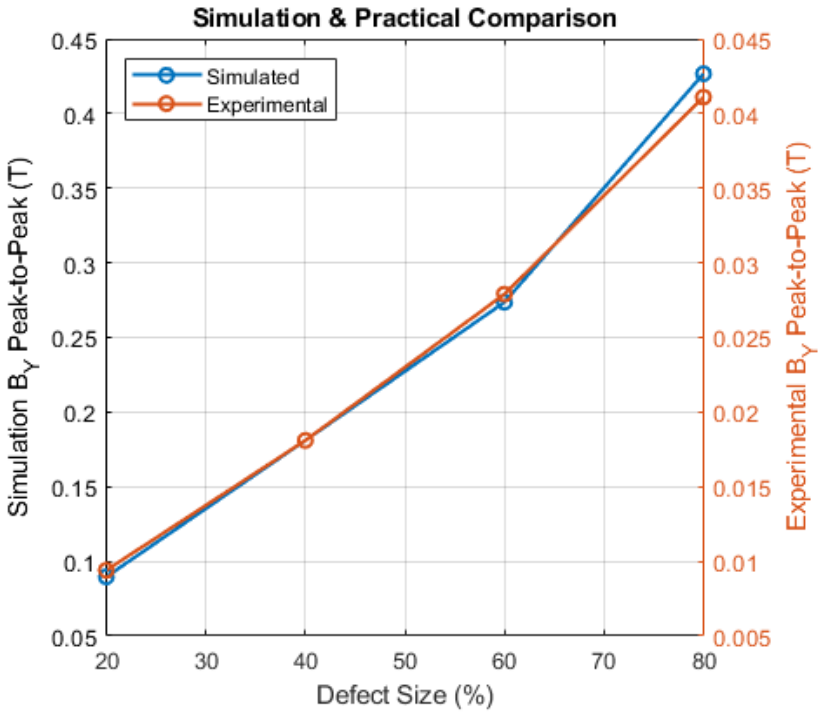

Figure 5.17: Simulated and Practical results displayed with defects sizes of 20 40 60 and 80% through wall thickness on a $6mm$ plate.

Chapter 6

Velocity Correction and Floating Calibration Curves

6.1 Introduction

Utilising the results from Chapters 4 and 5, this chapter provides an approach to velocity compensation. It is evident that in the 'real world' application that scanning velocity varies, both due to initial acceleration and final deceleration but also during general scanning where surface conditions can vary. The purpose of this chapter is therefore to correct for a change in B_Y signal offset and defect peak-to-peak responses using a method that can be applied across all plate thicknesses for both top and bottom side defects alike. As highlighted previously system offset is a function of velocity and plate thickness it is therefore possible to determine and correct for a change in system offset with velocity. This is most present in the acceleration and deceleration phases of an inspection. This can also be used to compensate for changes in scan speeds as a result of poor surface/scanning conditions where the inspection material's surface is not flat.

Secondly, a novel approach of a Floating Calibration Curve (FCC) is demonstrated allowing for the correction of calibration curves between two inspection velocities that can be determined in real time dependent on instantaneous velocity. This can then be used to adjust the signal to compensate for changes in peak-to-peak signal amplitude

reductions from bottom side defects as a means of overcoming the shortfall in reduced signal responses with increased velocity on unsaturated plates.

6.2 Correcting for Changes in Inspection Velocity

6.2.1 Floating Calibration Curve

This section proposes that a floating calibration curve can be generated for any inspection velocity within the range of the system. A typical MFL inspection requires a calibration process where a calibration plate with 20, 40, 60 and 80% defects is scanned. This is done for both top and bottom side defects by flipping the plate through 180^o so the defects are then on the opposing side. If this process is undertaken at multiple speeds, slow and fast, it is then possible to generate a floating calibration curve that operates within the bounds of the minimum and maximum velocities to correct peak-to-peak signal responses for changes in velocity. Undertaking multiple scans at varying inspection speeds will improve the accuracy of the calibration process. During the calibration process two curves are created, one for top side defects, and another for bottom side defects. As there are two calibration curves there is also a requirement for two Floating Calibration Curves (FCC) to be generated for top and bottom side defects. STARS is used in practice to discriminate between top and bottom side defects which can be used to determine which FCC calibration curve to use for improved defect sizing [21] [22]. The process of generating and implementing the FCC method is given in the following sections.

6.2.1.1 Interpolating Between Defect Responses

Firstly the data obtained from the work carried out in Chapters 4 and 5 is used to plot graphs that show the peak-to-peak signal response as a function of defect size at all speeds as seen in Figure 6.1a. From this point interpolating between each defect size across all velocities is required as shown in Figure 6.1b.

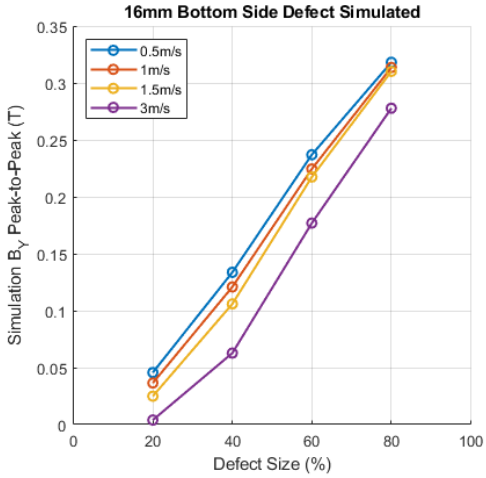

(a) Figure showing peak-to-peak $\mathbf{B}_Y$ signal response from as a function of defect size (%) for a $16mm$ plate with bottom side defects at 0.5, 1, 1.5, and $3m/s$.

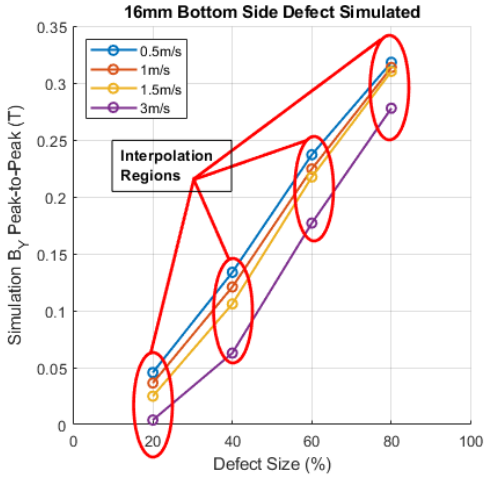

(b) Figure showing the region where the interpolation needs to take place in order to generate a floating calibration curve at any velocity between the maximum and minimum inspection speed.

Figure 6.1: Images showing the original data and initial stages of generating the FCC.

In order to interpolate between velocities of each defect size the data needs to be presented differently. This is achieved by plotting the peak-to-peak values of each defect 20, 40, 60, and 80% through wall thickness as a function of velocity as seen in Figure 6.2. This allows for a trendline to be generated between each peak-to-peak value at 0.5, 1, 1.5, and $3m/s$. The equation of the linear trendline of $y = mx + c$ is then taken and used to plot estimated defect amplitude points for any arbitrary velocity. Any velocity can then be chosen between the 0.5 and $3m/s$ boundaries and

in some instances extended beyond this, as seen in Equation 6.1 for a $16mm$ plate with a 40% bottom side defect. The data used to establish the trendline and plot the graphs seen in Figures 6.2 and 6.1 is displayed in Table 6.1.

$$\begin{aligned} y &= mx + c \\ y &= -0.0286x + 0.1487 \end{aligned} \tag{6.1}$$

Figure 6.2 displays the alternative plot created from the same data as seen in Table 6.1. This plot then gives the equations for each trendline, with the most significant being that of the 40% defect, which in this case returns an R^2 value of 0.9996 indicating the trendline is representative of the data it is generated from and will return accurate estimations of defect amplitudes.

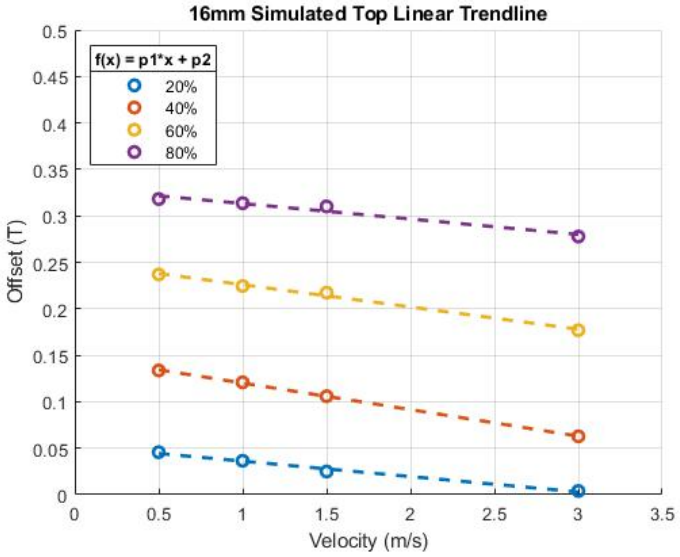

Figure 6.2: Graph showing the $\mathbf{B}_Y$ peak-to-peak values plotted as a function of velocity for simulated data of a $16mm$ thick plate.

Table 6.1: Table showing the simulated peak-to-peak $\mathbf{B}_Y$ results for a 40% bottom side defect at 0.5 - $3m/s$ for a $16mm$ thick plate.

		Velocity (m/s)			
		0.5	1	1.5	3
Defect Size (%)	20	0.045697	0.036487	0.024928	0.003962
	40	0.133687	0.120863	0.105948	0.062746
	60	0.236986	0.224473	0.217393	0.1769
	80	0.318119	0.31364	0.31014	0.277791

6.2.1.2 Plotting a Floating Calibration Curve

Once the equations for the trendlines have been generated from the simulated data, an example of which for a 16mm plate thickness with bottom side defects are given in Table 6.2 and Figure 6.2, the equations are then used to calculate the estimated $\mathbf{B}_Y$ values for each defect. This is achieved by substituting 'x' for the desired velocity in the individual equations, examples of which are listed in Table 6.2 for all defect sizes. New $\mathbf{B}_Y$ values for the selected velocity can then be displayed. A comparison between simulated and calculated $\mathbf{B}_Y$ peak-to-peak amplitudes are shown in Table 6.3 along with the associated errors for a 16mm thick plate at 3m/s.

Table 6.2: Table displaying the linear equation applied to the trendline of each defect depth displayed in Figure 6.2.

Defect Size (%)	Equation	R^2
20	y = -0.0166x + 0.0526	0.9885
40	y = -0.0286x + 0.1487	0.9996
60	y = -0.024x + 0.2499	0.9921
80	y = -0.0166x + 0.3299	0.9566

Table 6.3: Table showing the simulated and estimated $\mathbf{B}_Y$ results in T for for a trendline plotted against all velocities. The estimated velocities are calculated from the equations displayed in Table 6.2.

	Simulated Results	Estimated Results	Error
Defect Size (%)	3m/s	3m/s	
20	0.003962	0.0028	-0.00116
40	0.062746	0.0629	0.000154
60	0.1769	0.1779	0.001
80	0.277791	0.2801	0.002309

6.2.1.3 FCC: Testing the limits

Repeating the steps above an FCC curve is generated as shown in Figure 6.3 from lower and upper scan velocity limits. This curve is generated from simulated data of a 16mm thick plate with a bottom side defect. The blue uppermost line represents a scan velocity of 0.5m/s for 20, 40, 60, and 80% through wall defects, and the yellow lower line is from a results at 3m/s for the same defect sizes. The orange line is the

simulated data at $1m/s$, and the black dashed line is the calculated FCC estimation generated from a linear trendline applied the upper and lower limits of 0.5, and $3m/s$ for each defect size. The error between the simulated and the FCC calculated values are given in Table 6.4 indicating this method is accurate to 3-4 decimal places for this given data set. The following section will demonstrate this approach on experimentally acquired data.

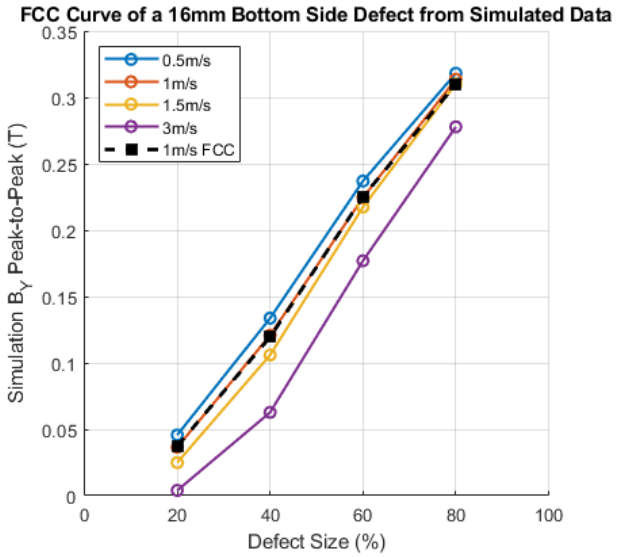

Figure 6.3: An image showing the accuracy of the FCC method on simulated data. The dashed line is calculated from the 0.5 and 3m/s peak-to-peak values. The orange line under the dashed in based on all simulated velocities.

Table 6.4: Table showing the $\mathbf{B}_Y$ peak-to-peak results for a 20, 40, 60, and 80% defects at $1m/s$ and the calculated FCC values and the associated errors.

Defect Size (%)	Simulated $\mathbf{B}_Y$	Calculated $\mathbf{B}_Y$	Error
20	0.0365	0.0373	0.0008
40	0.1209	0.1195	-0.0014
60	0.2245	0.2250	0.0005
80	0.3136	0.3101	-0.0035

6.2.1.4 FCC curves from Experimental data

To test the technique using real data the FCC approach is applied to multiple experimental data sets within this section. The method used is the same as that applied in the simulated example described in the previous section therefore a full work through

will not be provided again for each example. The peak-to-peak data as a function of velocity will be given accompanied by examples of the FCC calibration as applied to the data.

16mm Top side defects - Experimental

Utilising the FCC method of compensating for changes in velocity this method is applied to experimentally acquired data from a $16mm$ thick plate with top side defects. Generating an FCC using a linear trendline for this data set would be more accurate than calibrating for a singular velocity as shown in Figure 6.5. However, when comparing the results FCC generated data points it can be seen to have an increased error in comparison to the simulated data previously due to the limited fit of a linear trendline seen in Figure 6.4a. Although the error for a linear trendline is small and only requires two velocities, it may be possible to use a polynomial fit applied to the data set including the middle inspection velocity of $0.74m/s$ returning a result closer to the measured values as Seen in Table 6.5. Although a polynomial works for this data set it is not expected that this will work in all cases as over-fitting will occur, as seen in the following results for a $16mm$ thick plate with bottom side defects.

Table 6.5: Table showing the $\mathbf{B}_Y$ peak-to-peak results for a 20, 40, 60, and 80% defects at $0.74m/s$, the calculated FCC values and the associated errors between linear and polynomial trendlines.

Trendline	Defect Size (%)	Measured	Calculated	Error
Linear				
	20	0.0048	0.0045	-0.0003
	40	0.0071	0.0069	-0.0003
	60	0.0089	0.0086	-0.0003
	80	0.0099	0.0096	-0.0003
Polynomial				
	20	0.0048	0.0049	0.0001
	40	0.0071	0.0070	-0.0001
	60	0.0089	0.0088	0.0000
	80	0.0099	0.0099	0.0001

16mm Top side defects - Experimental Figures

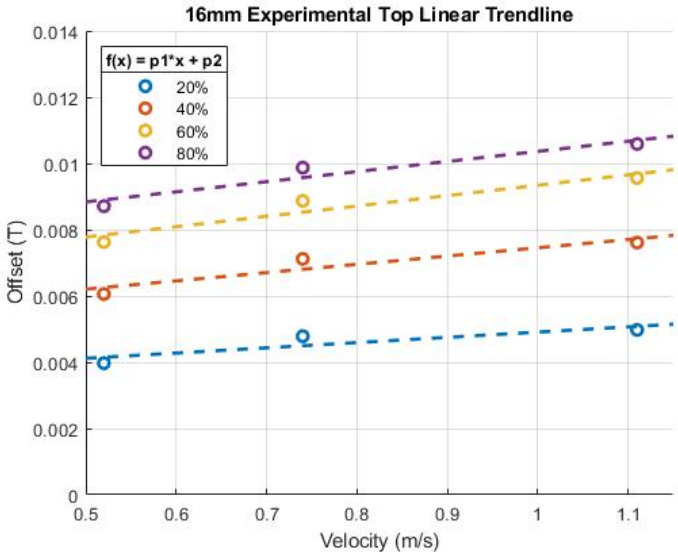

(a) Graph showing the $\mathbf{B}_Y$ peak-to-peak values and its linear trend-line plotted as a function of velocity taken from experimental data of a $16mm$ thick plate with top side defects. The R^2 values for each defect size are: 20% = 0.9284, 40% = 0.9136 60% = 0.8878 80% = 0.7882.

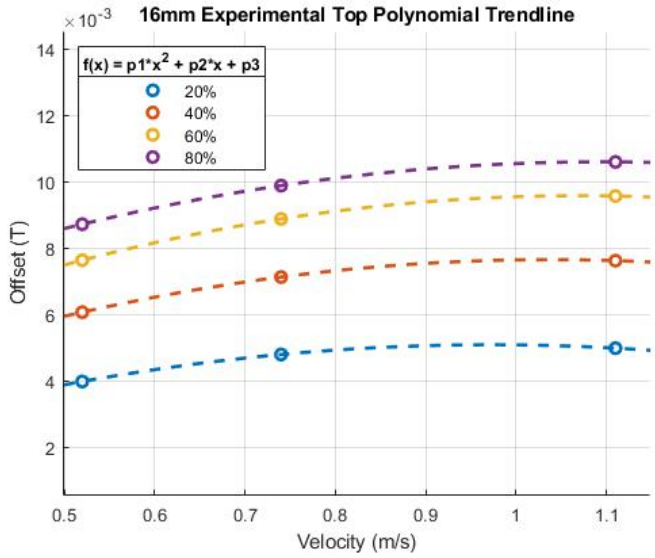

(b) Graph showing the $\mathbf{B}_Y$ peak-to-peak values and its polynomial trend-line plotted as a function of velocity taken from experimental data of a $16mm$ thick plate with top side defects.

Figure 6.4: Graphs demonstrating the trend-lines applied to the data from a $16mm$ thick plate with top side defects to generate the FCCs. The R^2 values for each defect size are: 20% = 1, 40% = 1 60% = 1 80% = 1.

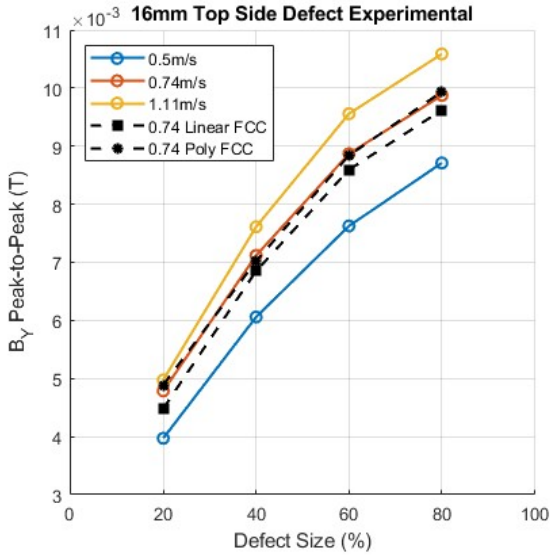

Figure 6.5: Graph showing the accuracy of the FCC method on experimental data. The dashed line is calculated from the peak-to-peak values at each velocity. The orange line under the dashed line is based on all simulated velocities. The dot-dashed line represents the FCC created from a polynomial fit.

16mm Bottom side defects - Experimental

The FCC method is again applied to experimentally acquired data from a $16mm$ thick plate but with bottom side defects. As previously discussed in chapter 5, the 20% bottom side defect in not detectable on a $16mm$ thick plate, therefore, the 20% defect cannot be compensated for. This example is given to demonstrate that applying a polynomial fit results in over-fitting, can lead to over-compensation as seen in Figure 6.7. At an arbitrary velocity of $0.9m/s$ it can be seen that the FCC generated from a linear trend-line as seen in Figure 6.6a is under-compensating whereas the polynomial generated FCC is over-compensating, as seen in Figure 6.7. As $0.9m/s$ is an arbitrary value to demonstrate the under and over-compensation of both methods a table of errors is not given. The issue is caused by the 0.74 and $1.11m/s$ providing similar peak-to-peak signal amplitudes.

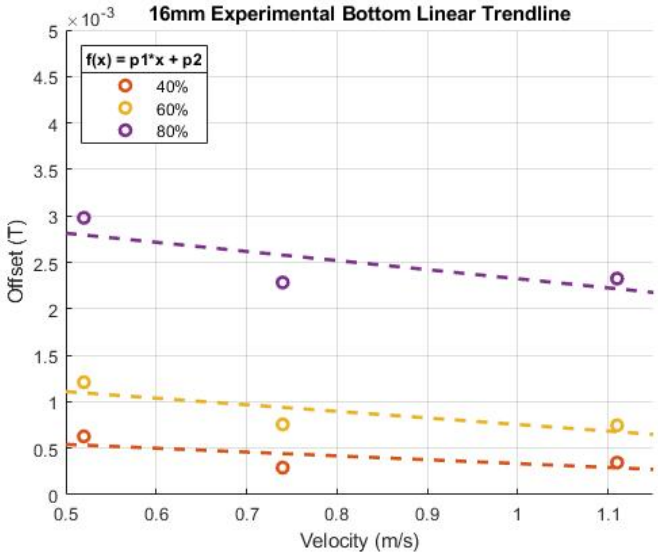

(a) Graph showing the $\mathbf{B}_Y$ peak-to-peak values and its linear trend-line plotted as a function of velocity taken from experimental data of a $16mm$ thick plate with bottom side defects. The R^2 values for each defect size are: $40\% = 0.5728$ $60\% = 0.6453$ $80\% = 0.4772$.

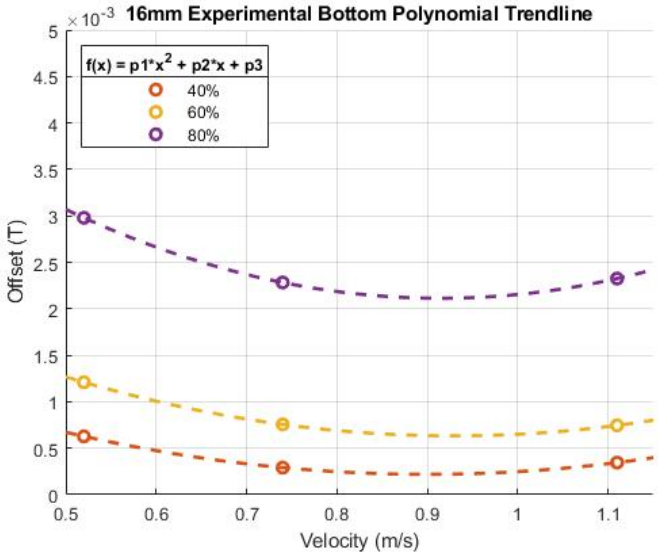

(b) Graph showing the $\mathbf{B}_Y$ peak-to-peak values and its polynomial trend-line plotted as a function of velocity taken from experimental data of a $16mm$ thick plate with bottom side defects. The R^2 values for each defect size are: $40\% = 1$ $60\% = 1$ $80\% = 1$.

Figure 6.6: Graphs demonstrating the trend-lines applied to the data from a $16mm$ thick plate with top side defects to generate the FCCs.

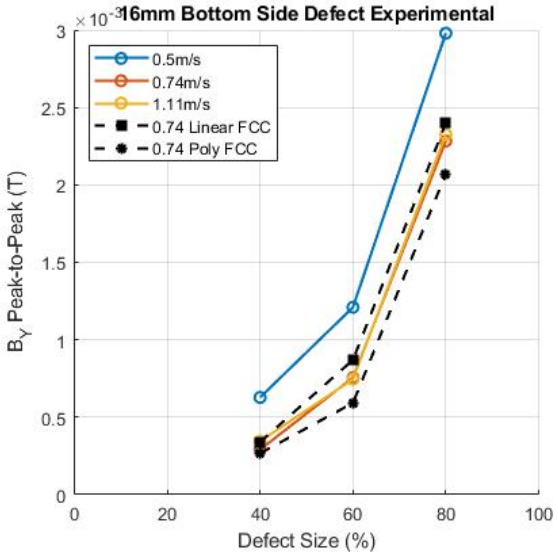

Figure 6.7: Graph showing the accuracy of the FCC method on experimental data. The dashed line is calculated from the peak-to-peak values at each velocity. The orange line under the dashed line is based on all simulated velocities. The dot-dashed line represents the FCC created from a polynomial fit.

6.3 Conclusions

This chapter has demonstrated that it is possible to compensate for variations in scan velocity through the means of a floating calibration curve approach. This approach requires two extreme velocity calibration curves (slow and fast) to generate a floating calibration curve for variation in velocity during scanning. This could be achieved through the the use of $\mathbf{B}_Y$ offset monitoring to estimate instantaneous velocity or alternatively though system positional and fixed sample rate calculations.

The FCC method has been demonstrated through the use of both simulation generated data as well as real-world experimentally acquired data. In practice this method would be applied during the calibration phase, before scanning. Four calibration scans are required, two at slow and fast scanning speeds for top side defects and two at slow and fast scanning speeds for bottom side defects. This does mean two additional calibration scans are needed but the benefit of improved sizing accuracy outweighs the additional two scans.

There are limits to this method, such as automatic curve fitting to produce the most accurate representation of the peak-to-peak values without over-fitting. Compensation outside the calibration velocity limits may also require further investigation.

Chapter 7

Conclusions and Future Work

7.1 Summary of Work

This chapter summarises the findings and the contribution to knowledge relevant to the work carried out in this thesis. The work consists of a parametric study of MFL inspection of mild steel plates with the yoke geometry taken from a commercial system, and typical plate thicknesses found when inspecting above ground storage tanks. This includes simulated extreme cases, static cases, and velocity considerations. Practical assessment is also undertaken to validate the simulated velocity effect results and to determine behaviour of MFL inspection undertaken during the acceleration and deceleration phases of an inspection. It considers how to compensate for this gradual change in velocity. Furthermore, the future direction of continuing this work is highlighted.

In review of the thesis chapter 1 provides an overview of the work carried out where the reader is introduced to MFL inspection and its advantages for scanning above ground storage tank floors due to tank scan area and the large scan area of the FM3Di. Also in the introductory section a brief scene-setting section is provided to highlight the significant effect velocity can have on MFL inspection. Following this the motivation, aims and objectives and the contributions to knowledge are discussed, along with the author's peer reviewed journal publications that have been published

in IEEE and The British Institute of Non-Destructive Testing journals based upon this work. The organisation/layout of the thesis is also provided and a brief overview is given on the contents of each chapter.

Chapter 2 contains a more detailed overview of the motivation to undertake the research by investigating storage tank failure rates and how this can be prevented by regular maintenance. The typical NDT inspection methods used to assess ASTs integrity are considered with a basic introduction on how the technology functions, with a more detailed review of MFL and the commercial system used as the focus of this thesis and the types of defects encountered. Later on in the chapter an overview of magnetic principles are given including; magnetic susceptibility of materials, hysteresis, **BH** curves and a chronological review of previous literature is undertaken from 1985 to 2023. The main findings from the literature provided a conflict of results where [3] reported an increased signal response to defects while undertaking MFL inspection at high speeds. This thesis highlights why both instances are correct finding that defect orientation has a significant impact of MFL signal amplitude when velocity is introduced. The work in this thesis concludes with a novel approach to correcting for velocity variations where the literature suggests moving the sensor is needed. This would only be the case if inspection velocity remained constant.

The methodology chapter (3), introduced the reader to the theoretical and experimental methods of MFL principles used to gather the data presented throughout this thesis. This is provided for computational and experimental methods. Firstly, an overview of magnetic theory is given to provide the reader with the necessary formulas and relationships to allow for a simple analytical model to be generated to highlight key magnetic circuit theory affecting the flux density **B** within a magnetic circuit. Then an overview of finite element modelling is given together with the process undertaken to generate and configure the parametric studies undertaken for the major chapters within this thesis. Consideration is given to the inspection velocity, plate thickness, materials used, defect volume, defect orientation and sensor position. It is

noted that for this study the sensor position is fixed at the optimum position for the commercial system the model is based on.

The experimental set-up is then given later on in this chapter where the modified FM3Di system is shown along with the equipment used. A shell of the FM3Di system was used with all the signal processing and onboard PC removed. The system was driven by a DC motor and a lead acid battery. A bespoke sensor array was manufactured and connected directly to the Eddyfi Technologies Ectane 2, and a laptop was used for data capture and processing. An overview of the specimens' range of plate thicknesses from 6 to 16mm are given along with sample velocities on plate thicknesses of 6, 12, and 16mm. A consistent defect pattern of 20, 40, 60, and 80% depth are scanned throughout all the experimental data gathered. The process of how inspection speed is measured is also given, where video capture is used to produce timestamps of the time taken for the system to travel a distance of 200mm. Finally, an overview of the data acquisition and signal processing schematic of the systems used to collect the data is shown.

Chapter 4 investigates and presents the results of the simulated parametric studies undertaken to investigate the affect of increasing scanning velocity of the commercial FM3Di system. The chapter begins by providing the reader with an extreme case scenario with plate thicknesses of 100mm in thickness both statically and at 3m/s. This is done to provide the reader with clear imagery of the affect velocity has on the distributed flux within a 1020 grade mild steel plate. Consideration to how the flux distribution throughout the plate is affected when velocity is introduced is investigated. This is undertaken for all plate thicknesses and velocities within this study where no defects are considered. The results of this are presented to the reader in an ordered format increasing in plate thickness. It is demonstrated that velocity has an impact on how distribution of the flux within the plate becomes distorted and unevenly distributed throughout the plate thickness. The results indicate that the lower the flux density within the plate, the more significant effect that velocity has on defect detectability and characterisation using a fixed sensor system. A study is

then conducted where defects of 20, 40, 60, and 80% are introduced and the $\mathbf{B}_Y$ signal response is displayed for all plate thicknesses at 0.5, 1, 1.5, and $3m/s$ with a summary provided for each defect size and also as a whole. The DC system offset is also noted to change when velocity is increased, a means of analysing this and presenting the data in such a way that velocity and offset are related and it is possible to estimate velocity based on the signal offset. This method only applies if the plate thickness is known. However, this offset is traditionally filtered out through signal processing.

The experimental results are given in chapter 5. This chapter provides a practical evaluation of the effect of scanning velocity on defect detection in mild steel plates of thicknesses from 6 to $16mm$. Data is exported from the Eddyfi Magnifi software into excel format where it is then manipulated in MATLAB R2019b. An example of a full data trace is given at the start of the chapter to highlight the acceleration, deceleration and the order and size of the defects. The data is presented in this way for an example of other plate thicknesses of 6, 12 and $16mm$ where general comments on the signal offset, acceleration and deceleration phases are made. In order to validate the simulated results a defect orientation study is undertaken when the average $\mathbf{B}_Y$ signal response for a specific defect is taken over 5 scans and then plotted. In agreement with the simulated results, scan velocity has a more pronounced affect on signal amplitudes when the plate is not considered to be saturated resulting in a lower $\mathbf{B}$ value in the plate. This is demonstrated by an increase in signal amplitude of top side defects and a reduction of bottom side defects indicating the shift in flux within the plate. The DC offset results also hold true in practice as they do in simulation, increasing with velocity to a maximum where the plate is no longer considered to be saturated.

Chapter 6 is where the novel approach to correcting for variations in velocity is given. This approach does not rely on the need to move the sensor when inspecting at increased velocities s suggested by other studies in the literature. Firstly, a step-by-step approach on how to generate and implement the FCC method is given. This

process begins by plotting signal peak-to-peak data as a function of defect size for all velocities. From there interpolating between peak-to-peak responses for a given defect size for the range of velocities considered. The peak-to-peak values for each defect size is then plotted as a function of velocity and a linear trendline added. The equation of the trendline is then used to plot a new calibration curve at any arbitrary velocity between the upper and lower inspection velocities. Examples of this applied to simulated and experimental data is then given to show that this works in practice and can be applied through DSP to compensate for variations in velocity during an MFL inspection that does not require the sensor position to be moved.

7.2 Contributions to Knowledge

In conclusion to the work carried out in this thesis a number of contribution to knowledge can be noted:

- A parametric study on a full range of typical plate thicknesses, and velocities are performed. The distortion of the magnetic flux induced into the specimen due to the motional eddy current effect had not previously been documented with how this affect alters the ability to detect and characterise flaws based on its orientation during an inspection. It is found that the effects alter the signal amplitude from a defect based on its orientation (top/bottom surface flaw). Bottom surface flaws show a decrease in signal amplitude whereas top surface flaws an increase in amplitude on unsaturated specimens. This is visible in both simulated and experimental data. As a direct result of this, if near surface flaws are to be singled out for detection then inspection speeds can be increased with no negative impact on detectability. Opposing this bottom side defects show a reduction in signal amplitude. As bottom side defects are of most interest during an MFL inspection e.g. storage tank floors, a method of overcoming this is also demonstrated.

- Literature suggests that to improve peak-to-peak signal amplitudes of defects

when undergoing MFL inspection the sensor should be moved [10], [11]. However, this is not feasible for systems where velocity can vary during scanning. To compensate for this, a novel method of creating a Floating Calibration Curve (FCC) is demonstrated so that the calibration changes as a function of velocity as given in chapter 6.

7.3 Suggestions for Future Work

Following on the from the work undertaken during this thesis, there are a number of directions this work can be taken and expanded upon. The simulation work undertaken is only in 2D. In 2D simulation there are a number of assumptions made including the defect geometry. The nature of the simulations assume the defect spans the entire width of the scanning assembly of $300mm$ in width, but in practice the maximum defect size is $22mm$ in diameter. 3D simulation work could be undertaken to improve the accuracy of the results so that the defects considered are true to what is seen in practice as discussed in the conclusion section of Chapter 5. Repeating the parametric study work undertaken in this thesis but in 3D can identify issues seen on lateral sensor position and investigate how amplitude correction may be applied on the outer Hall effect sensors to correct for lateral changes in defect amplitude and offset throughout the width of the scanning assembly. How the flux distribution in the plate varies should also be investigated in 3D and how this is affected at the outer edges of the magnet assembly. The lower flux density in this region of the plate would suggest the system would be more sensitive to changes in velocity within this region.

The work conducted in this thesis focuses solely on the $\mathbf{B}_Y$ signal responses of MFL inspection, this should be extended to ensure the same affects are present when the $\mathbf{B}_X$ signal is considered. However, as $\mathbf{B}_Y$ is a vector component, it is thought that $\mathbf{B}_X$ would show equivalent amplitude variations [8].

A continuation of the experimental work would be to conduct experiments on longer specimens so that a more consistent constant velocity is achieved and the ac-

celeration and deceleration phases do not interact and distort defect signal responses. This will remove inaccuracies in the measuring of inspection velocity in practice. Also a larger sensor array should be considered to span the full scan width of the system and an investigation of how the outer portions of the sensors are affected by velocity due to the flux density in the specimen being lower at the outer edges of the scan head.

Further investigation into the Digital Signal Processing required to compensate for velocity and investigate improved methods of doing so should be undertaken to determine improved sizing where there are variations in velocity. Investigation into the spatial resolution of defect responses would be conducted to determine other factors other than velocity, saturation and defect size has on the signal response.

Bibliography

[1] N. Pearson, "Band-limitations and non-linearities of magnetic flux leakage in context of non-destructive testing," Ph.D. dissertation, Swansea University, 2014.

[2] G. S. Park and S. H. Park, "Analysis of the velocity-induced eddy current in mfl type ndt," *IEEE Transactions on Magnetics*, vol. 40, no. 2, pp. 663–666, Mar. 2004, ISSN: 0018-9464. DOI: 10.1109/TMAG.2004.824717.

[3] P. Wang, Y. Gao, G. Tian, and H. Wang, "Velocity effect analysis of dynamic magnetization in high speed magnetic flux leakage inspection," *NDT & E International*, vol. 64, pp. 7–12, 2014, ISSN: 0963-8695. DOI: https://doi.org/10.1016/j.ndteint.2014.02.001.

[4] D. Rodger, T. Karguler, and P. J. Leonard, "A formulation for 3d moving conductor eddy current problems," *IEEE Transactions on Magnetics*, vol. 25, no. 5, pp. 4147–4149, Sep. 1989, ISSN: 0018-9464. DOI: 10.1109/20.42550.

[5] Y. S. Sun, W. Lord, G. Katragadda, and Y. K. Shin, "Motion induced remote field eddy current effect in a magnetostatic non-destructive testing tool: A finite element prediction," *IEEE Transactions on Magnetics*, vol. 30, no. 5, pp. 3304–3307, Sep. 1994, ISSN: 0018-9464. DOI: 10.1109/20.312644.

[6] Y.-K. Shin, "Magnetic flux leakage inspection of moving steel sheets," in *Review of Progress in Quantitative Nondestructive Evaluation: Volume 15A*, D. O. Thompson and D. E. Chimenti, Eds. Boston, MA: Springer US, 1996, pp. 2249–2256, ISBN: 978-1-4613-0383-1. DOI: 10.1007/978-1-4613-0383-1_295.

[7] D. L. Atherton and E. Quek, "Distinction between near and far-side corrosion pit signals using magnetic leakage flux detectors," *Canadian Electrical Engineering*

Journal, vol. 13, no. 1, pp. 27–31, Jan. 1988, ISSN: 0700-9216. DOI: 10.1109/CEEJ.1988.6592902.

[8] P. C. Charlton, "A theoretical and experimental study of the magnetic flux leakage method for the analysis of corrosion defects in carbon steel plate," Ph.D. dissertation, University of the West of England, Swansea Institute of Higher Education, Feb. 1995.

[9] Z. Wang, K. Yao, B. Deng, and K. Ding, "Theoretical studies of metal magnetic memory technique on magnetic flux leakage signals," *NDT & E International*, vol. 43, no. 4, pp. 354–359, 2010, ISSN: 0963-8695. DOI: https://doi.org/10.1016/j.ndteint.2009.12.006.

[10] M. Coramik, H. Citak, Y. Ege, S. Bicakci, and H. Gunes, "Determining the effect of velocity on sensor selection and position in non-destructive testing with magnetic flux leakage method: A pipe inspection gauge design study with ansys maxwell," *IEEE Transactions on Instrumentation and Measurement*, vol. 72, pp. 1–12, 2023. DOI: 10.1109/TIM.2023.3284023.

[11] Y.-K. Shin, "Numerical prediction of operating conditions for magnetic flux leakage inspection of moving steel sheets," *IEEE Transactions on Magnetics*, vol. 33, no. 2, pp. 2127–2130, Mar. 1997, ISSN: 0018-9464. DOI: 10.1109/20.582751.

[12] S. B. Vardeman, *Statistics for engineering problem solving*, D. Press, Ed. 1994.

[13] EVIDENT, *Phased Array Probes — Olympus IMS — olympus-ims.com*, https://www.olympus-ims.com/en/probes/pa/?apd=1&adid=ndt&acid=enbgle&utm_source=bing&utm_medium=cpc&creative=&keyword=olympus\%20phased\%20array\%20probes&matchtype=e&network=o&device=c&campaignid=408081616&adgroupid=1299623000192932&msclkid=207faa2661671b1c9be9cc13f
utm_campaign=NDT\%3E\%3EEMEA\%3E\%3EUK\%3E\%3EEN\%3E\%3EFlaw\%20Detectors\%3E\%3EBrand&utm_term=olympus\%20phased\%20array\%20probes&utm_content=Olympus\%20-\%20Probes\%20-\%20Phased\%20Array, [Accessed 04-05-2024], 2024.

[14] J. I. Chang and C.-C. Lin, "A study of storage tank accidents," *Journal of loss prevention in the process industries*, vol. 19, no. 1, pp. 51–59, 2006.

[15] R. Anvo, T. P. Sattar, T.-H. Gan, and I. Pinson, "Non-destructive testing robots (ndtbots) for in-service storage tank inspection," in *Human-Centric Robotics: Proceedings of CLAWAR 2017: 20th International Conference on Climbing and Walking Robots and the Support Technologies for Mobile Machines*, World Scientific, 2018, pp. 301–308.

[16] N. Pearson, J. Mason, and R. Priewald, "The influence of maintenance on the life cycle of above ground storage tanks," *Insight - Non-Destructive Testing and Condition Monitoring*, vol. 54, Jun. 2012. DOI: 10.1784/insi.2012.54.6.311.

[17] R. Thompson, "Ndt techniques: Ultrasonic," *Encyclopedia of Materials: Science and Technology*, pp. 6039–6043, 2001.

[18] J. Drury, "Ultrasonics. part 1. basic principles of sound," *Insight*, vol. 46, no. 11, pp. 650–652, 2004.

[19] P. Blakeley, J. Simkin, and S. Brown, "Validation of finite element analysis of the magnetic fields around fine cracks," *IEEE Transactions on Magnetics*, vol. 21, no. 6, pp. 2420–2423, Nov. 1985, ISSN: 0018-9464. DOI: 10.1109/TMAG.1985.1064218.

[20] T. Tadic and B. Fallone, "Design and optimization of superconducting mri magnet systems with magnetic materials," *IEEE Transactions on Applied Superconductivity - IEEE TRANS APPL SUPERCONDUCT*, vol. 22, pp. 4 400 107–4 400 107, Apr. 2012. DOI: 10.1109/TASC.2012.2183871.

[21] N. Pearson, "Discrimination of top and bottom discontinuities with mfl and the surface topology air-gap reluctance system (stars)," in *MENDT*, 2012.

[22] J. Costain, N. R. Pearson, M. Boat, and R. Boba, "Capability of modern tank floor scanning with magnetic flux leakage," *Bad. Nieniszcz. Diag*, vol. 3, pp. 20–23, 2017.

[23] J. C. Drury, *Ultrasonic flaw detection for technicians*. Silverwing, 2003.

[24] R. A. Dalan, "Magnetic susceptibility," *Remote sensing in archaeology: An explicitly North American perspective*, pp. 161–203, 2006.

[25] D. Jiles, *Introduction to magnetism and magnetic materials*. CRC press, 2015.

[26] C. G. Darwin, "The diamagnetism of the free electron," in *Mathematical Proceedings of the Cambridge Philosophical Society*, Cambridge University Press, vol. 27, 1931, pp. 86–90.

[27] J. Van Den Handel, "Paramagnetism," in *Advances in Electronics and Electron Physics*, vol. 6, Elsevier, 1954, pp. 463–518.

[28] W. Clegg, *Magnetism and Magnetics An Introductory Course*. 1993.

[29] A. Aharoni, *Introduction to the Theory of Ferromagnetism*. Clarendon Press, 2000, vol. 109.

[30] A. Hubert and R. Schäfer, *Magnetic domains: the analysis of magnetic microstructures*. Springer Science & Business Media, 2008.

[31] H. Sung and C. Rudowicz, "Physics behind the magnetic hysteresis loop—a survey of misconceptions in magnetism literature," *Journal of magnetism and magnetic materials*, vol. 260, no. 1-2, pp. 250–260, 2003.

[32] F. Förster, "New findings in the field of non-destructive magnetic leakage field inspection," *NDT International*, vol. 19, pp. 3–14, 1 1986, ISSN: 0308-9126. DOI: https://doi.org/10.1016/0308-9126(86)90134-3.

[33] D. Rodger, T. Karguler, and P. J. Leonard, "A formulation for 3d moving conductor eddy current problems," *IEEE Transactions on Magnetics*, vol. 25, pp. 4147–4149, 5 Sep. 1989, ISSN: 0018-9464. DOI: 10.1109/20.42550.

[34] M. Ito, T. Takahashi, and M. Odamura, "Up-wind finite element solution of travelling magnetic field problems," *IEEE Transactions on Magnetics*, vol. 28, no. 2, pp. 1605–1610, Mar. 1992, ISSN: 0018-9464. DOI: 10.1109/20.124007.

[35] Y. K. Shin and W. Lord, "Numerical modeling of moving probe effects for electromagnetic nondestructive evaluation," *IEEE Transactions on Magnetics*,

vol. 29, no. 2, pp. 1865–1868, Mar. 1993, ISSN: 0018-9464. DOI: 10.1109/20.250770.

[36] M. Marinescu and N. Marinescu, "Magnetic leakage fields from extended inhomogeneities in ferromagnetic plates," *IEEE Transactions on Magnetics*, vol. 30, pp. 2960–2963, 5 Sep. 1994, ISSN: 0018-9464. DOI: 10.1109/20.312558.

[37] E. Altschuler and A. Pignotti, "Nonlinear model of flaw detection in steel pipes by magnetic flux leakage," *NDT & E International*, vol. 28, no. 1, pp. 35–40, 1995, ISSN: 0963-8695. DOI: https://doi.org/10.1016/0963-8695(94)00003-3.

[38] Y. Zhang, K. Sekine, and S. Watanabe, "Magnetic leakage field due to subsurface defects in ferromagnetic specimens," *NDT & E International*, vol. 28, no. 2, pp. 67–71, 1995, ISSN: 0963-8695. DOI: https://doi.org/10.1016/0963-8695(94)00004-4.

[39] T. W. Krause, R. Donaldson, R. Barnes, and D. L. Atherton, "Variation of the stress dependent magnetic flux leakage signal with defect depth and flux density," *NDT & E International*, vol. 29, no. 2, pp. 79–86, 1996, ISSN: 0963-8695. DOI: https://doi.org/10.1016/0963-8695(95)00050-X.

[40] G. Skutt and F. C. Lee, "Examining flux distributions in ferrite magnetic structures," *Journal of Magnetism and Magnetic Materials*, vol. 160, pp. 318–322, 1996, Proceedings of the twelfth International Conference on Soft Magnetic Materials, ISSN: 0304-8853. DOI: https://doi.org/10.1016/0304-8853(96)00215-6.

[41] S. Leonard and D. L. Atherton, "Calculations of the effects of anisotropy on magnetic flux leakage detector signals," *IEEE Transactions on Magnetics*, vol. 32, no. 3, pp. 1905–1909, May 1996, ISSN: 0018-9464. DOI: 10.1109/20.492885.

[42] S. Mandayam, L. Udpa, S. S. Udpa, and W. Lord, "Invariance transformations for magnetic flux leakage signals," *IEEE Transactions on Magnetics*, vol. 32, pp. 1577–1580, 3 May 1996, ISSN: 0018-9464. DOI: 10.1109/20.497553.

[43] G. Katragadda, J. T. Si, W. Lord, Y. S. Sun, S. Udpa, and L. Udpa, "A comparative study of 3d and axisymmetric magnetizer assemblies used in magnetic flux leakage inspection of pipelines," *IEEE Transactions on Magnetics*, vol. 32, pp. 1573–1576, 3 May 1996, ISSN: 0018-9464. DOI: 10.1109/20.497552.

[44] Y.-K. Shin, "Numerical prediction of operating conditions for magnetic flux leakage inspection of moving steel sheets," *IEEE Transactions on Magnetics*, vol. 33, pp. 2127–2130, 2 Mar. 1997, ISSN: 0018-9464. DOI: 10.1109/20.582751.

[45] H. Zuoying, Q. Peiwen, and C. Liang, "3d fem analysis in magnetic flux leakage method," *NDT & E International*, vol. 39, no. 1, pp. 61–66, 2006, ISSN: 0963-8695. DOI: https://doi.org/10.1016/j.ndteint.2005.06.006.

[46] F. Al-Naemi, J. Hall, and A. Moses, "Fem modelling techniques of magnetic flux leakage-type ndt for ferromagnetic plate inspections," *Journal of Magnetism and Magnetic Materials*, vol. 304, no. 2, e790–e793, 2006, Proceedings of the 17th International Symposium on Soft Magnetic Materials, ISSN: 0304-8853. DOI: https://doi.org/10.1016/j.jmmm.2006.02.225.

[47] Y. Li, G. Y. Tian, and S. Ward, "Numerical simulation on magnetic flux leakage evaluation at high speed," *NDT & E International*, vol. 39, no. 5, pp. 367–373, 2006, ISSN: 0963-8695. DOI: https://doi.org/10.1016/j.ndteint.2005.10.006.

[48] C. Xiuli, Z. Dechang, and L. Guixiong, "Study on simulation and experiment of the magnetizer in magnetic flux leakage testing," Aug. 2007, pp. 3083–3087. DOI: 10.1109/ICMA.2007.4304053.

[49] D. Zhiye, R. Jiangjun, P. Ying, *et al.*, "3-d fem simulation of velocity effects on magnetic flux leakage testing signals," *IEEE Transactions on Magnetics*, vol. 44, no. 6, pp. 1642–1645, Jun. 2008, ISSN: 0018-9464. DOI: 10.1109/TMAG.2007.915955.

[50] L. Zhang, F. Belblidia, I. Cameron, J. Sienz, M. Boat, and N. Pearson, "Influence of specimen velocity on the leakage signal in magnetic flux leakage type

nondestructive testing," *Journal of Nondestructive Evaluation*, vol. 34, no. 2, p. 6, 2015.

[51] S. Lu, J. Feng, F. Li, and J. Liu, "Precise inversion for the reconstruction of arbitrary defect profiles considering velocity effect in magnetic flux leakage testing," *IEEE Transactions on Magnetics*, vol. 53, no. 4, pp. 1–12, Apr. 2017, ISSN: 0018-9464. DOI: 10.1109/TMAG.2016.2642887.

[52] L. Zhang, I. M. Cameron, P. D. Ledger, *et al.*, "Effect of scanning acceleration on the leakage signal in magnetic flux leakage type of non-destructive testing," *Journal of Nondestructive Evaluation*, vol. 42, no. 1, p. 14, 2023.

[53] A. Ampère, "Théorie mathématique des phénomènes électro-dynamiques uniquement déduite de l'expérience, paris, 1827," *Reprinted in the edition published by Hermann (Paris, 1883)*, p. 96, 1958.

[54] Emmetcosten, *FEA Mesh Elements & Nodes Guide*, https://asrengineering.com/2019/09/23/fea-mesh-elements-nodes-guide-intro-to-fea/, [Accessed 09-05-2024], 2020.

[55] L. Zhang, F. Belblidia, I. Cameron, J. Sienz, M. Boat, and N. Pearson, "Influence of specimen velocity on the leakage signal in magnetic flux leakage type nondestructive testing," *Journal of Nondestructive Evaluation*, vol. 34, no. 2, p. 6, 2015.

[56] M. Coramik, H. Citak, Y. Ege, S. Bicakci, and H. Gunes, "Determining the effect of velocity on sensor selection and position in non-destructive testing with magnetic flux leakage method: A pipe inspection gauge design study with ansys maxwell," *IEEE Transactions on Instrumentation and Measurement*, vol. 72, pp. 1–12, 2023. DOI: 10.1109/TIM.2023.3284023.

[57] J. Simkin, "Modelling ferromagnetic materials for electromagnetic non-destructive evaluation of ferromagnetic materials," Houston, Texas, USA: Western Atlas Int. Inc, 1988, pp. 109–113.

Chapter 8

Appendices

Publications

Magnetic Flux Leakage Scanning Velocities for Tank Floor Inspection

Ashley Laurent Pullen[1], Peter C. Charlton[1], Neil R. Pearson[2], and Nicola J. Whitehead[1]
[1]University of Wales Trinity Saint David, Mount Pleasant Campus, Swansea, SA1 6ED, Wales UK
[2]Eddyfi (UK) Ltd, Clos Llyn Cwm, Swansea Enterprise Park, Swansea, SA6 8QY, Wales UK

The Non-Destructive Testing (NDT) technique known as Magnetic Flux Leakage (MFL) is used for the inspection of storage tank floors (mild steel plate). This paper focuses on finite element analysis of the velocity effects on the induced flux and its distribution in plate thicknesses of 6 mm through to 20 mm thick 1020 grade steel. When there is a velocity difference between the plate and the excitation system, eddy currents are induced opposing the applied magnetic field distorting its profile. This has an adverse effect on MFL inspection by altering signal responses thus limiting achievable inspection velocities. An investigation of velocities ranging from 0.5 to 3 m/s is undertaken on both defect free plates and plates containing spherical 40 % through wall thickness defects simulated for both near/top and far/bottom surfaces. From the results, it is indicated that the flux density distribution through the plate decreases as a function of depth. Once a plate depth of 16 mm is reached it is shown that flux density is significantly reduced towards the underside of the plate. These combined effects influence defect detectability on larger plate thicknesses for the specific yoke design used in this paper.

***Index Terms*—Induced Eddy Currents, Magnetic Flux Distribution, Magnetic Flux Leakage, MFL, Storage Tank Inspection, Velocity Effects, Wake Effect.**

I. Introduction

THE Magnetic Flux Leakage (MFL) Non-destructive testing (NDT) technique can be employed to identify and map material loss on ferromagnetic mild steel plates. The advantage of using this method over others is its ability to inspect large areas rapidly. MFL systems are employed to detect loss of material with diameter of mm's, over expanses in excess of hundreds of m^2 [1]. Although this technique is known for its rapid inspection speed, eddy currents are produced in the plate by relative motion of the magnet assembly. The plate has an adverse effect on the signal response by distorting and opposing the induced magnetic fields [2]–[5]. In order to facilitate repair and keep storage tanks in-service for as long as possible defects need to be located and characterised. MFL inspection strength lies with detection.

MFL is governed by several components, including the level of induced magnetisation, defect orientation, sensor configuration, component magnetic properties as well as other parameters including scanning velocity. For a permanent magnet based system the level of magnetic saturation achieved within each plate varies with thickness. This is a direct result of the constant supplied flux from a permanent magnet assembly being distributed through increasing volumes of material as the plate thickness increases. Saturation is considered to be the major factor of an MFL inspection and when saturation is achieved it is possible to detect smaller flaws than in a material that is under-saturated. Saturation levels differ with material properties thus making MFL inspection difficult to characterise when alterations in material properties are seen through possible repairs or inconsistencies in material production. Due to the nature of a permanent non-adjustable magnetic field a non-homogeneous distribution of flux is induced into the plate. This effect is amplified when velocity effects are considered along with increased plate thickness.

The level of magnetisation of a material is described as the ratio between the applied magnetic field and the induced flux density within the material, conventionally described by a BH curve as seen in Figure 1. The BH curve refers to a materials capability to induce magnetic flux density (B) as a function of the magnetic field strength (H) applied to a material that has no residual magnetisation. An illustration of the magnetisation levels of a typical ferromagnetic material is given in Figure 1 where 4 regions are considered as H is increased [5].

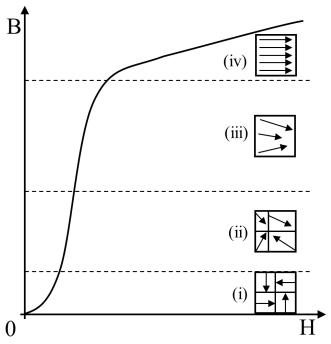

Fig. 1: Illustration of a typical BH curve trend with the corresponding magnetic domains of a ferromagnetic material at each stage of the curve as a function of H.

Stage (i) is the initial condition when the material is not influenced by an applied magnetic field, meaning that the magnetic domains are aligned randomly resulting in a net magnetisation of zero. Stage (ii) sees an increase in the applied H so that the plate becomes initially magnetised. This begins to align the domains within the plate. If the applied H field is increased further, stage (iii) results when the plate's domains

are becoming almost fully aligned in the direction of the applied magnetic field. Finally, stage (iv) is when the material is in the state of saturation. This occurs when all magnetic domains become fully aligned in the direction of the applied H field. From this point onwards any increase in H will not result in a significant change in B. This is a direct link to the increase of reluctance as the material's domains become aligned.

This paper investigates through simulation the velocity effects of a commercial MFL system for tank floor inspection. This system contains two permanent magnets and an array of Hall effect sensors with the capability of adjusting inspection velocity. For the purpose of this study, four velocities are taken into consideration, 0.5 m/s, 1 m/s, 1.5 m/s and 3 m/s.

II. Literature Review

In 1994 Sun [2] observed that when velocities are introduced into a non-destructive electromagnetic tool distortion of the corresponding signal responses from leakage are identified. Sun states that this problem is under-investigated with complex magnet assemblies with only the simplest of geometries being considered leading to a lack of application in real world NDT problems. The results published by Sun [2] indicate a consistent reduction in signal amplitudes to far surface defects when velocities are increased from 0 m/s up to 10 m/s. It is noted that these results are affected by multiple parameters such as sensor location, air gap size and permeability. It finishes with the requirement for further investigation into optimisation of such parameters for increased inspection sensitivity for the detection and characterisation of electromagnetic NDT tools.

In 2004 Park [3] investigates the distortion of MFL signals produced due to the velocity induced eddy currents. The distortion of defect signals with inspection velocities of 0, 1 and 2 m/s are investigated. It is also worth noting that the results from this study are of a magnetically saturated specimen again with a far surface defect. Park's findings state that due to the magnetic field applied being able to saturate the specimen and running at high speeds there are strong velocity-induced eddy currents which cause a distortion of corresponding MFL signals. Supporting Sun in 1994 it is concluded that increasing velocity reduces the peak amplitude of the signals.

In 2006 Li [4] comments that the need for MFL type inspection is in great demand for in-line metal inspection and defect characterisation with emphasis to rail track and pipeline applications. Li states that the induction of the eddy currents due to the relative velocities distort the magnetic field making it difficult for defect characterisation. The effects of the relative velocity and the induced eddy currents along with several defect depths are examined. Li further concludes that signal magnitudes are reduced resulting in lower signal to noise ratio for greater scanning velocities.

Using the 3-D finite element method (FEM) Zhiye [6] investigated the velocity effect of MFL signals in 2008. Again, it was noted that the induced eddy currents alter the profile of the magnetic field due to the relative motion between the magnetiser and a specimen. It is stated that not only do the eddy currents have an effect on the signal magnitude but also its shape. It is concluded that the effects are amplified when larger defects are modelled.

Wang [5] in 2014 further investigates the eddy current effects of moving electromagnetic inspection for defect characterisation. In this study for near surface flaws Wang indicates that signal responses of defects under high speed MFL testing results in an increase in signal amplitude and sensitivity. This is contradictory to previous work. There are three main differences seen in this investigation to that of previous studies, initially the defect size, orientation and high velocities of up to 200 km/h are investigated.

A similar study has been conducted with rectangular defects and only addressing the leakage signals monitored from sensors. In 2015 Zhang [7] found that the induced eddy current effect has a correlation with the optimal sensor position at multiple velocities ranging from 0.1 to 20 m/s. It is stated that the peak to peak value of the leakage field moves from the centre of the magnetic bridge opposite to the direction of yoke travel.

Most recently in 2017 Lu [8] has investigated the reconstruction of arbitrary defect profiles considering the velocity effects in MFL testing. Lu's simulation study indicates a reduction in signal amplitudes when velocities are increased following the trend of [2]–[4], [6], [7].

This paper will investigate why Wang 2014 [5] has achieved an increase in signal amplitude when all other work indicates a reduction of signal responses when using MFL with increasing velocities. It is initially noted that Wang uses a near surface defect and observes an increase and others who use far surface defects have a reduced signal amplitude. This paper bridges the gap between these scenarios and as to why this occurs.

III. Model Configuration

To emulate MFL inspection machined flaws are used in the form of a spherical defect with a variety of depths. In such a case the relative motion between the plate and yoke leads to change in the motional induced currents, resulting in a truly transient problem. Simulations are performed using a 2D magnetics translational transient capable software Oersted V930 [9].

As stated earlier, there are a number of parameters that will influence MFL signals. The main factors to consider include:

1) Velocity

The velocity difference between a plate and a permanent magnet yoke causes eddy currents to be introduced leading to a reduction in the applied magnetic field. Li [4] supports these statements by making similar claims.

2) Plate thickness

Increasing the thickness of plate has a direct result on its mean operating point on the BH curve. With a permanent magnetic yoke, only a finite amount of flux can be supplied into the plate. Taking this into consideration, increasing the area (thickness) causes a reduction in B when the same levels of H are applied.

3) Material

In this study a 1020 grade mild steel plate has been chosen for both the magnet assembly and the plate alike. Identical materials are introduced to maintain consistency to rule out dissimilar materials as a causing factor. 1020 grade steel is a typical parent material for storage tank floors.

4) Defect volume

For MFL inspection the volumetric loss of material causes the leakage field to occur when the flux can no longer be contained within the plate. In an attempt to mimic a corrosive medium coming into contact with the inspection material a spherical defect is chosen.

5) Sensor position

Sensor positioning is a crucial component in defect detection and characterisation when velocities are introduced. It is frequently reported in MFL applications where relative motion is a factor that the position of the sensors should be moved in the opposite direction to that of travel as the output from a defect is distorted in this direction [7]. It should also be noted there would be an optimal sensor position for a given velocity. There are also negative affects of moving the sensor closer to the magnetic poles where fringing is seen that would likely result in the saturation of sensors. Taking this into consideration and to reduce influences from the magnetic poles the sensor is positioned in the centre of the magnet assembly although as described by Zhang [7] there could be a more optimal sensor position.

6) Defect orientation (near/far surface flaw)

The orientation of a defect can have a direct effect on detection sensitivity. Therefore, defects are simulated for both near and far surfaces. This will investigate why far surface defects are reported to have lower signal responses where Wang [5] documents an increase in top surface feedback at velocities up to 200 Km/h.

A. Configuration

The magnetic assembly considered in this paper is from a commercial floor scanning system. The asymmetric shape of the magnetic yoke allows for sensors to be placed between the pole and the plate. These sensors measure top surface defects only. When coupled with MFL this allows discrimination of top and bottom surface defects, as described in [10]. However, for the purpose of this study when defects are being considered, only MFL signals indicated by the B_X and B_Y components in Figure 2 are extracted. The yoke is travelling with a defined velocity in the direction of the arrow labelled DoT (Direction of Travel) as illustrated in Figure 2. Multiple velocities are considered in the simulated experiments with a consistent defect shape used throughout with varying plate thickness.

B. Governing Equation

The governing equation for this 2-D. transient problem is;

$$\nu\nabla^2 A - \sigma\frac{\partial A}{\partial t} - \sigma V\frac{\partial A}{\partial x} = -J \tag{1}$$

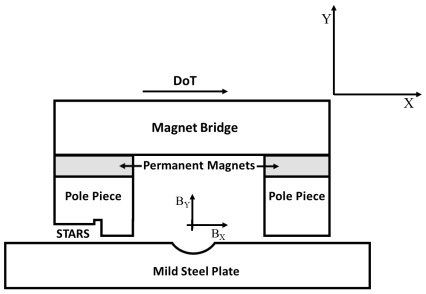

Fig. 2: Illustration of the magnet assembly and defect shape used in the parametric study accompanied by the corresponding B_X and B_Y directions relative to the model assembly.

Where ν, A, σ, V and J are the reluctivity, magnetic vector potential, conductivity, velocity of the plate and the current density respectively [11].

IV. Flux Distribution

A. Extreme case scenarios

To demonstrate the effects of velocity on a permanent magnet MFL system two simulations are conducted. Firstly, an extreme case scenario of a static case model with zero relative velocity on a 100 mm thick plate is performed to show an exaggerated effect seen on a un-saturated plate. The same assembly is simulated when relative motion is introduced between the magnet assembly and the plate with a velocity of 3 m/s. This is then repeated for plate thicknesses ranging from 6 to 20 mm.

1) Static case

From Figure 3 of a static simulation on the 100 mm thick plate it can be seen that the flux is distributed through the plate with a relatively even distribution.

2) Velocity case

From figure 4 the distribution of flux throughout the plate is significantly reduced resulting in a penetration of only 37 mm through the plate whereas in the static case flux is distributed through the entirety of the 100 mm thick plate. A wake effect is also evident where the flux enters and leaves the plate indicated within the dashed boxes in Figure 4 labelled (ii) and (iii) respectively [12].

3) Average flux density throughout plates of varying thicknesses for the static case

From Figures 3 and 4 the measurement of flux distributed through the 100 mm thick plate is taken along the vertical line central to the leading and trailing poles from the near surface of the plate through to the bottom. These measurements are used to provide two types of analysis. The first is to identify the mean level of induced flux density in the plate, for the static case results can be seen in Figure 3. Secondly, the distribution of the flux through the material plays a significant role in defect detection. This measurement is then taken when relative motion is introduced resulting in a non-linear distributed flux

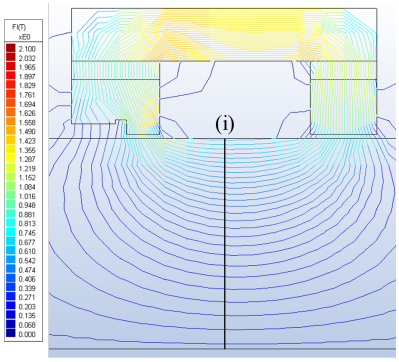

Fig. 3: Extreme static case of the magnetic flux distribution throughout a 100 mm steel plate with a fairly even distribution of flux penetrating the full depth of the plate. Measurements are taken from the vertical line marked (i) through to the far side of the plate.

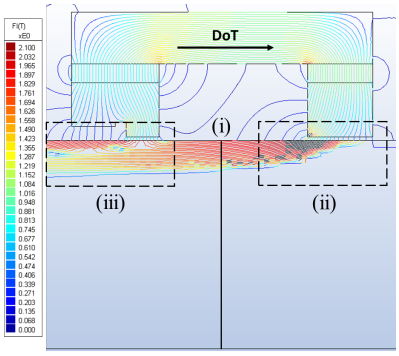

Fig. 4: Extreme moving case of the magnetic flux distribution throughout a 100 mm steel plate showing a distorted induced field with limited penetration of approximately 37 mm at 3 m/s. The direction of travel for the yoke is shown with the arrow labelled DoT (Direction of Travel). Measurements of flux distribution are taken from the vertical line labelled (i) at the near surface through to the far surface. The wake effect is also evident where the flux enters and leaves the plate indicated within dashed boxes labelled (ii) and (iii) respectively.

pattern through the plate material as illustrated previously in Figure 4.

B. Average $|B|$ value of a static model for varying plate thicknesses

A number of simulations are undertaken statically for range of plate thicknesses. The average $|B|$ value is calculated through the centre of the plate as previously described for Figure 3. The results of these simulations are shown in Figure 5. Taking into consideration the saturation level of the material used being 2.1 T only the 6 mm plate is saturated. Plates thicker than 6 mm are no longer in saturation. It is clear that plate thickness has a direct effect on the induced flux density. A typical inspection range for the design in question would be between 6 and 14 mm of plate thickness.

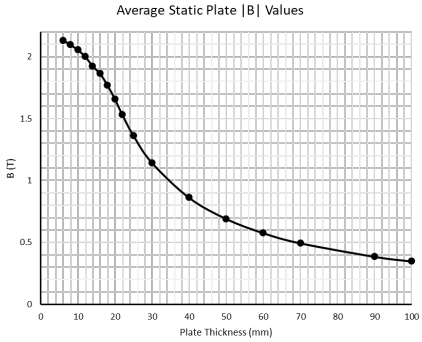

Fig. 5: Mean flux density results of plates varying from 6 to 100 mm. When an increase in plate thickness is seen, there is a resultant drop in the $|B|$ values throughout the plate

V. Plate Flux Density Distribution for Varying Velocities

Initial simulations were undertaken to benchmark the system to identify relationships between plate thickness and inspection velocity. In this study realistic velocities of 0.5, 1, 1.5 and 3 m/s were simulated on plate thicknesses of 6, 8, 10, 12, 14, 16 and 20 mm. This covers the full range of plate thicknesses normally encountered in the field.

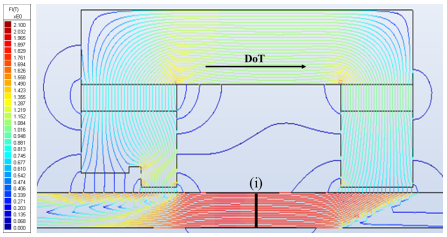

Fig. 6: 10 mm steel plate at 0.5 m/s with a consistent flux distribution with measurements taken from the black line labelled (i) as indicated on the illustration from the near surface through to the far surface.

Looking at the results for a 10 mm plate and at two velocities, depicted in Figure 6 which has the lower velocity, there is a higher overall level of induced flux density than that obtained at the higher speed illustrated in Figure 7. There is also an increase in the wake effect at the higher velocity.

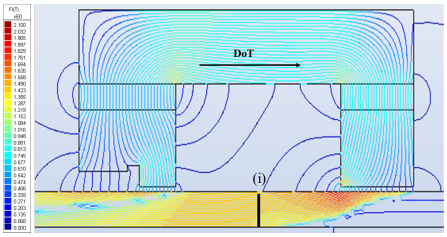

Fig. 7: Displaying measurement locations and distribution of flux at 3 m/s. The flux distribution in the plate is taken along the vertical black line labelled (i). Measurements are taken from the near surface through to the bottom.

For this part of the study measurements of the flux distribution through the plate are measured. This is taken at the centre point of the magnet assembly, through the thickness of the plate as depicted with a thick black line shown in Figures 6 and 7.

1) Results

Understanding how the flux is distributed in the cross-sectional area of the plate, (i) in Figures 6 and 7 will assist in understanding of how flaws may go undetected for increased plate thickness and higher scanning velocities.

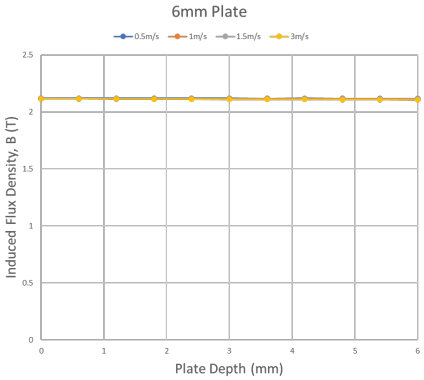

Fig. 8: Results of the distribution of flux throughout the 6 mm steel plate indicating an almost consistent level of induced flux through the whole of the plate at all velocities. This is where the plate has reached saturation.

A sample of the results are shown in Figures 8 and 9 where plate thicknesses of 6 mm and 16 mm are given as extreme examples. On the 6 mm plate it is evident that the distribution of induced flux from the near surface to the far is fairly consistent at all velocities.

When the 16 mm thick plate is taken into consideration it is clear that a significantly different trend occurs between 0.5 and 3 m/s velocities. The flux density at the near surface is 1.941 T at 3 m/s with a reduction at the far surface of 0.04347 T. In this scenario we can clearly identify a skin effect as a result of velocity induced eddy currents limiting the penetration of flux density within the plate.

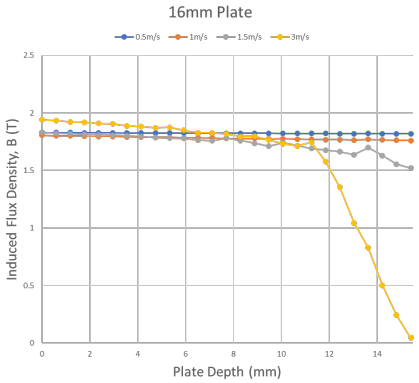

Fig. 9: Results of the distribution of flux throughout the 16 mm steel plate. It can be seen that the flux distribution at 1.5 and 3 m/s is non linear. There is a significant rate of change seen in the later 5 mm of the material at 3 m/s. This plate is under saturated.

VI. Orientation Sensitivity

Induced flux distribution can affect defect sensitivity (masking defects at higher velocities). When higher velocities are simulated a shift in flux concentration is seen within the plate. This shift takes place towards the near surface resulting in the flux manifesting in this region. This is more evident on thicker plates where even for the static case magnetic saturation is not achieved.

As a direct result of the distortion of the applied magnetic field and its concentration towards the near surface it is possible that a reduction in far surface defect sensitivity at higher velocities will be perceived. The orientation (either near or far surface) of the flaw will play a significant role in its detectability, and in particular in this case when plate thickness of 16 mm and thicker are encountered. Two bottom sided defect cases in a 16 mm plate with depths of 20 % and 40 % and a full range of velocities are considered.

Figure 10 shows that defects of 20 % and under will give significantly lower B_Y values and reduce the signal to noise ratio. It is observed that defects of 40 % through wall thickness on 16 mm plates will become less detectable due to the flux distribution shifting to the near surface at increased velocities. This is shown in Figure 11.

From the graphical representation of the B_Y values in Figures 10, 11 and 12 it can be seen that there is an increase in signal offset proportional to scanning velocity. This can have an adverse affect on the scanning system by potentially magnetically saturating its Hall effect sensors with the potential inability to detect flaws.

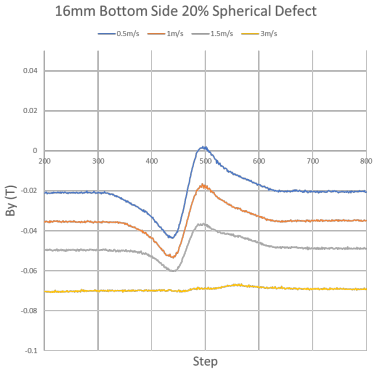

Fig. 10: B_Y Results for the 16 mm plate with a 20 % through wall defect. From these results it is clear to see that when a velocity of 3 m/s is reached a 20 % through wall spherical defect response on a 16 mm plate is insignificant and could reside within the noise levels of an inspection system.

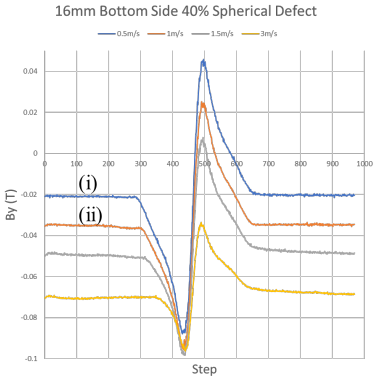

Fig. 11: B_Y results for the 16 mm plate with a 40 % through wall defect resulting in a reduction of signal peak-to-peak values when velocity is increased from 0.5 to 3 m/s. For (i) and (ii) see section VII.

An overall reduction in flux leakage is seen from the B_Y component when velocity is increased and can be seen in Figures 13 and 14. This effect becomes more significant when plate thickness is increased meaning this phenomenon can be reduced by achieving near saturation. It is not possible to fully mitigate this reduction in flux leakage due to the relative motion between the magnet assembly and the plate due to the velocity induced eddy currents.

It can also be observed from these results that an increase in velocity reduces far surface flaw signal magnitude. At a velocity of 0.5 m/s a peak to peak difference of 0.134 T is produced. Following this when the inspection speed is increased the B_Y peak to peak value reduces to 0.063 T at 3 m/s in a somewhat linear decay for the 16 mm plate. This results in an overall signal drop of 53 %. However, a near surface flaw does not follow the same trend. For the near surface flaw an initial peak to peak value of 0.145 T at 0.5 m/s is observed. When the velocity is increased to 3 m/s it is observed that the reduction in the peak to peak value of a near surface flaw is not the same as the far side flaw. The near surface is reduced to 0.087 T at 3 m/s returning a signal drop of 40 % for the same 16 mm plate thickness.

In agreement with Zhang [7] it can be seen that near surface flaws have an increased response when comparing higher

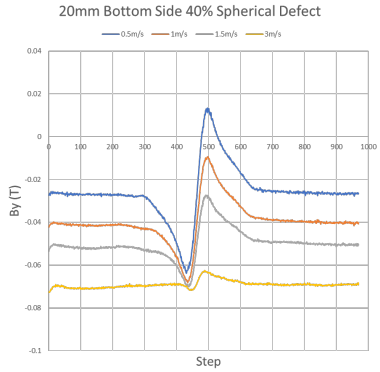

Fig. 12: B_Y results for the 20 mm plate with a 40 % through wall defect resulting in a reduction of signal peak to peak values when velocity is increased from 0.5 to 3 m/s.

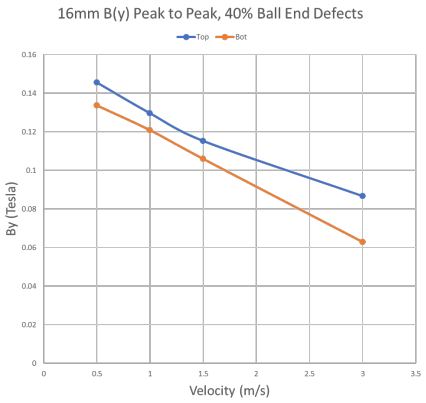

Fig. 13: B_Y peak to peak values for the 16 mm plate with a 40 % through wall defect a consistent reduction in the peak to peak value is seen from the top and far surface defects.

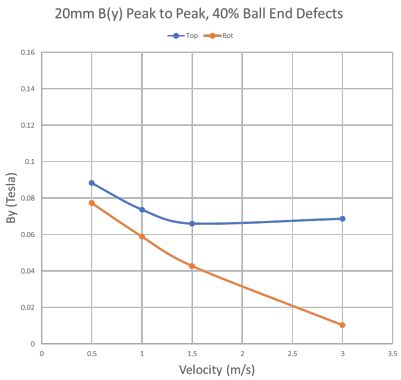

Fig. 14: B_Y peak to peak values for the 20 mm plate with a 40 % through wall defect indicates a consistent reduction of far surface peak to peak amplitude where the near surface flaw is amplified when increasing velocity from 1.5 to 3 m/s showing a separation between the two defects.

velocities to that of far surface flaws. This becomes significant on a 20 mm thick plate at 3 m/s resulting in an increased response of 0.069 T when compared to a velocity of 1.5 m/s with a value of 0.066 T resulting in a 4.55 % increase in the signal response. This increased leakage signal is caused by the flux concentrating at the near surface.

VII. Experimental Comparison

The practical comparison is performed using a variable speed controlled magnetic bridge of the same design used for the simulated results. A mild steel calibration plate of 15 mm nominal thickness is used with four machined spherical defects to represent simulated defects ranging from 20 % to 80 % through wall thickness. Two velocities of approximately 0.5 and 1 m/s are used. A Hall effect sensor array spanning 40 mm consisting of 8 elements is used to detect the leakage field. The experimental components are shown in Figure 15.

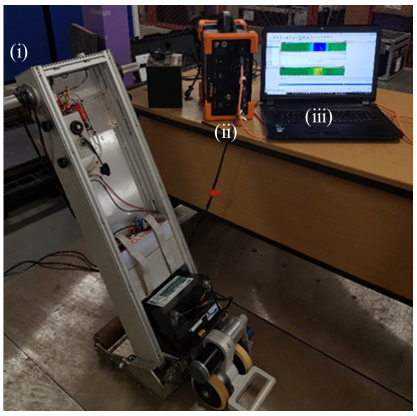

Fig. 15: Experimental set-up (i) Modified Floormap 3Di (FM3Di) with variable speed (ii) Eddyfi Ectane 2 multi-technology test instrument (iii) Eddyfi Magnifi data acquisition and analysis software.

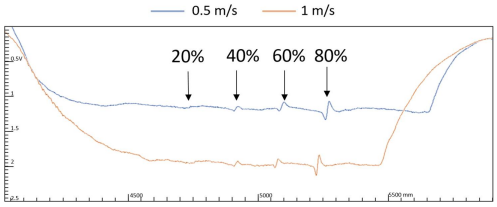

Fig. 16: Defect traces from bottom side defects on a 15 mm calibration plate at 0.5 and 1 m/s.

Figure 16 shows data obtained at the two velocities. For comparison with simulated results DC signal offsets and peak-to-peak values for the 40 % defects are extracted. These results are given in Tables I, II and III, along with an example of bottom surface results extracted from Figure 11.In practice the signal magnitude is represented in volts (V) and is directly proportional to the measured flux density in Tesla (T).

TABLE I: DC Offset Simulated and Experimental

Velocity (m/s)	Simulated (T)	Experimental (V)
0.5	-0.021	1.16
1	-0.035	1.95
% Increase	66.7	68.1

TABLE II: Peak-to-peak comparison of bottom surface defects

Velocity (m/s)	Simulated (T)	Experimental (V)
0.5	0.13	0.10
1	0.12	0.08
% Decrease	7.7	20

From the DC offset results it is clear that a high degree of correlation is present between the simulated and experimental results. The results for the peak-to-peak comparison, however, show a lesser correlation although the general direction is consistent for bottom surface defects. In table III for top surface defects a reduction in simulated amplitude is seen while the experimental data indicates an increased response with velocity. The key component influencing the discrepancy is the translation between 2D simulated and 3D real world defect geometries (i.e. slot type rather than spherical).

TABLE III: Peak-to-peak comparison of top surface defects

Velocity (m/s)	Simulated (T)	Experimental (V)
0.5	0.145	0.64
1	0.129	0.87
% Change	-11	35.9

VIII. Conclusion

In conclusion to this study a number of key findings have been noted:

- For the magnet assembly used a plate thickness of 6 mm is considered to be in saturation, all other plates above this thickness are not.
- As velocity is increased, the distribution of induced flux becomes focused to the near surface to the magnetiser resulting in an increased near surface response and a reduction in far surface signal magnitude. This is more apparent with increased plate thickness.
- A distortion in the distribution of flux throughout the plate is also seen, altering defect detection capabilities. The induced plate flux distribution is not linearly distributed across the plate thickness when velocity is introduced. Increasing the scanning velocity from 0.5 to 3 m/s results in a signal reduction of up to 53 % on a 16 mm plate with a far surface defect. This is reduced to 40 % for a near surface flaw with the same velocities and plate thickness of 16 mm.
- Magnetic saturation governs the speed at which an inspection can take place without significantly affecting results. When the plate being inspected is saturated inspection speeds can be increased up to 3 m/s while not significantly affecting the signal responses only the offset seen.
- At a velocity of 3 m/s, near surface defect responses are amplified on un-saturated plates. This is most evident in Figure 14 where a signal increase of 4.55 % is shown from 1.5 to 3 m/s.
- Similarly, this has the opposite effect on far surface flaws resulting in a reduction of signal responses on un-saturated plates. Again, this is most clear on the 20 mm plate where a signal reduction of 87 % is given from 0.5 to 3 m/s.
- An experimental comparison has been undertaken with results showing good correlation.

Future Work

Further work will expand on the analysis of velocity effects and the induced eddy currents in 3D. This will allow for further analysis of the distribution of flux across the width of the plate. This will aim to corroborate the practical results and identify trends and scaling factors considered in this paper. A full experimental analysis will be undertaken on a range of plate thicknesses from 6 to 20 mm in a subsequent paper.

Acknowledgement

The authors gratefully acknowledge funding from the Knowledge Economy Skills Scholarships (KESS 2) and Eddyfi (UK) Ltd. Knowledge Economy Skills Scholarships (KESS 2) is a pan-Wales higher level skills initiative led by Bangor University on behalf of the HE sector in Wales. It is part funded by the Welsh Governments European Social Fund (ESF) convergence programme for West Wales and the Valleys.

References

[1] N. Pearson, "Band-limitations and non-linearities of magnetic flux leakage in context of non-destructive testing," PhD thesis, Swansea University, 2014.

[2] Y. S. Sun, W. Lord, G. Katragadda, and Y. K. Shin, "Motion induced remote field eddy current effect in a magnetostatic non-destructive testing tool: A finite element prediction," *IEEE Transactions on Magnetics*, vol. 30, no. 5, pp. 3304–3307, Sep. 1994, ISSN: 0018-9464. DOI: 10.1109/20.312644.

[3] G. S. Park and S. H. Park, "Analysis of the velocity-induced eddy current in mfl type ndt," *IEEE Transactions on Magnetics*, vol. 40, no. 2, pp. 663–666, Mar. 2004, ISSN: 0018-9464. DOI: 10.1109/TMAG.2004.824717.

[4] Y. Li, G. Y. Tian, and S. Ward, "Numerical simulation on magnetic flux leakage evaluation at high speed," *NDT & E International*, vol. 39, no. 5, pp. 367–373, 2006, ISSN: 0963-8695. DOI: https://doi.org/10.1016/j.ndteint.2005.10.006.

[5] P. Wang, Y. Gao, G. Tian, and H. Wang, "Velocity effect analysis of dynamic magnetization in high speed magnetic flux leakage inspection," *NDT & E International*, vol. 64, pp. 7–12, 2014, ISSN: 0963-8695. DOI: https://doi.org/10.1016/j.ndteint.2014.02.001.

[6] D. Zhiye, R. Jiangjun, P. Ying, Y. Shifeng, Z. Yu, G. Yan, and L. Tianwei, "3-d fem simulation of velocity effects on magnetic flux leakage testing signals," *IEEE Transactions on Magnetics*, vol. 44, no. 6, pp. 1642–1645, Jun. 2008, ISSN: 0018-9464. DOI: 10.1109/TMAG.2007.915955.

[7] L. Zhang, F. Belblidia, I. Cameron, J. Sienz, M. Boat, and N. Pearson, "Influence of specimen velocity on the leakage signal in magnetic flux leakage type nondestructive testing," *Journal of Nondestructive Evaluation*, vol. 34, no. 2, p. 6, 2015.

[8] S. Lu, J. Feng, F. Li, and J. Liu, "Precise inversion for the reconstruction of arbitrary defect profiles considering velocity effect in magnetic flux leakage testing," *IEEE Transactions on Magnetics*, vol. 53, no. 4, pp. 1–12, Apr. 2017, ISSN: 0018-9464. DOI: 10.1109/TMAG.2016.2642887.

[9] *2d eddy current analysis guide*, Integrated Engineering Software, 220 - 1821 Wellington Avenue, Winnipeg, Manitoba, Canada R3H 0G4, 2015.

[10] N. Pearson, "Discrimination of top and bottom discontinuities with mfl and the surface topology air-gap reluctance system (stars)," 2012. DOI: https://www.silverwingndt.com/downloads/technical/Floormap3D_STARS.PDF.

[11] Y.-K. Shin, "Magnetic flux leakage inspection of moving steel sheets," in *Review of Progress in Quantitative Nondestructive Evaluation: Volume 15A*, D. O. Thompson and D. E. Chimenti, Eds. Boston, MA: Springer US, 1996, pp. 2249–2256, ISBN: 978-1-4613-0383-1. DOI: 10.1007/978-1-4613-0383-1_295.

[12] J. Simkin, "Modelling ferromagnetic materials for electromagnetic non-destructive evaluation of ferromagnetic materials," Houston, Texas, USA: Western Atlas Int. Inc, 1988, pp. 109–113.

Ashley Laurent Pullen received his BSc (Hons) in Automotive Engineering in 2014 and MSc with Distinction in Non-destructive Testing in 2015 from the University of Wales Trinity Saint David. Currently he is undertaking postgraduate research into the Magnetic Flux Leakage method as applied to Above Ground Storage Tank Floors.

Peter C. Charlton is currently Professor in Applied NDT at University of Wales Trinity Saint David. He has 30 years industrial and academic experience in the research and development of advanced automated electromagnetic and ultrasonic NDT imaging systems for the petrochemical, power generation and aerospace industries. He is responsible for engagement with key industrial partners and PhD and MSc research supervision within the School of Engineering.

Neil R. Pearson is the Principal Scientist at Eddyfi (UK) Ltd. Since graduating from Swansea University in 2003, he has been at the company researching and developing magnetic flux leakage (MFL) technology and automated ultrasonic testing products. Neil obtained his PhD in MFL technology in 2015 by presenting an approach to ascertain its capability for any given defect.

Nicola J. Whitehead is currently an Associate Professor in the School of Applied Computing at the University of Wales Trinity Saint David specialising in data visualisation and analysis. This has led to her working in a wide range of fields from human-computer interaction and usability to artificial intelligence and data mining. She leads the Schools usability research group and supervises PhD and MSc students in a range of data analysis fields.

DOI: 10.1784/insi.2020.62.2.73

Practical evaluation of velocity effects on the magnetic flux leakage technique for storage tank inspection

A L Pullen, P C Charlton, N R Pearson and N J Whitehead

Magnetic flux leakage (MFL) is a technique commonly used to inspect storage tank floors. This paper describes a practical evaluation of the effect of scanning velocity on defect detection in mild steel plates with thicknesses of 6 mm, 12 mm and 16 mm using a fixed permanent magnetic yoke. Each plate includes four semi-spherical defects ranging from 20% to 80% through-wall thickness. It was found that scanning velocity has a direct effect on defect characterisation due to the distorted magnetic field resulting from induced eddy currents that affect the MFL signal amplitude. This occurs when the inspection velocity is increased and a reduction in the MFL signal amplitudes is observed for far-surface defects. The opposite applies for the top surface, where an increase is seen for near-surface MFL amplitudes when there is insufficient flux saturating the inspection material due to the concentration of induced flux near the top surface. These findings suggest that procedures should be altered to minimise these effects based on inspection requirements. For thicker plates and when far-surface defects are of interest, inspection speeds should be reduced. If only near-surface defects are being considered then increased speeds can be used, provided that the sensor range is sufficient to cope with the increased signal amplitudes so that signal clipping does not become an issue.

1. Introduction

Magnetic flux leakage (MFL) is a non-destructive testing (NDT) method that is commonly used to ascertain the integrity of storage tank floors by mapping discontinuities. The advantage of MFL over other techniques is its capability to scan large areas rapidly. This is a desirable trait for storage tank inspection as tanks must be taken out of service to gain access, which involves an emptying and cleaning process. With the advantage of rapid inspection comes the disadvantage of magnetic field alterations with induced eddy currents that are exaggerated by increased scanning velocity.

MFL inspection is affected by a number of parameters, including saturation, scanning velocity, sensor position, variation in inspection material and defect orientation. These factors combined allow for a range of optimal settings for different combinations of plate thickness, scanning velocity and specific defect detection. The magnetisation level of the specimen is not adjustable with a fixed permanent magnet bridge and, therefore, saturation is limited by specimen thickness. Magnetically saturating a specimen allows for smaller flaws to be detected, although the level of saturation may change due to the non-homogeneous nature of mild steel among other non-system-related parameters. The ratio between the induced and the supplied magnetic field describes the magnetisation level of a specimen. This ratio can be shown in the form of a B-H curve. The inspection velocity has a direct effect on defect detectability depending on its orientation (top/bottom surface) and size, as previously published by the authors[1] in the form of simulated results backed up by practical validation. Here, it was found that when inspection velocity is increased the induced magnetic flux is unevenly distributed, resulting in a concentration to the top surface of the specimen when in a non-saturated state. This concentration to the top surface results in an amplitude increase from the same defect geometry but at a higher velocity. Similarly, the opposite occurs for a bottom-side defect decreasing in magnitude.

Submitted 05.06.19 / Accepted 14.10.19

Ashley Laurent Pullen is with the University of Wales Trinity Saint David, Waterfront Campus, Island Road, Swansea SA1 8EW, Wales, UK. He received a BSc (Hons) in automotive engineering in 2014 and an MSc with distinction in non-destructive testing (NDT) in 2015 from the university. He is currently undertaking postgraduate research into the magnetic flux leakage (MFL) method as applied to above-ground storage tank floors.

Peter C Charlton is currently a Professor in applied NDT at the University of Wales Trinity Saint David, Waterfront Campus, Island Road, Swansea SA1 8EW, Wales, UK. He has 30 years' industrial and academic experience in the research and development of advanced automated electromagnetic and ultrasonic NDT imaging systems for the petrochemical, power generation and aerospace industries. He is responsible for engagement with key industrial partners and PhD and MSc research supervision within the School of Engineering.

Neil R Pearson is the Principal Scientist at Eddyfi Technologies, Clos Llyn Cwm, Swansea Enterprise Park, Swansea SA6 8QY, Wales, UK. Since graduating from Swansea University in 2003 he has been at the company researching and developing MFL technology and automated ultrasonic testing products. He obtained a PhD in MFL technology in 2015 by presenting an approach to ascertain its capability for any given defect.

Nicola J Whitehead is currently an Associate Professor with the School of Applied Computing at the University of Wales Trinity Saint David, Waterfront Campus, Island Road, Swansea SA1 8EW, Wales, UK, specialising in data visualisation and analysis. This has led to her working in a wide range of fields, from human-computer interaction and usability to artificial intelligence and data mining. She leads the School's usability research group and supervises PhD and MSc students in a range of data analysis fields.

Taking this into consideration, the state of saturation of a specimen during inspection governs the ideal inspection speed. This paper focuses on the practical evaluation of such effects in greater depth to investigate the severity of the effects of velocity during an inspection. A simulated example of the impact that velocity has on the distribution of flux can be seen in Figure 1.

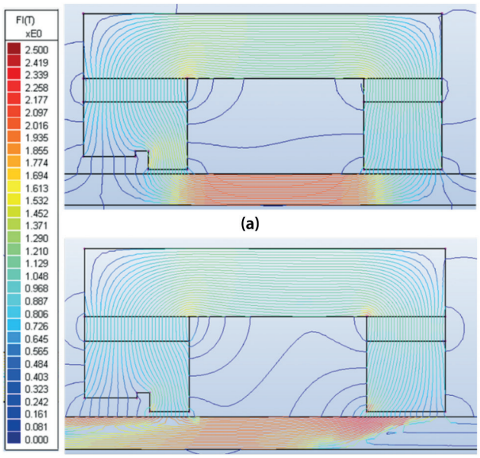

Figure 1. Two cases with an extreme thickness of 100 mm: (a) the static case scenario results in a somewhat uniform distribution of flux with a slight concentration nearer to the top surface; and (b) the results when a velocity of 3 m/s is taken into consideration[1]

Plate thicknesses of 6 mm, 12 mm and 16 mm are tested, each containing four machined flaws on each plate of 20% to 80% relative depths in 20% increments through the plate thickness. Results are given for both top- and bottom-orientated defects, with three different velocities per plate. It is commonly stated that when using a permanent magnet system to detect the leakage field from a ferrous material, increasing the scanning velocity leads to a decrease in the detected signal amplitude[2-4]. It has also been reported that increasing velocity amplifies the signals from such an inspection[5]. In a previous paper written by the authors[1], it was shown that both of these conditions are relevant and the reasons for why this occurs were explored through simulation. This paper provides practical validation, showing why both statements from[2-4] and[5] are correct under different circumstances.

2. Practical set-up

2.1 Plate thickness

Plate thickness has a direct effect on the magnetisation level within the plate. As the permanent magnet assembly of the commercial system used supplies enough flux to saturate plates with a thickness of up to 8 mm, an increase in plate thickness beyond this will result in a lower induced flux density. The result of this is a reduction in B as only a fixed amount of H can be applied by the permanent magnet assembly. In practical terms, this is constantly changing due to the manufacturing tolerances of mild steel plates altering in thickness engineered with a tolerance of ±0.3 mm together with the non-homogeneous composition of the material. The experimental work presented here utilised plate thicknesses of 6 mm, 12 mm and 16 mm. The plate thicknesses of 6 mm and 12 mm used in these experiments cover the range typically seen within the main section of storage tank floors, while the 16 mm plate represents the annular sections of the storage tanks, which are generally thicker to support the shell.

2.2 Defect characterisation

The defects considered in this paper are known spherical shapes bored with a 22 mm ball end cutter. These mimic corrosion at the specified depths of 20%, 40%, 60% and 80% through-wall thickness, as recommended in the UK Health and Safety Executive (HSE) 'Recommended practice for magnetic flux leakage inspection of atmospheric storage tank floors'[6]. The orientation of the defect (top side/bottom side) plays a significant role in defect detection and the shape of the corresponding signal responses is also considered.

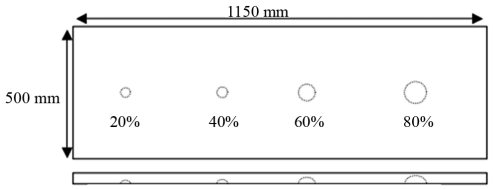

Figure 2. A typical calibration plate as recommended in[6]

2.3 Velocity

In the previous paper written by the authors[1], it was shown that the relative velocity difference between the plate and a permanent magnetic yoke causes eddy currents to be introduced, leading to a reduction in the applied magnetic field. This also influences the distribution of flux within the inspected material, resulting in changes to signal amplitudes. The net result is that the flux concentrates towards the near surface, leading to an increased signal response from near-surface defects as velocity increases, as shown earlier in Figure 1. The opposite happens for far-surface flaws, where a reduction in signal amplitude is seen due to the distribution concentrating nearer to the top surface again when saturation is no longer achieved. Plate thicknesses of 6 mm, 12 mm and 16 mm are tested at three velocities: slow (0.51-0.57 m/s); medium (0.74-1 m/s); and fast (0.95-1.25 m/s). The inspection velocity varies slightly as a function of plate thickness and is therefore specific to each plate.

2.4 Sensor position

The positioning of sensors is frequently noted as affecting defect characterisation in MFL applications. The sensor position for this experiment remains in the centre of the magnet bridge at a fixed height of 0.5 mm above the inspection surface. This is then secured within a 3D printed probe holder, as shown in Figure 3, where (a) is the probe holder and (b) is the array of Hall-effect sensors mounted between the magnetic poles. It has been suggested in other studies[7] that sensors should be offset opposite to the direction of travel. The sensor array being positioned centrally helps to minimise the interference of stray leakage fields from the magnet assembly with the Hall-effect sensors. It is also fixed in this position as the literature suggests that there is an optimal position for a given velocity. As the velocity varies between plate thicknesses, a different optimal position would be needed for each case. Taking this into consideration, it was decided to remove this as a variable and fix the position of the sensor to ensure the same point of interest was used for all measurements taken.

Figure 3. The sensor array in a 3D printed housing designed to give a lift-off of 0.5 mm, where: (a) is the 3D printed housing; and (b) is the array of eight 5 mV/G Hall-effect sensors

2.5 Data acquisition system

The experimental equipment is shown in Figure 4. A modified Silverwing Floormap 3Di (FM3Di) with variable speed is used during this test procedure. The system has been stripped back to a functional shell where all data capture is undertaken externally using Eddyfi Technologies' surface array and tube inspection test instrument, Eddyfi Ectane 2, coupled with Magnifi capture software. The sensor array consists of eight 5 mV/G Hall-effect sensors spanning 40 mm and positioned at a height of 0.5 mm above the inspection surface. The system uses an incremental encoder that produces a spatial resolution of 1 mm in the scan direction.

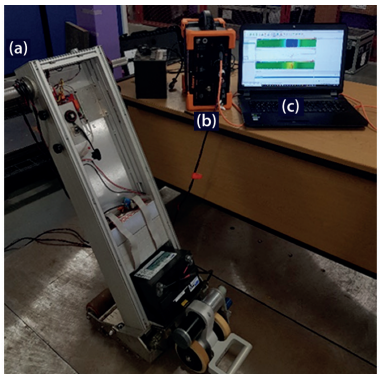

Figure 4. Experimental equipment: (a) modified Floormap 3Di (FM3Di); (b) Ectane 2; and (c) Magnifi data acquisition and analysis software and mild steel calibration plates with relative defect depths

2.5.1 *Data acquisition signal scaling*

The signal processing chain of the system is shown in Figure 5. As the data acquired is in the form of ADC values, reverse signal scaling is required to obtain flux density. An example dataset can be seen in Figure 6 with an eight-channel overlay, where each sensor is considered as a separate data channel. The left *Y*-axis shows the raw ADC values and the right *Y*-axis shows the values in T after the conversion to B has taken place. The process of converting the signal back to its raw format is given in Equations (1) and (2):

$$G_{dB} = 20\log_{10}\frac{V_{Amp}}{V_{HE}} \quad \text{..... (1)}$$

where G_{dB}, V_{Amp} and V_{HE} are the signal amplification applied in dB, the signal voltage after gain is applied and the voltage from the Hall-effect sensor before gain alteration, respectively. As the gain is fixed to 23 dB by the preamplifier of the system and the amplified signal voltage is a known factor, it is possible to convert the amplified data to its unamplified state using Equation (2):

$$V_{HE} = \frac{V_{Amp}}{10^{1.15}} \quad \text{..... (2)}$$

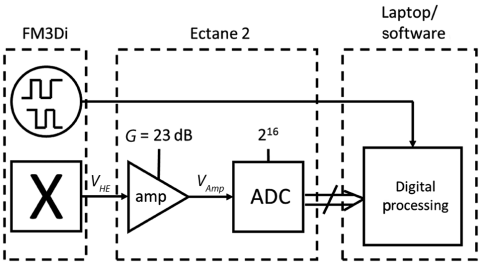

Figure 5. Illustration of the signal processing chain

This value may then be converted into gauss as the Hall-effect transfer function of 5 mV/G is known. The value for gauss is then divided by 10,000 to complete the conversion to T. Once scaling of the data is complete, the channel with the highest peak-to-peak (pk-pk) value is then recorded. Five independent scans are performed over each defect at each velocity and each plate thickness, allowing for an average pk-pk value to be calculated from five samples per defect. This is executed for both defect orientations.

3. Results and analysis

Figure 6 shows example data of a complete scan for plate thicknesses of 6 mm, 12 mm and 16 mm for bottom-side defects. It should be noted that there is an order of magnitude difference between the B values for Figures 6(a), 6(b) and 6(c), captured at velocities of 0.57, 0.51 and 0.52 m/s, respectively. In Figure 6(a), the sensor array has a consistent offset value where no defects are encountered, whereas plate thicknesses of 12 mm and 16 mm see a shift in offset at the start of the trace where the system is accelerating. In Figure 6, it is evident that each sensor channel has a difference in offset due to the lateral positioning of the sensor across the magnet yoke. The 6 mm plate has minimum offset, whereas plate thicknesses of 12 mm and above have a separation of 0.2 mT at the lowest velocities for each plate thickness. This leads to an apparent broadening of the resulting trace and the difference in offset between channels can be used to identify the relative saturation level of the inspection plate. The lower the saturation level of the plate, the wider spread the offsets between the sensors. Additionally, it is also noted that increasing plate thickness results in an increase in the mean DC signal offset due to levels of induced eddy currents resulting in the reduction of defect signal magnitude.

The data comparison of Section 3 utilises the channel with the maximum peak-to-peak value per defect to account for scanning drift. This also indicates the channel/sensor that is central to the defect providing the highest signal amplitude achievable. This process is repeated for five scans and an average is then taken of the highest peak-to-peak amplitudes for each defect.

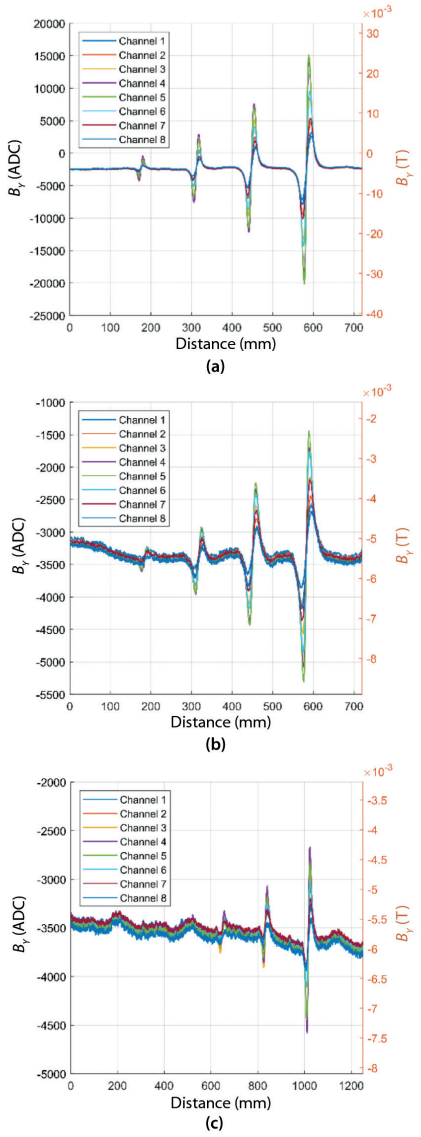

Figure 6. An example of a defect trace is shown for each plate thickness for bottom-side defects, along with the converted data range from ADC to B_y (T) as separate axes, where (a), (b) and (c) are the plate thicknesses of 6 mm, 12 mm and 16 mm at the minimum velocities of 0.57 m/s, 0.51 m/s and 0.52 m/s, respectively (note the scale difference between the *Y*-axes)

3.1 6 mm plate thickness

The data in Figure 7 and Table 1 show the pk-pk amplitudes generated by both top- and bottom-surface defects for a plate thickness of 6 mm at inspection velocities of 0.57 m/s, 1 m/s and 1.25 m/s. In Figures 7(a) and 7(b), the separation between the pk-pk values due to velocity is largest for the bottom-side 80% defect, giving a difference of 3.8334×10^{-3} T and resulting in a reduction of −6.82% for a velocity increase of 0.68 m/s. It can also be noted that all signal responses see a reduction in amplitude when the inspection speed is increased above 0.57 m/s. This lack of separation between defects and the reduction of amplitude are indicative of a magnetically saturated material.

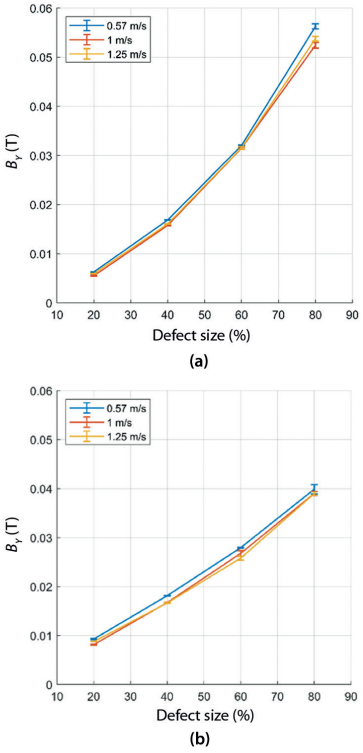

Figure 7. Average pk-pk values for a 6 mm calibration plate with both: (a) top-surface defects; and (b) bottom-surface defects

Table 1. pk-pk comparison of top- and bottom-surface defects at the three scanning velocities for a plate thickness of 6 mm

Velocity (m s^{-1})	Defect (%)	pk-pk top (mT)	pk-pk bottom (mT)
0.57	20	9.2608	6.2665
	40	18.1225	16.8317
	60	27.9355	32.0146
	80	39.8631	56.2401
1	20	8.116	5.496
	40	16.7206	15.7568
	60	26.766	31.492
	80	39.003	52.4067
1.25	20	8.7513	5.9186
	40	16.6604	16.0373
	60	25.7806	31.524
	80	38.9877	53.7309

In all cases, larger defects result in larger pk-pk amplitudes. For the 20% defect it can be seen that the pk-pk amplitude is greater for the top surface-orientated defect than is seen for the bottom-surface defect. The 40% defects have similar pk-pk amplitudes with only a 0.62313×10^{-3} difference between top- and bottom-surface defects at 1.25 m/s, showing a decrease of −3.74%. When a 60% defect is scanned, the bottom-surface signal becomes larger than that from the top surface. This observation has been made previously by Charlton[8]. This also applies for the 80% defect, resulting in a significantly higher amplitude of up to 56.2401×10^{-3} T, which is 1.41 times greater than the largest top-surface pk-pk amplitude.

3.2 12 mm plate thickness

In this section, the results for a plate thickness of 12 mm are given, together with how the distribution of the flux is affected by velocity and how this can, in turn, affect defect sensitivity. When higher velocities are used, a shift in flux concentration is observed within the plate. This shows that an almost linear distribution of flux is achieved in the static case. When a velocity of 3 m/s is applied a shift in the distribution of flux is seen. Here, the majority of flux is concentrated to the near surface of the specimen, reducing in magnitude towards the bottom surface.

In practice, this shift takes place on smaller plate thicknesses than that of 2D simulation, due to the assumption that the magnet assembly and plate are identical in depth. The shift towards the near surface, resulting in an increased flux density in this region, is more evident on larger plate thicknesses, resulting in an amplification of top-surface defects and making them easier to detect. The opposite effect occurs with bottom-surface defects. Here, a reduction in signal amplitude is encountered as the inspection velocity is increased due to the decrease in flux density in the lower part of the plate where the defect is situated. An increase of 0.6834×10^{-3} T or 7.63% is indicated for the 60% top-surface defect with an increase in velocity of 0.44 m/s, as seen in Figure 8(a).The bottom-side defect shows a reduction of 0.6669×10^{-3} T or −18.96%, with the same change in velocity as seen in Figure 8(b).

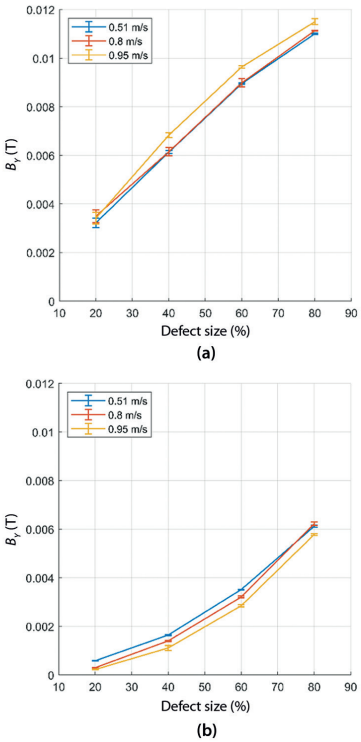

Figure 8. Average peak-to-peak values for a 12 mm calibration plate with both: (a) top-surface defects; and (b) bottom-surface defects

Table 2. pk-pk comparison of top- and bottom-surface defects at the three scanning velocities for a plate thickness of 12 mm

Velocity (m s^{-1})	Defect (%)	pk-pk top (mT)	pk-pk bottom (mT)
0.51	20	3.2255	0.5878
	40	6.1398	1.6439
	60	8.9563	3.5138
	80	11.0044	6.1188
0.8	20	3.4966	0.3009
	40	6.1489	1.4065
	60	8.9848	3.2084
	80	11.1337	6.2221
0.95	20	3.4111	0.2244
	40	6.8374	1.1127
	60	9.6397	2.8473
	80	11.4989	5.7787

3.3 16 mm plate thickness

The results for a plate thickness of 16 mm are shown in Figures 9(a) and 9(b). It is clearly demonstrated that the flux distribution within the 16 mm plate changes with velocity. An increase of 1.8193×10^{-3} T with a percentage increase of 20.89% is seen in the pk-pk amplitudes for an 80% top-surface defect with a change in velocity of 0.59 ms. Also, a decrease of 0.6535×10^{-3} T with a percentage decrease of −21.94% is seen in the pk-pk amplitude for the 80% bottom-surface defect.

Table 3. pk-pk comparison of top- and bottom-surface defects for a plate thickness of 16 mm at the three scanning velocities. A dash is used to indicate that no significant signal has been detected

Velocity (m s^{-1})	Defect (%)	pk-pk top (mT)	pk-pk bottom (mT)
0.52	20	3.9069	–
	40	6.0543	0.6088
	60	7.626	1.2002
	80	8.7109	2.9791
0.74	20	4.68711	–
	40	6.9352	0.2915
	60	8.821	0.7552
	80	9.8204	2.2828
1.11	20	4.8603	–
	40	7.4903	0.2914
	60	9.5389	0.6943
	80	10.5302	2.3256

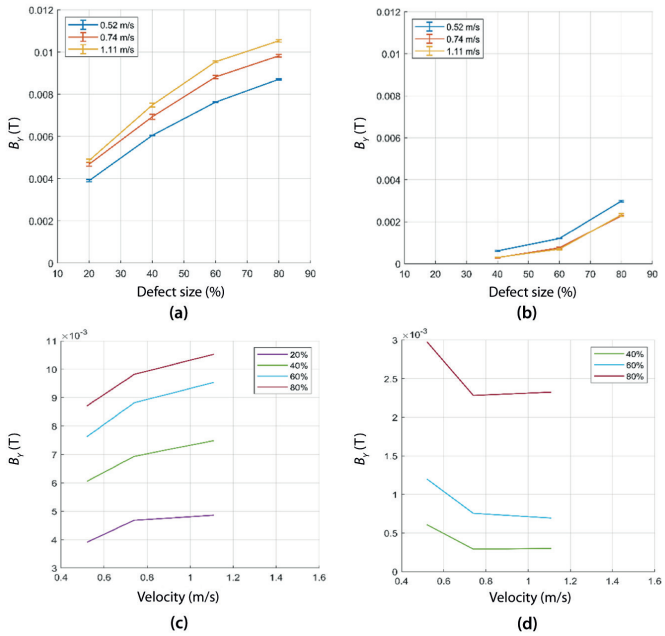

Figure 9. 16 mm pk-pk amplitudes of bottom-surface defects shown as a function of: (a)-(b) defect size; and (c)-(d) velocity

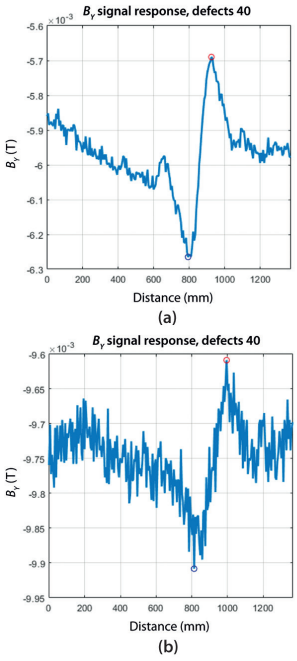

Figure 10. Showing two traces of a 40% through-wall thickness defect on the bottom side of the plate at: (a) 0.52 m/s; and (b) 1.11m/s (note the difference in *Y*-axis scaling)

The bottom-side defects have noticeably lower pk-pk amplitudes than the defects on the top surface. The 20% top-surface defect has a larger pk-pk amplitude than that of the 80% bottom-surface defect. This is due to a lack of flux penetrating through to the far surface and an insufficient flux density within the lower part of the inspection material. The 20% bottom-side defect becomes undetectable as the signal is lost within background noise. An example of how increasing velocity affects the detectability of bottom-side defects is shown in Figure 10, where a signal trace is given for two velocities, 0.52 m/s and 1.11 m/s, respectively, to highlight the increase in the signal-to-noise ratio (SNR). From Figures 10(a) and 10(b), it can be seen that there is a reduction in peak-to-peak amplitude when the velocity increases from 0.52 m/s to 1.11 m/s. This is also accompanied by an increase in signal offset.

3.4 DC offset

The resulting sensor DC offsets due to velocity are presented in Figure 11. These values are obtained by averaging a portion of the acquired data for each scan where the offset is at its most consistent in a defect-free region. This is carried out for the three speeds and plates as previously stated. These results indicate that the DC offset increases negatively when the inspection velocity is increased for this particular set-up. The results are given in tabular form in Table 4.

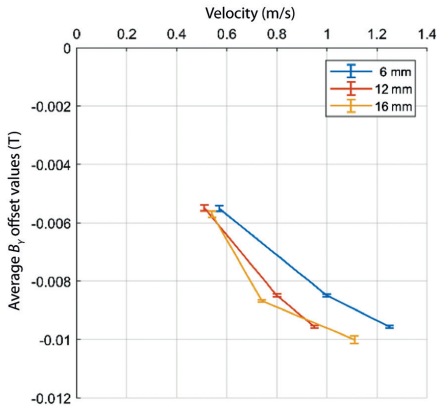

Figure 11. Average offset values as a function of velocity are shown at the three plate thicknesses of 6 mm, 12 mm and 16 mm

The DC offset values displayed indicate that an increase in inspection velocity results in an increase in the magnitude of the DC offset.

Table 4. DC offset values of plate thicknesses of 6 mm, 12 mm and 16 mm at the stated velocities

Plate thickness (mm)	Velocity (m s^{-1})	Offset (mT)
6	0.57	−5.5125
	1	−8.4922
	1.25	−9.5667
12	0.51	−5.489
	0.8	−8.4905
	0.95	−9.5657
16	0.52	−5.6988
	0.74	−8.6735
	1.11	−10.0065

3.5 Acceleration effects

When the system is accelerated to a constant inspection velocity, there is a continual change in the Hall-effect sensor reading from static to the point at which a constant velocity is achieved. This change in offset is dependent upon the velocity achieved. Therefore, the rate of change is the acceleration of the system. During this inspection the acquired data is encoded with respect to distance rather than in the time domain. Taking this into consideration, it is only possible to estimate the acceleration of the system, assuming it is constant, using Equation (3):

$$a = \frac{v^2 - u^2}{2s} \quad \text{(3)}$$

where a is the acceleration m/s^2, v is the final scanning velocity in m/s, u is the initial velocity (zero) in m/s and s is the displacement/distance travelled in m.

Figure 12 is a full scan trace for a plate thickness of 16 mm at 0.74 m/s. The points at which the acceleration values are taken are labelled as A at the 0 point and B at the point where a near constant velocity is achieved, with the results for all plate thicknesses shown in Table 5.

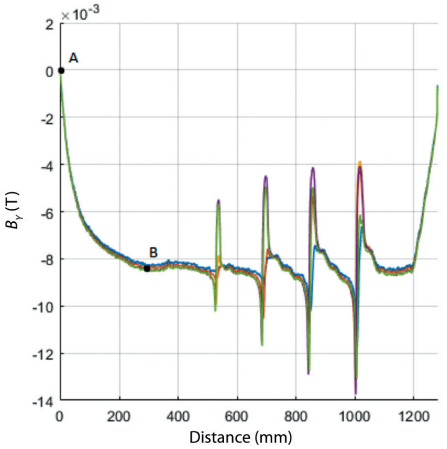

Figure 12. 16 mm acceleration from the start (A) and the point at which a constant velocity is achieved (B) across all eight channels

Table 5. Acceleration values for plate thicknesses of 12 mm and 16 mm

Plate thickness (mm)	Velocity (m s^{-1})	Distance (m)	Acceleration (m s^{-2})
12	0.51	0.124	1.049
	0.8	0.177	1.808
	0.95	0.211	2.139
16	0.52	0.13	1.04
	0.74	0.27	1.014
	1.11	0.298	2.067

For a plate thickness of 6 mm there is no significant change in the offset as the system is accelerated due to the high levels of B within the plate. During the acceleration phase it is likely that signal responses from defects will become altered and be characterised differently to those at a constant velocity.

3.5.1 *Deceleration*

Once the motor is disabled at the end of a scan, there is a period where the system is decelerating to a complete stop. This deceleration phase will also affect the total scan distance and potentially alter the response from a flaw. The deceleration values are given in Table 6, indicating that the lower plate thickness of 12 mm achieves greater deceleration values than that of the 16 mm plate.

Table 6. Deceleration values for plate thicknesses of 12 mm and 16 mm

Plate thickness (mm)	Velocity (m s^{-1})	Distance (m)	Deceleration (m s^{-2})
12	0.51	0.052	−2.6
	0.8	0.087	−3.147
	0.95	0.11	−5.6
16	0.52	0.053	−2.454
	0.74	0.088	−3.636
	1.11	0.114	−3.958

4. Conclusions

The main findings from the work presented are:

- Inspection speed can impact the minimum required reporting threshold. Both of these factors are determined by the capability of the magnet to magnetically saturate a plate. For the permanent magnet-based system used, a plate thickness of 12 mm and thicker should be scanned at the lowest speed possible (plate dependent) to increase the likelihood of bottom-surface defect detection. If the top surface is of interest, then inspection speeds may be increased to allow for a higher sensitivity.
- When analysing the full scan traces in Figures 6(a) to 6(c) it was found that a plate thickness of 6 mm has consistent offsets across the sensor range at the same speed, whereas plate thicknesses of 12 mm and 16 mm show a spread of offset values across the eight channels, becoming greater with increased plate thickness. This suggests that the smaller spread is due to the saturated material. When the spread of the channels increases, this is an indication that the material is undersaturated.
- A system with controllable speed is desirable for a more accurate comparison between velocities and to keep the speeds at

which tests are completed consistent. The resistance to motion varies with plate thickness and velocity due to the induced eddy currents. The maximum drive force is limited by the constant voltage supplied to the drive motor. Taking this into consideration, the tests are completed at three selected stages of the available voltage supply: minimum, half and maximum; therefore, the velocity is not directly controlled as a function of speed. A system where the velocity is consistent between plates regardless of thickness is desirable.

- During an MFL inspection, the acceleration and deceleration phase can affect the ability of the system to detect and characterise flaws. A more accurate method of calculating the acceleration/deceleration value at a given point is desired when a defect is present, to measure the impact that the acceleration/deceleration has on defect characterisation.

5. Future work

Further work will focus on 3D finite element analysis (FEA) investigation into the effects of velocity on the flux distribution underneath the magnet assembly. This is a point of interest, as the results presented in this paper suggest that the flux distribution underneath the magnet is uneven. This is seen across the lateral sensors, which indicate a change in offset across the width of the assembly. The effect that velocity and plate thickness have on this will be investigated. The distortion of the wake effect is also of interest, in particular how these changes apply laterally in 3D when velocity is introduced. Further analysis will look at the effect of the acceleration and deceleration phases on the characterisation of defects.

Acknowledgements

The authors gratefully acknowledge funding from the Knowledge Economy Skills Scholarships (KESS 2) and Eddyfi (UK) Ltd. KESS 2 is a pan-Wales higher level skills initiative led by Bangor University on behalf of the higher education sector in Wales. It is part funded by the Welsh Government's European Social Fund (ESF) convergence programme for West Wales and the Valleys.

References

1. A L Pullen, P C Charlton, N R Pearson and N J Whitehead, 'Magnetic flux leakage scanning velocities for tank floor inspection', IEEE Transactions on Magnetics, Vol 54, No 9, pp 1-8, September 2018.
2. Y S Sun, W Lord, G Katragadda and Y K Shin, 'Motion-induced remote field eddy current effect in a magnetostatic non-destructive testing tool: a finite element prediction', IEEE Transactions on Magnetics, Vol 30, No 5, pp 3304-3307, September 1994.
3. G S Park and S H Park, 'Analysis of the velocity-induced eddy current in MFL-type NDT', IEEE Transactions on Magnetics, Vol 40, No 2, pp 663-666, March 2004.
4. Y Li, G Y Tian and S Ward, 'Numerical simulation on magnetic flux leakage evaluation at high speed', NDT&E International, Vol 39, No 5, pp 367-373, 2006.
5. P Wang, Y Gao, G Tian and H Wang, 'Velocity effect analysis of dynamic magnetisation in high-speed magnetic flux leakage inspection', NDT&E International, Vol 64, pp 7-12, 2014.
6. N B Cameron, 'Recommended practice for magnetic flux leakage inspection of atmospheric storage tank floors', Mitsui Babcock Energy Limited, 2006.
7. L Zhang, F Belblidia, I Cameron, J Sienz, M Boat and N Pearson, 'Influence of specimen velocity on the leakage signal in magnetic flux leakage-type non-destructive testing', Journal of Nondestructive Evaluation, Vol 34, No 2, p 6, 2015.
8. P C Charlton, 'A theoretical and experimental study of the magnetic flux leakage method for the analysis of corrosion defects in carbon steel plate', University of the West of England, Swansea Institute of Higher Education, 1995.

Simulation Data Summary Table

Table 8.1: Table providing the complete set of simulated B_Y peak-to-peak results.

		Top				Bottom			
		0.5m/s	1m/s	1.5m/s	3m/s	0.5m/s	1m/s	1.5m/s	3m/s
6mm	20%	0.089602096	0.093264823	0.092500329	0.085051078	0.086084	0.083519	0.082892	0.084108
	40%	0.180832701	0.180556527	0.186366924	0.192378334	0.207353	0.206313	0.197821	0.197481
	60%	0.273582034	0.277884566	0.274662075	0.274722999	0.315777	0.318322	0.320672	0.307652
	80%	0.343997622	0.345245581	0.341549818	0.337926424	0.426691	0.426852	0.420794	0.405933
8mm	20%	0.098981977	0.101683477	0.099576761	0.089796266	0.089497	0.084678	0.085624	0.081846
	40%	0.203275547	0.200725293	0.200020488	0.189944632	0.215419	0.213309	0.210827	0.197779
	60%	0.301808744	0.297794561	0.287643812	0.280116172	0.332693	0.331209	0.33162	0.312953
	80%	0.365461466	0.364993375	0.350195803	0.346283969	0.435599	0.430841	0.424564	0.411342
10mm	20%	0.100622162	0.10001746	0.090978776	0.083995794	0.08328	0.079986	0.07856	0.069387
	40%	0.204491681	0.202058309	0.19547023	0.171766436	0.208367	0.204575	0.200987	0.17668
	60%	0.304609875	0.287742319	0.290192013	0.263874533	0.328192	0.323102	0.307431	0.286706
	80%	0.362371997	0.350037644	0.35589241	0.331059455	0.428372	0.42667	0.41998	0.387803
12mm	20%	0.086726893	0.08551692	0.080740043	0.063328237	0.074598	0.070291	0.066783	0.045695
	40%	0.193791925	0.189672351	0.176589658	0.1476697	0.204492	0.202058	0.19547	0.171766
	60%	0.275324133	0.265933591	0.253576962	0.232592356	0.295294	0.288284	0.278941	0.253995
	80%	0.345198736	0.341479441	0.336597596	0.315755729	0.407316	0.397593	0.397524	0.374362
14mm	20%	0.077292236	0.070971268	0.064032601	0.045326346	0.060551	0.055833	0.048534	0.01876
	40%	0.17262327	0.160686132	0.146774195	0.117480465	0.168673	0.15325	0.141078	0.102324
	60%	0.254327837	0.244401091	0.230259031	0.202985908	0.272328	0.266529	0.255477	0.220231
	80%	0.333629108	0.329389539	0.317620797	0.305426639	0.386435	0.38209	0.377087	0.352341
16mm	20%	0.061187705	0.051917677	0.044198438	0.041277185	0.045697	0.036487	0.024928	0.003962
	40%	0.145444885	0.129512365	0.115188886	0.086591217	0.133687	0.120863	0.105948	0.062746
	60%	0.231514444	0.223687321	0.215815842	0.187513303	0.236986	0.224473	0.217393	0.1769
	80%	0.305950143	0.310397642	0.3130211	0.297306353	0.363791	0.361142	0.353399	0.321531
20mm	20%	0.025588566	0.026863389	0.033679206	0.054707047	0.01392	0.00526	0.002647	0.003388
	40%	0.088265318	0.073716502	0.066079156	0.068713112	0.077177	0.058823	0.042715	0.010249
	60%	0.179401084	0.168127755	0.162192943	0.140530159	0.185271	0.173082	0.155039	0.110834
	80%	0.311185184	0.293310918	0.287621967	0.266821236	0.318119	0.31364	0.31014	0.277791

Matlab Code

```
%% Delete data stuff

close all
clear all
format shortEng
% Variables to Change
defect_size = [20 40 60 80]; % Defect wall loss
ratio = 1.6; % Encoder Correction Ratio
file_name = '6mm top_%d.csv';% Change the name (Keep %d in place of changing
number)


%% Number of scans/files
sample_size = 5;

%% Gain correction formula and checks
    gain = 23;
    output = 3.74;
    correlation_factor = 3.74/12231;
    sensor_mv_gauss = 5*10^-3;
    gain_corrected_input = (output)/(10^(gain/20));
    B_gauss = gain_corrected_input/sensor_mv_gauss;

    B_Tesla = B_gauss/10000;

    gauss2tesla = gain_corrected_input/10000;


   for i = 1:15

  %%File load and data correction
    file = sprintf(file_name,i);
    data = csvread(file);
    data = data(:,any(data));
    data = data(:,2:end);
    data = data*(correlation_factor);
    data = data*gain_corrected_input;
    data = data/sensor_mv_gauss;
    data = data/10000;
    data_defects = data;


    colu = length(data(1,:));
    dist = colu/ratio;

    minimum_20 = min(min(data_defects(:,300:450)));
    [row_20,col_20]=find(data_defects==minimum_20);


    minimum_40 = min(min(data_defects(:,400:700)));
    [row_40,col_40]=find(data_defects==minimum_40);

    minimum_60 = min(min(data_defects(:,650:850)));
    [row_60,col_60]=find(data_defects==minimum_60);
```

```
     minimum_80 = min(min(data_defects(:,900:1050)));
    [row_80,col_80]=find(data_defects==minimum_80);



  %%%%%%%
  figure
  plot_data_all = data(:,250:1020);

    line = linspace(0,dist,length(plot_data_all));

hold on
plot(line,plot_data_all,'LineWidth', 1)
hold off
title(sprintf('B_Y Signal Response, Scan %d',i))
    xlabel('Distance [mm]')
    ylabel('B_Y (Tesla)')
    xlim([0,line(end)])
    grid on
    axis square



%20%
     figure

  data_defects = data(row_20(1),250:500);
     line = linspace(0,dist,length(data_defects));
     plot(line,data_defects,'LineWidth', 2)
          title(sprintf('B_Y Signal Response, Defects 20'))
    xlabel('Distance [mm]')
    ylabel('B_Y (Tesla)')
    xlim([0,line(end)])
    grid on
    axis square

    smoothed = smooth(data_defects,0.001,'lowess');
    [pks, loc]=findpeaks(smoothed, line,'MinPeakProminence',0.001); %play
with these numbers for peak 2peak)

     data_inv = -smoothed;

    [troughs, loc_t]=findpeaks(data_inv, line,'MinPeakProminence',0.001 );

    pks_20 = pks;
    troughs_20 = troughs;

     hold on
    plot(loc, pks,'or')
    plot(loc_t, -troughs, 'ob')
    hold off

   %% 40%
```

```
        figure
  data_defects = data(row_40(1),500:650);
     line = linspace(0,dist,length(data_defects));
    plot(line,data_defects,'LineWidth', 2)
              title(sprintf('B_Y Signal Response, Defects 40'))
    xlabel('Distance [mm]')
    ylabel('B_Y (Tesla)')
    xlim([0,line(end)])
    grid on
    axis square

        smoothed = smooth(data_defects,0.001,'lowess');
        %smoothed_2 = smooth(data_defects(2,:),0.002,'lowess');
    [pks, loc]=findpeaks(smoothed, line,'MinPeakProminence',0.001);
     data_inv_1 = -smoothed;


    [troughs, loc_t]=findpeaks(data_inv_1, line,'MinPeakProminence',0.001 );

        pks_40 = pks;
    troughs_40 = troughs;


    hold on
    plot(loc, pks,'or')
    plot(loc_t, -troughs, 'ob')
    hold off

    % 60%
           figure

  data_defects = data(row_60(1),650:850);
     line = linspace(0,dist,length(data_defects));
    plot(line,data_defects,'LineWidth', 2)
              title(sprintf('B_Y Signal Response, Defects 60'))
    xlabel('Distance [mm]')
    ylabel('B_Y (Tesla)')
    xlim([0,line(end)])
    grid on
    axis square

        smoothed = smooth(data_defects,0.001,'lowess');
    [pks, loc]=findpeaks(smoothed, line,'MinPeakProminence',0.001); %alter
numbers for peak 2peak

     data_inv = -smoothed;

    [troughs, loc_t]=findpeaks(data_inv, line,'MinPeakProminence',0.001 );

        pks_60 = pks;
    troughs_60 = troughs;

     hold on
    plot(loc, pks,'or')
```

```
    plot(loc_t, -troughs, 'ob')
    hold off


    % 80%
                figure

  data_defects = data(row_80(1),850:1000);
     line = linspace(0,dist,length(data_defects));
    plot(line,data_defects,'LineWidth', 2)
                    title(sprintf('B_Y Signal Response, Defects 80'))
    xlabel('Distance [mm]')
    ylabel('B_Y (Tesla)')
    xlim([0,line(end)])
    grid on
    axis square

        smoothed = smooth(data_defects,0.001,'lowess');
    [pks, loc]=findpeaks(smoothed, line,'MinPeakProminence',0.001);

     data_inv = -smoothed;

    [troughs, loc_t]=findpeaks(data_inv, line,'MinPeakProminence',0.001 );

        pks_80 = pks;
    troughs_80 = troughs;

    hold on
    plot(loc, pks,'or')
    plot(loc_t, -troughs, 'ob')
     hold off



    pk_values_20 (i,:) = pks_20;
    pk_values_40 (i,:) = pks_40;
    pk_values_60 (i,:) = pks_60;
    pk_values_80 (i,:) = pks_80;

    trough_values_20 (i,:) = -troughs_20;
    trough_values_40 (i,:) = -troughs_40;
    trough_values_60 (i,:) = -troughs_60;
    trough_values_80 (i,:) = -troughs_80;

    pk2pk_20(i,:) = abs(pk_values_20 (i,:) - trough_values_20(i,:));
    pk2pk_40(i,:) = abs(pk_values_40 (i,:) - trough_values_40(i,:));
    pk2pk_60(i,:) = abs(pk_values_60 (i,:) - trough_values_60(i,:));
    pk2pk_80(i,:) = abs(pk_values_80 (i,:) - trough_values_80(i,:));
   end

%%%% Slow
   %% Calculating the mean pk2pk values
   mean_20_pk2pk_slow = mean(pk2pk_20(1:5,:));
   mean_40_pk2pk_slow = mean(pk2pk_40(1:5,:));
```

```
   mean_60_pk2pk_slow = mean(pk2pk_60(1:5,:));
   mean_80_pk2pk_slow = mean(pk2pk_80(1:5,:));

   mean_plot_slow = [mean_20_pk2pk_slow mean_40_pk2pk_slow mean_60_pk2pk_slow
mean_80_pk2pk_slow];


   %% Calculating standard deviation
   stdev_20_pk2pk_slow = std(pk2pk_20(1:5,:));
   stdev_40_pk2pk_slow = std(pk2pk_40(1:5,:));
   stdev_60_pk2pk_slow = std(pk2pk_60(1:5,:));
   stdev_80_pk2pk_slow = std(pk2pk_80(1:5,:));

   %%Square root of sample size
   sqrt_sample_size = sqrt(sample_size);

   %%Calculating the Standard Error
   SE_20_slow = (stdev_20_pk2pk_slow/sqrt_sample_size);
   SE_40_slow = (stdev_40_pk2pk_slow/sqrt_sample_size);
   SE_60_slow = (stdev_60_pk2pk_slow/sqrt_sample_size);
   SE_80_slow = (stdev_80_pk2pk_slow/sqrt_sample_size);

   SE_PLOT_slow = [SE_20_slow SE_40_slow SE_60_slow SE_80_slow];

   %% Calculating 95% confidence interval
   conf_95_20_slow = (1.96*SE_20_slow);
   conf_95_40_slow = (1.96*SE_40_slow);
   conf_95_60_slow = (1.96*SE_60_slow);
   conf_95_80_slow = (1.96*SE_80_slow);



%%%% Medium
   mean_20_pk2pk_medium = mean(pk2pk_20(6:10,:));
   mean_40_pk2pk_medium = mean(pk2pk_40(6:10,:));
   mean_60_pk2pk_medium = mean(pk2pk_60(6:10,:));
   mean_80_pk2pk_medium = mean(pk2pk_80(6:10,:));

   mean_plot_medium = [mean_20_pk2pk_medium mean_40_pk2pk_medium
mean_60_pk2pk_medium mean_80_pk2pk_medium];


   %% Calculating standard deviation
   stdev_20_pk2pk_medium = std(pk2pk_20(6:10,:));
   stdev_40_pk2pk_medium = std(pk2pk_40(6:10,:));
   stdev_60_pk2pk_medium = std(pk2pk_60(6:10,:));
   stdev_80_pk2pk_medium = std(pk2pk_80(6:10,:));

   %%Calculating the Standard Error
   SE_20_medium = (stdev_20_pk2pk_medium/sqrt_sample_size);
   SE_40_medium = (stdev_40_pk2pk_medium/sqrt_sample_size);
   SE_60_medium = (stdev_60_pk2pk_medium/sqrt_sample_size);
   SE_80_medium = (stdev_80_pk2pk_medium/sqrt_sample_size);
```

```
   SE_PLOT_medium = [SE_20_medium SE_40_medium SE_60_medium SE_80_medium];


   %%%%Fast
    %% Calculating the mean pk2pk values
   mean_20_pk2pk_fast = mean(pk2pk_20(11:15,:));
   mean_40_pk2pk_fast = mean(pk2pk_40(11:15,:));
   mean_60_pk2pk_fast = mean(pk2pk_60(11:15,:));
   mean_80_pk2pk_fast = mean(pk2pk_80(11:15,:));

   mean_plot_fast = [mean_20_pk2pk_fast mean_40_pk2pk_fast mean_60_pk2pk_fast
mean_80_pk2pk_fast];


   %% Calculating standard deviation
   stdev_20_pk2pk_fast = std(pk2pk_20(11:15,:));
   stdev_40_pk2pk_fast = std(pk2pk_40(11:15,:));
   stdev_60_pk2pk_fast = std(pk2pk_60(11:15,:));
   stdev_80_pk2pk_fast = std(pk2pk_80(11:15,:));

   %%Calculating the Standard Error
   SE_20_fast = (stdev_20_pk2pk_fast/sqrt_sample_size);
   SE_40_fast = (stdev_40_pk2pk_fast/sqrt_sample_size);
   SE_60_fast = (stdev_60_pk2pk_fast/sqrt_sample_size);
   SE_80_fast = (stdev_80_pk2pk_fast/sqrt_sample_size);

   SE_PLOT_fast = [SE_20_fast SE_40_fast SE_60_fast SE_80_fast];



%     upper_95_slow_20 = (mean_20_pk2pk_fast + conf_95_20_slow)


  %plotting
   figure
   hold on
    errorbar(defect_size,mean_plot_slow,SE_PLOT_slow,'linewidth',1.1)
    errorbar(defect_size,mean_plot_medium,SE_PLOT_medium,'linewidth',1.1)
    errorbar(defect_size,mean_plot_fast,SE_PLOT_fast,'linewidth',1.1)
    legend('0.57 m/s','1 m/s', '1.25 m/s','Location','northwest')

    %plotting 95%
%    plot(20, upper_95_slow_20,'ob')

   hold off
%title(sprintf('6mm Average B_Y Top Surface Defect'))
xlabel('Defect Size (%)')
ylabel('B_Y (Tesla)')
xlim([10,90])
ylim([0, 0.06])
grid on
axis square
print('average BY top.png', '-dpng', '-r600');
% saveas(gcf,'average BY top.png'
```